Sorption enhanced catalytic reforming of methane for pure hydrogen production : experimental and modeling

Sorption Enhanced Catalytic Reforming of Methane for Pure Hydrogen Production

Experimental and Modeling

PROEFSCHRIFT

ter verkrijging van de graad van doctor aan de
Technische Universiteit Eindhoven, op gezag van de
rector magnificus, prof.dr.ir. C.J. van Duijn, voor een
commissie aangewezen door het College voor
Promoties in het openbaar te verdedigen
op maandag 9 mei 2011 om 16.00 uur

door

Mohamed Hamzeh Mohamed Halabi

geboren te Mafraq, Jordanië

Dit proefschrift is goedgekeurd door de promotor:

prof.dr.ir. J.C. Schouten

Copromotor:
dr. M.H.J.M. de Croon

Technische Universiteit Eindhoven, 2011

A catalogue record is available from the Eindhoven University of Technology Library

ISBN: 978-90-386-2454-9

Printed by Gildeprint, Enschede, The Netherlands
Cover page design by Mohamed Halabi and Marina Klytina

Dedicated to the virtuous and serene souls of my parents:
Hamzeh Halabi and Samira Aqabani

Summary

H_2 is well perceived as a pollution-free energy carrier for future transportation as well as electricity generation. This thesis presents an experimental and modeling study for an improved process of sorption enhanced catalytic reforming of methane using novel catalyst/sorbent materials for low temperature high purity H_2 with in situ CO_2 capture. A highly active $Rh/Ce_{\alpha}Zr_{1-\alpha}O_2$ catalyst and K_2CO_3–promoted hydrotalcite and lithium zirconate are utilized as newly developed catalyst/sorbent materials for an efficient H_2 production at low temperature (400–500^{o}C) and pressure (1.5–4.5 bar) in a fixed bed reactor. Experimental results showed that direct production of high H_2 purity and fuel conversion (>99%) is achieved with low level of carbon oxides impurities (<100 ppm). The effect of temperature, pressure, and steam/carbon ratio on the process performance is demonstrated. The process performance is significantly improved in terms of CH_4 conversion and H_2 purity obtained using a much smaller reactor size and much less catalyst/sorbent ratio at mild operational conditions. Despite the high price of Rhodium catalyst compared to Ni catalyst, the enormous reduction of the reactor size, material loading, catalyst/sorbent ratio, and energy requirements are beneficial key factors for the success of the concept. Small size H_2 generation plants for residential or industrial application operated at a relatively low pressure range (<4.5 bar) seem to be a realistic approach according to our results.

An operational window of a gas hourly space velocity (GHSV) range from 1050 to 14000 hr^{-1}, a steam/carbon molar ratio of 4.5–6.0, and an oxygen/carbon molar ratio of 0.45–0.55 is characterized for an optimal operation of the autothermal reforming of methane in a laboratory scale fixed bed reactor. Thus, a fuel conversion of 93%, a dry-basis H_2 purity of 73%, a thermal reformer efficiency of 78%, and a yield of 2.6 mole H_2 per 1 mole of CH_4 fed are achieved at temperature of 500^{o}C and a pressure of 1.5 bar using a conventional Ni-based catalyst. The process performance under dynamic and steady state conditions is analyzed with respect to key operational parameters: temperatures of gas feed and catalyst bed, oxygen/carbon and steam/carbon ratios, GHSV, and feed contaminations.

The performance of sorption–enhanced autothermal reforming of methane for pure H_2 production is also examined. The process is theoretically analyzed for two candidate sorbents of K–promoted hydrotalcite and lithium zirconate in a fixed bed reactor using a conventional Ni/MgO steam reforming catalyst. A 1-D heterogeneous dynamic model is constructed to simulate the process, accounting for mass and thermal dispersion in the axial direction, pressure drop, and

intraparticle and interfacial resistances. The process is found to be efficient and applicable even at a low temperature of 500 ^{o}C for steam reforming reactions and at pressure as low as 4.47 bar for CO_2 adsorption. The hydrotalcite–based autothermal reforming process can provide CH_4 conversion and H_2 purity up to 85% and 96%, respectively, at operational conditions of 500 ^{o}C, 4.47 bar, steam/carbon ratio of 6, oxygen/carbon ratio of 0.45 and space velocity of 3071 hr^{-1}. The corresponding H_2 yield and purity on dry-basis are 3.6 and 95%, respectively. The lithium zirconate–based process demonstrated an enhanced CH_4 conversion of 99.5% and dry basis H_2 purity of 99.5% at similar conditions. Lithium zirconate provides higher CO_2 sorption capacity than hydrotalcite although it shows slower adsorption rates. The high heat generated during the CO_2 chemisorption on lithium zirconate is also investigated if it is sufficient to provide a heat supplement at lower oxygen/carbon ratio at adiabatic conditions of the autothermal reforming process. An oxygen/carbon ratio of less than 0.35 results in a CH_4 conversion of less than 95%.

The mechanistic aspects of the catalytic steam reforming of methane over $Rh/Ce_{0.6}Zr_{0.4}O_2$ catalyst are investigated. The kinetic experiments are performed in a tubular fixed bed reactor over a temperature range of 475 to 725 ^{o}C and a total pressure of 1.5 bar in the absence of mass transport limitations. The over all reaction orders in methane and steam are determined to be less than 1 from 475 to 625 ^{o}C. At low temperature, most of the gas product is composed of CO_2 and H_2 due to the pronounced influence of the water–gas shift reaction. At higher temperature and low steam/carbon ratio, this influence is diminished. Inhibitory effects of H_2, CO, and CO_2 on the CH_4 conversion rates are observed. Temperature–programmed steam reforming experiments over ceria–zirconia support revealed insignificant CH_4 adsorption on the surface from 550 to 725 ^{o}C. Catalyst deactivation and steady state stability over time were examined. The catalyst shows high stability and resistance to carbon formation even at a low steam/carbon ratio of 1. A molecular reaction mechanism is proposed to qualitatively explain the kinetic observations.

Detailed intrinsic kinetics of CH_4 steam reforming is developed over $Rh/Ce_{0.6}Zr_{0.4}O_2$ catalyst in a relatively low temperature range of 475–575 ^{o}C and a pressure of 1.5 bar. The kinetic experiments are conducted in an integral fixed bed reactor with no mass and heat transport limitations and far from equilibrium conditions. The model is based upon two-site adsorption surface hypothesis, and 14 elementary reaction steps are postulated. CH_4 is dissociatively adsorbed onto the Rh active sites, and steam is dissociatively adsorbed on the ceria support active sites as an influential adsorption surface shown in the model. Therefore, no competition between CH_4 and steam in adsorbing on the same site surface is observed. The kinetic rate expressions are derived according to the Langmuir-Hinshelwood formalism. The redox surface reactions between the carbon containing species and the lattice oxygen leading to CO and CO_2 formation are considered as rate determining steps. The inhibitory effect of gaseous product species is also reflected in the kinetics. The model is found to be statistically accurate and thermodynamically consistent. The reaction kinetics is validated by

steam reforming experiments at 550 ^{o}C and 1.5 bar using 150 mg catalyst in a diluted bed of 5 cm length. The kinetic model is implemented in a one-dimensional pseudo-homogenous plug flow reactor model and thus simulated at identical experimental conditions. The simulation results are in excellent agreement with the experimental values.

New set of adsorption data is reported for CO_2 adsorption over K-promoted hydrotalcite at 400 ^{o}C. The equilibrium sorption data obtained from column apparatus can be adequately described by the Freundlich isotherm. The sorbent shows fast adsorption rates and attains a relatively high sorption capacity of 0.95 mol/kg on the fresh material. The CO_2 desorption experiments are conducted to examine the effect of humidity content in the gas purge and the regeneration time on CO_2 desorption rates. Large portion of CO_2 is easily recovered in the first few minutes of a desorption cycle due to a fast desorption step, which is associated with a physi/chemisorption step on the monolayer surface of the fresh sorbent. The complete recovery of CO_2 was then achieved in a slower desorption step associated with a reversible chemisorption in a multi-layer surface of the sorbent. The sorbent shows a loss of 8% of its fresh capacity due to an irreversible chemisorption. Cyclic experiments showed that the sorbent maintains a stable working capacity of about 0.89 mol/kg suggesting a reversible chemisorption process and good thermal stability in the temperature range of 400–500 ^{o}C.

The presence of a highly active catalyst such as Rh dictates strict requirements on the associated sorbent in terms of fast CO_2 sorption kinetics for an efficient performance of the sorption–enhanced steam reforming process. Particle–based model, heterogeneous plug flow bulk–scale model, and homogenous plug flow bulk–scale model are constructed to theoretically analyze the process. The process is studied using two bed configurations of an integrated dual function particle and an admixture bed of catalyst/sorbent particles. The CH_4 conversion enhancement is found to be a strong function of the CO_2 sorption kinetics. This conversion enhancement is not affected by a higher sorbent capacity at slow adsorption kinetics. The optimal catalyst/sorbent ratio is determined to be a function of the operating conditions. This ratio is represented in a catalyst composition of 1–3 wt.% in the admixture bed or in the dual function particle at low temperature of 550^{o}C, intermediate pressure of 4.65 bar, and low gas flow rate of 0.05 kg/m^2.s. The catalyst composition is increased to 10 wt.% at a higher pressure of 15 bar and higher gas flowrate of 1.5 kg/m^2.s.

CH_4 conversion enhancement is studied at different temperature and pressure. The maximum conversion enhancement is obtained at a low temperature of 450 ^{o}C and a high pressure of 15.6 bar; at which carbon oxides impurities can be as low as 100 ppm. Optimal operating conditions for hydrotalcite–based system are identified to provide CH_4 conversion of 98% with high H_2 purity of 99.8% and low CO_2 contamination (<250 ppm). Lithium zirconate–based system can provide CH_4 conversion and H_2 purity of 99.9% at identical conditions. The dual function particle system and the admixture bed system show a very similar performance in

terms of the maximum CH_4 conversion and product composition in the case of the lithium zirconate sorbent. Discrepancy in performance is observed in the case of the hydrotalcite sorbent. The effect of the physical characteristics of the particle and the bed on CH_4 conversion and adsorption rates is determined at different particle size, particle voidage, pore diameter, tortuosity, and bed voidage.

Samenvatting

H_2 wordt beschouwd als een schone energiedrager voor toepassing in transport en elektriciteitsproductie. In dit proefschrift worden zowel een experimentele als een modelleringstudie gepresenteerd naar een door middel van sorptie versterkte katalytische omzetting van methaan met nieuwe katalysator/sorptie materialen waarmee op een lage temperatuur zeer zuiver waterstof geproduceerd wordt en CO_2 wordt afgevangen. Deze nieuwe materialen zijn een zeer actieve $Rh/Ce_{\alpha}Zr_{1-\alpha}O_2$ katalysator en K_2CO_3–promoted hydrotalciet en lithium zirconaat als sorptiematerialen voor een efficiënte H_2 productie bij een lage temperatuur (400–500^{o}C) en druk (1.5–4.5 bar) in een fixed bed reactor. Experimenten laten zien dat de directe productie van zeer zuiver waterstof (>99%) met een verwaarloosbare hoeveelheid aan koolstofoxides (<100 ppm) mogelijk is. De effecten van temperatuur, druk en S/C verhouding op dit proces zijn beschreven. Bij een lage druk en temperatuur verbeterden de methaanconversie en de waterstofzuiverheid aanzienlijk bij het gebruik van een kleinere reactor en een lagere verhouding katalysator/sorptiemateriaal. Ondanks de hoge kosten voor de rhodium katalysator vergeleken met de nikkel katalysator, is er veel voordeel te behalen door de reductie van de reactorgrootte, de katalysatorlading, de verhouding katalysator/sorptiemateriaal en door het lagere energie gebruik. Uit onze resultaten blijkt dat door de lage operationele druk (<4.5 bar), kleine waterstofproductie-units voor residentiële en industriële toepassingen een realistisch perspectief hebben.

Voor de optimale werking van een autotherme omzetting van methaan in een fixed bed reactor op laboratoriumschaal, is een optimaal operatiegebied gevonden voor een gas hourly space velocity (GHSV) van 1050 tot 14000 hr^{-1}, een molaire verhouding stoom/koolstof van 4.5–6.0 en een molaire verhouding zuurstof /koolstof van 0.45–0.55. In dit operatiegebied wordt een voedingsconversie van 93%, een droge waterstofzuiverheid van 73 %, een thermische omzettingsefficiëntie van 78% en een opbrengst van 2.6 mol waterstof per mol methaan gehaald, bij een temperatuur van 500^{o}C, een druk van 1.5 bar en met gebruik van een conventionele Ni-katalysator. De procesprestaties zijn voor dynamische en steady state operatie geanalyseerd met betrekking tot temperatuur van het voedingsgas en van het katalysatorbed, verhoudingen van zuurstof/koolstof en stoom/koolstof, GHSV en verontreinigingen in voedingsstroom.

Voor de productie van zuivere waterstof is gekeken naar de prestaties van de sorptie versterkte autotherme methaanreforming. Dit proces is theoretisch geanalyseerd voor twee adsorptiematerialen. Hierbij is gekeken naar de werking

van K–promoted hydrotalciet en lithiumzirconaat in een fixed bed reactor bij gebruik van een conventionele Ni/MgO stoomreformingkatalysator. Met een één-dimensionaal heterogeen dynamisch simulatiemodel is gekeken naar de massa- en temperatuurverdeling in axiale richting, de drukval en de interne en externe transportweerstanden van de katalysatordeeltjes. Het proces bleek efficiënt toepasbaar voor stoomreformingreacties bij lage temperaturen tot 500 ^{o}C en voor CO_2 adsorptie bij lage drukken tot 4.47 bar. De methaanconversie en waterstofzuiverheid van het op hydrocalciet gebaseerde autotherme reformingproces zijn respectievelijk 85% en 96%, bij een temperatuur van 500 ^{o}C, werkdruk van 4.47 bar, verhouding stoom/koolstof van 6, verhouding zuurstof/koolstof van 0.45 en een GHSV van 3071 hr^{-1}. De bijbehorende waterstofopbrengst en droge waterstofzuiverheid zijn 3.6 en 95%. Onder dezelfde omstandigheden geeft het op lithium zirconaat gebaseerde proces een verbeterde methaanconversie van 99.5% en een droge waterstofzuiverheid van 99.5%. Lithium zirconaat biedt een hogere CO_2 adsorptie capaciteit dan hydrocalciet hoewel de adsorptie-snelheid lager is. Ook is onderzocht of de vrijkomende warmte bij de CO_2 adsorptie aan het lithiumzicronaat voldoende is voor een lagere zuurstof/koolstof verhouding bij de adiabatische condities van het autothermische omzettingproces. Een verhouding zuurstof/koolstof van minder dan 0.35 resulteert in een methaanconversie van minder dan 95%.

Voor de katalytische stoomreforming van methaan over de $Rh/Ce_{0.6}Zr_{0.4}O_2$ katalysator is het reactiemechanisme onderzocht. De kinetische experimenten zijn uitgevoerd in een fixed bed buisreactor bij temperaturen van 475 tot 725 ^{o}C en bij een totale druk van 1.5 bar. Dit proces is kinetisch gelimiteerd. De ordes van de reactie voor methaan en stoom bleken kleiner dan 1 te zijn voor het temperatuurbereik van 475 to 625 ^{o}C. Bij een lage temperatuur bestaat het grootste deel van het gasproduct uit CO_2 en H_2 vanwege de grote invloed van de water-gas-shift reactie. Dit effect verdwijnt bij een hoge temperatuur en een lage verhouding stoom/koolstof. De remmende effecten van H_2, CO en CO_2 op de methaanconversie zijn waargenomen. Temperatuurgeprogrammeerde experimenten voor de stoomreforming met het ceria-zirconia dragermateriaal lieten een significante adsorptie van methaan aan het oppervlak zien bij temperaturen van 550 tot 725 ^{o}C. Katalysator deactivering en processtabiliteit in de tijd zijn onderzocht. De katalysator heeft een goede stabiliteit en weerstand tegen koolafzetting, zelfs bij een verhouding stoom/koolstof van 1. Voor een kwalitatieve uitleg van de kinetische waarnemingen is een moleculair reactiemechanisme opgesteld.

Een gedetailleerd intrinsiek kinetisch model is ontwikkeld voor de methaan stoomreforming over de $Rh/Ce_{0.6}Zr_{0.4}O_2$ katalysator voor een relatief laag temperatuur bereik van 475 tot 575 ^{o}C en een druk van 1.5 bar. De experimenten zijn uitgevoerd in een geintegreerde fixed bed reactor zonder massa- en warmteoverdracht limiteringen en buiten de evenwichtscondities. Het model is gebaseerd op de hypothese van twee verschillende actieve plaatsen op het oppervlak. Er zijn 14 elementaire reactiestappen gepostuleerd. Methaan wordt dissociatief geadsorbeerd op de actieve rhodium plaatsen. Stoom wordt dissociatief

geadsorbeerd op de actieve plaatsen op het ceria dragermateriaal wat een belangrijk adsorptieoppervlak bleek in het model. Er is dus geen concurrentie bij de adsorptie tussen het methaan en het stoom. De vergelijkingen voor de reactiesnelheden zijn opgesteld volgens het Langmuir-Hinshelwood model. De redox oppervlakreacties tussen de koolstof bevattende stoffen en de zuurstof in het rooster, welke leiden tot de vorming van CO en CO_2, worden beschouwd als de snelheidbepalend stappen. Het remmende effect van gasvormige producten komt tot uiting in de kinetiek. Het model blijkt statistisch correct en thermodynamisch consistent te zijn. De reactiekinetiek is gevalideerd voor stoomreforming experimenten bij 550 ^{o}C en 1.5 bar met 150 mg katalysator in een verdund bed van 5 cm lengte. Het kinetisch model is geïmplementeerd in een één-dimensionaal model van een pseudo homogene propstroomreactor. De gesimuleerde omstandigheden komen dus overeen met de experimentele reactor condities. De resultaten van de simulaties zijn in uitstekende overeenstemming met de gemeten experimentele waarden.

Er zijn nieuwe data gerapporteerd voor CO_2 adsorptie aan K-promoted hydrotalciet bij 400 ^{o}C. De evenwichtgegevens voor adsorptie is verkregen met een kolomapparaat dat goed kan worden beschreven met een Freundlich-isotherm. Het sorptiemateriaal toont een grote adsorptiesnelheid en bereikt een hoge adsorptiecapaciteit van 0.95 mol/kg op het verse materiaal. De CO_2 desorptie experimenten zijn uitgevoerd voor het bepalen van de effecten van het vochtgehalte in het spoelgas en regeneratietijd op de CO_2 desorptiesnelheden. Een groot deel van de CO_2 is eenvoudig terug te winnen in de eerste minuten van de cyclus vanwege een snelle desorptiestap welke te associëren is met de fysi/chemisorptie aan het monolaagoppervlak van het verse sorptiemateriaal. De volledige terugwinning van CO_2 gaat met een langzamere desorptiestap in verband met de omkeerbare chemisorptie van het multilaagoppervlak van het sorptiemateriaal. Er is een afname van capaciteit van 8 % ten opzichte van vers sorptiemateriaal vanwege onomkeerbare chemisorptie. Cyclische experimenten tonen aan dat het sorptiemateriaal een stabiele werkcapaciteit heeft van ongeveer 0.89 mol/kg, wat duidt op een omkeerbaar chemisorptieproces en een goede thermische stabiliteit voor het temperatuurgebied van 400-500 ^{o}C.

De aanwezigheid van een zeer actieve katalysator, zoals Rh, stelt strenge eisen aan het adsorptiemateriaal in termen van snelle CO_2-sorptie kinetiek voor een efficiënte prestatie van het sorptieversterkte stoomreformingproces. Een deeltjes model, een heterogeen propstroommodel op bulk schaal en een homogeen propstroommodel op bulk schaal zijn gebouwd voor het theoretisch analyseren van het proces. Het proces wordt bestudeerd met behulp van twee reactorbedconfiguraties, één met integraal dubbelfunctionele deeltjes en één als mengbed van katalysator- en sorptiedeeltjes. De verhoging van de methaanconversie blijkt sterk afhankelijk te zijn van de CO_2-sorptiekinetiek. Deze conversieverhoging wordt niet beïnvloed door een hogere capaciteit van het sorptiemateriaal bij een trage adsoptiekinetiek. De optimale verhouding katalysator/sorptiemateriaal is bepaald als functie van de procesomstandigheden. Deze verhouding is bepaald bij een katalysatorgehalte van 1-3 wt.% zowel in het mengbed als in de dubbelfunctionele deeltjes bij een lage

temperatuur van 550 ^{o}C, een middendruk van 4.65 bar en een lage gasstroom van 0.05 kg/ m^2.s. De verhoging van de methaanconversie is onderzocht bij verschillende temperaturen en drukken. De maximale conversieverhoging is gevonden bij een lage temperatuur van 450 ^{o}C en een hoge druk van 15.6 bar. Hierbij is de vervuiling met koolstofoxides rond de 100 ppm. De optimale procescondities voor het op hydrocalciet gebaseerde systeem, zijn bepaald voor een methaanconversie van 98% met een hoge waterstofzuiverheid van 99.8 en lage CO_2 vervuiling (<250 ppm). Het op lithiumzirconaat gebaseerde systeem kan een methaanconversie en waterstofzuiverheid van 99.9% halen bij dezelfde procescondities. Het bed met de dubbelfunctionele deeltjes en het mengbed vertonen zeer vergelijkbare prestaties voor de maximale methaanconversie en productsamenstelling in het geval van het lithiumzirconaat sorptiemateriaal. Een verschil in prestatie is waargenomen bij het hydrotalcietsorptiemateriaal. De effecten van fysische eigenschappen van de deeltjes en het reactorbed op de methaanconversie en de adsorptiesnelheden zijn bepaald voor verschillende deeltjegroottes, deeltjes porositeit, poriëndiameter, tortuositeit en bedporositeit.

Table of Contents

Chapter 1

Introduction

1.1 Hydrogen – status and future

Hydrogen is the lightest and the most abundant chemical species constituting about 75% of the universe's elemental mass, and as a gas, it is colorless, odorless, and has no taste. H_2 is a vital raw material in chemical and petrochemical industries. The vast majority of hydrogen produced today in the world is used in ammonia synthesis, methanol synthesis, and in various refinery hydrotreating processes [1–3]. H_2 can be practically produced from diverse resources including fossil fuels such as coal and natural gas, biomass, and other renewable sources such as wind, solar, geothermal, and hydroelectric power [4]. The demand for more H_2 in petrochemical industry is expected to grow as more hydrotreating processes are operated to clean heavy crude oils from high sulfur content. So far, natural gas is the most common source for H_2 production. There are several technologies used to convert natural gas into H_2 [5]: steam reforming, partial oxidation, and autoihermal reforming. CH_4 steam reforming is considered as the most important process; about 50% of the total H_2 produced in the world is achieved using steam reforming [3], see Figure 1. This is a multistep endothermic reforming process operated at a high temperature (800–950 ^oC) and high pressure (20–40 bar) to convert methane into a

mixture of syngas (H_2 and CO) and CO_2. Partial oxidation and catalytic partial oxidation of methane with oxygen achieve a H_2/CO product ratio of 1–1.8. Autothermal reforming uses oxygen and steam to generate H_2/CO ratio of about 2. Currently catalytic partial oxidation and autothermal reforming processes are subjected to more costs due to the oxygen required, especially for low volume H_2 production.

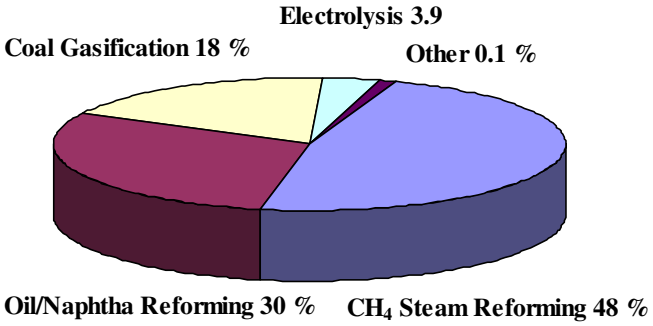

Fig. 1: Current distribution in the conversion of the primary energy sources into H_2 [3].

Excess steam/methane ratio of about 3 is used in standard steam reforming process to achieve high fuel conversion and to reduce carbon formation. A typical composition of a reformer outlet syngas is (74 vol% H_2, 18 vol% CO, 6 vol% CO_2, and 2 vol% CH_2) [6,7]. After two stages of high and low water–gas shift (WGS) conversion, CO concentration drops to 0.4 vol%. The gas passes further purification units to remove the bulk CO_2 and the residual CO_2. Average purity of H_2 after these stages are 97 vol%. High purity H_2 at 99.99% can be obtained by additional purification with pressure swing adsorption unit. Six major process steps are involved, reforming, two WGS stages, PSA separation and regeneration with amine scrubbing or steam stripping, and CO removal [5–7]. The process is very energy intensive, as it is operated at high temperature; the energy released from the exothermic WGS reaction is not efficiently used. The conventional process of steam reforming is limited in H_2 productivity and CH_4 feedstock conversion due to the thermodynamic bounds on the reversible steam reforming reactions. At such elevated temperature the catalyst undergoes deactivation due to carbon formation, also resulting in blockage of reformer tubes and increased pressure drops [7]. Expensive alloy reformer tubes must be used to withstand the harsh reaction conditions. Temperature, pressure, and gas composition must be carefully controlled to avoid carbon deposition and hot-spotting. Moreover, steam reforming process is associated with huge CO_2 emissions. The average total CO_2 emissions from this process approach 0.42 m^3 CO_2/m^3 H_2 produced [8]. Therefore, it will be extremely desirable if smart concepts for production of H_2 by steam reforming can be developed, which reduce the capital cost compared to the conventional route. Reaction enhancement, obtained by removing either H_2 or CO_2, may enable a lower

temperature of operation, which in turn may alleviate the problems associated with catalyst fouling, high process energy requirements and poor energy integration within the plant environment.

However, H_2 is also seen as a pollution-free energy carrier and may emerge as a promising alternative in electric power generation plants and as transportation fuel [9]. Given, the attractive application of H_2-powered fuel cells for small-scale energy generation, H_2 is essentially converted to water with no CO_2 emissions. Thus, if it produced from a non-fossil fuel, it can be considered as a truly green-fuel with zero pollution. The current forecast for H_2-based economy suggests a dramatic rise for H_2 production due to the increasing developments in the fuel cell technology. Other routes for H_2 production such as CO_2 reforming, steam reforming with CO_2 capture, CH_4 decomposition, biomass conversion, water electrolysis and photocatalysis, are all substantial techniques for H_2-based future economy [3].

1.2 CO_2 capture and storage

The increase in the average temperature of the air near the earth surface is nowadays defined as the global warming. CO_2 is characterized a major greenhouse gas that is responsible for the global warming effect due to escalating levels of this gas concentration into the atmopshere. The concentration of CO_2 has increased by 36% since the industrial revolution to reach 388 ppmv in 2010 [10] as a result of human activity represented mainly in burning of fossil fuel and deforestation or land use [11], see Figure 2. Scientists who have elaborated on the Arrhenius theory of global warming are much concerned that such huge emissions of CO_2 to the atmosphere are causing unprecedented rise in global temperature with potential harmful consequences on human health and environment. Carbon emissions forecast resulted mainly from energy generating plants and cement industry reaches about 9 billion tons on annual basis in the present day, see Figure 3.

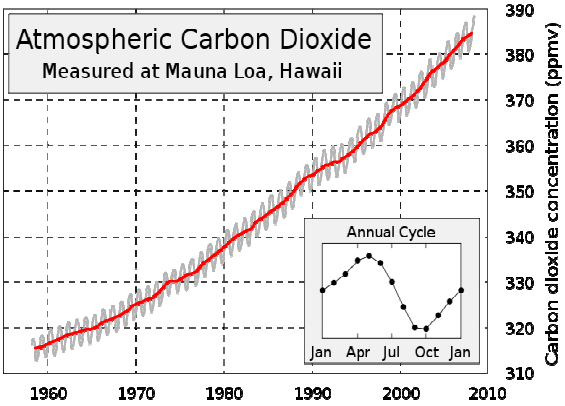

Fig. 2: CO_2 emissions to the atmosphere during the last 50 years [10].

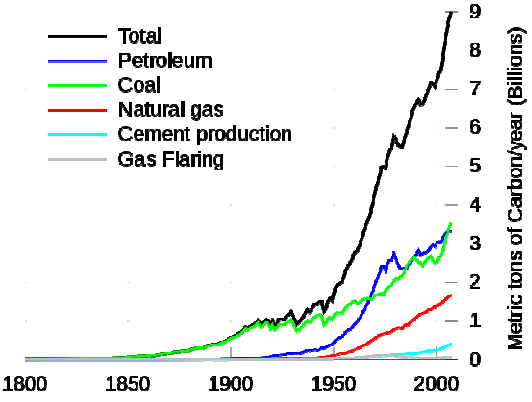

Fig. 3: Carbon emissions to the atmosphere as a result of fossil fuel burning and industrial activity [10].

Carbon capture and storage (or sequestration) (CCS) is recently presented as a technique of mitigating the contribution of fossil fuel emissions to the global

warming by capturing CO_2 from large point sources of CO_2 such as power generation plants and large industrial processes. Some of these sources could also directly supply decarbonized fuel such as H_2 to reduce CO_2 emissions. CCS simply involves the use of technology to collect and concentrate CO_2 produced in the industrial or energy related process, transport CO_2 to a suitable storage location, and eventually store it on a long term basis. Figure 4 globally presents the major three components of the CSS technology. For fuel burning process such as power generating plants CO_2 separation technology can be applied as a post-combustion stage or to decarbonize the fuel as a pre-combustion stage. Captured CO_2 should be compressed first to a high density at the plant facility to facilitate its transport. Thereafter, CO_2 is stored in one of the currently available storage methods; injection in deep geological formation, deep ocean, or industrial fixation in inorganic mineral carbonates [11].

In geological storage, CO_2 is generally injected in supercritical form into geological formation such as oil fields, gas fields, and saline formation. Physical and geochemical trapping mechanism would prevent CO_2 to escape to the atmosphere. CO_2 can also be injected in declining oil fields to enhance oil recovery.

Ocean storage presents serious risk due to poor understanding for the associated environmental effects. Large CO_2 concentration in the ocean kills the living organisms, and ocean acidity increases as CO_2 forms carbonic acid when it reacts with water. Moreover, the dissolved CO_2 would eventually equilibrate with the atmosphere, and thus no permanent storage is achieved.

Carbon sequestration in minerals such as those containing Mg and Ca has unique advantages. The produced carbonates have lower energy than CO_2, thus mineral carbonation is thermodynamically favorable and naturally occurs. The raw material such as Mg based minerals is abundant in nature. The produced carbonates are stable and thus, CO_2 escape to the atmosphere is not likely.

However, the long term carbon storage is a new concept. The first commercial application is an integrated CCS power plant that started operation in 2008 in eastern German power plant Schwarze Pumpe run by Vattenfall [10]. As the CCS technology reduces the CO_2 emissions to the atmosphere by 80-90%, it also requires much energy. Thus, the cost of energy from a power plant with CCS is expected to increase by at least 21%.

However, the captured CO_2 can find several useful re-use applications. CO_2 can be potentially converted into hydrocarbons where it can be reused as a fuel or a feedstock in plastic industry. Methanol can be rather easily synthesized from CO_2 and H_2. In high temperature of about 2400 ^oC, CO_2 can be split in CO and oxygen.

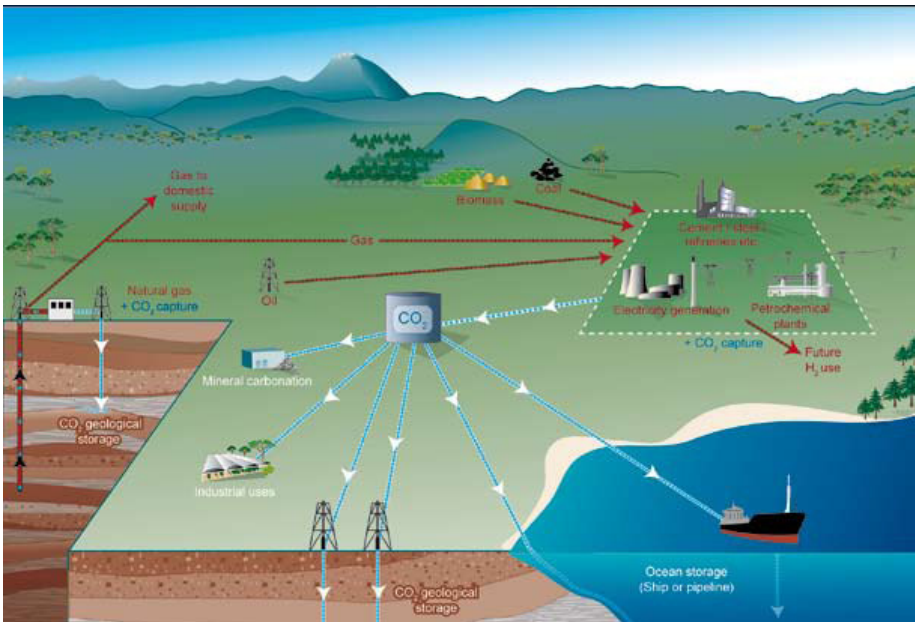

Fig. 4: Schematic diagram of possible carbon capture and storage systems (carbon capture, transport, and storage) [11].

1.3 Sorption–enhanced reforming technology

New concepts for CO_2 capture in pre-combustion stages associated with power generation plant are classified as membrane assisted process, chemical looping technology, and sorption enhanced technology. The sorption–enhanced steam reforming and autothermal reforming of natural gas is an innovative concept of pre-combustion decarbonization technology to convert fuel (natural gas) into higher heating value and high purity fuel (H_2) with in situ CO_2 capture. This transforms the standard steam reforming process that depends on natural gas into a clean technology. CO_2 emissions involved in the modified process are almost equal to those produced from renewable based processes such as wind or water electrolysis [3], see Figure 5. The key idea of the process is shifting the thermodynamic equilibrium imposed on steam reforming reactions toward the H_2 product direction via selectively adsorbing the co-generated CO_2 on a proper and an effective sorbent [12,13]. The reaction is performed over an admixture bed of a certain catalyst to sorbent ratio. Several advantages can be gained from this concept such as (1) lower operational temperatures (400–500 ^{o}C) than those in conventional steam reformers, (2) the process is presumed to achieve a conversion higher than 95% even at relatively lower temperatures, (3) production of high purity H_2 (> 95%) at feed gas pressure of 4 to 20 bar, (4) lower capital costs, (5) minimization of unfavorable side reactions, (6) elimination of downstream H_2 purification steps, (7) reduction of excess steam used in conventional steam reformers, and (8) reduction of CO in the gas effluent to ppm levels, and (9) the adsorbed CO_2 is purely obtained for sequestration in geological formation.

A typical CO_2 adsorbent material must have (1) high selectivity, (2) high adsorption capacity, (3) adequate adsorption/desorption kinetics at the operating conditions, (4) good stability after repeated adsorption/desorption cycles, (5) good

mechanical strength after cycle exposure to high pressure streams [13]. Hydrotalcite-like compounds (HTC), and lithium zirconate solids (LZC) seem to be potential CO_2 sorbents out of a family that also includes carbon-based adsorbents, metal-oxide sorbents, and zeolites [14].

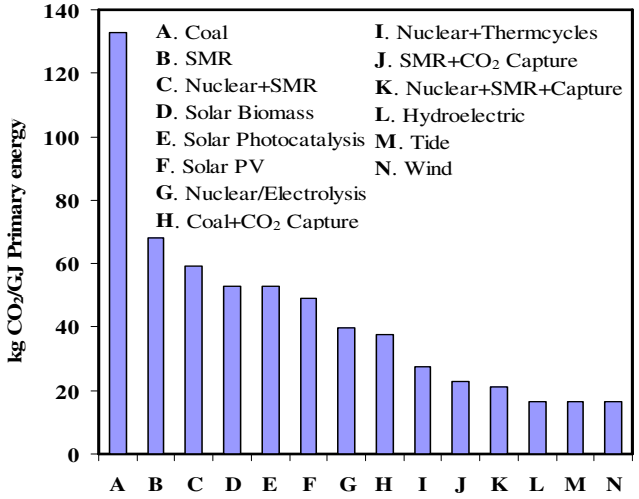

Fig. 5: Residual CO_2 associated with the conversion of 1 GJ of primary energy into H_2 from different sources [3].

Hydrotalcite–like materials have been found to have an adequate CO_2 working sorption capacity (0.45–1.0 mol/kg) at temperature of 400–450 ^oC [13,14], infinite selectively for CO_2 even in presence of steam, steam has been determined to enhance the sorption capacity and stability, very good cyclic stability, fast sorption kinetics, and relatively easy desorption rates due to low to moderate heats of chemisorption in the Henry's law region (weak bonding to CO_2) [14]. Therefore, these materials are considered to be promising sorbents for high purity H_2 production for the sorption–enhanced steam reforming of methane. However, the sorbent composition and the preparation methods will eventually determine the final properties of the material. So far, excluding our work, all sorption–enhanced reforming processes which are in the development stages use the conventional Ni-based catalyst. Ding and Alpay [12] obtained 75% CH_4 conversion and H_2 purity >90% in a laboratory scale fixed bed using a steam/carbon ratio of 6 at a temperature of 450 ^oC and a pressure of 4.45 bar. Hufton et al. [14] achieved a H_2 product stream with a purity of 95% and CH_4 fuel conversion of 80% and $CO+CO_2$ concentration of less than 50 ppm at 450 ^oC and 4.7 bar.

Recently, more attention has been given to the utilization of lithium zirconate (LZC) and lithium orthosilicate (LOS) materials as high capacity candidate sorbents at high temperature. LZC and LOS have recently received more attention due to their ability to retain good CO_2 chemisorption capacity at high temperature (5.0 mol/kg [15] and at 6.13 mol/kg [16] at 800^oC, respectively). However, the slow sorption kinetics and the high heat of reaction due to the strong chemical bonding to CO_2 require high regeneration temperature (900 ^oC for LZC [15] and 700 ^oC for LOS [16], respectively).

It was shown that pure Li_2ZrO_3 absorbs a large amount of CO_2 at a high temperature with a slow sorption rate. Addition of potassium carbonate (K_2CO_3) and lithium carbonate (Li_2CO_3) to the Li_2ZrO_3 remarkably improves the CO_2 sorption rate of the LZC materials. Fernandez et al. [15] demonstrated that using a hydrotalcite-derived Ni catalyst and lithium zirconate sorbent, H_2 purity of 90 to 95% with a corresponding CH_4 conversion of 70 to 87% can be obtained depending on the steam/carbon ratio.

1.4 Research scope and thesis layout

This thesis presents an experimental and modeling work for an innovative concept of H_2 production from natural gas with in situ CO_2 capture at relatively mild operational conditions of temperature and pressure. The project is performed in collaboration with the Energy Research Center of the Netherlands (ECN) and financially supported by SenterNovem (project no. 10002820). The focus of this research project is to demonstrate a proof-of-concept for the sorption–enhanced reforming technique using newly developed materials (sorbent and catalyst) for high purity H_2 production at low temperature (<500 ^oC). Hydrotalcite-like compounds (HTC) and lithium zirconate (LZC) solids are essentially examined as promising CO_2 sorbents. Nearly all the experimental attempts on the utilization of HTC in sorption–enhanced H_2 production apply a conventional low activity Ni-based catalyst. Hence, $Rh/Ce_\alpha Zr_{1-\alpha}O_2$ is investigated in this work as an effective catalyst, which provides high reaction rates in a low–temperature steam reforming process (<500 ^oC). This is beneficial in terms of energy saving, and production rates. Furthermore, the integration of a highly active catalyst and a proper sorbent implies several benefits in terms of (i) much lower capital costs due to the significantly smaller reactor volume, (ii) much lower catalyst loading, the reactor can be packed with catalyst as low as 1–10% only (as shown in this thesis), (iii) high purity fuel-cell grade H_2 production at low temperature (450–500 ^oC) and pressure (1.5–4.5 bar), and (iv) high pressure operation up to 25 bar can also yield high purity H_2 for electricity generation in gas turbine cycles.

The scope of this thesis is categorized in the following themes: (i) mathematical modeling of the autothermal reforming and the sorption–enhanced autothermal reforming of methane over two candidate sorbents (HTC and LZC), (ii) experimental study for the low-temperature steam reforming of methane over a Rh-based catalyst, (iii) intrinsic kinetics derivation for methane steam reforming over the catalyst, (iv) experimental and modeling investigation of the sorption–enhanced steam reforming process in a fixed bed reactor using an admixture bed consisited of catalyst/sorbent particles. $Rh/Ce_\alpha Zr_{1-\alpha}O_2$ is employed as a catalyst and K-promoted hydrotalcite is utilized as a sorbent.

The research can typically be projected in the multiphase reactor engineering field. However, the thesis consists of multi-disciplinary areas of: (i) catalysis in terms of catalyst characterization, activity testing, stability, and reaction performance study, (ii) catalytic reaction engineering in terms of kinetics derivation, kinetic modeling,

and reactor design, (iii) adsorption studies in terms of the development of CO_2 sorption isotherms, and sorption/desorption cyclic operation, and (iv) mathematical molding.

This thesis is an assemblage of a series of papers published and/or to be published in the relevant journals on this topic. Every chapter can be seen as a stand-alone research paper. However, some redundancy of information can be encountered especially in the first two chapters (1 and 2).

Chapter 1 includes an introduction to the thesis. A general overview, research scope and thesis outline are addressed. A concise relevant literature review for the H_2 production techniques and CO_2 capture techniques is provided in **Chapter 2**. The most important processes of steam reforming, catalytic partial oxidation, and autothermal reforming of natural gas for H_2 production are described. Classical CO_2 capture via chemical/physical absorption, adsorption, membrane separation, and cryogenic processes are briefly addressed. The novel concepts of CO_2 capture in pre-combustion decarbonization stages in the energy production plants using membrane assisted process, chemical looping technology, and sorption enhanced technology are discussed.

Chapter 3 presents an overview of the experimental fixed bed reactor setup. The design criteria, operational conditions, and gas analysis techniques are described. The definition and determination of gas transport parameters are also included.

Chapter 4 deals with methane autothermal reforming over a conventional Ni-based catalyst with a mathematical modeling approach at lab-scale conditions. The process is optimized in terms of fuel conversion, reforming efficiency, and H_2 purity and yield in a fixed bed reactor. The process performance under dynamic and steady state conditions is analyzed with respect to major operational parameters. An optimal operational window of GHSV, oxygen/carbon ratio, and steam/carbon ratio is characterized.

Up to the time that this research is conducted, there has been no work reported in literature that studies the process of sorption–enhanced autothermal reforming of methane over any type of sorbents. **Chapter 5** inherently provides a theoretical analysis for the sorption–enhanced concept coupled with the autothermal reforming of methane over K-promoted HTC and LZC as potential CO_2 sorbents. However, a conventional Ni-based catalyst is used for the reforming reactions. The benefit of utilizing these sorbents in improving the performance of methane autothermal reforming concerning mainly fuel conversion enhancement, H_2 output purity and productivity is demonstrated. The influence of major parameters such as steam/carbon, oxygen/carbon, catalyst/sorbent, gas temperatures, gas space velocity (GHSV), sorbent capacity, particle diameter, and total pressure is also examined.

Chapter 6 presents a solid experimental investigation of CH_4 stream reforming over a $Rh/Ce_aZr_{1-a}O_2$ catalyst at low temperature range of 475–700 ^oC. The

mechanistic aspects of the steam reforming reaction and catalyst performance are analyzed. Experimental kinetic results are demonstrated for the steam reforming and water–gas shift reactions over the $Rh/Ce_{\alpha}Zr_{1-\alpha}O_2$ catalyst and the $Ce_{\alpha}Zr_{1-\alpha}O_2$ support. The role of the support in steam reforming reactions is illustrated and the influence of gas phase product species on the CH_4 reaction rates is examined. A molecular reaction mechanism is proposed to qualitatively describe the kinetic observations and to serve as a solid basis for the derivation of an intrinsic kinetics model. Moreover, the catalyst activity, stability, and resistance towards carbon formation are also investigated.

Chapter 7 reveals a comprehensive derivation for the intrinsic kinetics of CH_4 steam reforming over $Rh/Ce_{\alpha}Zr_{1-\alpha}O_2$ in a low temperature range of 475–575 ^{o}C and 1.5 bar. The measured kinetic data are guaranteed to be far from equilibrium and diffusional limitations. The derived mathematical model is checked for thermodynamic consistency and validated with experimental data using one–dimensional pseudo–homogenous plug flow model.

Yet to date, the experimental and theoretical studies that have been reported in literature for sorption–enhanced steam reforming primarily deals with the Ni–based catalyst as a conventional steam reforming catalyst. The presence of a highly active catalyst such as Rh in an integrated reaction/adsorption process imposes strict kinetic and capacity requirements for the associated sorbent. Therefore, the applicability of integration between a highly active catalyst such as Rh with the currently available HTC and LZC solids are investigated in **Chapter 8** for an efficient H_2 production with in situ CO_2 capture. The chapter demonstrates a theoretical analysis for the sorption–enhanced process using three fundamental modeling levels: a heterogeneous particle–based level, a heterogeneous bulk–scale level, and a homogenous bulk–scale level for a fixed bed reactor at low temperature (<600 ^{o}C).

Chapter 9 consists of a solid experimental investigation of the sorption–enhanced steam reforming process over the $Rh/Ce_{\alpha}Zr_{1-\alpha}O_2$/K-promoted HTC as a novel catalyst/sorbent system for pure H_2 production with in situ CO_2 capture at low temperature (<500 ^{o}C). Direct production of high H_2 purity and high fuel conversion >99% with low level of carbon oxides impurities <100 ppm is experimentally demonstrated. The effect of temperature, pressure, and steam/carbon ratio on the process performance is illustrated. New set of experimental data for CO_2 sorption on a high capacity K-promoted HTC is presented. The sorbent performance is also studied in terms of CO_2 desorption phenomenon, cyclic stability and thermal resistance.

Finally **Chapter 10** summarizes the general conclusions of the research and implies several recommendations for the improvement of the process. Future perspective for the H_2 production process with in situ CO_2 capture is suggested in light of process intensification features, reactor design configuration, and catalysis and sorption materials.

References

1. Armor, J.N., Catalysis and the hydrogen economy, Catalysis Letters 101 (2005) 131–135.
2. Barreto, L., Makihira, A., Riahi, K., The hydrogen economy in the 21st century: a sustainable development scenario, Int. J. Hydrogen Energy 28 (2003) 267–84.
3. Ewan, B.C.R., Allen, R.W.K., A figure merit assessment of the routes to hydrogen, Int. J. Hydrogen Energy 30 (2005) 809–819.
4. Holladay, J.D., Hu, J., King, D.L., Wang, Y., An overview of hydrogen production technologies, 139 (2009) 244–260.
5. Rostrup-Nielsen, J.R. Production of synthesis gas. Catal. Tod. 18 (1993) 305–324.
6. Pena M.A.; Gómez, J.P.; Fierro, J.L.G. New catalytic routes for syngas and hydrogen production, App. Catal A, 144 (1996) 7–57.
7. Dybkjaer, I., Tubular reforming and autothermal reforming of natural gas—an overview of available processes, Fuel Process Tech. 42 (1995) 85–107.
8. Aasberg-Petersen, K., Christensen, T.S., Nielsen, C.S., and Dybkjaer, I., Recent developments in autothermal reforming and pre-reforming for synthesis gas production in GTL applications, Fuel Processing Tech. 83 (2003) 253–261.
9. Rostrup-Nielsen, J.R. Fuels and energy for the future: The role of catalysis. Catal. Rev. 46 (2004) 247–270.
10. http://en.wikipedia.org/wiki/Global_warming.
11. Rubin, E., Meyer, L., Coninck, H., carbon dioxide capture and storage. (2010) IPCC Special report.
12. Ding, Y., Alpay, E. Adsorption-enhanced steam-methane reforming. Chem. Eng. Sci. 55 (2000) 3929–3940.
13. Lee, K. B.; Beaver, M. G.; Caram, H. S.; Sircar, S. Reversible chemisorbents for carbon dioxide and their potential application. Ind. Eng. Chem. Res. 47 (2008) 8048–8062.
14. Hufton, J. R., Mayorga, S., Sircar, S. Sorption-enhanced reaction process for hydrogen production. AIChE J. 45 (1999) 248–256.
15. E. Ochoa-Fernandez, H.K. Rusten, H.A. Jakobsen, M. Rønning, A. Holmen, D. Chen, Sorption enhanced hydrogen production by steam methane reforming using Li_2ZrO_3 as sorbent: sorption kinetics and reactor simulation, Catal. Today, 106 (2005) 41–46.
16. Kato, M., Yoshikawa, S., Nakagawa, K., Carbon dioxide absorption by lithium orthosilicate in a wide range of temperature and carbon dioxide concentrations, J. Mater. Sci. Lett. 21 (2002) 485–490.

Chapter 2

Relevant Literature Review

Abstract

This chapter presents a concise overview of the available routes for hydrogen production technologies from fossil fuel and renewable sources. The most prominent reforming techniques for hydrogen production from natural gas such as steam reforming, partial oxidation, autothermal reforming are discussed. Non-reforming techniques such as biomass gasification, biological hydrogen, electrolysis, photolectrolysis, and thermochemical water splitting are presented. The current available technologies for CO_2 capture in power plants (post-combustion, pre-combustion, and oxyfuel combustion) are also reviewed. The new techniques of the sorption-enhanced reforming, membrane-assisted reforming, and chemical looping combustion are in particularly illustrated as novel alternatives for an efficient hydrogen production.

2. 1 Introduction

Since the industrial revolution started about 150 years ago on all levels of the human being civilization, the drastic demand for energy sources has not been pacified. This anxiety for energy utilization has caused severe unplanned elevation of harmful gases levels into the atmosphere including CO_2 as a principal greenhouse gas. CO_2 is thought to be a major reason for global warming. The global awareness of climate change has imposed stringent control and regulations on the reduction, the disposal, and even the elimination techniques of CO_2 emissions. Hence, over 140 nations have signed Kyoto protocol in which they committed to a new era of lower carbon emissions to the atmosphere. Clean and inherently efficient energy production has been the driving force for new alternatives of renewable energy sources and processing technologies.

The increasing demand for H_2 as a major feedstock in many petrochemical industries and as a green energy carrier in fuel cells or gas turbine cycles has been shifting the world into a hydrogen-based energy economy [1–3]. This chapter surveys the main routes for H_2 production from fossil fuel and from renewable sources such as biomass and water. CO_2 capture technologies involved in power generation plants are reviewed. More focus is implemented on the new novel techniques for intensified H_2 production processes with in situ CO_2 capture. This includes the sorption-enhanced reforming of natural gas, membrane-assisted process, and chemical looping combustion process.

2.2 Hydrogen production technologies

H_2 can be produced from a variety of feedstocks. These include fossil resources, such as natural gas and coal, as well as renewable resources, such as biomass and water with input from renewable energy sources (*e.g.* sunlight, wind, wave or hydro-power). A variety of process technologies can be used, including chemical, biological, electrolytic, photolytic and thermo-chemical. Each technology is in a different stage of development, and each offers unique opportunities, benefits and challenges. Local availability of feedstock, the maturity of the technology, market applications and demand, policy issues, and costs will all influence the choice and timing of the various options for H_2 production. An overview of the various feedstock and process technologies is presented in Fig.1.

2.2.1 Hydrogen from fossil fuel reforming

- Steam reforming

Steam reforming (SR) is a well-established industrial process that converts hydrocarbon fuel to synthesis gas, a reactive gas mixture consisting mainly of H_2 and CO at high temperature of 700 to 850 °C and pressures of 3 to 25 bar [4]. Synthesis gas is used for production of ammonia, methanol, synthetic fuels and other chemicals, as well as for production of pure H_2. Major reactions involved in steam reforming of CH_4, as the main component of natural gas are given as follows:

R1. $CH_4 + H_2O \leftrightarrow CO + 3H_2$ ΔH_{298K} = 206.2 kJ/mol

R2. $CO + H_2O \leftrightarrow CO_2 + H_2$ ΔH_{298K} = -41.1 kJ/mol

R3. $CH_4 + 2H_2O \leftrightarrow CO_2 + 4H_2$ ΔH_{298K} = 164.9 kJ/mol

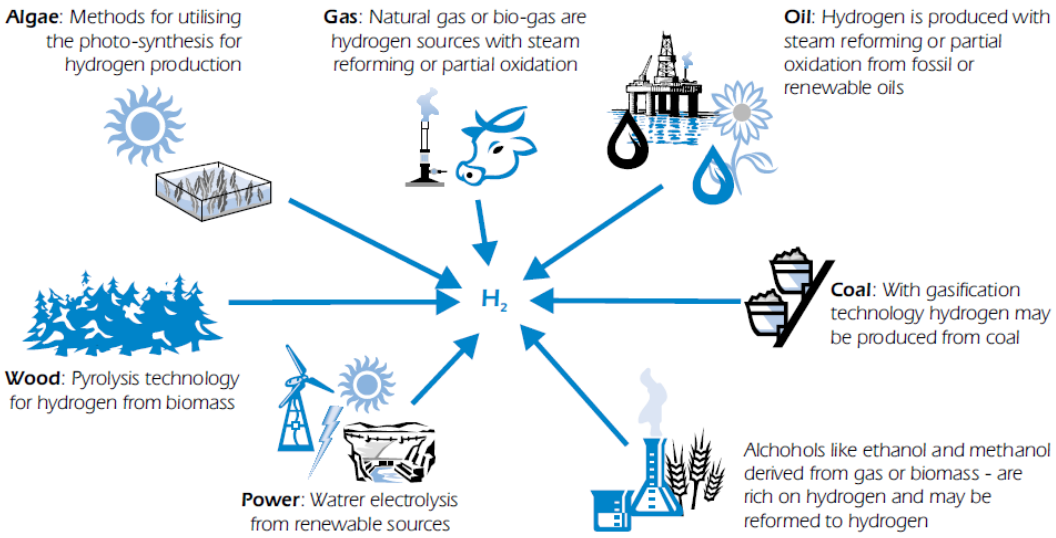

Fig. 1: Various feedstock and process alternatives for H_2 production.

Consequently, it is a highly endothermic process. In most facilities, SR takes place in tubes located inside a furnace. Reactor design is complex. Heat for the endothermic reformer reactions is provided by direct firing of a fuel in the furnace. Consequently, the reformer tubes are subject to very high thermal stress. There are also unwanted reactions such as formation of solid carbon that needs to be avoided. Much knowledge is required for successful choice of tube dimensions, furnace temperature, operating pressure and heat flux profile. Generally, reformer tubes are made up of some high alloy steel. The diameter of the tubes is in the range of 70–160mm with a wall thickness of 10–20 mm. The heated tube length is 6–15 m, depending on furnace type. The tubes are packed with catalyst material, typically made from nickel and some inert binding agent. The size and shape of the catalyst are optimized to achieve maximum activity and maximum heat transfer while minimizing the pressure drop. Desulfurization of the fuel is necessary since small amounts of sulfur are enough to poison the catalyst. The process parameter varies. In most cases the outlet temperature from the reformer is in the interval of 700–950 ◦C, the outlet pressure between 15 and 40 bar and the steam/carbon ratio in the feedstock 3.0–6.0. The reforming reactions are fast and the resulting product composition is usually close to thermodynamic equilibrium.

If H_2 is the desired product, SR is followed by water–gas shift, reaction (2), which is an exothermic reaction that transforms CO and H_2O to CO_2 and H_2. Water–gas shift takes place in one or two separate reactor vessels. The first one, the high-temperature shift reactor, operates at temperatures in the order of 350–500 ◦C and utilizes an iron/chrome catalyst. Additional steam can be added to improve the degree of CO conversion. This is not necessary for reformer gas from SR since it already contains excess steam. A typical CO concentration after high-temperature water–gas shift is 3.5 mol% on dry basis. If lower CO concentration is required, the

high-temperature shift reactor is followed by a second shift reactor operating at lower temperature. Today, the primary alternative for H_2 purification is pressure-swing adsorption (PSA). This technology utilizes two basic physical principles. Firstly, highly volatile compounds with low polarity such as H_2 are more or less non-adsorbable on conventional adsorbents. Secondly, the same adsorbents are capable of adsorbing more CH_4, CO2, CO and other impurities at a high gas-phase partial pressure than at a lower. In a pressure swing adsorption facility for H_2 purification the impurities are adsorbed at high pressure, while H_2 is just passing through the adsorber vessel. When the vessel is full it is disconnected from the process and the pressure is decreased, thus releasing most of the impurities. A small fraction of the produced H_2 is needed for purging and regeneration of the adsorbers, so the H_2 recovery is limited to about 90%. The offgas from the adsorber vessel consists of CO_2, purge H_2, unreformed CH4, some CO and minor fractions of other impurities. The offgas has substantial heating value and is generally recirculated and used as fuel in the reformer furnace. PSA is a batch process, but by using multiple adsorbers it is possible to provide constant flows. The pressure drop for H_2 is usually about 0.5 bar. There is no need for power, heating or chemicals. H_2 with very high purity, 99.9% or higher, is produced. Large-scale SR of natural gas has been practiced for decades and involved technologies can be considered as quite mature. Consequently, the number of papers dealing with the subject is very large. Informative reviews are presented in literature by Rostrup-Nielsen [4,5], Pena et al. [6], Dybkjær [7], Aasberg-Petersen [8] and Holladay et al. [9].

- Partial oxidation

Partial oxidation (POX) of hydrocarbons and catalytic partial oxidation (CPO) of hydrocarbons have been proposed for use in H_2 production for automobile fuel cells and some commercial applications [6–9]. The non-catalytic partial oxidation of hydrocarbons in the presence of oxygen typically occurs with flame temperatures of 1300–1500 ^oC to ensure complete conversion and to reduce carbon or, in this case, soot formation [9]. Major reactions are given as follows:

R_4.	$CH_4 + 1/2\,O_2 \leftrightarrow CO + 2H_2$	ΔH_{298K} =-36 kJ/mol
R_5.	$CH_4 + O_2 \leftrightarrow CO_2 + 2H_2$	ΔH_{298K} =-319 kJ/mol
R_2.	$CO + H_2O \leftrightarrow CO_2 + H_2$	ΔH_{298K} = -41.1 kJ/mol

Catalysts can be added to the partial oxidation system to lower the operating temperatures. However, it is hard to control temperature because of coke and hot spot formation due to the exothermic nature of the reactions [8]. For natural gas conversion, the catalysts are typically based on Ni or Rh; however, Ni has a strong tendency to coke formation and Rh cost has increased significantly. Typically the thermal efficiencies of POX reactors with CH_4 fuel are 60–75%, based on the higher heating values [9]. POX process provides a simplified system due to absence of external water and heat supply, therefore, it is potentially less expensive. POX reactor potentially has the capability to process a variety of gaseous and liquid hydrocarbon fuels including methane, LPG, gasoline, diesel fuel, methanol, etc.

POX process suffers from two major disadvantages: (i) POX reformate, which is heavily diluted with nitrogen, has lower calorific value, (ii) since POX process is exothermic and involve significantly higher temperatures, it might have greater thermal loses. Moreover, the presence of dry CO results in metal dusting problmes

- Autothermal reforming

Autothermal reforming (ATR) adds steam to catalytic partial oxidation. It consists of a thermal zone where POX or CPO is used to generate the heat needed to drive the downstream steam reforming reactions in a catalytic zone [6–9]. Major reactions of the ATR process are given as follows:

R_1.	$CH_4 + H_2O \leftrightarrow CO + 3H_2$	ΔH_{298K} = 206.2 kJ/mol
R_2.	$CH_4 + O_2 \leftrightarrow CO_2 + 2H_2$	ΔH_{298K} = -41.1 kJ/mol
R_3.	$CH_4 + 2H_2O \leftrightarrow CO_2 + 4H_2$	ΔH_{298K} = 164.9 kJ/mol
R_6.	$CH_4 + 2O_2 \rightarrow CO_2 + 2H_2O$	ΔH_{298K} = -802.7 kJ/mol

Therefore the temperature profile in the reactor is characterized by a sharp rise in the thermal zone, and then the temperature steadily decreases in the catalytic zone due to the endothermic reactions. ATR process is typically conducted at low pressure than POX process and has a low CH_4 slip. The heat from the POX negates the need for an external heat source, simplifying the system and decreasing the start-up time. Autothermal reforming is typically conducted at a lower pressure than POX reforming and has a low CH_4 slip. A significant advantage for this process over SR is that it can be stopped and started very rapidly while producing a larger amount of H_2 than POX alone. For ATR to operate properly both the oxygen to fuel ratio and the steam/carbon ratio must be properly controlled at all times in order to control the reaction temperature and product gas composition while preventing coke formation [6, 7]. There is some expectation that this process will gain favorability with the gas–liquids industry due to favorable gas composition for the Fischer-Tropsch synthesis, relative compactness of the process, and lower capital cost [8]. For CH_4 reforming the thermal efficiency is comparable to that of POX reactors 60–75%, based on the higher heating values, and slightly less than that of steam reformers [9]. A comparison of the three natural gas reforming processes is presented in Table 1.

- Plasma reforming

In plasma reforming the overall reforming reactions are the same as conventional reforming; however, energy and free radicals used for the reforming reaction are provided by a plasma typically generated with electricity or heat [9, 10–15].When water or steam is injected with the fuel, H, OH, and O radicals in addition to electrons are formed, thus creating conditions for both reductive and oxidative reactions to occur [15].

Proponents maintain that plasma reforming overcomes many limitations of conventional techniques such as cost and deterioration of the catalysts, size and weight requirements, sluggish response, and limitations on H_2 production from

heavy hydrocarbons [12–18]. In addition, they can also be configured to operate at lower temperatures than traditional reforming [9, 20]. In the cases where no catalysts are used to assist the reforming, the process is highly sulfur tolerant [19–22]. The main reported disadvantages include the electrical requirements and high electrode erosion at elevated pressures [71]. There are essentially two main categories of plasma reforming: thermal and non-thermal [74]. In thermal plasma reforming a high electric discharge (>1 kW) is used. A great deal of power is consumed in raising both the electrons and the neutral species to a very high temperature (5000–10,000 K). In non-thermal plasmas, only the electron temperatures are increased to high temperatures (>5000 K), while the bulk species temperature does not increase significantly [18–22]. Since only the electrons are directly excited, only a few hundred watts of power are required [22].

Table 1: Comparison of the major natural gas reforming technologies [9].

Technology	Advantages	Disadvantages
Steam reforming	Most extensive industrial experience Oxygen is not required Lowest process temperature Best H_2/CO ratio for H_2 production Easier operation at high pressure	High CO_2 emissions
Partial oxidation	Decreased desulfurization requirements No catalyst required Low CH_4 slip	Low H_2/CO Very high process temperature Soot formation adds process complexity
Autothermal reforming	Lower process temperature than POX Lower CH_4 slip Tough operation at high pressure	Limited commercial experience Requires air or oxygen

2.2.2 Hydrogen from pyrolysis

Pyrolysis is another H_2 producing technology where the hydrocarbon is decomposed (without water or oxygen present) into H_2 and carbon [23–29]. Pyrolysis can be done with any organic material [9, 23–29] and is used for the production of hydrocarbons [25] and carbon nanotubes and spheres [26]. Since no water or air is present, no carbon oxides (e.g., CO or CO_2) are formed, eliminating the need for secondary reactors (WGS, POX, etc.). Consequently, this process offers significant emissions reduction. However, if air or water is present, for example the materials have not been dried, and then significant CO_2 and CO emissions will be produced. Among the advantages of this process are fuel flexibility, relative simplicity and compactness, clean carbon by-product, and reduction in CO_2 and CO emissions [25]. The reactions can be written in the following form [29]:

R_7.

$$C_nH_m \rightarrow nC + \frac{1}{2}mH_2$$

One of the challenges with this approach is the potential for fouling by the carbon formed, which can be minimized by appropriate design [28]. Since it has the potential for lower CO and CO_2 emissions and it can be operated in such a way as to recover a significant amount of the solid carbon which is easily sequestered, pyrolysis may play a significant role in the future.

2.2.3 Hydrogen from coal

H_2 can be produced from coal through a variety of gasification processes (e.g. fixed bed, fluidized bed or entrained flow) [2–9]. In practice, high-temperature entrained flow processes are favored to maximize carbon conversion to gas, thus avoiding the formation of significant amounts of char, tars and phenols. Since this conversion is endothermic, additional heat is required, as with CH_4 reforming. The CO is further converted to CO_2 and H_2 through the water-gas shift reaction. H_2 production from coal is commercially mature, but it is more complex than the production of H_2 from natural gas. The cost of the resulting H_2 is also higher. But since coal is plentiful in many parts of the world and will probably be used as an energy source regardless, it is worthwhile to explore the development of clean technologies for its use.

2.2.4 Hydrogen from water

H_2 can be produced from the splitting of water through various processes [30–40]. The major processes of water electrolysis and photo-electrolysis are briefly discussed.

- Water electrolysis

Water electrolysis is the process in which water is split into H_2 and oxygen through the application of electrical energy. The total energy that is needed for water electrolysis is increasing slightly with temperature, while the required electrical energy decreases. A high-temperature electrolysis process might, therefore, be preferable when high-temperature heat is available as waste heat from other processes. This is especially important globally, as most of the electricity produced is based on fossil energy sources with relatively low efficiencies. Future cost forecasts for electrolytic H_2 are speculating considerable reduction in the production costs [30].

- Photo-electrolysis (photolysis)

Photovoltaic (PV) systems coupled to electrolysers are commercially available [30, 35–39]. The systems offer some flexibility, as the output can be electricity from photovoltaic cells or H_2 from the electrolyser. Direct photo-electrolysis represents an advanced alternative to a PV-electrolysis system by combining both processes in a single apparatus. This principle is illustrated in Fig. 2. Photoelectrolysis of water is the process hereby light is used to split water directly into H_2 and oxygen. Such systems offer great potential for cost reduction of electrolytic H_2, compared with conventional two-step technologies.

2.2.5 Hydrogen from biomass

In the near term, biomass is the most likely renewable organic substitute to petroleum [9, 40–49]. Biomass is available from a wide range of sources such as animal wastes, municipal solid wastes, crop residues, short rotation woody crops, agricultural wastes, sawdust, aquatic plants, short rotation herbaceous species (i.e. switch grass), waste paper, corn, and many more [42, 43]. For H_2 generation, the current biomass technologies include: gasification, pyrolysis, conversion to liquid fuels by supercritical extraction, liquefaction, hydrolysis, etc. followed in some cases by reformation, and biological H_2 production [9, 45].

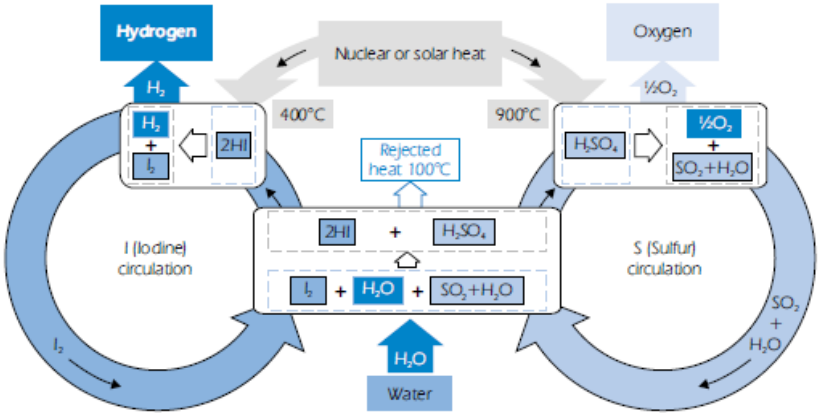

Fig. 2: Schematic of the thermo-chemical water splitting [30]

- Biomass gasification

Gasification technology, commonly used with biomass and coal, is very mature and commercially used in many processes. It is a variation of pyrolysis and, therefore, is based upon partial oxidation of the materials into a mixture of H_2, CH_4, CO, CO_2, and N_2 known as a producer gas [42]. The gasification process typically suffers from low thermal efficiency since moisture contained in the biomass must also be vaporized [45]. It can be done with or without a catalyst [41] and in a fixed bed or fluidized bed reactor, with the fluidized bed reactor typically yielding better performance [42]. A new advanced scrubbing technique is reported for an efficient tar removal in the biomass gasification process [46,47]. This technique results no condensation of the organic compounds, no system fouling, no pollution of the process water, and clean gas that is suitable for chemical synthesis or fuel cells.

- Biological hydrogen

Due to increased attention to sustainable development and waste minimization, research in bio-hydrogen has substantially increased over the last several years [46–50]. The main bioprocess technologies used for bio- H_2 production include: photolytic H_2 production from water by green algae or cyanobacteria (also known as direct photolysis), dark-fermentative H_2 production during the acidogenic phase of anaerobic digestion of organic material, photo-fermentative processes, two stage dark/fermentative, and H_2 production by water-gas shift [48, 49].

2.3 Carbon capture technologies

The most dominant technologies which are currently involved in CO_2 emission reduction in power generation plants are: post-combustion, pre-combustion decarbonization, and oxyfuel combustion. The concentration of CO_2 in the gas stream, the pressure of the gas stream and the fuel type (solid or gas) are important factors in selecting the capture system. The current status and potential of these technologies are summarized according to Oljire [50].

2.3.1 Post-combustion CO_2 capture

This involves separating CO_2 from the flue gas produced by fuel combustion. Post-combustion capture is a downstream process and in many respects is analogues to flue gas desulphurization (FGD), which is widely used to capture SO_2 from flue gas in coal and oil fired power plants. This method requires separating the CO_2 from other flue gases because sequestration of combustion gases is not feasible due in part to the cost of gas compression and storage. The low concentration of CO_2 in power-plant flue gas (typically 4–14%) means that a large volume of gas has to be handled, which results in large equipment sizes and high capital costs. Post-combustion capture offers a significant design challenge due to the relatively low partial pressure of the CO_2 in the flue gas. In addition, the relatively high temperature of the flue gases offers an additional design challenge. A further disadvantage of the low CO_2 concentration is that powerful chemical solvents have to be used and regeneration of the solvents to release the CO_2 will require a large amount of energy. There are several separation technologies that can be employed within this category: chemical absorption, gas separation membranes and low temperature distillation.

2.3.2 Pre-combustion CO_2 capture

In pre-combustion capture, fuel is reacted with oxygen or air, and in some cases steam, to give mainly CO and H_2 in gasification, partial oxidation or reforming process. The mixture of mainly CO and H_2, is passed through a catalytic reactor, called a shift converter, where the CO reacts with steam to give CO_2 and more H_2. The CO_2 is separated and the H_2 is used as fuel in a gas turbine combined-cycle plant. This technology is usually used for coal gasification (IGCC), however it could be applied to liquid and gaseous fuel. Typical reaction for IGCC is shown in the following equations [50].

R_2. $$CO + H_2O \leftrightarrow CO_2 + H_2$$

R_8. $$2C + O_2 + H_2O \rightarrow CO + CO_2 + H_2$$

R_9. $$C + H_2O \rightarrow CO + H_2$$

Biomass and natural gas can also be used for pre-combustion capture technology. As gasification of biomass is similar to IGCC, for gasification of natural gas, several methods, which include steam reforming, partial oxidation and autothermal reforming are used. After shift reaction, gas mixture is cooled and Selexol acid gas removal unit separates CO_2 and sulphur compound steams [50]. The profit of pre-

combustion capture is based on transformation of carbon fuel to carbonless fuel. Gasification process uses chemical energy of carbon and transforms it to chemical energy of H_2. H_2 combustion does not emit any sulphur dioxide. H_2 seems to be useful fuel, as it could be used for gas boilers, gas turbines, fuel cells and other technologies. The CO_2 concentration and pressure are both higher in pre-combustion capture than in post-combustion capture, so the CO_2 capture equipment is much smaller and different solvents can be used, with lower energy penalties for regeneration. Pre-combustion capture offers a more moderate energy penalty of 10% based on gasification or steam reforming. The high partial pressure of CO_2 could allow for the use of more efficient capture technologies (i.e, physical absorption), which would further reduce the energy penalty. Pre-combustion capture also has more potential for future use. The primary disadvantage of pre-combustion capture is that total capital costs of the facility are very high [50].

2.3.3 Oxyfuel combustion

Oxyfuel combustion is actually modified post-combustion method. Fuel is combusted in almost pure oxygen instead of air, which results in high concentration of CO_2 in flue gases. If fuel is burnt in pure oxygen, the flame temperature is excessively high, thus some CO_2-rich flue gas would be recycled to the combustor to make the flame temperature similar to that in normal air-blown combustor. The advantage of O_2-blown combustion is that the flue gas has a CO_2 concentration of over 80%, therefore only simple CO_2 purification is required. Another advantage is that NO_x formation is suppressed, with attendant benefits in the post-combustion removal of NO_x, and the volume of the gas to be treated in the flue gas desulphurization plant is greatly reduced. Additionally, other than a need for the gas desulphurization, oxyfuel combustion relies mainly on physical separation processes for O_2 production and CO_2 capture thereby avoiding the use of any reagent and/or solvents that contribute to operating costs and environmental disposal of any related solid or liquid wastes. The main disadvantage of oxyfuel combustion is that a large quantity of oxygen is required, which is expensive, both in terms of capital cost and energy consumption. Advances in oxygen production processes, such as new and improved membranes that can operate at high temperatures could improve overall plant efficiency and economics [50]. Oxyfuel combustion has so far only been demonstrated in small scale test rigs [50].

2.4 Intensified techniques for hydrogen production

The conventional process of steam reforming is limited in H_2 productivity and CH_4 feedstock conversion due to the thermodynamic bounds of the reversible steam reforming reactions. Thus, the reaction temperature has to be in the range of 800–900 ^oC to achieve complete conversion of methane. At this elevated temperature the catalyst undergoes deactivation due to carbon formation, also resulting in blockage of reformer tubes and increased pressure drops [1–5]. Temperature, pressure and gas composition must be carefully controlled to avoid catalyst deactivation due to coking. Therefore, it will be extremely desirable if smart concepts for production of H_2 by steam reforming can be developed which reduce

the capital cost compared to the conventional route. Reaction enhancement, obtained by removing either H_2 or CO_2, may enable a lower temperature of operation, which in turn may alleviate the problems associated with catalyst fouling, high process energy requirements and poor energy integration within the plant environment.

2.4.1 Sorption–enhanced catalytic reforming

The sorption enhanced catalytic reforming concept presents a potential intensified technique in which the co-generated CO_2 is selectively removed from the product gas mixture by an efficient sorbent material [51,57]. The sorbent is then regenerated via a temperature or pressure swing operation. This eventually circumvents the thermodynamic equilibrium limitations and implies a high purity H_2 production (>95%) and high CH_4 conversion (>90%) with very low impurities of CO and CO_2 at relatively much lower temperature (400–500 ^oC). A typical sorbent that can employed in this process must have several requirements [56] (i) selective sorption of CO_2 at the process temperature and in presence of steam, CH_4, CO, and H_2, (ii) adequate working CO_2 capacity at the process operational temperature, (iii) adequate rates of sorption and desorption, and (iv) adequate thermal and cyclic stability at the process conditions.

A variety of materials have been studied and reported in literature for CO_2 (ad)sorption. These materials can be classified as (i) microporous and mesoporous inorganic and organic materials such as zeolites [58–60], silica gel [51, 61], alumina [62], and activated carbon [63–65], (ii) Mixed oxide materials such as CaO [66–73], (iii) Lithium metal oxides such as lithium zirconate (LZC) [74–81] and lithium orthosilicate (LOS) [82,83], (iv) and Hydrotalcite-like materials (HTC) [84–90]. The first type of materials tend to show a high physical adsorption rate for CO_2 with a reasonable high adsorption capacity at low temperature (near ambient) [58–60]. The low to moderate isosteric heats of adsorption of these materials allow reversible adsorption and desorption of CO_2 at relatively low temperature [58, 60]. However, these physisorbents have major operational limitations: (i) CO_2 working capacity drastically diminishes to be almost negligible as the temperature increases above 250 ^oC , (ii) polar adsorbents such as silica gel, alumina, and zeolites show very poor performance in presence of polar gases as they selectively adsorb water over CO_2.

- Ca–based process

CaO has also been reported to show strong affinity for CO_2 sorption at high temperature above 500 ^oC. CaO can react with CO_2 in a bulk chemical carbonation reaction according to:

R_{10}. $\quad CaO + CO_2 \leftrightarrow CaCO_3 \qquad \Delta H_{298K}$ = -182 kJ/mol

CaO offers a very high temperature-independent stoichiometric sorption capacity of 17.8 CO_2 mol/kg [53–56]. However, CaO has also some operational limitations [51, 57]: (i) the CO_2 working capacity is much lower than the stoichiometric

capacity unless the material is regenerated at high temperature of 900 ^{o}C due to the thermodynamically unfavorable desorption of CO_2, thus (ii) slow kinetics of sorption/desorption at low temperature of about 500 ^{o}C, (iii) the cyclic stability of CaO in terms of CO_2 is significantly reduced due to the buildup of the irreversible $CaCO_3$, and (iv) sintering of the CaO active surface is also a concern during desorption at high temperature. Moreoever, temperature swing regeneration can only be used in such process

Calcium carbonate and dolomite are inexpensive, easy to find and characterized by high adsorption ability. Otherwise, the sorbents, constituted mainly by inert, need a greater energy amount for their regeneration [31]. Sintering at high calcination temperatures causes rapid decay in capacity upon multiple re-carbonation. (After 45 cycles, this reduction is less than 20% and about 40% and 60% for huntite, dolomite and calcium carbonate, respectively.) Adsorption reaction is rapid during the early stages, but undergoes an abrupt transition and becomes extremely slow before complete CaO conversion is achieved. The effectiveness of both sorption enhanced steam reforming and the use of Ca-based CO_2 sorbents have been demonstrated in previous works. Balasubramanian et al. [67] showed that a gas with a H_2 content up to 95% (dry basis) could be produced in a single reactor containing reforming catalyst and CaO formed by calcination of high-purity $CaCO_3$. The reported methane conversion was 88%. For a typical calcium oxide sorbent process, the typical operating temperatures are about 500–650 ^{o}C.

- Hydrotalcite–based process

Hydrotalcite (HTC), which is an anionic clay consisting of positively charged layers of metal oxide (or metal hydroxide) with inter-layers of anions, such as carbonate, see Fig. 3. Hydrotalcite–like materials have been found to have an adequate CO_2 working sorption capacity (0.45–1.0 mol/kg) at high temperature of 400–450 ^{o}C [84–90], infinite selectivity for CO_2 even in the presence of steam, steam has been determined to enhance the sorption capacity and stability [87], very good cyclic stability, fast sorption kinetics, and relatively easy desorption rates due to low to moderate heats of chemisorption in the Henry's law region (weak bonding to CO_2). Therefore, these materials are considered to be promising sorbents for high purity H_2 production in the sorption enhanced steam reforming of methane. However, the sorbent composition and the preparation methods will eventually determine the final properties of the material [90,91].

Both adsorption and regeneration temperature is around 400 ^{o}C int his process. Promoted K_2CO_3/HTC was tested by Hufton et al. [53, 54] and it results indeed in a stable equilibrium CO_2 capacity of 0.3–0.45 mmol/g (0.018 gCO2/g sorbent) over nearly 6000 cycles. Although high stability upon multi-cycle test, the adsorption capacity is very low, most likely restricting its potential as a sorbent on an industrial scale. Relative to sorbent multi-cycle durability, the research activities are currently focused on the development of new synthetic sorbents with high mechanical stability (some products are indicated in Table 2 together with

adsorption ability and regeneration temperature), but their costs of production are still too high and require them to sustain at least 10 000 cycles to compete with natural sorbents [31]. Moreover, the reported rate of reaction for this kind of sorbents is too slow to compete with calcium-based ones. Hufton et al. [54] reported on H_2 production through SE-SMR using a K_2CO_3-treated HTC sorbent, although the extremely low CO_2 working capacity above discussed. Average purity of H_2 was about 96% while CO and CO_2 contents were less than 50 ppm. The methane conversion to H_2 product reaches 82%. The conversion and product purity are substantially higher than the thermodynamic limits for a catalyst-only reactor operated at these same conditions (28% conversion, 53% H_2, 13% CO/CO_2).

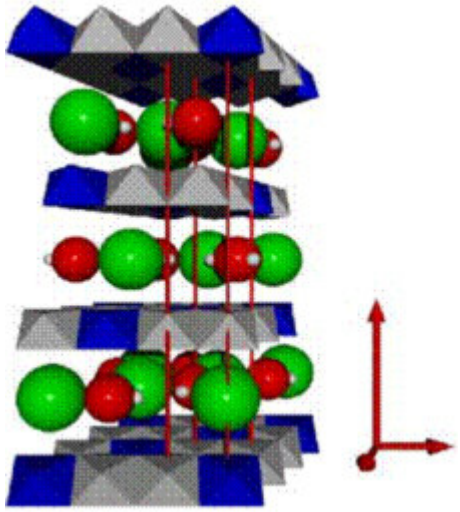

Fig. 3: Hydrotalcite structure

Table 2: Sorption capacities and regeneration temperatures for various sorbents [31].

	Sorbent	Stoichiometric sorption capacity [mol/kg]	Regeneration temperature [^oC]	Stoichiometric sorption capacity after 45 cycles [mol/kg]
Natural sorbents	Calcium carbonate $CaCO_3$	17.96	900	7.18
	Dolomite $CaCO_3 \times MgCO_3$	10.45	900	3.64
	Huntite $CaCO_3 \times 3MgCO_3$	5.68	900	4.55
	Hydrotalcite, K-promoted hydrotalcite	0.65	400	Stable
Synthetic sorbents	Lithium orthosilicate Li_4SiO_4	8.4	750	Stable until 100 cycles
	Lithium zirconate Li_2ZrO_3	6.5	690	Stable until 100 cycles
	Sodium zirconate Na_2ZrO_3	5.5	790	Stable until 100 cycles

Nearly all the experimental attempts on the utilization of HTC in sorption enhanced H_2 production apply a conventional low activity Ni-based catalyst in an admixture

fixed bed reactor [90–94]. Hufton et al. [54] achieved a H_2 product stream with a purity of 95% and CH_4 fuel conversion of 80% and $CO+CO_2$ concentration of less than 50 ppm at 450 ^oC and 4.7 bar. They further [57] determined that the multi-cycle operation failed to maintain the same performance of a single cycle process due to the unrecovered sorbent capacity during the pressure swing regeneration cycles. They obtained CH_4 conversion and H_2 purity of 54 and 88.7%, respectively.

Ding and Alpay [928] obtained 75% CH_4 conversion and H_2 purity >90% in a laboratory scale fixed bed of 22 cm in length using S/C ratio of 6 at 450 ^oC and 4.45 bar. Lee et al. [93] demonstrated improved process performance in larger scale column (2.0 m length and 1.73 cm diameter) using the temperature swing regeneration and better capacity HTC sorbent. They reached a CH_4 conversion and H_2 purity of 96 and 99.99%, respectively at reaction temperature of 490 ^oC and 1.5 bar. The bed is regenerated using steam purge at 590 ^oC. Beaver et al. [94] reported almost the same performance for a fuel-cell grade H_2 with CO impurity <20 ppm at a slightly higher temperature range of 520–550 ^oC and ambient pressure in a 1.73 m long reactor.

- Lithium zirconate–based process

Lithium zirconate (LZC) and lithium orthosilicate (LOS) have recently received more attention due to their ability to retain good CO_2 chemisorption capacity at high temperature (5.0 mol/kg [80] and at 6.13 mol/kg [83], respectively). However, the slow sorption kinetics and the high heat of reaction due to the strong chemical bonding to CO_2 require a high regeneration temperature (900 ^oC for LZC [74–80] and 700 ^oC for LOS [83], respectively). Recently, more attention has been given to the utilization of lithium zirconate materials as high capacity candidate sorbents at high temperature [74–80]. Ida and Lin [74] studied the mechanism of the CO_2 sorption/desorption process on Li_2ZrO_3 by analyzing the phase and microstructure change of Li_2ZrO_3 during the CO_2 sorption/desorption process.

R_{11}. $\quad Li_2ZrO_3 + CO_2 \leftrightarrow Li_2CO_3 + ZrO_2 \quad \Delta H_{298K} = -160$ kJ/mol

R_{12}. $\quad Li_4SiO_4 + CO_2 \leftrightarrow Li_2SiO_3 + Li_2CO_3 \quad \Delta H_{298K} = -142$ kJ/mol

It was shown that pure Li_2ZrO_3 absorbs a large amount of CO_2 at high temperature with a slow sorption rate. Addition of potassium carbonate (K_2CO_3) and lithium carbonate (Li_2CO_3 in the Li_2ZrO_3) remarkably improves the CO_2 sorption rate of the Li_2ZrO_3 materials. Xiong et al. [75] established a mathematical model based on the double-shell sorption mechanism for CO_2 sorption kinetics. Above 500 ^oC, the rate-limiting step of CO_2 sorption is the diffusion of oxygen ions through the ZrO_2 shell formed during the carbonation reaction. Fernandez et al. [80] demonstrated a dynamic one-dimensional pseudo-homogenous model for a fixed bed reactor where they used hydrotalcite-derived Ni catalyst and lithium zirconate sorbent. They showed H_2 purity of 90 to 95% with a corresponding CH_4 conversion of 70 to 87% depending on the S/C ratio.

2.4.2 Chemical looping combustion

Chemical looping combustion (CLC) is a novel process for heat and power production with inherent CO_2 capture [32, 95–103]. It has also been called unmixed combustion since direct contact between fuel and combustion air is avoided. Instead, an oxygen carrier performs the task of bringing oxygen from the air to the fuel. Suitable oxygen carriers are small particles of metal oxide such as Fe_2O_3 (hematite), NiO (nickel oxide), CuO (copper oxide) or Mn_2O_3 (manganese oxide). In this chapter, the abbreviation Me is used to describe a generic oxygen carrier in its reduced form while MeO is used for the oxidized form. A basic CLC system, shown in Fig. 4, has two reactors, one for air and one for fuel. The oxygen carrier circulates between the reactors. In the air reactor, it is oxidized with oxygen from the combustion air according to reaction (13). In the fuel reactor, it is reduced to its initial state by the fuel, which in turn is oxidized to CO_2 and H_2O (water vapor) according to reaction (14).

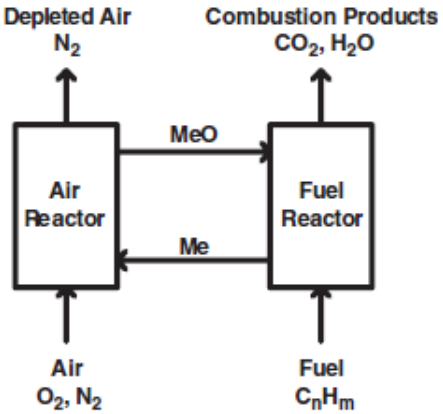

Fig. 4: Chemical-looping combustion. Me is the oxygen carrier in its reduced form and MeO is its oxidized form.

R_{13}. $O_2 + 2Me \rightarrow 2MeO$ Air rector

R_{14}. $C_nH_m + (2n + 0.5m)MeO \rightarrow nCO_2 + 0.5mH_2 + (2n + 0.5m)Me$ Fuel reactor

The amount of energy released or required in the reactor vessels depends on the nature of the oxygen carrier and the fuel, as well as the temperature of reaction. Reaction (13) is strongly exothermic. Reaction (14) is usually endothermic but for some combinations of fuel and oxygen carrier it is slightly exothermic. In principle, all kinds of fuels can be utilized in a Chemical-looping combustor. If CH_4 is used as fuel and NiO as oxygen carrier, reactions (15 and 16) will occur in the reactors. The total amount of energy released in the reactor system is the same as for combustion of the fuel.

R_{15}. $4Ni + 2O_2 \rightarrow 4NiO$ Air rector

R_{16}. $CH_4 + 4NiO \rightarrow CO_2 + 2H_2O + 4Ni$ Fuel reactor

R_8. $CH_4 + 2O_2 \rightarrow CO_2 + 2H_2O$ Total oxidation

The sum of reactions (15 and 16) is complete combustion of CH_4 with oxygen. CLC has several potential benefits compared with conventional combustion. The exhausts from the oxidation reactor are harmless, consisting mainly of N_2 and, if a surplus of air is used in the oxidation reactor, some oxygen.

In a well-configured system, there should be no thermal formation of nitrogen oxides (NO_x) since regeneration of the oxygen carrier takes place without flame and at moderate temperatures. The gas from the reduction reactor consists of CO_2 and H_2O, so a condenser is the only equipment needed to obtain almost pure CO_2. This is a major advantage with CLC. About three quarters of the energy required for CO_2 capture and storage with conventional methods, such as amine scrubbing of flue gases, is associated with the separation of CO_2 and N_2. With CLC this can be avoided completely since CO_2 and N_2 are never mixed. In practice, a CLC process can be designed in several ways. But circulating fluidized beds are likely to have an advantage over other alternatives since it provides good contact between gas and solids and allows a smooth flow of oxygen carrier between the reactors. Circulating fluidized beds are well-known technology that is used for many large-scale industrial applications. CLC has recently been successfully demonstrated in a 10 kW prototype using circulating fluidized beds [95–100]. A total of 99.5% fuel utilization at 800 ◦C with no detectable leakage between the reactors and very small losses of oxygen carrier material was achieved [32, 95].

2.4.3 Membrane–assisted hydrogen production

Membranes may act as perm-selective barriers, or as an integral part of the catalytically active surface. Particular membranes used in H_2 production from steam reforming and water-gas shift reactions are briefly discussed in this chapter.

- Oxygen and hydrogen transport membranes

The concept involves integration of syngas generation from natural gas, shift reaction and H_2 separation into a single membrane-reactor separator [31, 104–108]. The key elements required to make this possible are an oxygen transport membrane (OTM) and a H_2 transport membrane (HTM). Both membranes are based on ceramic mixed conducting materials and operate at similar temperatures (800–1000 ^{o}C) [104]. The OTM conducts oxygen ions and electrons and has infinite selectivity for oxygen over other gases. Similarly, the HTM conducts only protons and electrons and therefore infinitely selective for H_2. A schematic diagram of the integrated-membrane reactor separator is shown in Fig. 5. The reactor is divided in three compartments by integrating both OTM and HTM into a single unit. Air at low pressure (~0.17 kPa) is passed to the cathode side of the OTM, while compressed natural gas (1.36–2 kPa) and water/steam are passed to the anode side of OTM. Oxygen is transported across OTM to the anode side, where it reacts with natural gas to form syngas. A portion of natural gas also reacts with steam to form syngas. Catalyst is incorporated in the reactor to promote reforming reaction.

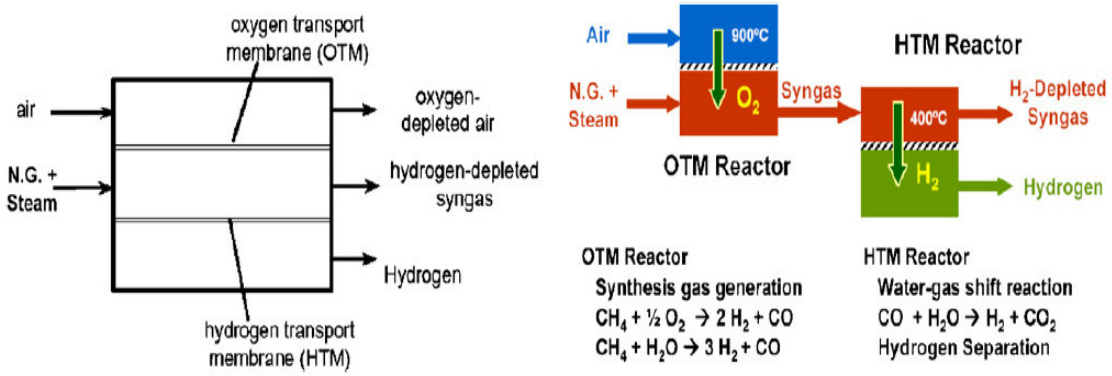

Fig. 5: Integrated membrane-reactor separator [31]

- Ion transport membrane (ITM)

The ITM technology may simplify the H_2 production from natural gas and its separation by combining these processes into a single step, achieving lower costs and greater efficiencies [105, 106]. ITM systems combine the separation of air to produce oxygen and the subsequent use of that oxygen (in partial oxidation process) to generate synthesis gas [31, 105]. The technology uses non-porous ceramic membranes fabricated from multi-component metallic oxides that conduct both electrons and oxygen ions at temperatures greater than 700 ^{o}C. During operation, oxygen from a hot air stream is reduced by catalysts at one surface of the membrane to create oxygen ions.

- Palladium membrane

This kind of membrane is made of palladium alloy, which allows only H_2 to permeate. Installing reforming catalysts and the membrane modules in the same reactor, simultaneous generation and separation of H_2 is achieved [107]. This not only makes the reactor drastically compact, but also drastically lowers the reaction temperature [107]. However, in the case of membrane made of palladium alloy, the reaction temperature can be lowered to 500–550 ^{o}C, which enhances high thermal efficiency, and H_2 separation unit can be eliminated, which makes the unit as compact as 1/3 in volume and 1/2 in terms of area of the conventional unit.

- Porous inorganic membranes for high temperature H_2 separation

Inorganic membranes with pore sizes less than 1 nm offer many advantages over thin-film palladium membranes and ion-transport membranes for the separation of H_2 from a mixed-gas stream [108]. Microporous membranes become the more attractive option for systems that operate at high pressure. Moreover microporous membranes permeance increases dramatically with temperature [108]. Consequently, inorganic membranes have the potential to produce very high fluxes at elevated temperatures and pressures.

2.5 Conclusions

Steam reforming is still the most dominant route to convert natural gas as a fossil fuel into hydrogen. Significant research has been performed during the recent decade to attain this process to its ultimate boundaries in terms of high performance efficiency and low production costs. The innovative concepts of sorption-enhanced reforming, membrane assisted reforming, and chemical looping are proved to be applicable and might replace the conventional steam reformers in the forthcoming period for certain applications. Table 3 presents the current status of the available technologies including their efficiency and maturity level [9]. However, the future of hydrogen-based economy is open for utilization of a wide range of feedstock and technologies. Water electrolysis is viewed as a promising route for a renewable energy generation with zero emissions.

Table 3: Summary of current technology status [9].

Technology	Feedstock	Efficiency, %	Maturity
Steam reforming	Hydrocarbon	70-85	Commercial
Partial oxidation	Hydrocarbon	60-75	Commercial
Autothermal reforming	Hydrocarbon	60-75	Near term
Plasma reforming	Hydrocarbon	9-85	Long term
Aqueous phase reforming	Carbohydrates	35-55	Med. term
Ammonia reforming	Ammonia	NA	Near term
Biomass gasification	Biomass	35-50	Long term
Photolysis	Sunlight + water	0.5	Long term
Dark fermentation	Biomass	60-80	Long term
Photo fermentation	Biomass + sunlight	0.1	Long term
Microbial electrolysis	Biomass + electricity	78	Long term
Alkaline electrolyzer	Water + electricity	50-60	Commercial
PEM electrolyzer	Water + electricity	55-70	Near term
Solid oxide electrolysis	Water + electricity	40-60	Med. term
Thermochemical water splitting	Water + electricity + heat	NA	Long term
Phtoelectrochemical water splitting	Water + sunlight	12.4	Long term

References

1. Armor, J.N., Catalysis and the hydrogen economy, Catalysis Letters 101 (2005) 131–135.
2. Barreto, L., Makihira, A., Riahi, K., The hydrogen economy in the 21st century: a sustainable development scenario, Int. J. Hydrogen Energy 28 (2003) 267–84.
3. Ewan, B.C.R., Allen, R.W.K., A figure merit assessment of the routes to hydrogen, Int. J. Hydrogen Energy 30 (2005) 809 – 819.
4. Rostrup-Nielsen, J.R. Production of synthesis gas. Catal. Tod. 18 (1993) 305-324.
5. Rostrup-Nielsen, J.R. Fuels and energy for the future: The role of catalysis. Catal. Rev. 46 (2004) 247–270.
6. Pena M.A.; Gómez, J.P.; Fierro, J.L.G. New catalytic routes for syngas and hydrogen production, App. Catal A, 144 (1996) 7-57.
7. Dybkjaer, I., Tubular reforming and autothermal reforming of natural gas—an overview of available processes, Fuel Process Tech. 42 (1995) 85–107.
8. Aasberg-Petersen, K., Christensen, T.S., Nielsen, C.S., and Dybkjaer, I., Recent developments in autothermal reforming and pre-reforming for synthesis gas production in GTL applications, Fuel Processing Tech. 83 (2003) 253–261.
9. Holladay, J.D., Hu, J., King, D.L., Wang, Y., An overview of hydrogen production technologies, 139 (2009) 244-260.
10. Hammer, T., Kappes, T., Baldauf, M., Plasma catalytic hybrid processes: gas discharge initiation and plasma activation of catalytic processes, Catalysis Today 89 (2004) 5–14.
11. Biniwale, R.B., Mizuno, A., Ichikawa, M., Applied Catalysis A: General 276 (2004) 169–177.
12. Bromberg, L., Cohn, D.R., Rabinovich, A., Alexeev, N., International Journal of Hydrogen Energy 24 (1999) 1131–1137.
13. O'Brien, C.J., Hochgreb, S., Rabinovich, A., Bromberg, L., Cohn, D.R., in: Proceedings of the Intersociety Energy Conversion Engineering Conference, Hydrogen Production via Plasma Reformers, IEEE, Piscataway, NJ, USA, 1996, pp. 1747–1752.
14. Matsui, Y., Kawakami, S., Takashima, K., Katsura, S., Mizuno, A., Energy and Fuels 19 1561–1565.
15. Bromberg, L., Cohn, D.R., A. Rabinovich, International Journal of Hydrogen Energy 22 (1997) 83–94.
16. Muradov, N., Emission-free Fuel Reformers for Mobile and Portable Fuel Cell Applications, Journal of Power Sources 118 (2003) 320–324.
17. Wu, W., Yoshikawa, K., JSME International Journal Series B-Fluids and Thermal Engineering 45 (2002) 487–491.
18. Demirbas, A., Arin, G., Hydrogen from biomass via pyrolysis: relationships between yield of hydrogen and temperature, Energy Sources 26 (2004) 1061–1069.
19. Demirbas, A., Temperature on Pyrolysis Products from Biomass from Biomass Energy Sources 25 (2003) 67–75.

20. Demirbas, A., Current Technologies for the Thermo-Conversion of Biomass into Fuels and ChemicalsEnergy Sources 27 (2005) 1313–1319.
21. Yi Zheng, J., G. Chao, H. Wen Kuang, Z. Yanqiu, A. Huczko, M. Bystrzejewski, M. Roe, L. Chi Young, S. Acquah, H. Kroto, D.R.M. Walton, Carbon 43 (2005) 1944–1953.
22. Karaeva, A.P., Mordkovich, V.Z., Tretyakov, V.F., Solid Fuel Chemistry 39 (2005) 61–76.
23. W. Wu, K. Yoshikawa, JSME International Journal Series B-Fluids and Thermal Engineering 45 (2002) 487–491.
24. Yi Zheng, Y., Chao, G., Wen Kuang, H., Yanqiu, Z., Huczko, H., Bystrzejewski, M., Roe, M., Chi Young, L., Acquah, S., Kroto, H., Walton, D.R.M., Carbon 43 (2005) 1944–1953.
25. Karaeva, A.P., Mordkovich, V.S., Tretyakov, V.F., Solid Fuel Chemistry 39 (2005) 61–76.
26. Riis, T., Hagen, E.F., Viel, P.J.S., Ullenberg, O., Hydrogen production R&D: priorities and gaps, International Energy Agency Reports, OECD/IEA, 2006.
27. Barelli, L., Bidini, G., Gallorini, F., Servilli, S., Hydrogen production sorption-enhanced steam methane reforming and membrane technologuy: A review, Energy 33 (2008) 554-570.
28. Ryden, M., Lyngfelt, Using steam reforming to produce hydrogen with carbon dioxide capture by chemical looping Int. J. Hydrogen Energy, 31 (2006) 1271-1283.
29. Norbeck, J.M., Heffel, J.W., Durbin, T.D., Tabbara, B., Bowden, J.M., Montani, M.C., Hydrogen Fuel for Surface Transportation, Society of Automotive Engineers Inc., Warrendale, PA, 1996, p. 548.
30. Turner, J., Sverdrup, G., Mann, M.K., Maness, P.C., Kroposki, Ghirardi, Evans, R., Blake, D., International Journal of Hydrogen Energy 32 (2008) 379–407.
31. Grigoriev, S., Porembsky, V.I., Fateev, V.N., International Journal of Hydrogen Energy 31 (2006) 171–175.
32. Funk, J.E., International Journal of Hydrogen Energy 26 (2001) 185–190.
33. Lewis, M., Serban, M., Basco, J., Figueroa, J., Low Temperature Thermochemical Cycle Development, Chicago, IL, 2003.
34. Turner, J., Deutsch, J. Head, P. Vallett, Photoelectrochemical water systems for H_2 production, in: DOE Hydrogen ProgramT., Annual Merit Review, U.S. Department of Energy, Washington, DC, 2007, http://www.hydrogen.energy.gov/pdfs/review07/pd_10_turner.pdf.
35. Akikusa, J.,Khan, S.U.M., International Journal of Hydrogen Energy 27 863–870, (2002).
36. Asadullah, M., S.-I. Ito, K. Kunimori, M. Yamada, K. Tomishige, Environmental Science and Technology 36 (2002) 4476–4481.
37. Demirbas, A., Demirbas, M.F., Energy Sources 25 (2003) 317–329.
38. X. Hao, L. Guo, Huagong Xuebao, Journal of Chemical Industry and Engineering, 53 (2002) 221–228.
39. Demirbas, D., Progress in Energy and Combustion Science 30 (2004) 219–230.
40. Weber, G., Fu, Q., Wu, H., Developments in Chemical Engineering and Mineral Processing 14 (2006) 33–49.

41. Jo-Shu, C.,. Wu, S.Y.S.Y., Chi-Neng, L., Jian-Sheng, C., International Journal of Hydrogen Energy 30 (2005) 1375–1381.
42. Cai, M., Liu, J., Wei, Y., Environmental Science and Technology 38 (2004) 3195–3202.
43. Levin, D.B., Pitt, L., Love, M., International Journal of Hydrogen Energy 29 (2004) 173–185.
44. Gavala, H., Skiadas, I., Ahring, B., Lyberatos, V., Water Science and Technology 52 (2005) 209–215.
45. Khanal, S.K., Chen, W.H., Li, L., Sung, S., Water Environment Research 78 (2006) 110–117.
46. Zwart, R.W.R., van der Drift, A., Bos, A., Visser, H.J.M. , Cieplik, M.K. ., Könemann, H.W.J. , "Oil-Based Gas Washing – Flexible Tar Removal for High-Efficient Production of Clean Heat and Power as well as Sustainable Fuels and Chemicals", Environmental Progress & Sustainable Energy, 2009, 28 (3), pp. 324-335
47. Rabou, L.P.L.M., Zwart, R.W.R. , Vreugdenhil, B.J., Bos, L., "Tar in Biomass Producer Gas, the Energy research Centre of the Netherlands (ECN) Experience: An Enduring Challenge", Energy & Fuels, 2009, 23 (12), pp. 6189-6198
48. Olajire, A., CO_2 capture and separation technologies for end of pipe applications–A review 35 (2010) 2610-2628.
49. Harrison, D.P. Sorption-enhanced hydrogen production: A Review, Ind. Eng. Chem. Res., 47 (2008) 6486–6501.
50. Feng, B.; An, H.; Tan, E. Screening of CO_2 adsorbing materials for zero emissions power generation systems. Energy and Fuel. 21 (2007) 426-434.
51. Hufton, J. R., Mayorga, S., Sircar, S. Sorption-enhanced reaction process for hydrogen production. AIChE J. 45 (1999) 248–256.
52. Hufton, J., Waldron, W., Weigel, S., Rao, M., Nataraj, S., Sircar, S., Sorption enhanced reaction process SERP) for the production of hydrogen, in: Proceedings of the 2000 US DOE Hydrogen Program Review, 2000.
53. Waldron, W. F.; Hufton, J. R.; Sircar, S. Production of hydrogen by cyclic sorption enhanced reaction process. AIChE J. 47 (2001) 1477–1479.
54. Yong, A., Mata, V., Rodrigues, A.E. Adsorption of carbon dioxide onto hydrotalcite-like compounds (HTlcs) at high temperatures, Ind. Eng. Chem. Res. 40 (2001) 204-209.
55. Lee, K. B.; Beaver, M. G.; Caram, H. S.; Sircar, S. reversible chemisorbents for carbon dioxide and their potential application. Ind. Eng. Chem. Res. 47 (2008) 8048-8062.
56. Dı´az, E.; Mun˜oz, E.; Vega, A.; Ordo´n˜ez, S. Enhancement of the CO_2 retention capacity of X zeolites by Na- and Cs-treatments. Chemosphere 70 (2008) 1375–1382.
57. Inui, T.; Okugawa, Y.; Yasuda, M. Relationship between properties of various zeolites and their CO_2-adsorption behaviors in pressure swing adsorption operation. Ind. Eng. Chem. Res. 27 (1988)1103–1109.
58. Rege, S. U.; Yang, R. T.; Buzanowski, M. A. Sorbents for air prepurification in air separation. Chem. Eng. Sci. 55 (2000) 4827–4838.

59. Keller, G. E.; Anderson, R. A.; Yon, C. M. Adsorption In Handbook of Separation Process Technology; Rousseau, R. W., Ed.; Wiley Interscience: New York, 1987; Chapter 12, pp 644-696.
60. Cao, D. V.; Sircar, S. Heats of Adsorption of Pure SF6 and CO_2 on Silicalite Pellets with Alumina Binder. Ind. Eng. Chem. Res. 2001, 40,
61. Sircar, S. Gas Separation and Storage by Activated Carbons. In Adsorption by Carbons; Bottani, E., Tascon, J., Eds.; Elsevier: New York, 2008; Chapter 22, pp 565-592.
62. Yong, Z.; Mata, V. G.; Rodrigues, A. E. Adsorption of Carbon Dioxide on Chemically Modified High Surface Area Carbon-Based Adsorbents at High Temperature. Adsorption 2001, 7, 41.
63. Abanades, J. The Maximum Capture Efficiency of CO_2 Using a Carbonation/Calcination Cycle of $CaO/CaCO_3$. Chem. Eng. J. 2002, 90, 303.
64. Lopez, A.; Harrison, D. P. Hydrogen Production Using Sorption Enhanced Reaction. Ind. Eng. Chem. Res. 2001, 40, 5102.
65. Balasubramanian, B.; Lopez, A.; Kaytakoglu, S.; Harrison, D. P.Hydrogen From Methane in a Single-Step Process. Chem. Eng. Sci. 1999, 54, 3543.
66. Yi, K. B.; Harrison, D. P. Low Pressure Sorption Enhanced Hydrogen Production. Ind. Eng. Chem. Res. 2005, 44, 1665.
67. Bandi A.; Specht, M.; Sichler, P.; Nicoloso, N. In Situ Gas Conditioning on Fuel Reforming for Hydrogen Generation. Proceedings of the 5th International Symposium on Gas Cleaning, Pittsburgh, PA, Sept. 2002.
68. Grasa, G. S.; Abanades, J. C. CO_2 Capture Capacity of CaO in Long Series of Carbonation/Calcination Cycles. Ind. Eng. Chem. Res. 2006,45, 8846.
69. Sun, P.; Lim, C.; Grace, J. R. Cyclic CO_2 Capture of Limestone-Derived Sorbent During Prolonged Calcination/Carbonation Cycling. AIChEJ. 2008, 54, 1668.
70. Hughes, R. W.; Lu, D.; Anthony, E. J.; Wu, Y. Improved Long-Term Conversion of Limestone Derived Sorbents for In-Situ Capture of CO_2 in a Fluidized Bed Combustor. Ind. Eng. Chem. Res. 2004, 43, 5529.
71. Manovic, V.; Anthony, E. J. Steam Reactivation of Spent CaO-Based Sorbent for Multiple CO_2 Capture Cycles. EnViron. Sci. Technol. 2007, 41, 1420.
72. Ida, J.-I., Lin, Y.S. Mechanism of high-temperature CO_2 sorption on lithium zirconate, Environ. Sci. Technol. 37 (2003) 1999.
73. Xiong, R., Ida, J., Lin, Y., Kinetics of carbon dioxide sorption on potassium-doped lithium zirconate, Chem. Eng. Sci. 58 (2003) 4377-4385.
74. Ida, J., Xiong, R., Lin, Y.S., Synthesis and CO_2 sorption properties of pure and modified lithium zirconate, Sep. Purif. Technol. 36 (2004) 41-51.
75. Fauth, D.J., Frommell, E.A., Hoffman, J.S, Reasbeck, R.P., Pennline, H.W., Eutectic salt promoted lithium zirconate: novel high temperature sorbent for CO_2 capture, Fuel Process. Technol. 86 (2005) 1503-1521.
76. Wang, Y.-J., Qi, L., Wang, X.-Y., The study of Li_2ZrO_3 used for absorption of CO_2 at high temperature, Chin. J. Inorg. Chem. (2003), 19 531.
77. Nair, B.N., Yamaguchi, T., Kawamura, H., Nakao, S., Processing of lithium zirconate for applications in carbon dioxide separation: structure and properties of the powders, J. Am. Ceram. Soc. (2004) 87, 68.

78. Ochoa-Fernandez, E., Rusten, H.K., Jakobsen, H.A, Rønning, M., Holmen, A., Chen, D., Sorption enhanced hydrogen production by steam methane reforming using Li_2ZrO_3 as sorbent: sorption kinetics and reactor simulation, Catal. Today, 106 (2005) 41-46.
79. Essaki K, Nakagawa K, Kato M, Uemoto H. CO_2 absorption by lithium silicate at room temperature. J. Chem Eng Jpn 2004;37(6):772e7.
80. Kato M, Nakagawa K, Essaki K, Maezawa Y, Takeda S, Kogo R, et al. Novel CO_2 absorbents using lithium-containing oxide. Int J Appl Ceramic Technol. 2005;2(6):467e75.
81. Kato, M., Yoshikawa, S., Nakagawa, K., Carbon dioxide absorption by lithium orthosilicate in a wide range of temperature and carbon dioxide concentrations, J. Mater. Sci. Lett. (2002) 21, 485.
82. Ebner, A. D.; Reynolds, S. P.; Ritter, J. A. Non-equilibrium kinetic model that describes the reversible adsorption and desorption behavior of CO_2 in a K-promoted hydrotalcite-like compound. Ind. Eng. Chem. Res. 2007, 46, 1737–1744.
83. Ebner, A. D.; Reynolds, S. P.; Ritter, J. A. Understanding the Adsorption and Desorption Behavior of CO2 on a K-Promoted HTLC Through Non-Equilibrium Dynamic Isotherms. Ind. Eng. Chem. Res. 2006, 45, 6387.
84. Ding, Y., Alpay, E. High temperature recovery of CO_2 from flue cases using hydrotalcite adsorbent. Trans IChemE. 79-B1 (2001) 45–51.
85. Ding, Y., Alpay, E. Eluilbria and kinetics of CO_2 adsorption on hydrotalcite adsorbent. Chem. Eng. Sci. 55 (2000) 3461–3474.
86. Lee, K. B.; Verdooren, A.; Caram, H. S.; Sircar, S. Chemisorption of carbon dioxide on potassium-carbonate-promoted hydrotalcite. J. Colloid Interface Sci. 2007, 308, 30–39.
87. Oliveira, E. L. G.; Grande, C. A.; Rodrigues, A. E. CO_2 Sorption on hydrotalcite and alkali-modified (K and Cs) hydrotalcites at high temperatures. Sep. Purif. Technol. 2008, 62, 137–147.
88. Leon, M; Diaz, E.; Bennici, S.; Vega, A.; Oronez, S.; Auroux, A. Adsorption of CO2 on Hydrotalcite-Derived Mixed Oxides: Sorption Mechanisms and Consequences for Adsorption Irreversibility. Ind. Eng. Chem. Res. 47 (2010) 3663–3671.
89. Yang, J.; Kim, J.-N. Hydrotalcite for adsorption of CO_2 at high temperature. Korean J. Chem.Eng. 23 (2006) 77-80.
90. Ding, Y., Alpay, E. Adsorption-enhanced steam-methane reforming. Chem. Eng. Sci. 55 (2000) 3929–3940.
91. Lee, K. B.; Beaver, M. G.; Caram, H. S.; Sircar, S. Novel Thermal Swing Sorption Enhanced Reaction Process Concept for Hydrogen Production by Low Temperature Steam-Methane Reforming. Ind. Eng. Chem. Res. 2007, 46, 5003.
92. Beaver, M. G.; Caram, H. S.; Sircar, S. Sorption enhanced reaction process for direct production of fuel-cell grade hydrogen by low temperature catalytic steam-methane reforming. J. Power Sour. 195 (2010) 1998-2002.
93. Mattisson T, Järdnäs A, Lyngfelt A. Reactivity of some metal oxides supported on alumina with alternating methane and oxygen—application for chemical-looping combustion. Energy Fuels 2003;17:643–51.

94. Mattisson T, Johansson M, Lyngfelt A. Multi-cycle reduction and oxidation of different types of iron oxide particles—application to chemical-looping combustion. Energy Fuels 2004;18:628–37.
95. Cho P, Mattisson T, Lyngfeldt A. Comparison of iron, nickel, copper and manganese based oxygen carriers for chemical looping combustion. Fuel 2004;83:1215–25.
96. Jin H, Okamoto T, Ishida M. Development of a novel chemical looping combustion: synthesis of a solid looping material of $NiO/NiAl_2O_4$. Ind Eng Chem Res 1999;38:126–32.
97. Ishida M, Yamamoto M, Ohba T. Experimental results of chemical-looping combustion with $NiO/NiAl_2O_4$ particle recirculation at 1200 ◦C. Energy Conversion Manage 2002;43:1469–78.
98. Song KS, Seo YS, Yoon HK, Cho SJ. Characteristics of the NiO/Hexaaluminate for chemical looping combustion. Korean J Chem Eng 2003;20:471–5.
99. Ryu HJ, Bae DH, Jin GT. Effect of temperature on reduction reactivity of oxygen carrier particles in a fixed bed chemical looping combustor. Korean J Chem Eng 2003;20:960–6.
100. Adánez J, de Diego LF, García-Labiano F, Gayán P, Abad A. Selection of oxygen carriers for chemical-looping combustion. Energy Fuels 2003;18:371–7.
101. Villa R, Christiani C, Groppi G, Lietti L, Forzatti P, Cornaro U, Rossini S. Ni based mixed oxide materials for CH_4 oxidation under redox cycle conditions. J Mol Catal A: Chem 2003;203–204:637–46.
102. Shah MM, Drnevich RF, Balachandran U. Integrated ceramic membrane system for hydrogen production. In: Proceedings of the 2000 hydrogen program review NREL/CP-570-28890.
103. Air products and chemicals ‘‘Ion transport membrane module and vessel system’’ USP 10/635,695.
104. Wright JD, Copeland RJ. Report no. TDA-GRI-90/0303, Gas Research Institute, September 1990.
105. Roy S, Cox BG, Adris AM, Pruden BB. Economics and simulation of fluidized bed membrane reforming. Int J Hydrogen Energy 1998; 23(9):745.
106. Bischoff BL, Judkins RR. Development of inorganic membranes for Hydrogen separation. Oak Ridge National Laboratory (2009).

Chapter 3

Experimental Setup and Design Parameters

Abstract

An overview of the designed experimental setup and the experimental diagnostic criteria employed in the kinetic experiments are presented in this chapter. A fixed bed tubular reactor setup is designed for studying the steam reforming reactions over the $Rh/Ce_{\alpha}Zr_{1-\alpha}O_2$ catalyst, and thereafter derivation of an intrinsic kinetic model, CO_2 adsorption over K-promoted hydrotalcite sorbent, and the sorption-enhanced steam reforming process over an admixture catalyst/sorbent bed. Much attention is considered in conducting the kinetic experiments that the data acquired are in plug-flow operation and not affected by external and internal mass and heat transfer limitations, axial and radial temperature variations, and bed dilution. Therefore, empirically derived criteria are used for that purpose to assure appropriate analysis intrinsic kinetic data and eventually reliable results. Correlations used to determine the gas transport parameters are also presented.

3.1 Experimental setup

The process is basically divided into three main sections; gas feed section, reaction section, and online analysis section. Process and instrumentation diagram for the lab-scale experimental reactor setup is shown in Figure 1. The operational conditions proposed for experimental testing are ranging from ambient temperature until 750^{o}C and atmospheric pressure up to 6 bars. The feed section includes the reacting gases (CH_4, Air, H_2, CO, CO_2), water, and carrier gases (Ar or N_2). Gas flow rates of CH_4, CO, CO_2, and H_2 in a range of 0–50 nml/min are applied, Ar and/or N_2 are used as an inert and a carrier gas in the flow range of 0–500 nml/min. Gas flows are controlled by thermal mass flow controllers. Steam is applied to the system by evaporating distilled water in a static evaporator mixer (CEM unit) at 80 ^{o}C with a maximum flow rate of 1500 mg/hr. The fluctuation in the measured water concentration is within ±7% of the set-point. The overall gas mixture contains up to 25% water on a relative humidity basis. The reactor is a fixed bed column of 1.0 m in length and is composed of three zones; two upper–part heating zones and one reaction zone of 19.5 cm in length. The reactor is a quartz-made tube with the possibility to use two internal diameters of 4.0 and 9.0 mm along the heating and the reaction zones. The temperature is measured along the reactor and controlled in a temperature range of 25–750 ^{o}C. The total pressure of the reactor is maintained by means of a back pressure controller in the desired range of 1.0–6.0 bar. The process lines are traced at 80 ^{o}C and insulated to prevent any condensation of steam. The reactor outlet stream is fed to a knock-out unit where water is condensed and drained and gases are ventilated. The online sampling section is implemented for the inlet and outlet lines. The product stream is traced up to 120^{o}C and then fed to the GC or the MS gas analysis units to prevent any water condensation.

At the reactor section, several control actions are considered. Temperature thermocouples are connected to control loops at the reactor wall of the upper part of the unit (the heating section), and the lower part of the unit (fixed bed), other temperature sensors and control loops are considered for safety reasons in case of temperature overshoot in the fixed bed zone. The immediate action implemented is to promptly switch off the major feed gas solenoid control valve and the electric heat supply of the unit. Multipoint well thermocouples are implemented at equal distances along the heating section and the fixed bed reaction section to measure the temperature. A back pressure regulator is used to create and control the pressure inside the reactor (if pressure needed is above 1 bar). Gas leakage in the spacing of the reactor shell and in the setup cabinet is detected via a gas sampling loop with a controlled valve, line reducer, vacuum pump, and ppm level detecting devices for both of H_2 and CO gases. A planned safety actions program for the temperature overshoot and the gas level concentrations are given in Table 1. Photos of the experimental setup are displayed in Figures 2 and 3.

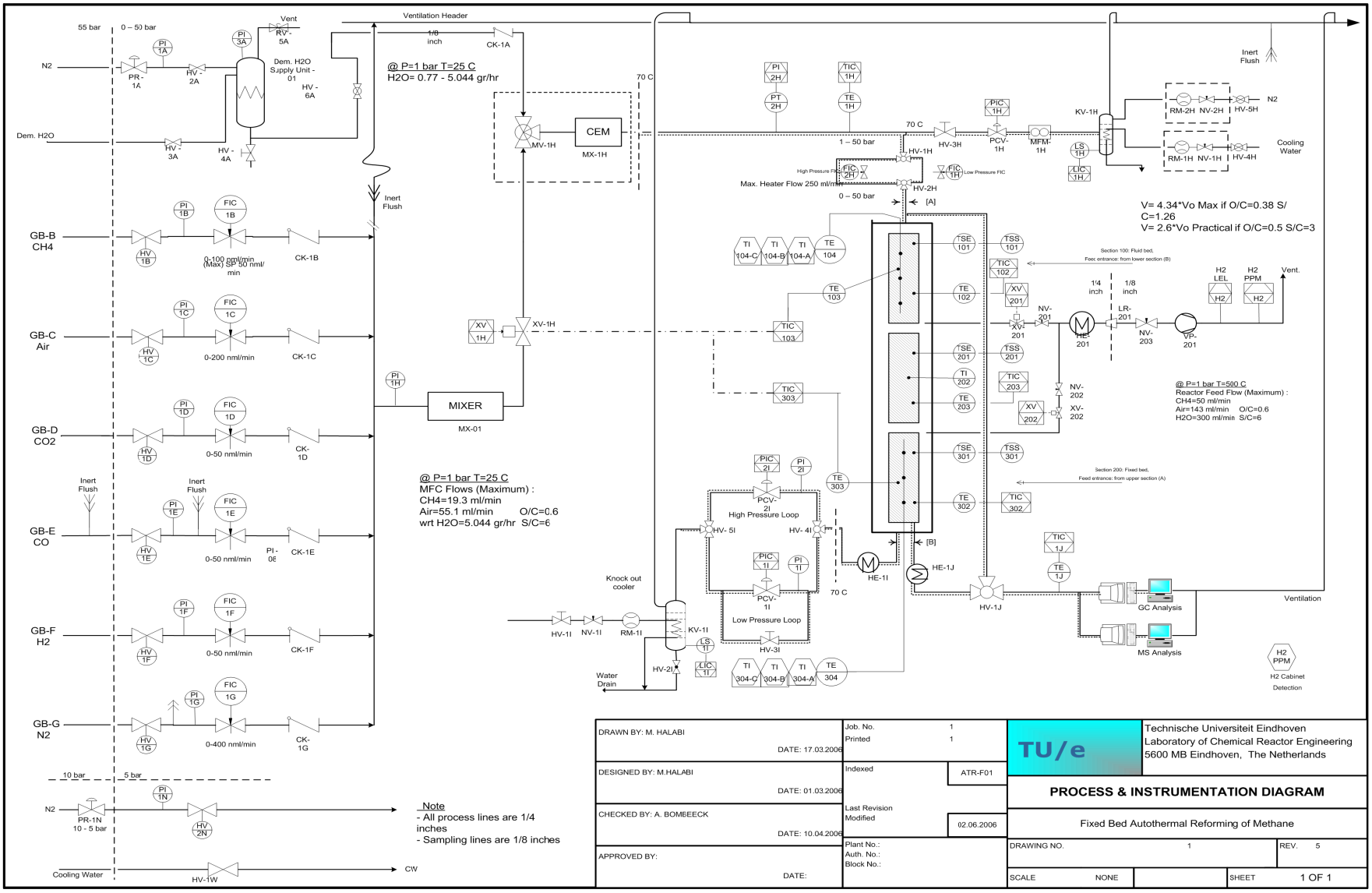

Fig. 1: Process and Instrumentation Diagram of the Lab-scale Fixed Bed Reactor Setup

Table 1: Safety cautions and control actions

Device	Prime Level	Critical Leve	Alarm Signal Acoustic	Alarm Signal Light	Control Action
Fixed bed operation mode					FSV-116 is ON
H_2 and CO Gas detection in tube-shell suction loop					
LT 128	1000 ppm		√	√	
LT 127		10% LEL	√	√	FSV 106 OFF
H_2 and CO Gas detection in cabinet					
LT 129	500 ppm		√	√	
LT 129		1000 ppm	√	√	FSV 106 OFF
Ventilation (suction) loop					
PS 130		False	√		FSV 106 OFF
Water leakage detection					
LIA 140			√	√	
Reactor temperature control					
TT 122 B, TT120 B, TT118 B	750 ^oC		√	√	
TT 122 B, TT120 B, TT118 B		800 ^oC	√	√	Heating OFF + FSV 106 OFF

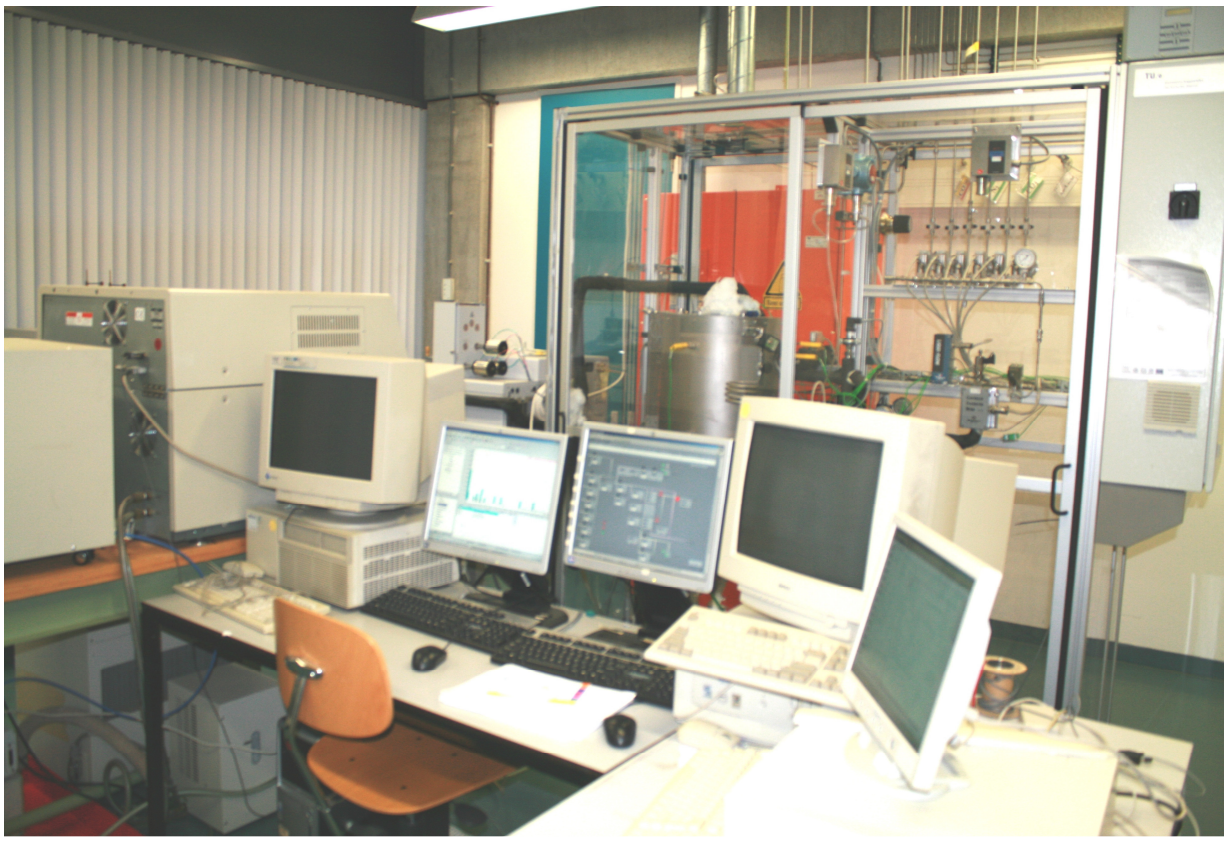

Fig. 2: An overview photo of the experimental fixed bed reactor setup

(a)

(b)

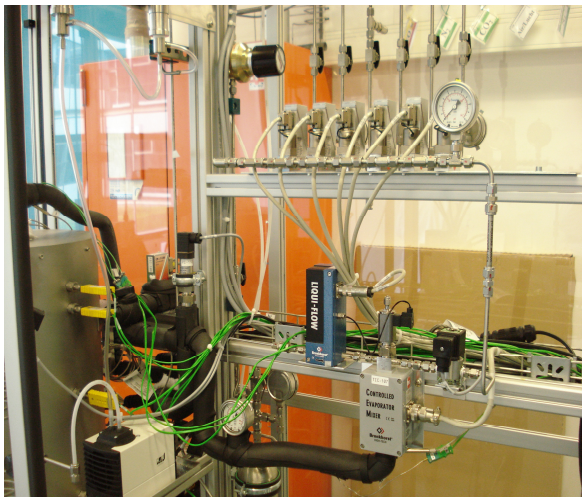

(c)

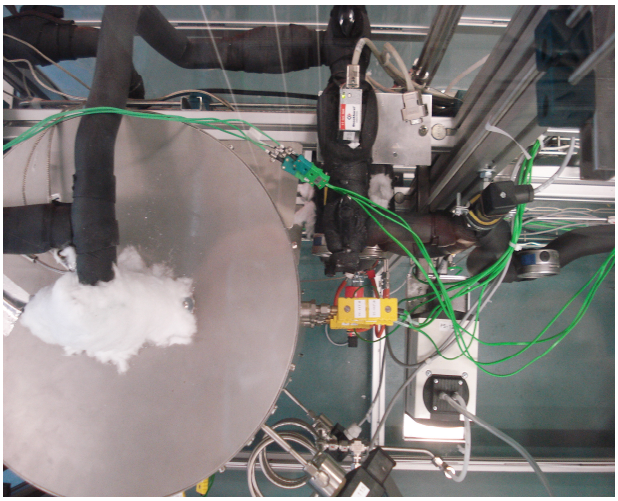

(d)

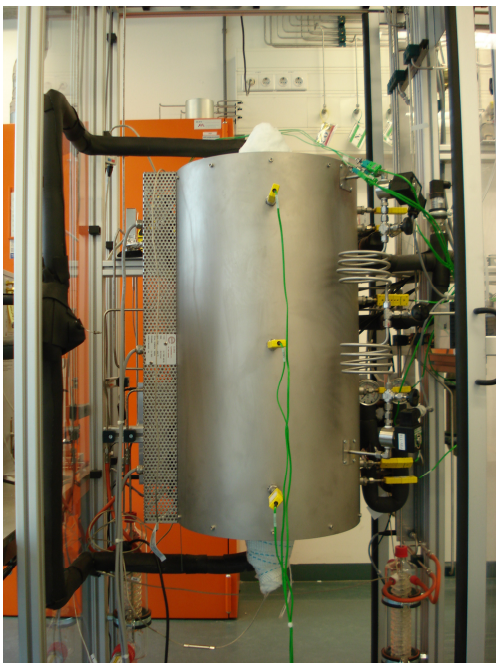

(e)

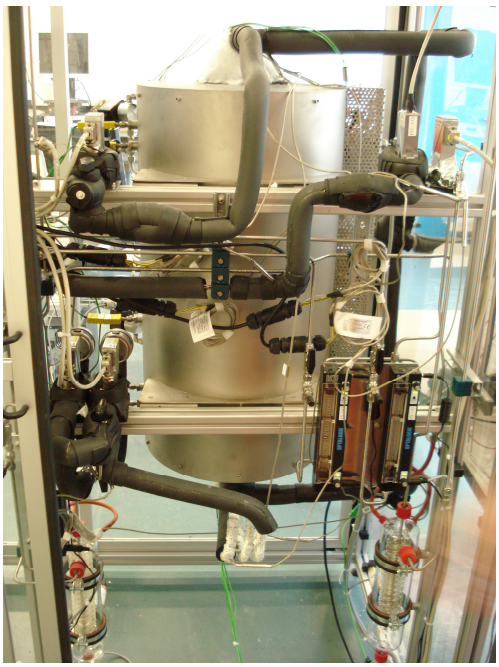

(f)

Fig. 3: Photos of the experimental fixed bed reactor setup. (a) GC gas analysis unit, (b) mass spectrometer gas analysis unit. (c) mass flow controllers and water SEM unit in the gas feed section, (d) top projection of the reactor installations; (e) front profile of the reactor and the temperature thermocouples, (f) rear profile of the reactor and the inlet-outlet gas installations.

3.2 Gas analysis

3.2.1 Gas chromatography

The gas composition is measured at feed and product gas sections using online analysis gas chromatography (GC Varian CP-3800). The GC is utilized for the gas analysis during the steady state steam reforming experiments over the ceria-zirconia supported Rh catalyst. From these experiments the steam reforming process performance, catalyst activity and stability are evaluated, and the intrinsic kinetics data are acquired. The GC is equipped with one Molsieve 5A column (25mm × 0.53 mm × 50 μm) and two PoraBOND Q columns (25mm × 0.53 mm × 10 μm) connected in parallel. The Molsieve 5A column is coupled to a thermal conductivity detector which is used for the analysis of H_2 where Ar is used a carrier gas. One of the PoraBOND Q columns is connected to a thermal conductivity detector and flame ionization detector and is used for the analysis of CH_4, CO, CO_2, N_2, O_2, and H_2O where He is used as a carrier gas. The gas peaks are identified for the components according to their retention times (CO_2=1.45, H_2=1.64, H_2O=2.06, O_2=4.68, N_2=6.03, CH_4=7.34, CO=14.85). A complete analysis interval takes 16 minutes. Peak integration and data acquisition are performed using the Galaxie software for Chromatography Data Analysis.

3.2.2 Mass spectrometer

The gas composition of the feed and the product is measured using online mass spectrometer (ESS II). This mass spectrometer is utilized during the transient CO_2 sorption experiments and the sorption–enhanced steam reforming experiments. Quadrupole mass analyzer (QMS 422) is used to sort out the generated ions according to their mass/charge ratios under electromagnetic field. Multiple ion detector (MID) of CH-THRON type is used to measure the current intensities of the ions. Direct quantitative analysis for the gases was possible through the multiple concentration detection channel (MCD) in which the concentration of the element is calculated by multiplying the ion current intensity measured in the MID detector by its corresponding calibration factor. Mass scale is calibrated for the gases according to the following mass/charge (amu) ratios: H_2=2, CH_4=15, H_2O=18, CO=28, Ar=40, CO_2=44. Ar gas is used as an internal standard throughout all the measurements. The mass scale calibration is corrected for any deviation from the theoretical mass/charge ratios in order to identify the exact peak locations. The gas sampling line (1/16″) was insulated and traced at 130 ^{o}C to prevent any steam condensation. The mass scale is re-calibrated for each set of experiments that are performed at a certain pressure to minimize any inaccurate measurements, (i.e. each pressure is associated with a new calibration). The mass scale is also re-calibrated if any contaminant gases reach to the vacuum chamber in case that the reactor is opened to ambient atmosphere.

3.3 Design parameters

The reactant conversion rate can either by controlled by the intrinsic chemical reaction kinetics or by external mass transport rate from the gas phase to the

catalyst surface or the internal diffusion rate in the pores. In exothermic and endothermic reactions, the temperature gradient over the catalyst bed or the difference in temperature between the bulk gas and the catalyst surface may also affect the observed reaction rate. In deriving the intrinsic kinetics of steam reforming reactions over the Rh-based catalyst in a fixed bed, it is mandatory to guarantee plug-flow operation in which internal and external mass and heat transport limitations are not predominant. Hence, the data obtained from the experiments can represent intrinsic kinetic data and consequently the mathematically derived rate expression is a reliable kinetic model. However, several other conditions must be assured, such as axial and radial isothermicity and negligible pressure drop can be major issues to be verified. In this section, key design criteria are applied and to be satisfied in order to realize accurate results from the mathematical analysis models.

3.3.1 Plug-flow conditions

In non-catalytic operation of the reactor and for the purpose for a kinetic modeling it is assumed the reactor was operated in a plug-flow. This assumption can be justified if the criterion of Cleland & Wilhelm [1] is satisfied:

$$Fo_m = \frac{D_m \tau}{d^2} > 0.25 \tag{1}$$

Fo_m is the Fourier time for mass transport,
D_m is the molecular diffusion coefficient (m^2/s),
τ is the gas residence time along the reactor central axis (s),
d is the reactor tube diameter (m).

This criterion is derived from solving a complete continuity equation taking into account the convective flow, axial and radial diffusion, and a first order reaction. The error in the calculation process of a certain concentration in the plug-flow regime can be ignored when this criterion is satisfied.

In the presence of a catalyst, the catalytic fixed bed reactor can be safely considered in a plug-flow operation if the following criteria presented by Mears [2] are satisfied:

$$\frac{d}{d_p} > 10 \qquad \frac{L}{d_p} > 50 \tag{2}$$

d_p is the catalyst pellet diameter (m),
L is the catalyst bed length (m).

3.3.2 External (interfacial) mass transfer limitations

Generally external mass transfer limitations can be neglected if the concentration difference between the bulk gas phase and the outside surface of the catalyst results in a reaction rate of less than 5% [3]. The concentration gradient over the boundary film can be determined from the following equation at steady state conditions where the rate of mass transfer and the reaction rates are equal.

$$R_v = k_g a_v (C_b - C_s) \tag{3}$$

a_v is the external surface area per unit volume of the catalyst (m^2/m^3),
R_v is the volumetric reaction rate (mol/m^3s),
C_b is the gas concentrations in bulk gas phase (mol/m^3),
C_s is the gas concentrations on the solid catalyst surface (mol/m^3).

The external mass transport limitations are experimentally investigated. CH_4 conversion is measured using different total volumetric flow rates at constant residence time with respect to CH_4 molar feed. The inlet reaction gas composition including the inert gas was modified at every total flow rate to provide a certain presumed space time. When the measured conversion and consequently the reaction rate reach steady values using a specific total gas flowrate, therefore, any higher total gas flowrate can preclude the effect of interfacial mass transport limitations.

3.3.3 Internal (intraparticle) mass transfer limitations

The effectiveness factor must be calculated to investigate whether the intraparticle diffusion rate is high enough in order to neglect the intraparticle concentration gradients. The internal mass transport limitations are experimentally and theoretically checked. CH_4 conversion is measured at a predefined gas flow rate, gas composition, temperature, and pressure using different catalyst pellet sizes. When CH_4 conversion does not change using a pellet size smaller than a specific diameter, thus, internal mass transfer limitations are not affecting measured reaction rates. However, Weisz modulus (Φ) [4] is used as a diagnostic criterion to check that the internal pore diffusion is not binding. The value of Weisz modulus calculated according to Eq. 4 should be small enough (in the range of 10^{-2}). Weisz modulus with a value smaller than 0.25 suggests a high effectiveness factor greater than 0.95.

$$\Phi = \frac{(n+1) R_{obs} \cdot \rho_{cat} \left(d_p / 6 \right)^2}{2 D_{eff} C_s} \tag{4}$$

n is the reaction order,
D_{eff} is the effective intraparticle diffusion coefficient (m^3/m^2s),
R_{obs} is the observed reaction rate ($mol/kg_{cat}s$),
ρ_{cat} is the bulk catalyst density (kg/m^3).

3.3.4 External (interfacial) heat transfer

If the temperature in the bulk gas and on the solid surface results in a less than 5% difference in the measured reaction rates, it is acceptable to ignore the interfacial temperature gradients according to Mears [5]. Thus, the following diagnostic criterion should be satisfied in order to exclude the effect of the external heat transfer limitations

$$\frac{\left|\Delta H^{o}_{rxn}\right| R_{obs} \cdot \rho_{cat} d_p E}{h_f T^2 R} < 0.3 \tag{5}$$

E is the reaction activation energy (kJ/mol)
ΔH^{o}_{rxn} is the reaction enthalpy (kJ/mol),
h_f is the heat transfer coefficient Gas to solid heat transfer coefficient (W/m.K),
R is the universal gas constant (J/mol.K)
T is the gas phase temperature (K).

3.3.5 Internal (intraparticle) heat transfer limitations

The following criterion developed by Mears [5] can be utilized to identify the presence of intraparticle heat transfer limitations. If the criterion is fulfilled it is safe to neglect the effect of the internal heat limitations:

$$\frac{\left|\Delta H^{o}_{rxn}\right| R_{obs} \cdot \rho_{cat} d_p E}{\lambda_p T^2 R} < 3.0 \tag{6}$$

λ_p is the solid thermal conductivity (W/m.K).

3.3.6 Pressure drop

Pressure drop along the axial direction of the catalyst bed can be determined by the Ergun equation [6]. This relation is composed of two terms accounting for the contributions of the laminar and turbulent flows.

$$K_D = \frac{150\mu_g(1-\varepsilon_b)^2 u_s L}{d_p^2 \varepsilon_b^3} + \frac{1.75(1-\varepsilon_b)\rho_f u_s^2 L}{d_p \varepsilon_b^3} \tag{7}$$

u_s is the superficial gas velocity (m/s),
μ_g is the average gas dynamic viscosity (kg/m.s),
ρ_f is the average density of the gas, (kg/m^{3}s),
ε_b is the packing bed porosity.

3.3.7 Axial isothermicity

Isothermicity along the axial direction of the catalytic bed is checked using a multipoint thermocouple. During the kinetics experiments, the temperature difference along the bed was about 2 ^{o}C. Thus, the measured reaction rates will not be affected by this negligible temperature gradient.

3.3.8 Radial isothermicity

The variation of the temperature in the radial direction of the bed has negligible effect on the reaction rates if the following criterion is satisfied [5]:

$$\frac{\left|\Delta H^{o}_{rxn}\right| R_{obs} \cdot \rho_{cat} d_t^2 (1-\varepsilon_b)(1-b)}{\lambda_{e,r} T^2} < \frac{1.6\,RT/E}{1+8 d_p / d_t Bi_h} \tag{8}$$

$$Bi_h = \frac{h_{f,w} d_p}{\lambda_{e,r}} \tag{9}$$

b is the bed dilution degree (m^3_d/m^3_{c+d}),
Bi_h is the Biot number for radial heat transfer,
$h_{f,w}$ is the heat transfer coefficient at the wall ($W/m^2.K$),
$\lambda_{e,r}$ is the effective radial bed conductivity (W/m.K)
This criterion assumes that difference in the reaction rates corresponding to the highest and lowest temperatures may not be greater than 5%.

3.3.9 Effect of bed dilution

Catalyst dilution with an inert used in the exothermic reactions to provide close to isothermal operation in fixed bed reactor may have an influence on the conversion rates. A dilution criterion based on a stochastic model developed by van den Bleek et al. [7] is used to examine this effect. If the following criterion is satisfied, the effect of dilution can be ignored. The relative experimental error considered in this criterion is taken as 5%.

$$\frac{v_n d_p}{L_{UB} \delta} < 4 \cdot 10^{-3} \tag{10}$$

v_n is the fraction inert,
L_{UB} is the length of the undiluted catalyst bed (m),
δ is the relative experimental error.(%).

3.3.10 Axial dispersion coefficient

The effect of the non-ideal flow and the local mixing at turbulent velocities in addition to the diffusive flow can be accounted for using the axial dispersion coefficient (D_Z). The correlation for the axial dispersion coefficient is taken from Edwards and Richardson [8].

$$D_Z = 0.73 D_m + \frac{0.5 u_s d_p}{1 + 9.49 D_m / u_s d_p} \tag{11}$$

D_m is the molecular diffusion coefficient (m^2/s).

3.4 Gas transport coefficients

3.4.1 Effective diffusion coefficient

The major contributions to the effective diffusion coefficient in a catalyst or a sorbent pellet are composed of the molecular and the pore (Knudsen) diffusion coefficients. Knudsen diffusion has key role when the mean free path of a gaseous molecule is larger than pore radius of the catalyst or sorbent pellet. The effective diffusion coefficient and the Knudsen diffusion coefficient are calculated by the correlations presented in Froment and Bischoff [3]. Molecular diffusivities are determined from [9] and [10].

$$D_{eff,i} = \frac{\varepsilon_P}{\tau} \frac{1}{\left(\frac{1}{D_{m,i}} + \frac{1}{D_{k,i}} \right)} \tag{12}$$

$$D_{k,i} = \frac{d_{pore}}{3} \left(\frac{8RT}{\pi M w_i} \right)^2 \tag{13}$$

$D_{eff,i}$ is the effective diffusion coefficient (m^2/s),
$D_{m,i}$ is the molecular diffusion coefficient (m^2/s),
$D_{k,i}$ is the Knudsen diffusion coefficient (m^2/s),
d_{pore} is the pore diameter of the pellet (m),
Mw_i is the molecular weight of the gas species (mol/g),
τ is the tortuosity factor of the pellet,
ε_P is the pellet porosity.

3.4.2 Mass transfer coefficient

The mass transfer coefficient from gas to solid phase is calculated from Chilton-Colburn j_D factor for mass transfer [3,10]. The empirical correlation of Dwivedi & Upadhyay [11] can be used for the calculation of the j_D factor according to the following equations:

$$k_g,i = j_D Re.Sc_i^{1/3} \frac{D_{eff,i}}{d_p} \tag{14}$$

$$\varepsilon_b j_{D,i} = 0.765 Re^{-0.82} + 0.365 Sc_i^{-0.398} \qquad 0.25 < \varepsilon_b < 0.96 \tag{15}$$

$$Re = \rho_f u_s d_p / \mu_g \qquad 0.01 < Re < 1500 \tag{16}$$

$$Sc_i = \mu_g / \rho_f D_{m,,i} \qquad 0.6 < Sc < 7000 \tag{17}$$

$k_{g,i}$ is the gas to solid mass transfer coefficient of species i (m^3/m^2s)
Re Reynolds number
Sc_i Schmitt number of species i.

3.4.3 Heat transfer coefficient

The heat transfer coefficient can be calculated from Chilton-Colburn j_H factor, which can be determined from various empirical correlations [3, 12].

$$h_f = j_H \frac{C_{pg} G_s}{Pr^{2/3}} \tag{18}$$

$$Pr = \frac{C_{pg} \mu_g}{\lambda_g} \tag{19}$$

$$j_H = 0.91 Re^{-0.51} \psi \qquad 0.01 < Re < 50 \tag{20}$$

$$j_H = 0.61 Re^{-0.41} \psi \qquad 50 < Re < 1000 \tag{21}$$

C_{pg} is the specific heat of the fluid (J/kg.K),

h_f is the gas to solid heat transfer coefficient (W/m^{2}K),

λ_g is the average gas thermal conductivity (W/m.K),

Pr is Prandtl number of the gas flow,

ψ is a particle shape factor (for spherical particles has a value of 1).

3.4.4 Effective thermal conductivity

The effective axial thermal conductivity of the bed is calculated according to Yagi et al. [13], see also [14–17].

$$\frac{\lambda_z^f}{\lambda_g} = \frac{\lambda_z^{f,o}}{\lambda_g} + 0.75 \cdot Pr \cdot Re_p \tag{22}$$

$$\frac{\lambda_z^{f,o}}{\lambda_g} = \varepsilon_b + \frac{1 - \varepsilon_b}{0.139 \varepsilon_b - 0.0339 + (2/3) \lambda_g / \lambda_s} \tag{23}$$

λ_z^f is the effective axial thermal bed conductivity (W/mK),

λ_s is the solid thermal conductivity (W/m.K),

ε_b is the packing bed porosity.

3.5 Gas properties

Gas properties such as the fluid density, heat capacity, thermal conductivity, and viscosity are naturally functions of temperature as well as of composition, and they are changing along the reactor length and might vary with time. Temperature and composition dependent expressions are employed in the developed models to calculate the gas properties throughout the reactor [9,10]. However, average values are only used to calculate the gas viscosity and thermal conductivity, the solid thermal conductivity, and the bed heat capacity [18].

References

1. Cleland, F.A., Wilhelm, R.H., Diffusion and reaction in viscous flow tubular reactor, AIChE.J. 2 (1956), 489.
2. Mears, D.E., The role of axial dispersion in trickle-flow laboratory reactors, Chem.Eng.Sci, 26 (1971) 1361.
3. Froment, G.F., Bischoff, K.B, Chemical reactor analysis and design, Wiley, London, (1990).
4. Weisz, P.B, Prater, C.D., Interpretation of measurements in experimental catalysis, Adv.Catal. 6 (1954) 143-196.
5. Mears, D.E., diagnostic criteria for heat transport limitations in fixed bed reactors, J. Catal. 20 (1971) 127-131.
6. Ergun, S., Fluid flow through packed columns, Chem.Eng.Prog. 48 (1952) 89–94.
7. van den Bleek, C.M., van der Wiele, K., van der Berg, P., The effect of dilution on the degree of conversion in fixed bed catalytic reactors, Chem.Eng.Sci., 24 (1969) 681-694.
8. Edwards, M.F., and J.F. Richardson, Gas dispersion in packed beds, Chem.Eng.Sci. 23 (1968) 109–123.
9. Reid, R.C., Prausnitz, J.M., and Poling, B.E., The Properties of gases and liquids, McGraw-Hill, New York, (1988).
10. Bird, R.B., Stewart, W.E., and Lightfoot, E.N., Transport phenomena, 2nd Ed., Wiley, New York, (2002).
11. Dwivedi, P.N. and Upadhyay, S.N., Particle-fluid mass transfer in fixed and fluidized beds. Industrial and Engineering Chem.Proc.Des.Dev.16, (1977) 157–165.
12. Geankoplis, C.J., Transport processes and unit operations, 3rd Ed., Prentice Hall Int., 1993.
13. Yagi, S., Kunii, D., and Wakao, N., Studies on axial effective thermal conductivities in packed beds, AIChE J. 6, (1960) 543–546.
14. Kunii, D., Smith, J.M., Heat transfer characteristics of porous rocks, AIChE J. 6 (1960) 71–78.
15. De Wash, A.P., Froment, G.F., Heat transfer in packed bed, Chem.Eng.Sci. 27 (1972) 567–576.
16. Li, C.H., Finlayson, B.A., Heat transfer in packed bed – a reevaluation, Chem. Eng.Sci. 32 (1977) 1055–1066.
17. Wakao, N., Kaguei, S., Heat and mass transfer in packed bed, Gordon and Breach, New York, (1982).
18. Perry, R.H., Green, D.W., Perry's Chemical Engineering's Handbook, 7th Ed. McGraw Hill, (1997).

Chapter 4

Modeling of Methane Autothermal Reforming in a Fixed Bed Reactor

This chapter has been published as
M.H. Halabi, M.H.J.M. de Croon, J. van der Schaaf, P.D. Cobden, J.C. Schouten, Modeling and analysis of autothermal reforming of methane to hydrogen in a fixed bed reformer, Chem.Eng.J. 137, 568-578, 2008.

Abstract

This chapter presents a performance analysis for the autothermal reforming process of methane in a fixed bed reformer for hydrogen production. The process is simulated using a 1-D heterogeneous reactor model under small-scale conditions. The model accounts for mass and thermal dispersion in the axial direction, axial pressure distribution, and interfacial and intraparticle transport. The process performance under dynamic and steady state conditions is analyzed with respect to key operational parameters: temperatures of gas feed and catalyst bed, oxygen/carbon and steam/carbon ratios, gas hourly space velocity (GHSV), and feed contaminations. The influence of these parameters on gas temperature, methane conversion, hydrogen yield and purity, and reforming efficiency is investigated. An optimal operational window of a GHSV range from 1050 to 14000 hr^{-1}, steam/carbon molar ratio of 4.5 – 6.0, and oxygen/carbon molar ratio of 0.45-0.55 is obtained to achieve a high conversion level of 93%, hydrogen purity of 73%

on dry basis, thermal reformer efficiency of 78%, and a yield of 2.6 mole hydrogen per 1 mole of methane fed. The simulation studies are performed using gas feed temperature and pressure of 500^{o}C and 1.5 bar, respectively.

4. 1 Introduction

Hydrogen is a major feedstock in many chemical and petrochemical industries and well perceived as a pollution-free primary energy carrier for future transportation fuel as well as electricity generation. The recent surge in demand for small-scale, cheap, and efficient hydrogen production is driven by the high interest in the application of fuel cells for electricity generation [1, 2, 3]. Fuel cells offer a promising path for hydrogen based energy systems as clean, flexible, and efficient devices utilized in either stationary or portable power generation applications and in transportation [3, 4].

A typical gas mixture feed to a fuel cell can be obtained by converting the hydrocarbon fuel first into synthesis gas in a reformer. For a proton exchange membrane fuel cell, the gas feed must be purified in a water gas shift reactor where CO is converted into CO_2 and additional hydrogen is obtained. The remaining traces of CO have to be removed further, for instance by selective oxidation, before the final gas mixture is fed to the anode side of the fuel cell.

A complete transition towards hydrogen as a standard energy carrier within the next decade is unlikely, due to the current difficulties in its economically and technically feasible production routes and storage. The ultimate goal towards hydrogen economy is to use renewable energy for hydrogen production. Thus, reforming fuel for hydrogen production is solely an intermediate solution. Nevertheless, the ongoing research on hydrogen technology may significantly improve the energy efficiency [5, 6].

Methane reforming is currently a well-established technology and has been the most important industrial process for the production of hydrogen and/or synthesis gas in the manufacture of ammonia, methanol, and other chemicals. This technology has been adequately reviewed [7–12]. The major reforming processes include steam reforming (SR), partial oxidation reforming (POX), catalytic partial oxidation (CPO), and autothermal reforming (ATR).

SR is a highly endothermic process and therefore demands an efficient heat supply to the system. It is usually operated in a temperature range of 850 – 950^{o}C on Ni – based catalyst. It is a very energy- and capital-intensive process although the present technology approaches 90% of the maximum thermodynamic efficiency [14]. However, steam reforming is economically unattractive option for low-volume and low-pressure hydrogen production [6, 12]. POX uses pure oxygen and achieves H_2 to CO ratios from 1.6 to 1 in the product syngas. CPO uses a catalyst that permits flameless partial combustion to H_2 and CO [13]. Conventional ATR uses a partial oxidation burner followed by a catalyst bed with natural gas, steam

and oxygen to produce syngas with H_2 to CO ratios of 2 to 1 [6]. CPO typically operates at low steam/carbon ratio (S/C from 0 to 1), while ATR operates at relatively higher steam load (S/C > 1). In CPO, the catalyst bed temperatures tend to be higher than ATR and thus higher reaction rates and consequently a higher space velocity is possible even the syngas yield is somewhat lower than ATR [2]. However, premixing and preheating is more straightforward because there is no steam is fed to the process. Currently, CPO and ATR require added oxygen which increases the costs for low volume hydrogen production. In both processes, the target is to achieve the thermodynamic equilibrium composition, which is governed by feed conditions (composition, temperature), pressure, and heat loss. These factors must be optimized to maximize the syngas yield, and to minimize the hydrocarbon slip.

Because of thermodynamic reversibility of the SR reactions and the POX reactions, limits are imposed on the maximum methane conversion and hydrogen yield that can be attained in conventional fixed bed large-scale units. Therefore, a strong necessity in such technologies is to include further purification units of hydrogen using shift reactors, CO_2 separation units, preferential CO oxidation units (PROX), and pressure-swing absorption units (PSA). These operational units, particularly the PSA, are highly cost intensive and inconvenient for small-scale applications such as onboard fuel cells. Extensive thermodynamic calculations have been performed on ATR of natural gas to analyze the equilibrium product composition and the influence of the natural gas composition on optimizing hydrogen yield and minimizing CO co-generation [15, 16, 17].

The catalytic ATR has received much attention in research during the recent years as a viable process for hydrogen generation for fuel cell systems [6, 11, 12]. It offers advantages of small unit size and lower operational temperature, easier startup, and wider choice of materials. Moreover, it has a higher energy efficiency compared to SR or POX. ATR has major advantages over other reforming alternatives mainly for low energy requirements, high GHSV (at least one order of magnitude relative to SR), and lower process temperature than POX, higher H_2/CO ratio, and easily regulated H_2/CO ratio by the inlet gas composition.

Although ATR has an interesting potential in industrial application, there has been only a limited amount of work reported in the field of reactor design and simulation [18]. In this chapter, the autothermal reforming of methane is optimized in terms of fuel conversion, reforming efficiency, and H_2 purity and yield in a fixed bed reactor with a mathematical modeling approach at small-scale conditions. The process performance under dynamic and steady state conditions is analyzed with respect to major operational parameters: temperatures of gas feed and catalyst bed, oxygen/carbon and steam/carbon ratios, gas feed space velocity, and feed contaminations. An optimal operational window of GHSV, oxygen/carbon ratio, and steam/carbon ratio is characterized under relatively mild conditions of temperature and pressure. The influence of the reforming-oxidation kinetic model and reactor conditions on catalyst and gas temperatures is discussed. Furthermore,

the formation of undesired hot spots in the fixed bed reformer as a function of oxygen partial pressure can be predicted with the model. Special attention must be paid to this point in the design and construction stage of such reactor.

4. 2 Autothermal reforming of natural gas

ATR combines the effects of both the endothermic steam reforming and the exothermic partial oxidation by feeding the fuel together with the oxidant (air fed or oxygen fed) and steam over a catalyst in a fixed bed reactor.

4.2.1 ATR reactions

In a reforming process of natural gas, many reactions are likely to occur. If we consider that methane is the major dominating species in natural gas, the following set of reactions shown in Table 1 will be involved. The first four reactions are considered as the prevailing reaction routes in the autothermal reforming process. The water gas shift reaction tends to influence the final H_2/CO ratio depending on the feed S/C ratio. At high operational temperature, the reaction will favor production of CO instead of H_2; that is the reason why a large S/C ratio is used in methane reforming.

Table 1: Autothermal reforming reactions

	Reaction	ΔH_{298K} kJ/mol
R_1. Steam reforming	$CH_4 + H_2O \leftrightarrow CO + 3H_2$	206.2
R_2. Steam reforming	$CH_4 + 2H_2O \leftrightarrow CO_2 + 4H_2$	164.9
R_3. Water gas shift	$CO + H_2O \leftrightarrow CO_2 + H_2$	-41.1
R_4. Total combustion	$CH_4 + 2O_2 \rightarrow CO_2 + 2H_2O$	-802.7
R_5. Partial oxidation	$CH_4 + 1/2\,O_2 \leftrightarrow CO + 2H_2$	-36
R_6. Partial combustion	$CH_4 + O_2 \leftrightarrow CO_2 + 2H_2$	-71
R_7. Dry reforming	$CH_4 + CO_2 \leftrightarrow 2CO + 2H_2$	247
R_8. Boudouard reaction	$2CO \leftrightarrow C + CO_2$	-172
R_9. Decomposition	$CH_4 \leftrightarrow C + 2H_2$	75

It is also theoretically possible to reform methane with CO_2, this is known as dry reforming as represented in reaction 7. The catalysis research for such a reforming route of methane is still very challenging and the formation of acceptable amounts of syngas or H_2 via this route alone does not appear feasible yet [6].

The reforming reactions may also be associated with coke formation in some cases as in reactions 8 and 9. The coke formation reactions are definitely undesired routes due to the reduced process efficiency attained, catalyst deactivation, corrosion of material of construction and unfavorable reactor cleaning. However, coke formation is usually suppressed by higher temperatures, and high O/C and S/C operational ratios [1, 4, 15]. A similar set of reactions is expected to occur with ethane and other hydrocarbons in the feed.

4.2.2 Thermal neutrality condition of ATR

The overall ATR reforming of methane is ideally expressed by the following reaction equation:

$$CH_4 + x(O_2) + (2-2x)H_2O \Leftrightarrow CO_2 + (4-2x)H_2 \quad (1)$$

where x is the O/C molar ratio. This ratio is the key stoichiometric parameter that determines the theoretical S/C molar ratio required to convert CH_4 into CO_2 and H_2, the maximum H_2 yield, and the heat of reaction at adiabatic conditions at a defined temperature. Autothermicity of the reaction can be theoretically attained when the net adiabatic heat of reaction is zero:

$$\Delta H_T = \sum_i v_{i(x)} H_{i(T)} = 0 \quad (2)$$

However, due to heat transfer losses through the reactor walls, the operating O/C ratio should be slightly higher than the stoichiometric ratio to account for any heat loss or to raise the gas temperature to control the product composition and to limit coke formation.

4. 3 Mathematical model

A 1-D heterogeneous model is constructed to investigate the ATR process behavior at dynamic and steady state conditions in a fixed bed reformer. The major assumptions in the model can be listed as follows:

1. Ideal gas behavior;
2. Adiabatic operation;
3. Mass axially dispersed plug-flow conditions are considered with negligible radial gradients;
4. Thermal dispersion in the axial direction is also considered with negligible radial gradients;
5. Concentration and temperature gradients in the radial direction are ignored;
6. No temperature gradient in the catalyst particles;
7. Six reactive species (CH_4, O_2, CO, CO_2, H_2, H_2O) and one inert component (N_2) are involved in the model;
8. No homogenous gas phase reactions are considered as the temperatures are lower than 600^{o}C.
9. Uniform particle size;
10. Constant bed porosity.

4.3.1 Reaction kinetic model

To reduce the complexity of the mathematical model development and solution, only the reactions with significant rates will be considered. Among the possible set of reactions previously discussed, the two steam reforming reactions R_1 and R_2, water gas shift R_3, and the total combustion reaction R_4 prove to have significant rates [15]. Therefore, the partial oxidation reaction R_5, the partial combustion reaction R_6, the dry reforming reaction R_7, the Boudouard reaction R_8, and the decomposition reaction R_9 are ignored in this modeling study. There is a large

number of kinetic models for steam reforming and water-gas shift reactions in literature. The model of Xu & Froment [19] over Ni – based catalyst is considered to be more general and has been extensively tested under labscale conditions [20]. It is investigated on a temperature range from 500°C to 575°C. The kinetic model of Trimm & Lam [21] is considered as a rigorous study for methane combustion. The kinetic rate expression developed in their model at 557°C is adopted for the methane combustion reaction in this work. However, since it was derived over supported Pt – based catalyst, the model adsorption parameters are adjusted for Ni – based catalyst [22]. The combined model for the kinetic rate equations of ATR is given in Table 2. The reaction equilibrium constants and Arrhenius kinetic parameters are listed in Table 3. Van't Hoff parameters for species adsorption are given in Table 4.

Table 2: ATR kinetic reaction model

Reaction rate equation	
$R_1 = \frac{k_1}{p_{H_2}^{2.5}}\left(p_{CH_4}p_{H_2O} - \frac{p_{H_2}^3 p_{CO}}{K_I}\right) * \frac{1}{\Omega^2}$	(3)
$R_2 = \frac{k_2}{p_{H_2}^{3.5}}\left(p_{CH_4}p_{H_2O}^2 - \frac{p_{H_2}^4 p_{CO_2}}{K_{II}}\right) * \frac{1}{\Omega^2}$	(4)
$R_3 = \frac{k_3}{p_{H_2}}\left(p_{CO}p_{H_2O} - \frac{p_{H_2}p_{CO_2}}{K_{III}}\right) * \frac{1}{\Omega^2}$	(5)
$R_4 = \frac{k_{4a}p_{CH_4}p_{O_2}}{\left(1+K_{CH_4}^C p_{CH_4} + K_{O_2}^C p_{O_2}\right)^2} + \frac{k_{4b}p_{CH_4}p_{O_2}}{\left(1+K_{CH_4}^C p_{CH_4} + K_{O_2}^C p_{O_2}\right)}$	(6)
$\Omega = 1 + K_{CO}p_{CO} + K_{H_2}p_{H_2} + K_{CH_4}p_{CH_4} + K_{H_2O}\frac{p_{H_2O}}{p_{H_2}}$	(7)

Table 3: Reaction equilibrium constants and Arrhenius kinetic parameters

Reaction, j	Equilibrium constant, K_j	k_{oj} (mol/kg$_{cat}$.s)	E_j (J/mol)
1	K_I = exp(-26830/T_s+30.114) (bar^2)	1.17*10^{15} bar$^{0.5}$	240100
2	$K_{II} = K_I \cdot K_{III}$ (bar^2)	2.83*10^{14} bar$^{0.5}$	243900
3	K_{III} = exp(4400/T_s - 4.036)	5.43*10^5 bar^{-1}	67130
4		8.11*10^5 bar^{-2}	86000
		6.82*10^5 bar^{-2}	86000
$k_j = k_{oj} * \exp(-E_j / RT)$			

The rate of consumption or formation of species i, r_i (mol/kg$_{cat}$.s) is determined by summing up the reaction rates of that species in all the reactions R_j (mol/kg$_{cat}$.s). Effectiveness factors η_j are used to account for the intraparticle transport limitation [23, 24, 25]. Therefore, the reaction rate of each species becomes:

$$r_{CH_4} = -\eta_1 R_1 - \eta_2 R_2 - \eta_4 R_4 \quad \text{(8-a)}$$

$$r_{O_2} = -2\eta_4 R_4 \quad \text{(8-b)}$$

$r_{CO_2} = \eta_2 R_2 + \eta_3 R_3 + \eta_4 R_4$ (8-c)

$r_{H_2O} = -\eta_1 R_1 - 2\eta_2 R_2 - \eta_3 R_3 + 2\eta_4 R_4$ (8-d)

$r_{H_2} = 3\eta_1 R_1 + 4\eta_2 R_2 + \eta_3 R_3$ (8-e)

$r_{CO} = \eta_1 R_1 - \eta_3 R_3$ (8-f)

where $\eta_1 = 0.07$, $\eta_2 = 0.06$, $\eta_3 = 0.7$, $\eta_4 = 0.05$ [23].

Table 4: Van't Hoff parameters for species adsorption

	K_{oi} (bar^{-1})	ΔH_i (J/mol)	K_{oi}^C (bar^{-1})	ΔH_i^C (J/mol)
CH_4	$6.65*10^{-4}$	-38280		
CO	$8.23*10^{-5}$	-70650		
H_2	$6.12*10^{-9}$	-82900		
H_2O	$1.77*10^{5}$ bar	88680		
CH_4 (combustion)			$1.26*10^{-1}$	-27300
O_2 (combustion)			$7.78*10^{-7}$	-92800
$K_i = K_{oi} * \exp(-\Delta H_i / RT)$				
$K_i^C = K_{oi}^C * \exp(-\Delta H_i^C / RT)$				

4.3.2 Governing equations

The mathematical model developed is typically composed of mass and energy balance equations in the gas and the solid phases as shown in Table 5. Pressure drop along the axial direction in the fixed bed is described by the Ergun equation [27]. K_D and K_V are parameters corresponding to the viscous and kinetic loss terms, respectively and given in Table 6. The axial dispersion coefficient to account for the non-ideal flow and local mixing at turbulent velocities plus the diffusive flow is estimated using the equation of Edwards and Richardson [28], see Table 6. The axial thermal effective conductivity of the bed shown in Table 6 is determined from [29], see also [30, 31, 32, 33]. The gas and catalyst temperatures are initially equal to the feed temperature at the start up conditions. Therefore, the catalyst bed is heated up to the feed temperature. The initial and boundary conditions are summarized in Table 5.

4.3.3 Gas properties and transport coefficients

Gas properties such as the fluid density, heat capacity, thermal conductivity, and viscosity are naturally functions of temperature as well as of composition, and they are changing along the reformer length and might vary with time. Temperature and composition dependent expressions are employed in the model to calculate the gas properties throughout the reactor [34, 35]. However, average values are only used to calculate the gas viscosity and thermal conductivity, the solid thermal conductivity, and the bed heat capacity [34]. The mass transfer coefficient from gas to solid, $k_{g,i}$, is calculated from the Chilton-Colburn factor, j_D, for mass transfer [36], see also [35]. The heat transfer coefficient, h_f, is also determined from the Chilton-Colburn factor, j_H [36]. The transport coefficients are presented in Table 6.

Table 5: Reactor simulation model with corresponding boundary and initial conditions

Mass and energy balances in the gas phase

$$\varepsilon_b \frac{\partial C_i}{\partial t} + \frac{\partial (uC_i)}{\partial z} + k_{g,i} a_v (C_i - C_{i,s}) = \varepsilon_b D_Z \frac{\partial^2 C_i}{\partial z^2} \quad (9)$$

$$\varepsilon_b \rho_f C_{pg} \frac{\partial T}{\partial t} + u \rho_f C_{pg} \frac{\partial T}{\partial z} = h_f a_v (T_s - T) + \lambda_z^f \frac{\partial^2 T}{\partial z^2} \quad (10)$$

Mass and energy balances in the solid phase

$$k_{g,i} a_v (C_i - C_{i,s}) = (1 - \varepsilon_b) \rho_{cat} r_i \quad (11)$$

$$\rho_{bed} C_{p,bed} \frac{\partial T_s}{\partial t} + h_f a_v (T_s - T) = \rho_{cat} (1 - \varepsilon_b) \sum -\Delta H_{rxn,j} \eta_j R_j \quad (12)$$

Note: rate of accumulation of the concentration in the solid particle ($C_{i,s}$) is ignored, due to small particle size, see [26].

Pressure drop

$$\partial P / \partial z = -K_D u - K_V u^2 \quad (13)$$

Boundary conditions

At the reformer inlet z = 0.0

$$C_i = C_{i,o} \quad T = T_o \quad T_s = T_{s,o} \quad P = P_o \quad (14)$$

At the reformer exit z = L

$$\partial C_i / \partial z = 0 \quad \partial T / \partial z = 0 \quad \partial T_s / \partial z = 0 \quad (15)$$

Initial conditions

$$C_i = C_{i,o} \quad T = T_o \quad T_s = T_{s,o} \quad (16)$$

Table 6: Empirical correlations employed in the model

Semi-empirical relations for K_D and K_V [27]:

$$K_D = \frac{150 \mu_g (1 - \varepsilon_b)^2}{d_p^2 \varepsilon_b^3} \text{ (Pa.s/m}^2\text{)}; \quad K_V = \frac{1.75(1 - \varepsilon_b) \rho_f}{d_p \varepsilon_b^3} \text{ (Pa.s}^2\text{/m}^3\text{)}$$

Mass axial dispersion coefficient [28]:

$$D_Z = 0.73 D_m + \frac{0.5 u d_p}{1 + 9.49 D_m / u d_p}$$

Effective thermal conductivity [29]:

$$\frac{\lambda_z^f}{\lambda_g} = \frac{\lambda_z^{f,o}}{\lambda_g} + 0.75 \cdot Pr \cdot Re_p \ , \qquad \frac{\lambda_z^{f,o}}{\lambda_g} = \varepsilon_b + \frac{1 - \varepsilon_b}{0.139 \varepsilon_b - 0.0339 + (2/3) \lambda_g / \lambda_s}$$

Mass transfer coefficient [36]:

$$k_{g,i} = j_{D,i} Re . Sc_i^{1/3} \frac{D_i}{d_p}$$

$$\varepsilon_b j_{D,i} = 0.765 Re^{-0.82} + 0.365 Sc_i^{-0.398}$$

$$Re = \rho_f u d_p / \mu \ ; \quad Sc_i = \mu / \rho_f D_i \qquad 0.01 < Re < 1500 \ , \quad 0.6 < Sc < 7000 \ , \quad 0.25 < \varepsilon_b < 0.96$$

Heat transfer coefficient [36]

$$h_f = j_H \frac{C_{pg} G_s}{Pr^{2/3}} \qquad Pr = \frac{C_{pg} \mu_g}{\lambda_g}$$

$$j_H = 0.91 Re^{-0.51} \psi \quad 0.01 < Re < 50 \ ,$$

$$j_H = 0.61 Re^{-0.41} \psi \quad 50 < Re < 1000 \ ,$$

4.3.4 Numerical solution

The mathematical model consisting of coupled partial differential and algebraic equations is implemented and solved in gPROMS modeling environment (Process Systems Enterprise Ltd.). Backward difference of first order is used as a spatial discretization method over a uniform grid of 100 intervals. The integration over the time domain is performed by the DAE integrator based on the variable time step of the backward differentiation formula. Reactor parameters, operating conditions, and average gas properties used globally throughout this simulation study are listed in Table 7.

Table 7: Reactor parameters, operating conditions, and average gas properties used in the model simulations

	Unit	Value
Reactor length	m	0.4
Gas feed temperature	^oC	500
Catalyst temperature	^oC	500
Pressure	bar	1.5
Solid density [18]	kg/m^3	1870
Bed voidage	-	0.4
Particle diameter	m	$2*10^{-3}$
Gas mass flow velocity	kg/m^2s	0.15
Steam/carbon molar ratio	-	6.0
Oxygen/carbon molar ratio	-	0.45
Average gas properties		
Molecular diffusivity, D_m	m^2/s	$1.6*10^{-5}$
Gas viscosity, μ_g	kg/m.s	$0.031*10^{-3}$
Gas thermal conductivity, λ_g	W/m.K	0.0532
Solid thermal conductivity, λ_s	W/m.K	13.8
Bed heat capacity, $C_{p,bed}$ [34]	J/kg.K	850
LHV_{H_2}	MJ/kmol	240
LHV_{CH_4}	MJ/kmol	800

4. 4 Results and discussion

The most recent work for modeling of autothermal reforming of CH_4 for H_2 production by Hoang and Chan [18], presents potential operating conditions for high CH_4 conversion and H_2 purity (on dry basis) at a S/C ratio of 1 and an air/carbon ratio (A/C) of 3.5 (equivalent to an O/C ratio of 0.74). They obtained a conversion of 98% and H_2 purity and yield of 42% and 1.9, respectively. However, a further insight in the reforming process can generate improved operation performance in terms of reforming efficiency, and H_2 purity and yield using higher S/C ratios to boost the reaction selectivity towards H_2 production and lowering the air or oxygen to carbon ratios to merely provide sufficient energy for the endothermic reforming reactions. Figure 1 shows the composition distribution during autothermal reforming at different temperatures at thermodynamic equilibrium at a pressure of 1.5 bar and molar ratios of S/C and O/C of 6 and 0.45,

respectively. Higher CH_4 conversion is naturally favored at elevated temperatures. Conversion levels greater than 96% can be achieved at temperatures above 500°C. However, the H_2 purity (defined as mole fraction of H_2 on dry basis, $Y_{dry}(H_2)$) obtained is gradually increasing with temperature until it reaches a maximum value of 74.1% at 500°C, beyond which it starts to slightly decrease at higher temperatures and no further improvement can be attained. This is contributed to the fact that equilibrium between CO and CO_2 tends to favor the reverse water gas shift reaction and the equilibrium conditions are disturbed resulting in reduced H_2 concentration and increased CO concentration. Therefore, the gas feed temperature must be selected above 500°C to give a maximum H_2 purity, taking into account that the adiabatic temperature rise of the reformer will already lead to a higher CH_4 conversion.

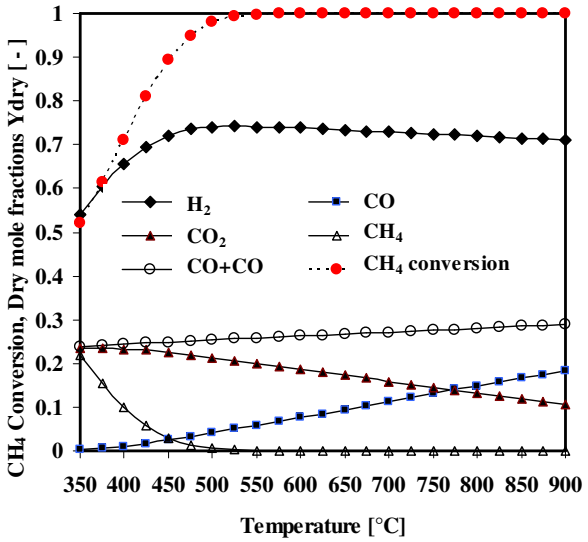

Fig. 1: ATR product gas composition at 1.5 bar, O/C= 0.45, S/C= 6 at thermodynamic equilibrium.

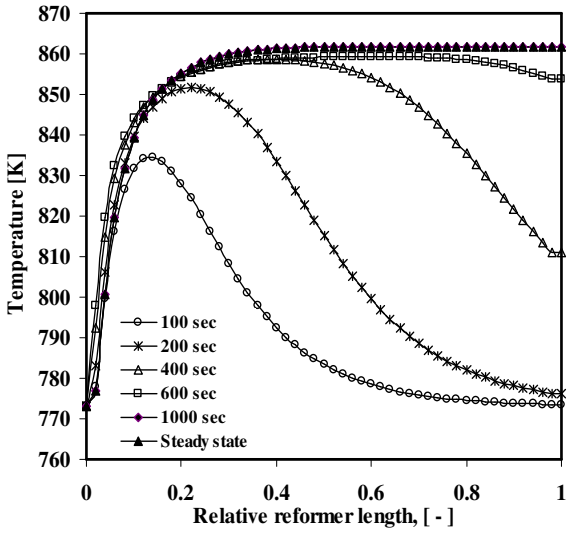

Fig. 2: Dynamic temperature profiles along the axial reformer direction at 500°C, 1.5 bar, O/C= 0.45, S/C= 6.

Figure 2 shows the dynamic profiles of the gas temperature along the axial reformer direction at different times using the simulation parameters and conditions listed in Table 7 for gas feed flow, space velocity, pressure, and O/C and S/C ratios. The temperature is changing with time until it monotonically approaches steady state conditions at 862 K in about 13 minutes with a maximum rise of 89°C above the feed inlet temperature. The simulation curves show no peak value attained in the front part of the reformer and then are gradually flattening or even decreasing in the rear part as might be expected for the typical behavior of a catalytic partial oxidation reformer and even for a high O/C fed autothermal reformer [23, 38, 39]. This phenomenon is further discussed for high concentrations or high-pressure operation below.

The steady state composition profiles of the gas species on dry basis as a function of the axial reactor coordinate are given in Figure 3. The H_2 purity obtained at the S/C ratio of 6, and O/C ratio of 0.45 is 72% with corresponding CH_4 conversion of 93%, H_2 yield of 2.6 mol H_2 produced/mol CH_4 fed, and thermal reforming efficiency of 78%. This thermal efficiency of the reforming process is defined as

$$eff = \frac{n_{H_2}, \text{mol } H_2 \text{ produced}}{n_{CH_4}, \text{mol } CH_4 \text{ fed}} \cdot \frac{LHV_{H_2}}{LHV_{CH_4}} \quad (17)$$

The wet concentration profiles show a peak for water in the first 10% of the reformer length as increased product concentration from the oxidation reaction (see Fig. 4). Thereafter, the water concentration decreases along the reformer length due to its consumption via the endothermic reforming reactions. However, feed oxygen is fully consumed by the catalytic oxidation reaction in the first 10% of the reformer.

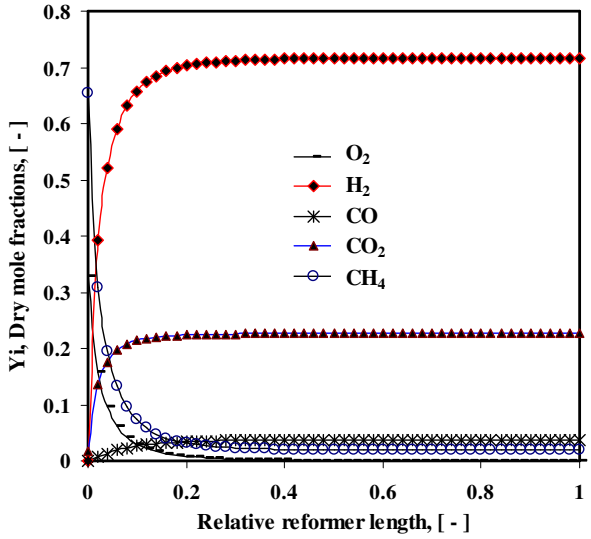

Fig. 3: Steady state composition profiles (on dry basis), at 500°C, 1.5 bar, O/C= 0.45, S/C= 6.

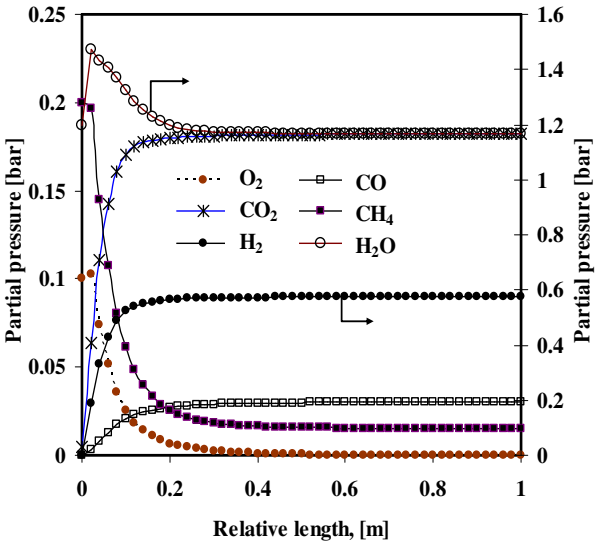

Fig. 4: Steady state component partial pressure profiles, at 500°C, 1.5 bar, O/C= 0.45, S/C= 6.

The front part of the reformer is obviously utilized to generate sufficient energy for the process, so that the oxidation reaction is dominating the front section while the rest of the reformer is dominated by the endothermic reforming reactions. Due to the high concentration of steam and relatively low concentration of oxygen in the reactor, the oxidation and the reforming reaction rates are of the same order of magnitude (see Fig. 5).

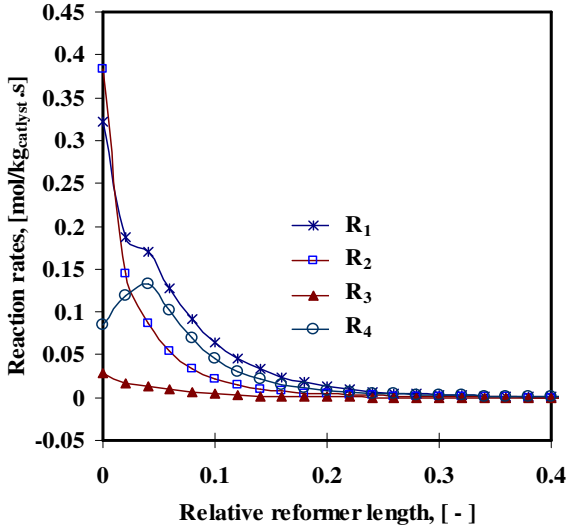

Fig. 5: ATR reaction rates along the reformer length at 500°C, 1.5 bar, O/C= 0.5, S/C= 6.

Figures 6, 7, and 8 reveal how the ATR process behaves under the given simulated conditions in terms of heat transfer. Figure 6 depicts the temperature profiles along the reformer at steady state in the gas and solid phases. It is evident that heat transfer is quite effective and the interfacial resistances between the catalyst and the gas are relatively small along the reformer, although the catalyst surface is about 11°C higher in temperature than the bulk gas at the front section. This is due to the fact that heat of combustion generated in the catalyst is effectively transported to the bulk gas. The two profiles are almost identical after the first 20% of the reformer length.

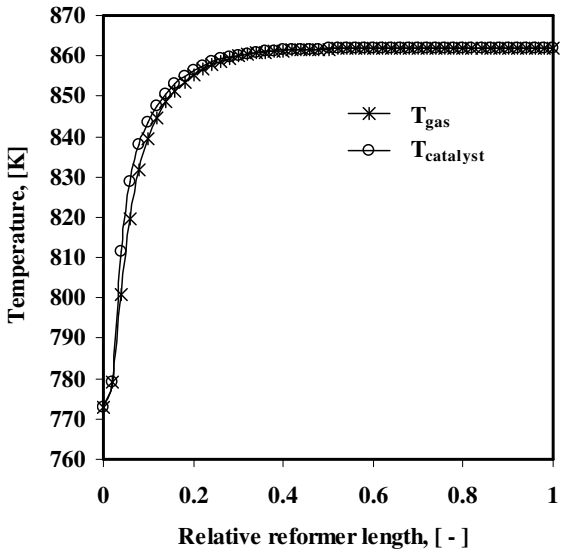

Fig. 6: Temperature profiles of bulk gas and solid catalyst at 500 °C, 1.5 bar, O/C=0.45, S/C=6.

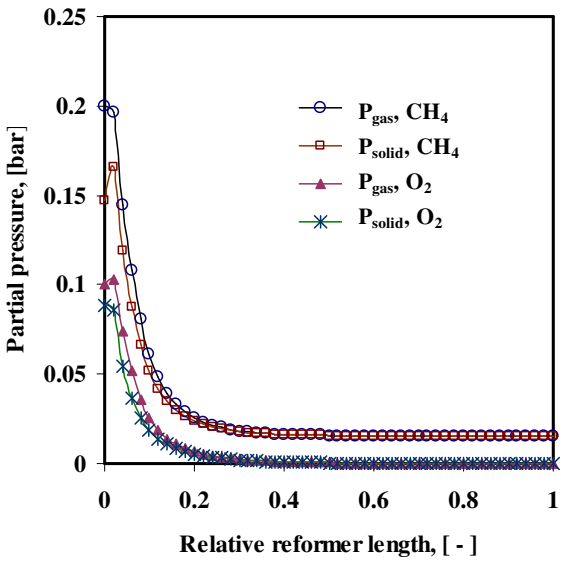

Fig. 7: Partial pressure profiles of CH_4 and O_2 reactants in the bulk gas and solid catalyst at 500 °C, 1.5 bar, O/C=0.45, S/C=6.

Similarly, the interfacial concentration gradients are found to be negligible due to effective mass transport in the gas film. Figure 7 presents the partial pressures of CH_4 and O_2 as reactant examples in the bulk gas phase and in the catalyst solid phase.

At relatively low O/C ratio of 0.45, S/C ratio of 6.0, a total pressure of 1.5 bar, and a GHSV of 3071 hr^{-1} (residence time of 1.17 sec, G_s=0.15 kg/m^2s), the monotonic behavior of the temperature profile is reasonably predicted as shown in Figure 8.

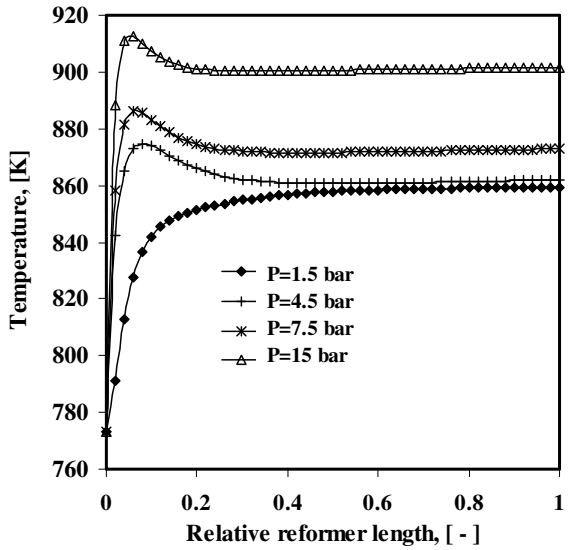

Fig. 8: Gas phase temperature profiles at different pressures and at 500°C, O/C= 0.45, S/C= 6.

At relatively low gas concentrations at low pressure of 1.5 bar, the oxidation kinetics [21] is somewhat slower than the reforming kinetics [19], (see Fig. 5), which results in gradual increase in temperature along the reformer. Conversely, at higher operating pressure (higher concentrations), a temperature peak appears in the front part of the reformer (more than 150°C gas temperature rise at 15 bar). Figure 9 shows the reaction rates of steam reforming R_1 and the oxidation reaction R_4 along the axial reformer length at two pressures of 1.5 and 15 bar. Apparently, the oxidation rate becomes faster than the reforming rates at high pressure and lower temperatures at least in the front part of the reformer. The temperature peak generated gets sharper at higher pressures.

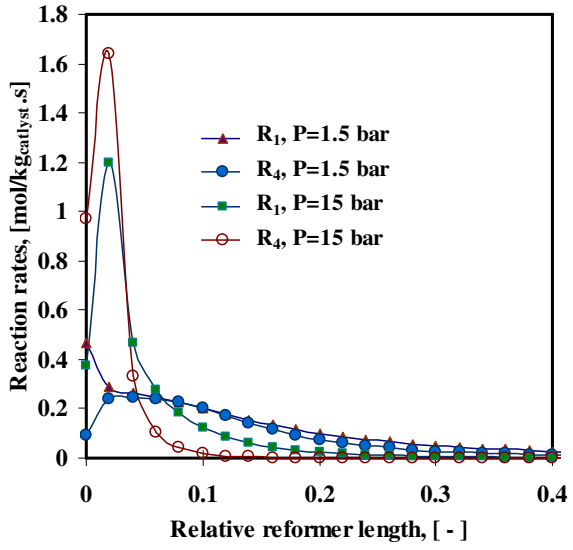

Fig. 9: Steam reforming and oxidation reaction rates along the axial reformer length at 500°C, 1.5 bar, O/C= 0.5, S/C= 6.

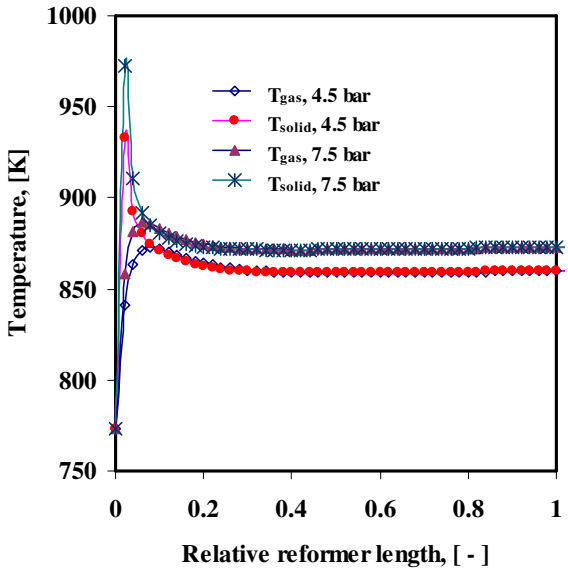

Fig. 10: Gas temperature profiles and spike-like catalyst temperature profiles at high concentration (pressure), at 500°C, O/C= 0.45, S/C= 6.

The catalyst temperature profiles at pressures of 4.5 and 7.5 bar are given in Figure 10. Hot spot formation in the catalyst is observed due to the fast oxidation reaction at high oxygen partial pressures in the reformer front part. This phenomenon deserves considerable attention during reactor design, construction, and the distribution of the temperature sensing devices along the reactor length. Non-uniformity of oxygen distribution throughout the reactor may also escalate the occurrence of hot spots especially on an industrial scale operation.

Hoang and Chan [40] have recently investigated the partial oxidation process using radial distribution oxygen through a permeable membrane reactor. One side of the membrane is exposed to gas in the tubular catalyst bed, while the other side is exposed to air. The difference of oxygen partial pressures between the adjacent sides due to oxidation reaction in the catalyst bed causes oxygen to permeate from the airside to the catalyst bed through the membrane by ionic and electronic diffusion mechanism. This can provide uniform oxygen distribution and better control for the process in addition to higher concentration of hydrogen in the product gas as air nitrogen is abandoned in the supply feed using the membrane.

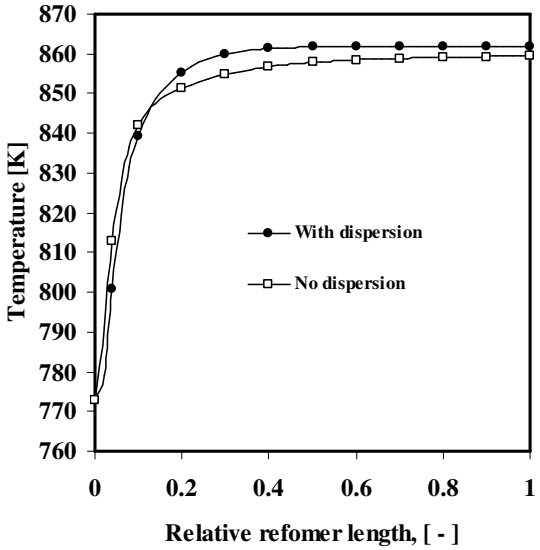

Fig. 11: Effect of axial thermal dispersion on ATR temperature profile.

Axial mass dispersion is found to have a negligible effect on the concentration profiles. This is an expected result as the L/d_p ratio used in investigating the reactor operation is 200, which is much higher than the Carberry criterion (L/d_p >50) . The axial thermal dispersion, however, slightly influences the temperature behavior along the reactor. Figure 11 shows the steady state temperature profiles along the axial direction of the reformer in the two cases of presence and absence of the heat axial dispersion term in the model. Neglecting the axial dispersion of heat generates an axial shift in the local temperatures varying along the front part of the reactor. At the first 4% of the axial direction, the shift is 11.8°C, at 10% of the length the shift is 2.63°C, while it results in an offset of -2.75°C in temperature in the rear part of the reformer.

The influence of the S/C and O/C molar ratios on the ATR performance is presented in Figures 12 and 13 in terms of CH_4 conversion, thermal reforming efficiency, and H_2 purity obtained on dry basis. Figure 12 shows the S/C ratio versus conversion, efficiency, and H_2 purity at fixed O/C ratio of 0.45 and at a pressure of 1.5 bar. Apparently, there is a maximum or saturation value for the ratio of steam that can be mixed with the fuel in the reformer in order to enhance its behavior. Beyond a ratio of S/C of 6, there is no further increase in the dry basis H_2 composition (73%) and CH_4 conversion (93%). There is still a little increase in the amount of H_2 produced per mol of CH_4 fed to the reformer and consequently in the thermal efficiency of the unit, which can reach about 83% at high load of steam (S/C ratio).

This, however, means more economic burden on the process in terms of raw material operational costs, and construction costs of a bigger reformer, and therefore might not make it a promising alternative. Thus the optimal operational window for the steam load (S/C ratio) can be taken as 4.5 to 6.0 where a fuel conversion of 90% to 93%, an H_2 purity of 70% to 73%, and a thermal efficiency of 71.5% to 78% can be realized.

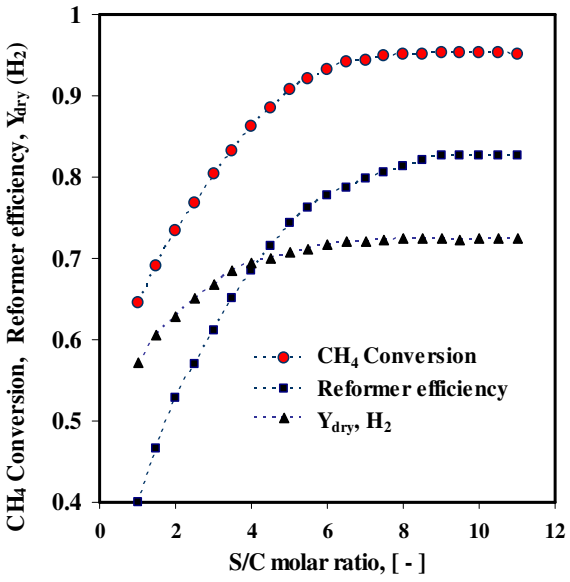

Fig. 12: Effect of S/C ratio on ATR performance, at 500°C, 1.5 bar, O/C= 0.45.

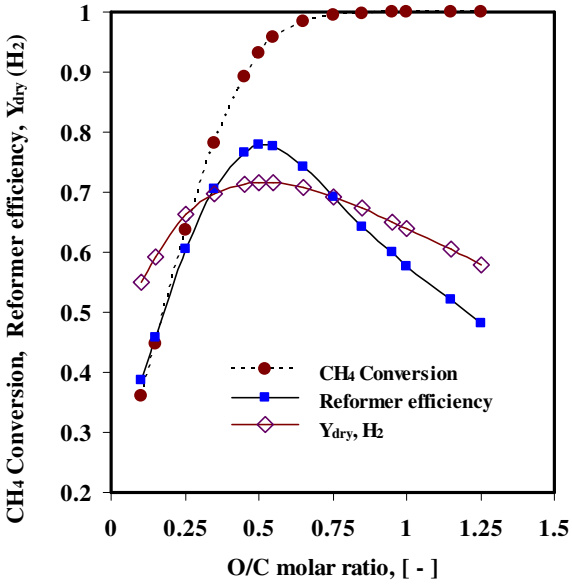

Fig. 13: Effect of O/C ratio on ATR performance, at 500°C, 1.5 bar, S/C= 6.

Figure 13 shows a local optimal window for oxygen load (O/C ratio) to the reformer of 0.45 to 0.55 on molar basis at a fixed S/C ratio of 6 that can produce a maximum H_2 purity of 73% and a thermal efficiency of 78%, and naturally a yield of 2.59 H_2 produced per mol of CH_4 fed. However, the fuel conversion is always favored by a high O/C ratio, but on the balance of low H_2 selectivity because most of the CH_4 in this case will be consumed via the oxidation reaction to CO_2.

Figure 14 gives a relatively wide window of operation for the gas feed flow velocity through the reformer from which an improved ATR performance in terms of fuel conversion and thermal efficiency can be attained. A GHSV in the range of

204.8 hr^{-1} to 28664 hr^{-1}, corresponding to a residence time of 17.6 s to 0.12 s, is investigated at fixed ratios of O/C and S/C of 0.5 and 6, respectively. It can be seen that at a low gas flow velocity, meaning a high residence time of the species in the reactor, the conversion obtained is as low as 74.8% and the thermal efficiency is around 58%.

This is an expected result due to the fact that at low gas flow velocity, the mass transport between the bulk gas and the catalyst surface is certainly a limiting factor. Thus, low production rates and conversion levels are obtained. On the other hand at very high gas feed velocity (very short residence times through the reactor), there is indeed not enough time for the reactions to provide sufficient conversion or to reach equilibrium compositions. However, a relatively wide regime of space velocities (1050 hr^{1} to 14000 hr^{-1}) can provide optimal values for conversion and efficiency around 93% and 78%, respectively. The process at this plateau can be recognized as a kinetically limited process, where the internal kinetic limitations are controlling.

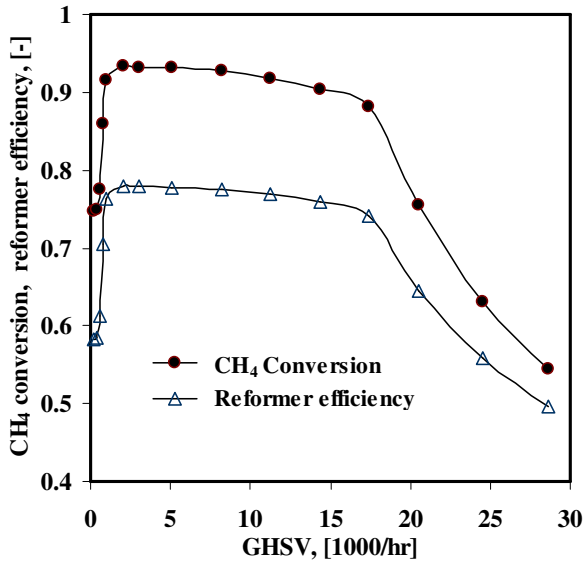

Fig. 14: Effect of GHSV on ATR performance, at 500°C, 1.5 bar, O/C= 0.5, S/C= 6.

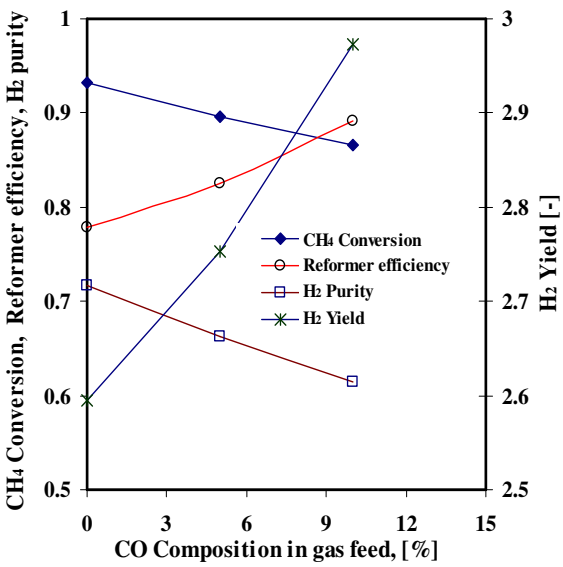

Fig. 15: Effect of CO co-feeding on ATR performance, at 500°C, 1.5 bar, O/C= 0.5, S/C= 6.

Figure 15 presents the effect of CO co-feeding to the ATR reforming gas mixture on the process performance. CH_4 conversion and H_2 purity obtained are found to be decreasing as higher CO ratio is inserted in the reaction feed gas mixture. This is attributed to the fact that at relatively low temperature, water-gas shift reaction is playing an influential role and competing with CH_4 in reacting with steam. Conversely, the apparent H_2 yield and consequently the thermal reformer efficiency show increasing values due to this reaction.

4. 5 Conclusions

The ATR process performance in terms of fuel conversion, reforming efficiency, and H_2 purity and yield is demonstrated in a fixed bed reformer of 0.4 m in length using a 1-D heterogeneous reactor model. The reformer temperature and product gas composition are directly affected by the operating ratios of S/C and O/C in the feed, in addition to feed temperature and residence time along the catalyst bed. Unsuitable feed composition, i.e. high oxygen partial pressure (corresponding to an O/C ratio greater than 0.45) at high-pressure operation (greater than 4.5 bar), can generate serious hot-spot formation at the catalyst surface. High-pressure operation will lower the fuel conversion and demands high steam loads (S/C ratio). Improved performance of the ATR is determined to provide up to 93% methane conversion, reformer efficiency of 78%, H_2 yield and purity of 2.6 and 73%, respectively using an O/C ratio of 0.45, an S/C ratio of 6, a feed temperature of 500^{o}C, a pressure of 1.5 bar, and a GHSV of 3071 hr^{-1}. An optimal window of operation is given in Table 8. The gas and catalyst temperatures are shown to have good proximity with only 11^{o}C difference within the first 10% of the reformer front and 89^{o}C above feed temperature at the aforementioned operational conditions. Steady state conditions are reached in about 13 minutes. The ATR process is kinetically limited with the catalyst properties investigated here.

Table 8: Summary of optimal operational conditions for the ATR process

Performance criteria				
Fuel conversion	Reforming efficiency		H_2 yield	H_2 purity
93%	78%		2.6	73%
Optimal operational parameters				
GHSV, hr^{-1}	O/C molar ratio	S/C molar ratio	Temperature [^{o}C]	Pressure [bar]
1050 – 14000	0.45 – 0.55	4.5 – 6.0	500	1.5

Nomenclature

Symbol	Definition	Unit
a_v	External catalyst surface area per unit volume of catalyst bed	m^2/m^3
C_i	Concentration of species i in the gas phase	mol/m^3
$C_{i,s}$	Concentration of species i in the solid phase	mol/m^3
$C_{p,bed}$	Specific heat of the catalyst bed	J/kg.K
C_{pg}	Specific heat of the fluid	J/kg.K
D_i	Effective diffusion coefficient	m^2/s
D_m	Average molecular diffusivity	m^2/s
D_Z	Axial dispersion coefficient	m^2/s
d_p	Catalyst particle diameter	m
E_j	Activation energy of reaction j	J/mol
G_s	Gas mass flow velocity	kg/m^2s
h_f	Gas to solid heat transfer coefficient	W/m^2s
j_D	Chilton-Colburn factor for mass transfer	-
j_H	Chilton-Colburn factor for heat transfer	-
$k_{g,i}$	Gas to solid mass transfer coefficient of component i	m^3/m^2s
k_j	Temperature dependent kinetic rate constant of reaction j	
k_{oj}	Reference temperature dependent kinetic rate constant of reaction j	
K_j	Thermodynamic equilibrium constant of reaction j	
K_{oi}	Reference adsorption constant of species i	
K_i	Adsorption constant of species i	
K_{oi}^C	Reference adsorption constant of combusting species i	
K_i^C	Adsorption constant of combusting species i	
K_D	Parameter corresponding to the viscous loss term	$Pa.s/m^2$
K_V	Parameter corresponding to the kinetic loss term	$Pa.s^2/m^3$
LHV_{H_2}	Lower heating value of H_2	MJ/kmol
LHV_{CH_4}	Lower heating value of CH_4	MJ/kmol
p_i	Partial pressure of gas species i	bar
P	Total gas pressure	bar
Pr	Prandtl number	-
r_i	Rate of consumption or formation of species i	$mol/kg_{cat}.s$
R_j	Rate of reaction j	$mol/kg_{cat}.s$
R	Universal gas constant	J/mol.K
Re	Reynolds number	-
Sc_i	Schmitt number	-
T	Gas phase temperature	K
T_s	Solid catalyst temperature	K
t	Time	s
u	Superficial gas flow velocity ($=\varepsilon_b u_{inst}$)	m/s
u_{inst}	Interstitial gas velocity	m/s
Y_i	Dry mole fraction of species i	mol/mol
z	Axial dimension	m

Greek symbols		
ΔH_i	Heat of adsorption of species i	J/mol
ΔH_i^C	Heat of adsorption of combusting species i	J/mol
ΔH_{298K}	Heat of reaction of at STP	kJ/mol
ε_b	Packing bed porosity	-
η_j	Effectiveness factor of reaction j	-
λ_g	Average gas thermal conductivity	W/m.K
λ_s	Solid thermal conductivity	W/m.K
λ_z^f	Effective thermal conductivity	W/m.K
μ_g	Average gas viscosity	kg/m.s
ρ_{bed}	Density of the catalyst bed	kg/m^3
ρ_{cat}	Density of the catalyst pellet	kg/m^3
ρ_f	Density of the fluid	kg/m^3
ψ	Particle shape factor (for spherical particles, ψ = 1)	-
Ω	Dominator term in the reaction kinetics	-

References

1. Ahmed, S., Krumpelt, M., Hydrogen from hydrocarbon fuels for fuel cells, Int. J. Hydrogen Energy 26 (2001) 291–301.
2. Biesheuvel, P.M, Kramer, G.J., Two-section model for autothermal reforming of methane to synthesis gas, AIChE J. 49 (2003) 1827–1837.
3. Barreto, L., Makihira, A., Riahi, K., The hydrogen economy in the 21st century: a sustainable development scenario, Int. J. Hydrogen Energy 28 (2003) 267–84.
4. Lee, H.D., Applegate, D.V., Ahmed, S., Calderone, S.G., and Harvey, T.L, Hydrogen from natural gas: part I - autothermal reforming in an integrated fuel processor, Int. J. Hydrogen Energy 30 (2005) 829 – 842.
5. Ewan, B.C.R., Allen, R.W.K., A figure merit assessment of the routes to hydrogen, Int. J. Hydrogen Energy 30 (2005) 809 – 819.
6. Armor, J.N., Catalysis and the hydrogen economy, Catalysis Letters 101 (2005) 131–135.
7. Dybkjaer, I., Tubular reforming and autothermal reforming of natural gas—an overview of available processes, Fuel Process Tech. 42 (1995) 85–107.
8. Bharadwaj, S.S, Schmidt, L.D., Catalytic partial oxidation of natural gas to syngas, Fuel Process Tech. 42 (1995) 109–27.
9. Ma, L., Trimm, D.L., Alternative catalyst bed configurations for the autothermic conversion of methane to hydrogen, Applied Catalysis A, 138 (1996) 265–273.
10. Pena, M.A., Gomez, J.P., and Fierro, J.L.G., New catalytic routes for syngas and hydrogen, Applied Catalysis A 144 (1996) 7–57.
11. Aasberg-Petersen, K., Christensen, T.S., Nielsen, C.S., and Dybkjaer, I., Recent developments in autothermal reforming and pre-reforming for synthesis gas production in GTL applications, Fuel Processing Tech. 83 (2003) 253–261.
12. Heinzel A, Vogel B, Hubner P., Reforming of natural gas—hydrogen generation for small scale stationary fuel cell systems, J. Power Sources 105 (2002) 202–207.

13. Mleczko, L., Baerns, M., Catalytic oxidative coupling of methane – reaction engineering aspects and process schemes, Fuel Processing Tech. 42 (1995) 217–248.
14. Stitt, E.H., Multifunctional reactor? 'Up to a point lord copper', Chem. Eng. Res. Des. 82 (2004) 129–139.
15. Chan, S.H, Wang, H.M., Thermodynamic analysis of natural gas fuel processing for fuel cell applications, Int. J. Hydrogen Energy 25 (2000) 441–449.
16. Chan, S.H, Wang, H.M., Effect of natural gas composition on autothermal fuel reforming products, Fuel Process Tech. 64 (2000) 21–39.
17. Chan, S.H, Wang, H.M, Carbon monoxide yield in natural gas autothermal reforming process, J. Power Sources, 101 (2001) 188–95.
18. Hoang, D.L., Chan, S.H., Modeling of a catalytic autothermal methane reformer for fuel cell applications, Applied Catalysis A 268 (2004) 207–216.
19. Xu, J. and Froment, G.F., Methane steam reforming, methanation and water–gas shift: I. intrinsic kinetics, AIChE. J. 35 (1989) 88–96.
20. Xiu, G., Li, P., Rodrigues, A., Sorption Enhanced reaction process with reactive regeneration, Chem.Eng.Sci. 57 (2002) 3893–3908.
21. Trimm, D.L. and Lam, C-W., The combustion of methane on platinum-alumina fibre catalysts—I. Kinetics and mechanism, Chem.Eng.Sci. 35 (1980) 1405–1413.
22. De Smet, C.R.H., de Croon, M.H.J.M., Berger, R.J., Marin, G.B., and Schouten, J.C., Design of adiabatic fixed-bed reactors for the partial oxidation of methane to synthesis gas. Application to production of methanol and hydrogen-for-fuel-cells, Chem.Eng.Sci. 56 (2001) 4849–4861.
23. De Groote, A.M. and Froment, G.F., Simulation of the catalytic partial oxidation of methane to synthesis gas", Applied Catalysis A 138 (1996) 245–264.
24. De Groote, A.M., Froment, G.F. and Kobylinski, Th., Synthesis gas production from natural gas in a fixed bed reactor with reversed flow, Canadian J. Chem.Eng. 74 (1996) 735–742.
25. Gosiewski, K., Bartmann, U., Moszczynski, M. and Mleczko, L., Effect of intraparticle transport limitations on temperature profiles and catalytic performance of the reverse-flow reactor for the partial oxidation of methane to synthesis gas, Chem.Eng.Sci. 54 (1999) 4589–4602.
26. Froment, G.F., Bischoff, K.B, Chemical reactor analysis and design, Wiley, London, (1990).
27. Ergun, S., Fluid flow through packed columns, Chem.Eng.Prog. 48 (1952) 89–94.
28. Edwards, M.F., and J.F. Richardson, Gas dispersion in packed beds, Chem.Eng.Sci. 23 (1968) 109–123.
29. Yagi, S., Kunii, D., and Wakao, N., Studies on axial Effective thermal conductivities in packed beds, AIChE J. 6, (1960) 543–546.
30. Kunii, D., Smith, J.M., Heat transfer characteristics of porous rocks, AIChE J. 6 (1960) 71–78.
31. De Wash, A.P., Froment, G.F., Heat transfer in packed bed, Chem.Eng.Sci. 27 (1972) 567–576.

32. Li, C.H., Finlayson, B.A., Heat transfer in packed bed – a reevaluation, Chem.Eng.Sci. 32 (1977) 1055–1066.
33. Wakao, N., Kaguei, S., Heat and Mass Transfer in Packed Bed, Gordon and Breach, New York, (1982).
34. Reid, R.C., Prausnitz, J.M., and Poling, B.E., The Properties of Gases and Liquids, McGraw-Hill, New York, (1988).
35. Bird, R.B., Stewart, W.E., and Lightfoot, E.N., Transport Phenomena, 2nd Ed., Wiley, New York, (2002).
36. Geankoplis, C.J., Transport Processes and Unit Operations, 3rd Ed., Prentice Hall Int., 1993.
37. Ding, Y., Alpay, E., Adsorption-enhanced steam-methane reforming, Chem.Eng.Sci. 55 (2000) 3929–3940.
38. Dissanayake, D., Rosynek, M.P., Kharas, K.C.C., and Lunsford, J.H., Partial oxidation of methane to CO and H_2 over a Ni/Al_2O_3 catalyst, J. Catalysis 132 (1991) 117–127.
39. Ma, L., Trimm, D.L. and Jiang, C., The design and testing of an autothermal reactor for the conversion of light hydrocarbons to hydrogen. I. The kinetics of the catalytic oxidation of light hydrocarbons, Applied Catalysis A 138 (1996) 275–283.
40. Hoang, D.L., Chan, S.H., Effect of reactor dimensions on the performance of an O_2 pump integrated partial oxidation reformer – a modelling approach, Int. J. Hydrogen Energy 31 (2006) 1–12.

Chapter 5

Modeling of Sorption Enhanced Methane Autothermal Reforming Process

This chapter has been published as
1. M.H. Halabi, M.H.J.M. de Croon, J. van der Schaaf, P.D. Cobden, J.C. Schouten, Reactor modeling of sorption–enhanced autothermal reforming of methane. Part I: Performance study of hydrotalcite and lithium zirconate–based processes, Chem. Eng. J, doi:10.1016/j. cej.2011.02.015, 2011.
2. M.H. Halabi, M.H.J.M. de Croon, J. van der Schaaf, P.D. Cobden, J.C. Schouten, Reactor modeling of sorption–enhanced autothermal reforming of methane. Part II: Effect of operational parameters, Chem. Eng. J. doi:10.1016/j. cej.2011.02.016, 2011.

Abstract

This chapter presents a performance analysis for the sorption–enhanced autothermal reforming of CH_4 in a fixed bed reformer for pure H_2 production with in situ CO_2 capture. The process is analyzed for two candidate sorbents of K–promoted hydrotalcite and lithium zirconate in a fixed bed reactor using a conventional Ni/MgO steam reforming catalyst. A 1-D heterogeneous dynamic model is constructed to simulate the process, accounting for mass and thermal dispersion in the axial direction, pressure drop, and intraparticle and interfacial resistances. The process is found to be efficient and applicable even at a low temperature of 500 ^{o}C for steam reforming reactions and at pressure as low as 4.47 bar for CO_2 adsorption. The hydrotalcite–based autothermal reforming process can

provide CH_4 conversion and H_2 purity up to 85% and 96%; respectively, at operational conditions of 500°C, 4.47 bar, steam/carbon ratio of 6, oxygen/carbon ratio of 0.45 and space velocity of 3071 hr^{-1}. This is associated with a low level of $CO+CO_2$ impurities of less than 300 ppm. The lithium zirconate–based process demonstrated an enhanced CH_4 conversion of 99.5% and dry basis H_2 purity of 99.5% at similar conditions. The process is found to benefit from the high CO_2 sorption capacity of lithium zirconate with respect to the CH_4 conversion and the useful operational time. Nonetheless, lithium zirconate–based process shows a slip of $CO+CO_2$ impurities up to 1000 ppm in the gas effluent during the transient sorption–enhanced regime before breakthrough. This is mainly attributed to the slow sorption kinetics of lithium zirconate. The process performance is analyzed under dynamic conditions with respect to key operational parameters: gas hourly space velocity, oxygen/carbon ratio, steam/carbon ratio, catalyst/ sorbent ratio, operating pressure, and particle size. The high heat of reaction generated during the CO_2 chemisorption on lithium zirconate is also investigated if it is sufficient to provide a heat supplement at lower oxygen/carbon ratio at the adiabatic conditions of the autothermal reforming process. Oxygen/carbon ratio of less than 0.35 results in methane conversion of less than 95%.

5. 1 Introduction

H_2 is well perceived as a pollution-free primary energy carrier for future transportation as well as electricity generation. Steam reforming (SR) is the most vital route to convert CH_4 into H_2. The conventional steam reforming process is usually operated at a high temperature range of 700–900 °C due to the highly endothermic nature of the process [1– 3]. The thermodynamic equilibrium of the reactions involved dictates limitations on the CH_4 conversion and H_2 productivity attained. The sorption enhanced catalytic reforming of natural gas is an innovative concept of high purity H_2 production with in-situ CO_2 capture [4–9]. The principal idea of the process is shifting the thermodynamic equilibrium of the reactions towards the H_2 product direction via selectively adsorbing the co-generated CO_2 on a proper and effective sorbent [4, 5]. Hufton et al. [4] reported several advantages that can be gained from this concept such as (1) lower operational temperatures (400–500 °C) than those in conventional steam reformers, (2) lower capital costs, (3) production of high purity H_2 (> 95%) at feed gas pressure of 4 to 20 bar, (4) minimization of unfavorable side reactions, (5) elimination of downstream H_2 purification steps, (6) reduction of excess steam used in conventional steam reformers, and (7) reduction of CO in the gas effluent to ppm levels.

Several experimental [4–9] studies have been published on the process of the sorption–enhanced steam reforming of CH_4. Ding and Aplay [6] demonstrated a laboratory scale homogenous experimental system of catalyst and adsorbent uniformly packed in a fixed bed reactor of 22 cm in length. The obtained 75% CH_4 conversion and H_2 purity of 90% using S/C ratio of 6 at 450 °C and 4.45 bar. Waldron et al. [9] have experimentally presented the sorption enhanced concept on a pilot scale steam reformer of 6.1 m in length. They measured a CH_4 conversion

and H_2 purity of 54.4 and 88.7%, respectively in multi-cycle operation at 490 ^oC and 4.5 bar using steam/carbon (S/C) ratio of 6. They used different types of CO_2 chemisorbent and SR catalyst in equal weight ratio. Recently, Reijers et al. [10] have tested several K–promoted hydrotalcite (HTC) samples for their suitability as a CO_2 sorbent for the sorption–enhanced steam reforming of CH_4. They also found that the purge gas to adsorbed CO_2 ratio is influential in determining the process economics.

There are significant attempts made to theoretically understand the process performance [11–18]. Xiu et al. [11] developed a mathematical model to describe the sorption–enhanced SR in a fixed bed. They considered a multi-component system with overall mass and energy balances, pressure drop, nonlinear adsorption equilibrium for CO_2 over hydrotalcite in addition to the SR reactions. They obtained a CH_4 conversion of 65% and an average H_2 purity up to 80% with traces of CO and CO_2. Using more reactor length, Xiu et al. [12] reached 88% H_2 purity and less than 30 ppm CO. Kapil et al. [16] developed heterogeneous bulk scale and particle scale models. They found that the H_2 purity and productivity at bulk scale are sensitive to wall temperature, bed voidage, and feed composition. At particle scale, they highlighted the role of the catalyst to sorbent distribution inside the particle and the ratio of pore radius to tortuosity. Koumpouras et al. [17, 18] modeled a reactor–regenerator in which the adsorbent particles are passed through a stationary SR catalyst monolith. They concluded that the CH_4 conversion enhancement and CO_2 recovery show a strongly nonlinear dependency on both sorption capacity and kinetics.

Hydrotalcite-like compounds (HTC) [10, 19–27], and lithium zirconate (LZC) [28–35] solids have received considerable attention during the recent years as promising CO_2 sorbents out a family that also includes carbon-based adsorbents, metal-oxide sorbents, and zeolites. The proper sorbent material must have (i) high adsorption capacity, (ii) adequate adsorption/desorption kinetics, (iii) high selectivity for CO_2, (iv) adequate mechanical strength, and (v) stable capacity versus adsorption/ desorption cycles in operation. HTC and K–promoted HTC are typical examples of sorbents having relatively fast kinetics but low capacity [6–9]. LZC is considered to offer relatively high capacity but relatively slow kinetics due to the large reaction enthalpy associated with the strong chemisorption of CO_2 on LZC [36–38].

The catalytic autothermal reforming of CH_4 (ATR) has received much attention in research during the recent years as a viable process for H_2 generation for fuel cell systems [39– 45]. ATR has major advantages over other reforming alternatives mainly for higher energy efficiency and lower energy requirements compared to the conventional steam reforming process. It offers advantages of smaller unit size and lower operational temperature, easier startup, higher GHSV (at least one order of magnitude relative to SR), higher H_2/CO ratio, and easily regulated H_2/CO ratio required [39, 40]. Recently, Halabi et al. [39] determined an operational window of temperature, S/C, O/C, GHSV, and pressure for an optimal performance of ATR in

a fixed bed reformer in terms of CH_4 conversion, H_2 yield, and reformer thermal efficiency.

Yet to date there has been no work reported in literature that studies the process of sorption–enhanced CH_4 autothermal reforming of over any type of sorbents. This chapter inherently presents the applicability of the sorption–enhanced concept coupled with the autothermal reforming of CH_4 over K-promoted hydrotalcite and lithium zirconate as candidate sorbents. A conventional Ni/MgO catalyst is adopted as SR catalyst in this work. The performance of sorption enhanced ATR process is theoretically analyzed for the two presumed sorbents in an adsorptive fixed bed reactor. A 1-D heterogeneous dynamic model is constructed to simulate the process, accounting for mass and thermal dispersion in the axial direction, pressure drop, and intraparticle and interfacial resistances. The motivation of this study is to investigate the benefit of utilizing K-promoted HTC and LZC solids in improving the performance of autothermal reforming of CH_4 concerning mainly conversion enhancement, H_2 output purity and productivity. The ultimate target is to produce high purity H_2 >99% with in situ CO_2 capture (CO and CO_2 levels <300 ppm) and a corresponding CH_4 conversion >95% at relatively low temperature <550 ^oC. The influence of major parameters such as steam/carbon, oxygen/carbon, catalyst/sorbent, gas temperatures, gas space velocity (GHSV), sorbent capacity, particle diameter, and total pressure is also examined and demonstrated.

5. 2 Autothermal reforming of methane

5.2.1 ATR reaction and kinetics

The effect of the endothermic CH_4 steam reforming and the catalytic CH_4 combustion are both combined in the autothermal reforming process. The fuel is fed over the packed bed catalyst in the reactor together with steam and pure oxygen or air feed line. Table 1 presents the most likely reactions that can be involved in the ATR process. The primary CH_4 steam reforming (R_1), reverse methanation (R_2), water–gas shift reaction (R_3), and the catalytic CH_4 combustion (R_4) are considered as the prevailing reaction routes in the ATR process. Water–gas shift and reverse methanation reactions are usually involved with steam reforming reaction over a catalyst at high temperatures (typically higher than 700 ^oC). However, the reverse methanation reaction is thermodynamically a resultant from CH_4 steam reforming and water–gas shift reactions but it is determined to be kinetically independent [1–3]. CH_4 can also be catalytically reformed to H_2 using CO_2 known as dry reforming (R_7). However, the generation of high H_2 or syngas yield via this route is still in research [40]. The final H_2/CO ratio in the product is largely influenced by the water–gas shift reaction (R_3). High S/C ratio is inserted in the reaction feed mixture at high operational temperature to reduce the formation of CO via the backward path of the equilibrium water–gas shift reaction, and to enhance the production of H_2. The efficiency of the process is generally reduced due the drawbacks of the carbon formation reactions (R_8 and R_9). Carbon formation can lead to a serious catalyst deactivation, lower fuel conversion and H_2 yield, and corrosion of material. The carbon formation from Boudouard reaction is conventionally

suppressed at high operational temperatures, and high O/C and S/C ratios [7, 44, 45]. However, the reactions (R_5–R_9) are ignored in this work for two reasons: (1) due to their insignificant rates or effect on the process [45], (2) and to reduce the complexity of the analysis.

Table 1: Autothermal reforming reactions

	Reaction	ΔH_{298K} kJ/mol
R_1. Steam reforming	$CH_4 + H_2O \leftrightarrow CO + 3H_2$	206.2
R_2. Steam reforming	$CH_4 + 2H_2O \leftrightarrow CO_2 + 4H_2$	164.9
R_3. Water gas shift	$CO + H_2O \leftrightarrow CO_2 + H_2$	-41.1
R_4. Total combustion	$CH_4 + 2O_2 \rightarrow CO_2 + 2H_2O$	-802.7
R_5. Partial oxidation	$CH_4 + 1/2\,O_2 \leftrightarrow CO + 2H_2$	-36
R_6. Partial combustion	$CH_4 + O_2 \leftrightarrow CO_2 + 2H_2$	-71
R_7. Dry reforming	$CH_4 + CO_2 \leftrightarrow 2CO + 2H_2$	247
R_8. Boudouard reaction	$2CO \leftrightarrow C + CO_2$	-172
R_9. Decomposition	$CH_4 \leftrightarrow C + 2H_2$	75

The kinetic reaction model of Xu & Froment [47] developed for CH_4 steam reforming over a $Ni/MgAl_2O_4$ catalyst is adopted in this work. Their kinetic data are derived in a temperature range of 500–575 ^oC; which is in the range of the analysis of this study. The kinetic rate expression of Trimm & Lam [48] generated for catalytic CH_4 combustion over Pt–based catalyst at 557^oC is considered in this work. However, the activation energy and the model adsorption parameters are adjusted for the Ni–based catalyst [49]. The combined kinetic model of the ATR process is demonstrated in Table 2.

Table 2: ATR kinetic reaction model

Reaction rate equation	
$R_1 = \frac{k_1}{p_{H_2}^{2.5}}\left(p_{CH_4}p_{H_2O} - \frac{p_{H_2}^3 p_{CO}}{K_I}\right) * \frac{1}{\Omega^2}$	(1)
$R_2 = \frac{k_2}{p_{H_2}^{3.5}}\left(p_{CH_4}p_{H_2O}^2 - \frac{p_{H_2}^4 p_{CO_2}}{K_{II}}\right) * \frac{1}{\Omega^2}$	(2)
$R_3 = \frac{k_3}{p_{H_2}}\left(p_{CO}p_{H_2O} - \frac{p_{H_2}p_{CO_2}}{K_{III}}\right) * \frac{1}{\Omega^2}$	(3)
$R_4 = \frac{k_{4a}p_{CH_4}p_{O_2}}{\left(1 + K_{CH_4}^C p_{CH_4} + K_{O_2}^C p_{O_2}\right)^2} + \frac{k_{4b}p_{CH_4}p_{O_2}}{\left(1 + K_{CH_4}^C p_{CH_4} + K_{O_2}^C p_{O_2}\right)}$	(4)
$\Omega = 1 + K_{CO}p_{CO} + K_{H_2}p_{H_2} + K_{CH_4}p_{CH_4} + K_{H_2O}\frac{p_{H_2O}}{p_{H_2}}$	(5)

The reaction equilibrium constants and the Arrhenius kinetic parameters are listed in Table 3. The Van't Hoff adsorption parameters are given in Table 4. Effectiveness factors η_j are used to account for the intraparticle transport limitation

[50, 51, 52]. The rate of consumption or formation of species i, r_i (mol/kg_{cat}.s) is then presented as:

$$r_{CH_4} = -\eta_1 R_1 - \eta_2 R_2 - \eta_4 R_4 \quad (6\text{-a})$$

$$r_{O_2} = -2\eta_4 R_4 \quad (6\text{-b})$$

$$r_{CO_2} = \eta_2 R_2 + \eta_3 R_3 + \eta_4 R_4 \quad (6\text{-c})$$

$$r_{H_2O} = -\eta_1 R_1 - 2\eta_2 R_2 - \eta_3 R_3 + 2\eta_4 R_4 \quad (6\text{-d})$$

$$r_{H_2} = 3\eta_1 R_1 + 4\eta_2 R_2 + \eta_3 R_3 \quad (6\text{-e})$$

$$r_{CO} = \eta_1 R_1 - \eta_3 R_3 \quad (6\text{-f})$$

Table 3: Reaction equilibrium constants and Arrhenius kinetic parameters

Reaction, j	Equilibrium constant, K_j	k_{oj} (mol/kg_{cat}.s)	E_j (J/mol)
1	K_I = exp(-26830/T_s+30.114) (bar^2)	$1.17*10^{15}$ $bar^{0.5}$	240100
2	$K_{II} = K_I \cdot K_{III}$ (bar^2)	$2.83*10^{14}$ $bar^{0.5}$	243900
3	K_{III} = exp(4400/T_s - 4.036)	$5.43*10^5$ bar^{-1}	67130
4		$8.11*10^5$ bar^{-2}	86000
		$6.82*10^5$ bar^{-2}	86000

$$k_j = k_{oj} * \exp(-E_j / RT)$$

Table 4: Van't Hoff parameters for species adsorption

	K_{oi} (bar^{-1})	ΔH_i (J/mol)	K_{oi}^C (bar^{-1})	ΔH_i^C (J/mol)
CH_4	$6.65*10^{-4}$	-38280		
CO	$8.23*10^{-5}$	-70650		
H_2	$6.12*10^{-9}$	-82900		
H_2O	$1.77*10^5$ bar	88680		
CH_4 (combustion)			$1.26*10^{-1}$	-27300
O_2 (combustion)			$7.78*10^{-7}$	-92800

$$K_i = K_{oi} * \exp(-\Delta H_i / RT)$$

$$K_i^C = K_{oi}^C * \exp(-\Delta H_i^C / RT)$$

The overall ATR reforming of CH_4 can be represented by the following equation:

$$CH_4 + \delta(O_2) + (2 - 2\delta)H_2O \Leftrightarrow CO_2 + (4 - 2\delta)H_2 \quad (7)$$

The autothermicity of the overall reaction process at a predefined temperature can be solely defined by the key stoichiometric parameter of O/C molar ratio (δ) which results in a net adiabatic heat of reaction of zero.

$$\Delta H_T = \sum_i v_{i(x)} H_{i(T)} = 0 \quad (8)$$

In practice, the operational O/C ratio is slightly higher than the stoichiometric O/C ratio (δ) to overcome any heat losses on the reactor walls, provide more control for the product composition, and to suppress carbon formation.

5.2.2 CO_2 adsorption kinetics

HTC–based system

CO_2 adsorption on hydrotalcite is considered to show a rapid irreversible chemisorption on the fresh sorbent followed by relatively weaker physical adsorption on the sorbent according to Ding and Alpay [23]. The CO_2 rate of adsorption is given by the linear driving force model (LDF). The effective mass transfer coefficient, which is appearing in the LDF model, considers the intraparticle mass transfer limitation which is governed by the internal pore diffusion. The molecular diffusion and surface diffusion are found to be insignificant in comparison to pore diffusion [23]. The CO_2 adsorption equilibrium model is given by the Langmuir isotherm at wet conditions assuming a monolayer adsorption. The maximum saturation capacity used in this study is 0.65 mol/kg, which represents a relatively low sorbent capacity. The temperature dependent Langmuir model parameter is given by the Van't Hoff equation. Table 5 presents the CO_2 adsorption model on hydrotalcite.

Table 5: CO_2 adsorption kinetics on hydrotalcite (HTC), [23]

CO_2 rate of adsorption is given by the LDF model

$$r_{ads}\frac{\partial q_{CO_2}}{\partial t} = k_{CO_2}\left(q^*_{CO_2} - q_{CO_2}\right) \tag{9}$$

q_{CO_2} is the CO_2 concentration in the solid sorbent, $q^*_{CO_2}$ is the equilibrium CO_2 concentration following the Langmuir isotherm

Effective mass transfer coefficient

$$k_{CO_2} = \frac{15}{r_p^2}\cdot\frac{\varepsilon_p D_p}{\varepsilon_p + (1-\varepsilon_p)\rho_p RT\cdot\left(\partial q^*_{CO_2}/\partial p_{CO_2}\right)} \tag{10}$$

$D_p = 3.3*10^{-7}$ m^2/s (sorbent pore diffusion coefficient) and $\rho_p = 1300$ kg/m^3 (sorbent pellet density)

Langmuir adsorption isotherm on hydrotalcite

$$q^*_{CO_2} = \frac{m_{CO_2} b_{CO_2} p_{CO_2}}{1 + b_{CO_2} p_{CO_2}} \tag{11}$$

m_{CO_2} is the maximum saturation capacity of the sorbent (0.65 mol CO_2/kg sorbent)

Temperature dependent adsorption isotherm constant

$$b_{CO_2} = b_{CO_2,ref}\, exp\left[-\frac{\Delta H_{ads}}{R}\right]\left(\frac{1}{T} - \frac{1}{T_o}\right) \tag{12}$$

$b_{CO_2,ref} = 23.6$ bar^{-1}, ΔH_{ads} is the heat of adsorption of CO_2 on HTC (-17 kJ/mol), and T_o is 673 K.

LZC–based system

CO_2 can be chemically sorbed on lithium zirconate at high temperature (600^{o}C) and generating relatively a high amount of heat according to the following reaction

$$Li_2ZrO_3 + CO_2 \leftrightarrow Li_2CO_3 + ZrO_2 \qquad \Delta H_{298\,K} = -160 \text{ kJ/mol} \tag{13}$$

The high sorption capacity of this material is a beneficial factor to be employed in sorption enhanced reforming, although lithium zirconate sorbents suffer from relatively slow kinetics comparing to autothermal reforming reactions. The CO_2 rate of adsorption is represented by the extent rate of reaction of CO_2 uptake according to Ochoa-Fernandez et al. [38]. However, this rate is modified in this work to be in terms of the CO_2 concentration on the solid q_{CO_2} for the consistency with the LDF model on hydrotalcite as shown in Table 6.

Table 6: CO_2 adsorption kinetics on lithium zirconate (LZC), [38]

CO_2 rate of adsorption is given by

$$r_{ads} = \frac{dq_{CO_2}}{dt} = k_{CO_2} C_{CO_2}^{n} \left(m_{CO_2} - q_{CO_2}\right) \quad (14)$$

C_{CO_2} is the concentration in the gas phase, q_{CO_2} is the CO_2 concentration on solid sorbent,

m_{CO_2} is the saturation capacity of the sorbent (5 mol CO_2/kg sorbent) , n is 1.93

Temperature dependant adsorption constant

$$k_{CO_2} = k_{ref} e^{\left(\frac{-E_{ads}}{R}\left(\frac{1}{T_s} - \frac{1}{T_o}\right)\right)} \quad (15)$$

$k_{ref} = 4.9*10^{-5}$, $E_{ads} = 8.94*10^{4}$ J/mol, and the heat of adsorption of CO_2 on LZC is -160 kJ/mol.

5. 3 Mathematical modeling

A 1-D heterogeneous fixed bed reactor model is constructed to analyze the dynamic behavior of the sorption enhanced ATR process. The following assumptions are made:

1. Ideal gas behavior;
2. Adiabatic operation;
3. Plug-flow conditions with axial dispersion of mass and heat;
4. Concentration and temperature gradients in the radial direction are ignored;
5. No temperature gradient in the catalyst particles;
6. No homogenous gas phase reactions are considered as the temperatures are lower than 600^{o}C.
7. Uniform particle size;
8. Constant bed porosity.
9. Six reactive species (CH_4, O_2, CO, CO_2, H_2, H_2O) and one inert component (N_2) are involved in the model;
10. CO_2 is the only species adsorbed on the sorbent; the rate of adsorption is zero for non-adsorbing species.

These assumptions are considered to be realistic and valid for a laboratory–scale reformer and operating conditions as it is suggested in this study.

5.3.1 Governing equations

The constructed model is typically composed of mass and energy balances in the gas and the solid phases as presented in Table 7. The initial conditions and Danckwert boundary conditions listed in Table 7 are used in the model. The effect of the non-ideal flow and local mixing at turbulent velocities in addition to the diffusive flow is accounted for using the axial dispersion coefficient. Edwards and Richardson [55] presented an estimation for this coefficient according to the equation shown in Table 8. The axial thermal effective conductivity of the bed is determined from Yagi et al. [56] and given in Table 8, see also [57–60]. Pressure drop along the axial direction in the fixed bed is described by the Ergun equation [54, see Table 8.

5.3.2 Gas properties and transport coefficients

Temperature and composition dependent expressions are utilized to determine the gas properties used in the model [61, 62]. However, average values of the gas viscosity and thermal conductivity, the solid thermal conductivity, and the bed heat capacity [60] are employed. Chilton-Colburn factor, j_D, for mass transfer is used to calculate the mass transfer coefficient from gas to solid ($k_{g,i}$) [61], see also [63]. Chilton-Colburn factor, j_H, for heat transfer is used to calculate the heat transfer coefficient (h_f) [63]. The transport coefficients are given in Table 8.

Table 7: Reactor simulation model with corresponding boundary and initial conditions

Mass and energy balances in the gas phase

$$\varepsilon_b \frac{\partial C_i}{\partial t} + \frac{\partial (u C_i)}{\partial z} + k_{g,i} a_v (C_i - C_{i,s}) = \varepsilon_b D_Z \frac{\partial^2 C_i}{\partial z^2} \tag{16}$$

$$\varepsilon_b \rho_f C_{pg} \frac{\partial T}{\partial t} + u \rho_f C_{pg} \frac{\partial T}{\partial z} = h_f a_v (T_s - T) + \lambda_z^f \frac{\partial^2 T}{\partial z^2} \tag{17}$$

Mass and energy balances in the solid phase

$$k_{g,i} a_v (C_i - C_{i,s}) = v \rho_{cat} r_i - (1-v) \rho_{ads} r_{ads} \tag{18}$$

$$\rho_{bed} C_{p,bed} \frac{\partial T_s}{\partial t} + h_f a_v (T_s - T) = v \rho_{cat} \sum -\Delta H_{rxn,j} \eta_j R_j + (1-v) \rho_{ads} \sum -\Delta H_{ads} r_{ads} \tag{19}$$

Note: rate of accumulation of the concentration in the solid particle ($C_{i,s}$) is ignored, due to small particle size, see [53].

Pressure drop [54]

$$\partial P / \partial z = -K_D u - K_V u^2 \tag{20}$$

Boundary conditions

At the reformer inlet z = 0.0

$$-D_Z \partial C_i / \partial z = u (C_{i,o} - C_i)$$
$$-\lambda_Z^f \partial T / \partial z = u \rho_f C_{Pg} (T_o - T)$$
$$-\lambda_Z^f \partial T / \partial z = u \rho_f C_{Pg} (T_{in} - T_s)$$
$$P = P_o$$

At the reformer exit z = L

$$\partial C_i / \partial z = 0 \quad \partial T / \partial z = 0 \quad \partial T_s / \partial z = 0 \tag{21}$$

Initial conditions

$$C_i = C_{i,o} \quad T = T_o \quad T_s = T_{s,o} \tag{22}$$

5.3.3 Numerical solution

The mathematical model is namely composed of partial differential equations, algebraic equation, initial and boundary conditions. The model is implemented and solved in gPROMS modeling software (Process System Enterprise). The axial direction is discretized according to the spatial discretization method of first order backward difference. The spatial integration is performed over a uniform grid of 100 intervals. The time domain integration is performed by the DAE integrator based on the variable time step of the backward differentiation formula. Global reactor parameters, operating conditions, and average gas properties used in this work are listed in Table 9.

Table 8: Empirical correlations employed in the model

Semi-empirical relations for K_D and K_V [54]:

$$K_D = \frac{150\mu_g(1-\varepsilon_b)^2}{d_p^2\varepsilon_b^3}\ \text{(Pa.s/m}^2\text{)};\quad K_V = \frac{1.75(1-\varepsilon_b)\rho_f}{d_p\varepsilon_b^3}\ \text{(Pa.s}^2\text{/m}^3\text{)}$$

Mass axial dispersion coefficient [55]:

$$D_Z = 0.73D_m + \frac{0.5ud_p}{1+9.49D_m/ud_p}$$

Effective thermal conductivity [56]:

$$\frac{\lambda_z^f}{\lambda_g} = \frac{\lambda_z^{f,o}}{\lambda_g} + 0.75\cdot Pr\cdot Re_p\ ,\qquad \frac{\lambda_z^{f,o}}{\lambda_g} = \varepsilon_b + \frac{1-\varepsilon_b}{0.139\varepsilon_b - 0.0339 + (2/3)\lambda_g/\lambda_s}$$

Mass transfer coefficient [62, 63]:

$$k_{g,i} = j_{D,i}Re.Sc_i^{1/3}\frac{D_i}{d_p}$$

$$\varepsilon_b j_{D,i} = 0.765Re^{-0.82} + 0.365Sc_i^{-0.398}$$

$$Re = \rho_f u d_p/\mu;\quad Sc_i = \mu/\rho_f D_i \qquad 0.01 < Re < 1500\ ,\quad 0.6 < Sc < 7000\ ,\quad 0.25 < \varepsilon_b < 0.96$$

Heat transfer coefficient [63]

$$h_f = j_H\frac{C_{pg}G_s}{Pr^{2/3}} \qquad Pr = \frac{C_{pg}\mu_g}{\lambda_g}$$

$$j_H = 0.91Re^{-0.51}\psi \quad 0.01 < Re < 50\ ,$$

$$j_H = 0.61Re^{-0.41}\psi \quad 50 < Re < 1000\ ,$$

Table 9: Reactor parameters, operating conditions, and average gas properties

	Unit	Value
Reactor length	m	1.0
Gas feed temperature	^{o}C	500
Catalyst temperature	^{o}C	500
Pressure	bar	4.47
Bed voidage	-	0.4
Particle diameter (catalyst or sorbent)	m	$5*10^{-4}$
Gas mass flow velocity	kg/m^{2}s	0.05
Steam/carbon molar ratio	-	6.0
Oxygen/carbon molar ratio	-	0.45

Hydrotalcite–based system		
Catalyst solid density	kg/m^3	900
Sorbent solid density	kg/m^3	1300
Pore voidage		0.4
Solid thermal conductivity, λ_s	W/m.K	13.8
Bed heat capacity, $C_{p,bed}$ [34]	J/kg.K	850
Lithium zirconate–based system		
Catalyst solid density	kg/m^3	235
Sorbent solid density	kg/m^3	1000
Solid thermal conductivity, λ_s	W/m.K	50
Bed heat capacity, $C_{p,bed}$ [34]	J/kg.K	900
Average gas properties		
Molecular diffusivity, D_m	m^2/s	$1.6*10^{-5}$
Gas viscosity, μ_g	kg/m.s	$0.031*10^{-3}$
Gas thermal conductivity, λ_g	W/m.K	0.0532
LHV_{H2}	MJ/kmol	240
LHV_{CH4}	MJ/kmol	800

5. 4 Results and Discussion

5.4.1 Hydrotalcite–based system:

The dynamic behavior of the sorption–enhanced autothermal reformer based on Ni/MgO and a K-promoted HTC as a catalyst and sorbent, respectively, is analyzed at 500°C and 4.47 bar, using a S/C ratio of 6, an O/C ratio of 0.45, and a gas feed mass velocity of 0.05 kg/m^2s in a 1.0 meter reactor in length. H_2 can be produced in the transient sorption-enhanced regime with purity up to 96% on dry basis. Fig. 1 shows the dry-basis gas effluent composition of the key components versus time at the reactor exit. The H_2 concentration drops afterwards in the non-enhanced sorption regime after the sorbent is saturated with CO_2 to reach a purity of 67%, which is the ATR H_2 concentration at steady state. The effluent gas mixture contains less than 30 and 300 ppm of CO and CO_2, respectively.

Fig. 2 presents the dynamic profiles of CH_4 conversion and H_2 yield obtained at the reactor exit in the conventional autothermal reformer and the sorption-enhanced autothermal reformer. CH_4 conversion attained in the sorption-enhanced regime is 84%. This is an enhancement of 43% in conversion in comparison with the conversion in an autothermal reformer without sorbent. The thermal reforming efficiency obtained in the sorption enhanced process is 1.08 with a H_2 yield of 3.6 mol/mol of CH_4 fed, while a reforming efficiency of 0.6 and a H_2 yield of 2 can be achieved in a non-assisted sorption autothermal reformer at steady state.

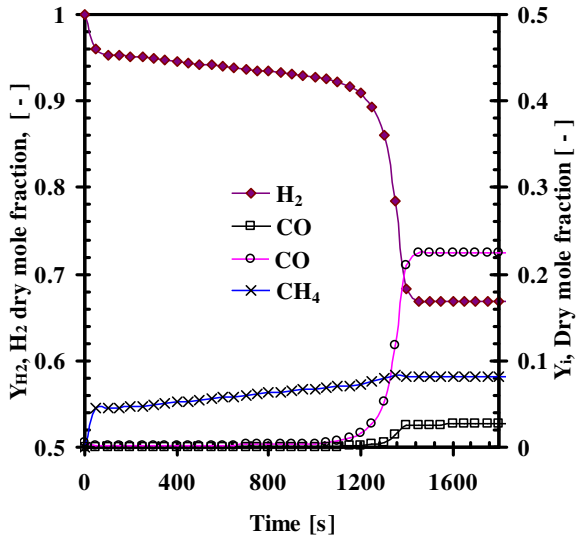

Fig. 1. Dry basis effluent concentration profiles of HTC–based sorption enhanced ATR process.

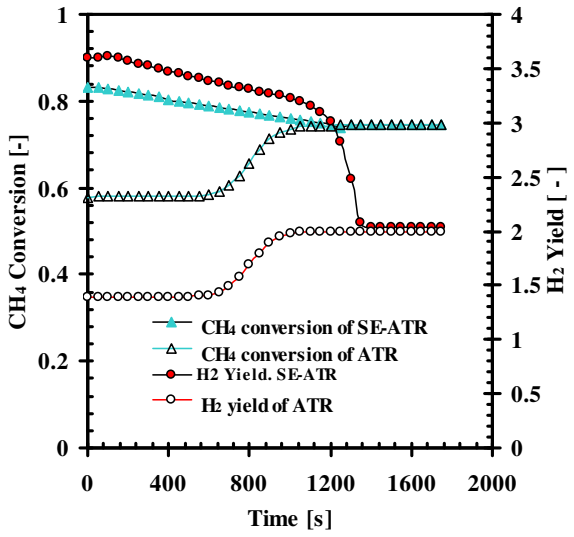

Fig. 2. Dynamic profiles of effluent CH_4 conversion and H_2 yield obtained in ATR with and without HTC.

Fig. 3 shows the dynamic temperature profiles at different locations along the bed for the sorption-enhanced and the sorption non-assisted autothermal reforming processes. The temperature sharply increases at the front part of the reformer in both cases of sorption–enhanced autothermal reforming (SE-ATR) and only–ATR due to the effect of CH_4 oxidation. The dip observed in the temperature at the reformer exit in the SE-ATR process is contributed to the large shift in equilibrium for the endothermic steam reforming reactions due to the local CO_2 adsorption at the exit. The gas temperature reached a maximum value of 574 ^oC with a rise of 74 ^oC above the feed temperature. The slight temperature difference of about 4 ^oC that the sorption enhanced ATR process can reach over the only–ATR process is explained by the small amount of heat generated from CO_2 sorption on hydrotalcite (-17 kJ/mol) and the slight difference in the solids packing densities in the two cases.

A maximum conversion enhancement of 45% can be obtained in the dynamic regime as a result of CO_2 sorption from the gas mixture, see Fig. 4. Slight negative enhancement in conversion is observed just at the onset of breakthrough and the approach to equilibrium. This can be attributed to the propagation of a thermal wave prior to steady state. The temperature dip occurred as a result of CO_2 sorption leads to a reduction in CH_4 conversion in comparison to the only–ATR conversion. This behavior is also observed by Ding and Alpay [3] in studying the sorption-enhanced steam reformer (SE–SR).

The dynamic profiles of adsorbed CO_2 and its equilibrium concentration on hydrotalcite at different locations along the reformer are given in Fig. 5. A sharp jump in the CO_2 sorption curve occurs at the reformer front due to the large amount of CO_2 generated by CH_4 combustion.

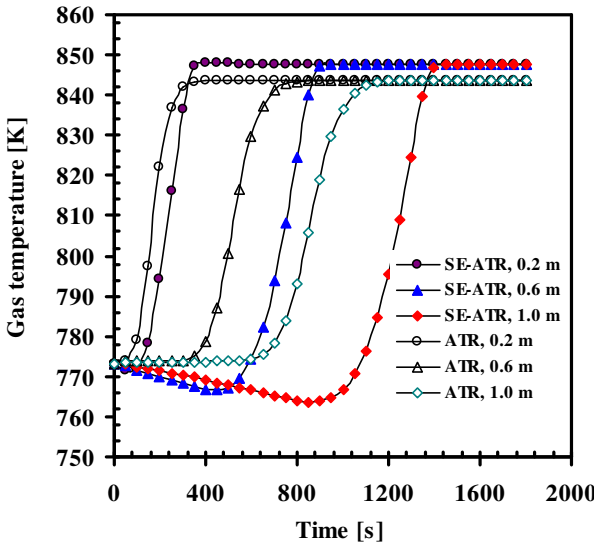

Fig. 3. Dynamic temperature profiles at different bed locations for ATR process with and without HTC.

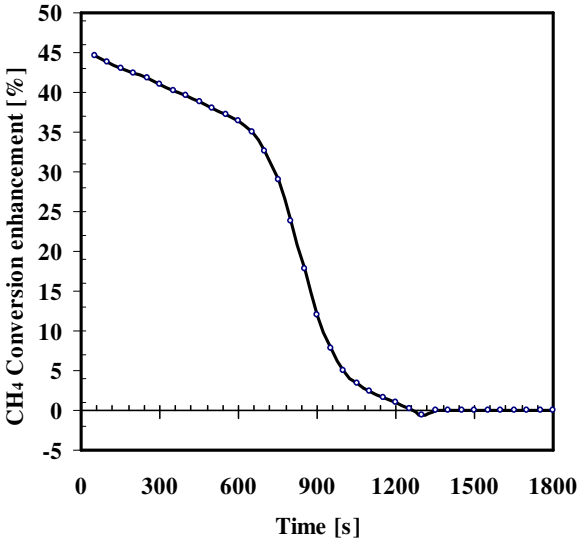

Fig. 4. Dynamic conversion enhancement profile of the HTC–based sorption enhanced ATR.

The adsorption wave moves on along the bed at a rate of 0.005 mol CO_2 adsorbed/kg.s with an average film mass transfer coefficient of 0.13 1/s as given in Fig. 6. The rate of CO_2 adsorption has been found to have a comparable value to the sum of the rate of CO_2 production by the steam reforming reaction R_1 and the reverse CH_4 reaction R_3. The ratio of (R_1+R_3) to the CO_2 adsorption rate is 2.51, which is an expected result due to the relatively fast kinetics of CO_2 sorption on hydrotalcite.

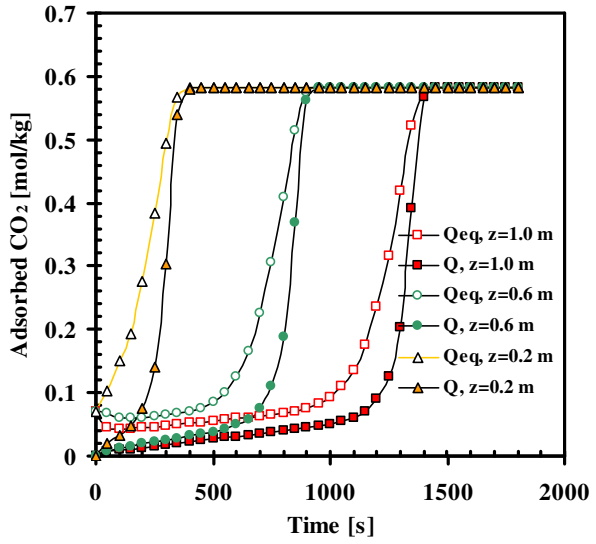

Fig. 5. Dynamic profiles of CO_2 adsorbed concentration and its equilibrium value on hydrotalcite.

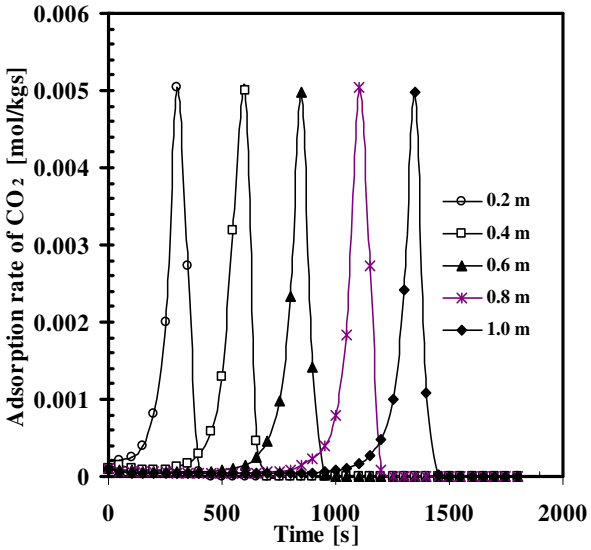

Fig. 6. CO_2 adsorption rates on hydrotalcite at different locations along the reformer.

5.4.2 Effect of sorbent capacity

Hydrotalcite has a low CO_2 sorption capacity in comparison to other sorbents for CO_2 recovery from flue gases. Many researchers are developing new techniques to boost the capacity of hydrotalcite [25–27]. Fig. 7 demonstrates the effect of HTC

sorbent capacity on the maximum CH_4 conversion that can be attained. CH_4 conversion can approach to 93% with sufficiently long operational time at sorbent capacity of 1.4 mol/kg comparing to the low sorbent capacity of 0.65 mol/kg. H_2 purity is strongly benefited from increasing the sorbent capacity to reach a value of 98% as represented in Fig. 8. The effect of capacity is further studied by enlarging the sorbent capacity up to 6 mol/kg. A sorbent capacity (> 2 mol/kg) is found to be sufficiently high to provide a CH_4 conversion and H_2 purity > 95 and 99%, respectively. If an active catalyst is used (such as Rh or Pt) in steam reforming or autothermal reforming reactions, it is evidently possible to accomplish high production rates with low catalyst mass at low temperatures. This will favor higher adsorption rates of CO_2 and thus much less catalyst/sorbent can be employed in the bed. According to the current results, it is beneficial to utilize an improved capacity hydrotalcite (> 2 mol/kg), which inherently provides fast adsorption kinetics in an efficient catalyst-sorbent system for pure H_2 production with in situ CO_2 capture.

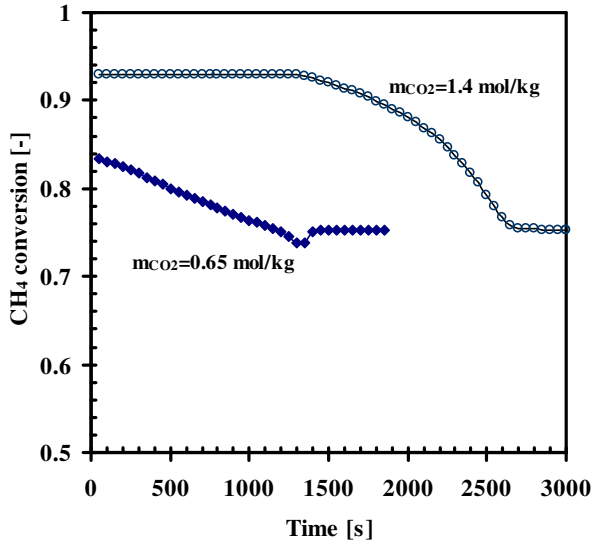

Fig. 7. Dynamic CH_4 conversion profiles at the reactor exit using different sorbent capacity of 0.65, and 1.4 mol/kg.

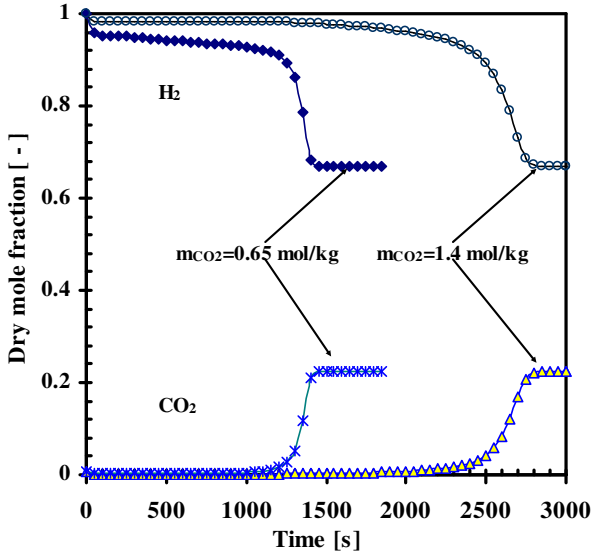

Fig. 8. Dynamic H_2 and CO_2 concentrations at the reactor exit using different sorbent capacity of 0.65, and 1.4 mol/kg.

5.4.3 Lithium zirconate–based system

The autothermal reforming process is studied at identical operational conditions using lithium zirconate (LZC) as a candidate sorbent. LZC has a relatively high adsorption capacity of 5 mol/kg [36], which is one order of magnitude higher than the HTC capacity in addition to a high temperature resistance up to 800 ^oC [33–37]. However, this sorbent suffers from slow sorption kinetics. The typical dry basis effluent concentration profiles are given in Fig. 9. In this process H_2 can be produced with a high purity of more than 99.5% and a corresponding CH_4 conversion of 99.5%. The high conversion attained is benefited from the high gas temperature, which is produced by the relatively high heat of sorption of CO_2 on LZC (- 160 kJ/mol). The maximum temperature reached is 684 ^oC with a rise of 184 ^oC above the gas feed temperature as represented in Fig. 10.

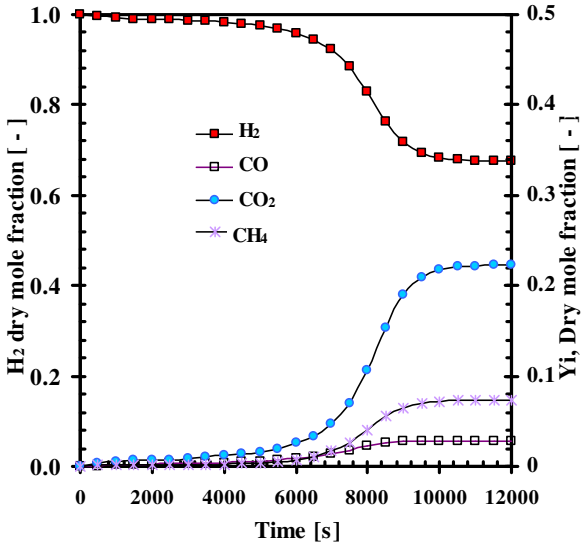

Fig. 9. Dry basis effluent concentration profiles at the reactor exit of LZC–based sorption enhanced ATR process.

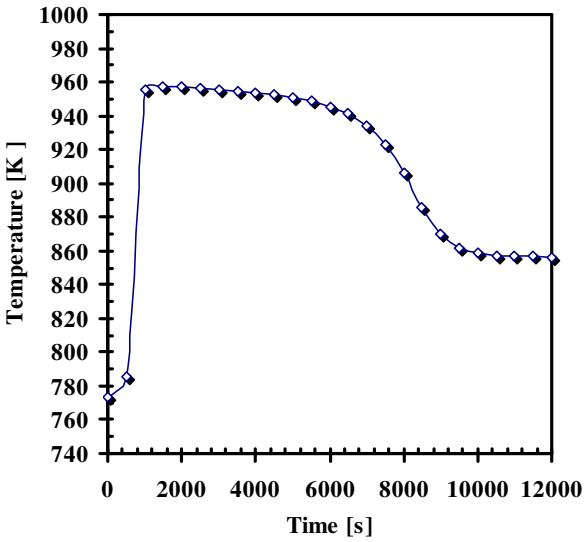

Fig. 10. Dynamic temperature profile at the reactor exit of LZC–based sorption enhanced ATR process.

Unfortunately, it is observed that carbon slip in the sorption enhanced transient regime is relatively large. ($CO+CO_2$) concentrations are almost 1% prior to the breakthrough up to 5000 s. However, this ratio can be as low as 0.1% during the initial transient state for the ATR reactions up to 400 s. This is mainly attributed to the weak sorption kinetics. The gain in the LZC high capacity over HTC is apparent in the large operational time before the breakthrough.

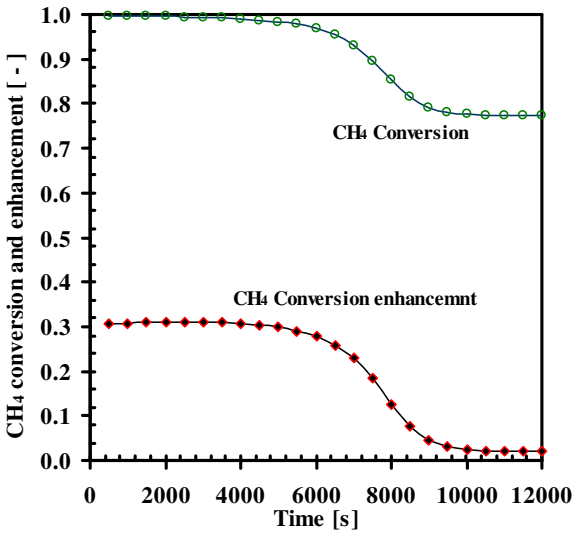

Fig. 11. CH_4 conversion and conversion enhancement profiles of the LZC–based sorption enhanced ATR process.

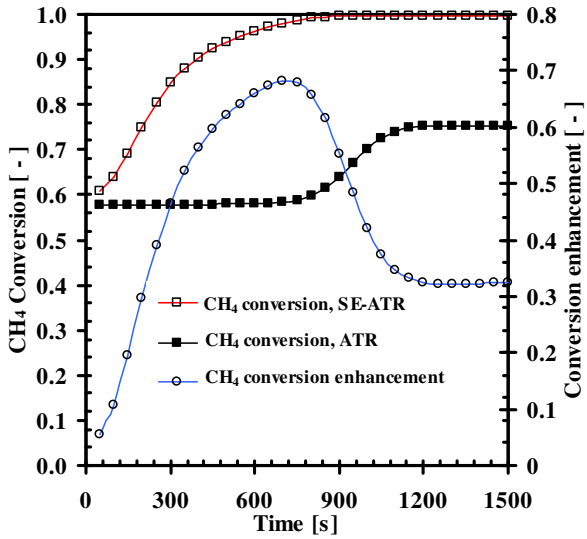

Fig. 12. CH_4 conversion and conversion enhancement profiles of the LZC–based sorption enhanced ATR process during the transient state of only-ATR reactor.

Fig. 11 shows the dynamic CH_4 conversion and conversion enhancement at the reactor exit. Sorption enhanced ATR on LZC suggests almost a constant enhancement of 31% over a large plateau of operational time up to 6000 s. It is

worth to mention that this can be seen as an apparent conversion enhancement over the final steady state conversion (74%) of the only–ATR reactor at identical conditions. However, the true conversion enhancement can be identified during the transient regime of only–ATR up to 900 s as given in Fig. 12. The only–ATR conversion profile rises up as the temperature wave goes along the reactor until it approaches the equilibrium conversion of 74%. In this time interval CH_4 conversion enhancement due to the high local CO_2 adsorption can reach 71% (with respect to 57% ATR conversion) and therefore resulting in an approximately 100% CH_4 conversion.

Fig. 13 shows the dynamic profiles of CO_2 adsorbed at different locations along the reformer length. The curves are less sharp than the CO_2 adsorption curves on hydrotalcite indicating slower adsorption kinetics. Fig. 14 presents local CO_2 adsorption rates at different bed locations in comparison to the local CO_2 production rates (R_1+R_3) from the ATR reactions. The CO_2 adsorption rate is slower than the reforming reaction rate by a factor of 8. The maximum local adsorption rate of CO_2 on lithium zirconate is found to be 0.002 mol/kg.s which is lower than the adsorption rates on hydrotalcite with a factor of 2.5. The CO_2 chemical adsorption constant on lithium zirconate is found to be $5*10^{-5}$1/s. This is 4 orders of magnitude lower than the CO_2 adsorption constant on hydrotalcite. This can be attributed to the slower sorption kinetics of CO_2 in addition to the fact that the adsorption constant of lithium zirconate is a strong function of temperature, while the adsorption constant on hydrotalcite has a much weaker dependency on temperature.

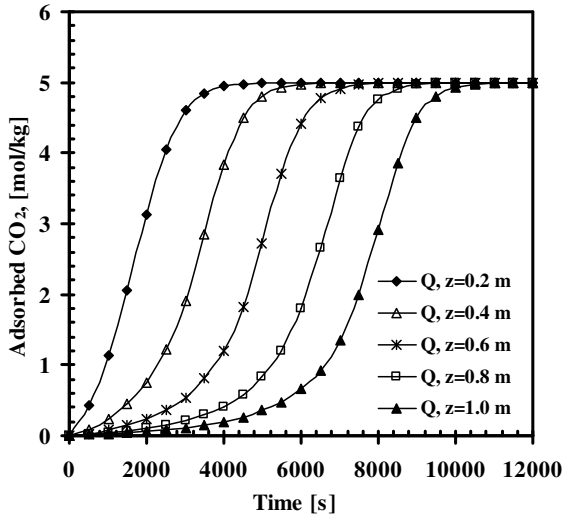

Fig. 13. CO_2 adsorbed concentration profiles on LZC– based sorption enhanced ATR process at different locations.

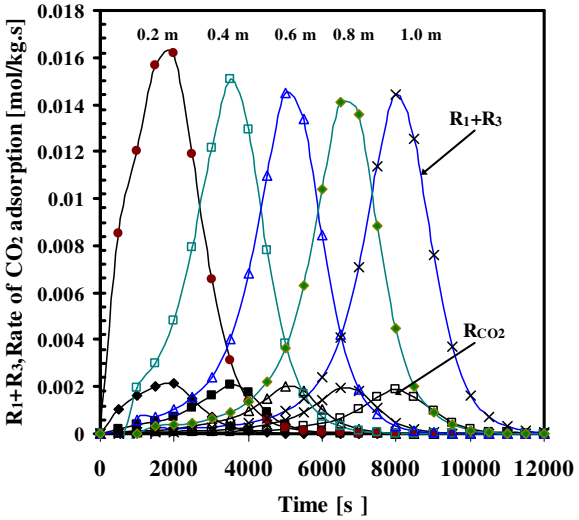

Fig. 14. CO_2 adsorption rates and CO_2 production rates from reforming reactions (R_1+R_3) at different bed location of LZC-based sorption enhanced ATR process.

Table 10 presents a comparison of the key operational parameters between this work and the processes reported in literature. CH_4 conversion and H_2 purity are considered as efficiency criteria for the process performance.

Table 10: Key parameters of sorption-enhanced ATR process in comparison with literature

	Hufton et al. [5]	Ding & Alpay [6]	Xiu et al.[11]	Fernandez et al.[38]	This work	This work
System	SE-SR	SE-SR	SE-SR	SE-SR	SE-ATR	SE-ATR
Sorbent	HTC	HTC	HTC	HTC	HTC	LZC
Catalyst	Ni	Ni	Ni	Ni	Ni	Ni
CH_4 Conversion	45%	70%	65%	87%	85%	99.5%
H_2 Purity	85%	80%	80%	95.5%	96%	99.5%
Temperature, ^oC	490	450	450	575	500	500
Pressure, bar	4.47	4.47	4.47	5	4.47	4.47
Reactor length, m	6.1	0.22	2	12	1.0	1.0
Gas velocity, m/s	0.037	0.13	0.05	-	0.038	0.038
Sorbent capacity, mol/kg	0.85	0.65	0.65	5	0.65	5
Catalyst bulk density, kg/m^3	769	139	249	140	189	165
Sorbent bulk density, kg/m^3	769	609	498	596	507	520
Particle diameter, mm	3	0.5	0.5	5	0.5	0.5
S/C ratio	6	6	6	6	6	6
O/C ratio	–	–	–	–	0.45	0.45

In this respect, the hydrotalcite–based ATR process presented in this work is more efficient than the sorption enhanced steam reforming processes studied by Hufton et al. [2], Ding and Alpay [3], and Xiu et al. [7]. The lithium zirconate–based ATR also shows improved performance in terms of CH_4 conversion and H_2 purity in comparison to the sorption enhanced steam reforming studied by Fernandez et al. [36], although they used much longer reactor (12 m) and a relatively higher temperature (575 ^oC).

5.4.4 Effect of space velocity

The space velocity is a key operational parameter in the sorption-enhanced reforming process. Fig. 15 shows the dynamic concentration profiles of H_2 and CO_2 for the K-promoted HTC-based process on dry-basis at the reactor exit using two different space velocities of 0.05 and 0.12 $kg/m^2.s$ (corresponding residence times of 25.9 s and 10.8 s; respectively). Fig. 16 gives the dynamic profiles of CH_4 conversion and H_2 yield using the same space velocities. Decreasing the space velocity (i.e. increasing residence time) results in an increase in H_2 purity, CH_4 conversion, and the operational time of the reactor before the breakthrough. Using a limiting operational ratio for ($CO+CO_2$) concentration level < 300 ppm, the allowed operational time is then defined as the time at which the ($CO+CO_2$) concentrations break the level of 300 ppm. This time increases for the reformer from 400 s to 1150 s by decreasing the space velocity from 0.12 to 0.05 $kg/m^2.s$. This is also reflected in an increase in the H_2 purity from 92% to 96%, an increase in CH_4 conversion from 77% to 84%, and an enhancement in the H_2 yield from 3.2 to 3.6 mol/mol CH_4 fed. CO_2 adsorption is benefited from low space velocity operation due to the fact that the intraparticle mass transfer limitation is reduced. However, at high space velocity, the production rate of CO_2 is lower and the

inhibition due to the reversible backward reactions is minimal. Thus, the benefit of local CO_2 adsorption on CH_4 conversion enhancement is diminished.

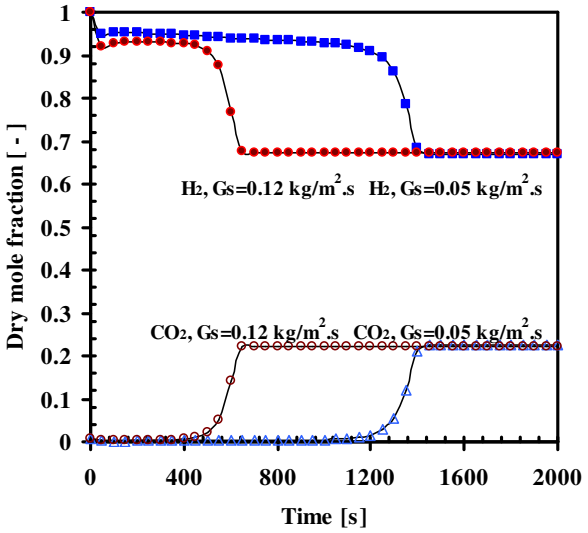

Fig. 15. Dynamic H_2 and CO_2 concentration profiles at the reformer exit using two space velocities of 0.05 and 0.12 kg/m^{2}s.

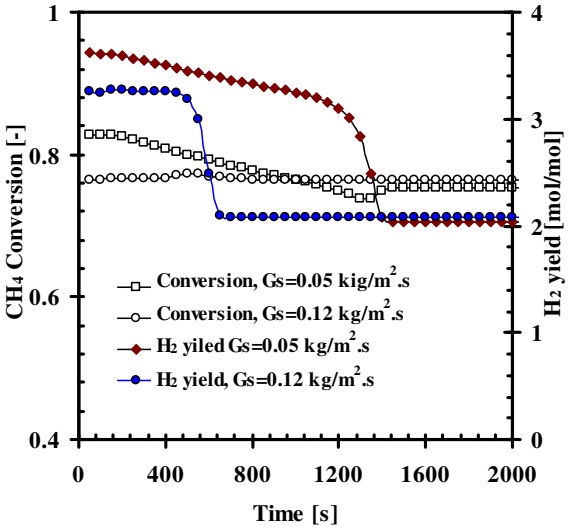

Fig. 16. Dynamic CH_4 conversion and H_2 at the reformer exit using two space velocities of 0.05 and 0.12 kg/m^{2}s.

5.4.5 Effect of the catalyst/sorbent ratio

The distribution of sorbent and catalyst in the bed or the ratio between the sorbent to catalyst inside one impregnated particle plays a decisive role in the final fuel conversion and accordingly the purity of H_2 produced. If the ratio of sorbent to catalyst in the bed is increased, H_2 can be produced with higher purity and higher operational time before the breakthrough concentrations approach equilibrium as the sorbent is fully saturated with CO_2.

Figures 17 and 18 envisage the influence of this ratio on the performance of K-promoted HTC-based sorption-enhanced ATR process. As the ratio of catalyst/sorbent increases from 0.15 to 0.55, the H_2 purity drops from 95% to 86% at an allowable operational time of 1500 and 750 s, respectively. The allowed operational time is defined as mentioned earlier. However, CH_4 conversion is benefited from a higher catalyst/sorbent ratio. The end application of the process determines the suitable value of this ratio. This situation is a compromise between high fuel conversion, high H_2 yield, and low H_2 purity at high catalyst/sorbent ratio on one side and the low conversion, high H_2 purity, and larger operational time of the unit on the other side.

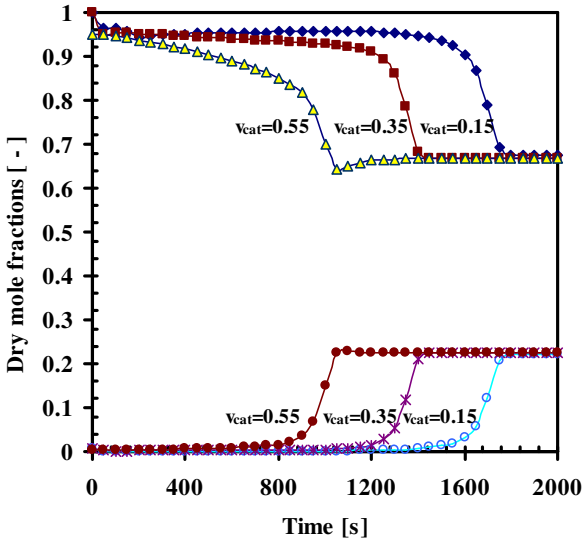

Fig. 17. Dynamic H_2 and CO_2 concentration profiles at the reactor exit using different catalyst/sorbent ratios of 0.15, 0.35, and 0.55.

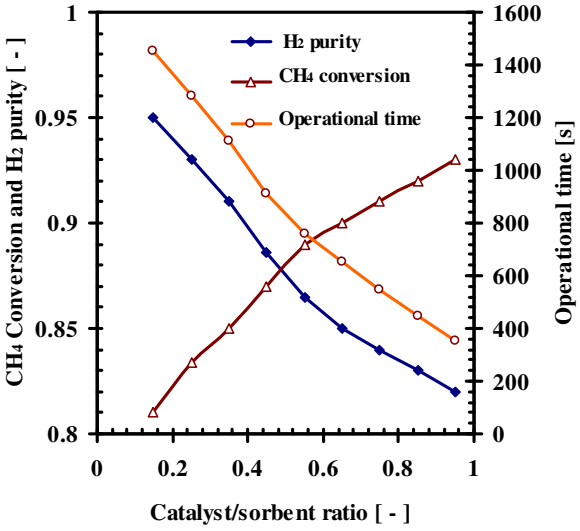

Fig. 18. Effect of catalyst/sorbent ratio on the performance of sorption-enhanced ATR in terms of CH_4 conversion, H_2 purity and allowed operational time.

5.4.6 Effect of pressure

The thermodynamic equilibrium conversion of steam and autothermal reforming reactions naturally benefit from low pressure operation, while CO_2 adsorption is benefited from high pressure operation. The pressure effect on the sorption enhanced ATR process is also investigated at identical conditions in a range of 1.5 to 16.4 bar, see Figures 19 and 20. The results suggest that both the conversion and H_2 purity achieved do not benefit from working at higher operating pressure. The conversion and purity obtained at 1.5 bar are 90% and 97%, respectively, whereas 72% conversion and 91% H_2 purity are reached at 16.4 bar. This is mainly attributed to the low capacity of hydrotalcite that can not facilitate more local adsorption of the CO_2 generated. In this case, the effect of pressure is more dominant. However, in the case of a high capacity sorbent, working at relatively high pressure may yield to a reasonable CH_4 conversion and H_2 purity. Thus, this is considered as an asset for a process where direct H_2 delivery is economically crucial.

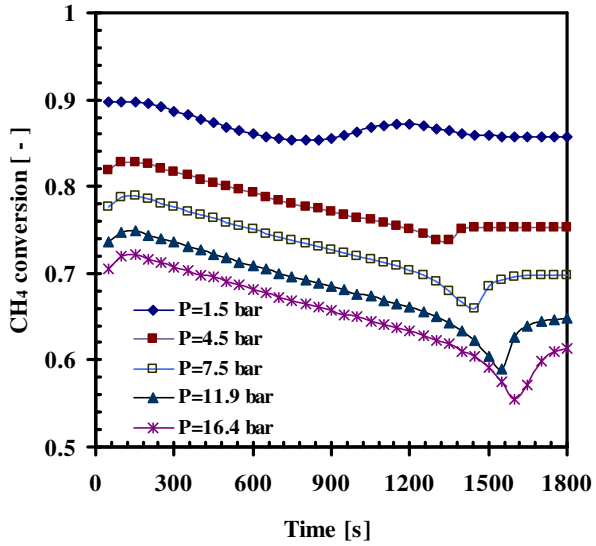

Fig. 19. Dynamic CH_4 conversion profiles at the reactor exit using different pressure of 1.5, 4.5, 7.5, 11.9, and 16.4 bar.

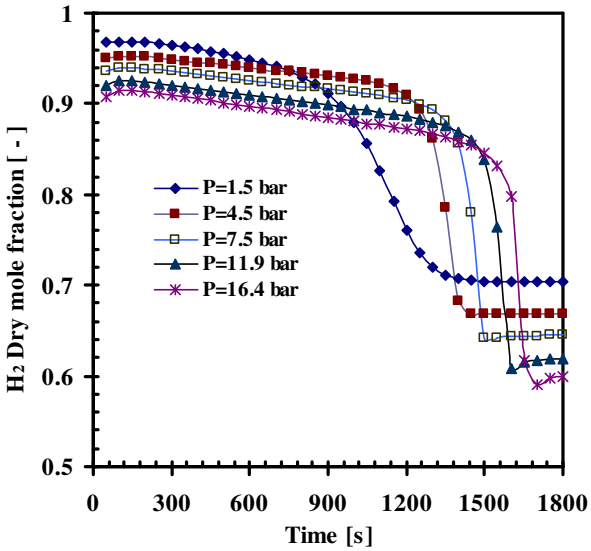

Fig. 20. Dynamic H_2 dry concentration profiles at the reactor exit using different pressure of 1.5, 4.5, 7.5, 11.9, and 16.4 bar.

5.4.7 Effect of particle size

The rate of reaction can be enhanced using smaller particle diameter as a result of diminished impact of the intraparticle mass transport limitation. It is likely to be crucial for CO_2 adsorption rates more than that for ATR reactions rates due to the fact that CO_2 adsorption on HTC is limited by the pore diffusion [19]. This effect is studied using different particle diameter of 1.0, 1.5, and 2.0 mm. It is found that both CH_4 conversion and H_2 purity are improved at smaller particle diameter. Figure 21 shows the dry H_2 concentration at the reactor exit using different particle diameters.

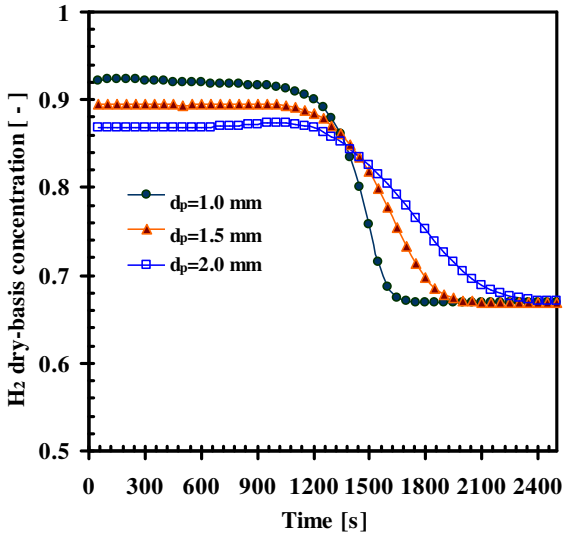

Fig. 21. Dynamic H_2 dry concentration profiles at the reactor exit using different particle diameter of 1.0, 1.5, and 2.0 mm.

Analysis of the results shows that the CO_2 adsorption rates become steeper at breakthrough due to a higher CO_2 mass transfer coefficient. This result can also be mathematically envisaged in the corresponding equation. If the particle diameter is

reduced by a half, then the effective mass transport coefficient is increased by a factor of 4. However, very small particles can generate severe operational problems when they tend to have static interaction and lowering the bed bulk porosity and consequently leading to a higher pressure drop.

5.4.8 Effect of steam/carbon ratio

The dynamic reformer behavior is studied for the K-promoted HTC-based process at different operational S/C ratios. The results are given in Figures 22 and 23. CH_4 conversion and high purity H_2 production are favored by higher S/C ratios. Increasing the S/C ratio from 3.0 to 6.0 enhances CH_4 conversion in the transient sorption enhanced regime from 56% to 85% and H_2 purity from 87 to 96%. The temperature profile at different S/C ratios is shown in Figure 23. The steady state CH_4 conversion is slightly reduced when the S/C ratio is increased due to the fact that lower temperatures are attained. At S/C ratios of 3.0 and 6.0, the CH_4 conversion is 71% and 75%, respectively.

With respect to the conversion enhancement caused by the local CO_2 adsorption, it is found that the maximum CH_4 conversion enhancement can be achieved at low S/C ratios. At low partial pressure of steam (S/C=1–2), the equilibrium conversion is low and the backward reactions can be significant; therefore CO_2 adsorption can efficiently enhance the CH_4 conversion. Contrary, at high steam partial pressure, high equilibrium CH_4 conversion exits and the affinity to enhance the CH_4 conversion by local CO_2 adsorption has less impact.

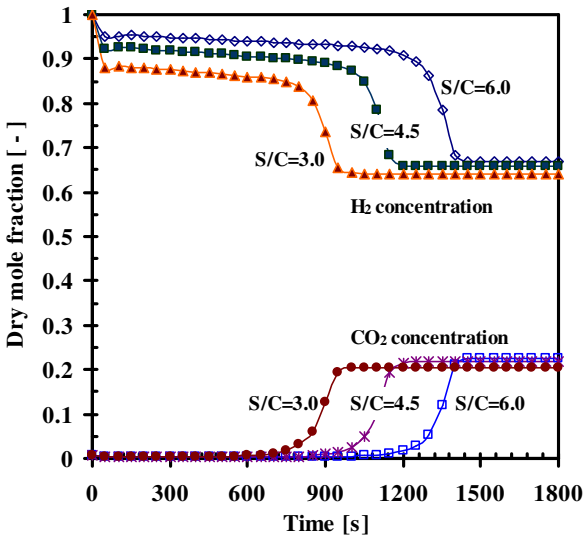

Fig. 22. Dynamic H_2 and CO_2 concentration profiles at the reactor exit using different S/C ratios of 6.0, 4.5, and 3.0.

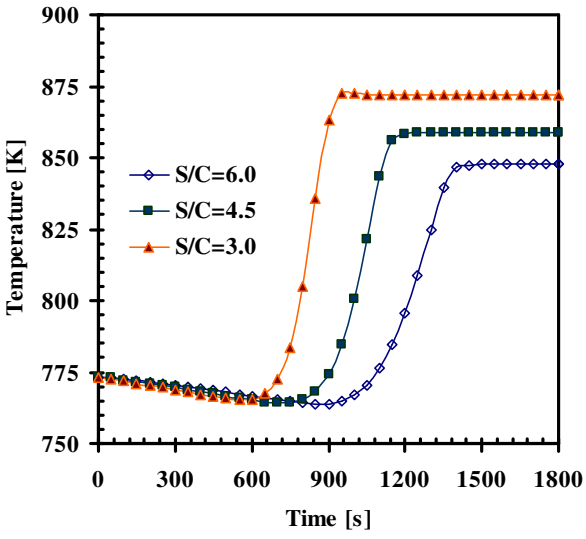

Fig. 23. Dynamic temperature profile at the reactor exit using different S/C ratios of 6.0, 4.5, and 3.0.

Using a conventional Ni-based catalyst supported on an inert in a highly oxidative media resulting from the presence of excessive S/C and/or O/C ratios can lead to catalyst deactivation due to the loss of the Ni reduced state. A high S/C ratio (>3) is usually applied to reduce the CO production from the reverse water-gas shift reaction and thus increasing fuel conversion and reducing carbon formation via the

Boudouard reaction. However, at the adiabatic ATR conditions of this process catalyst deactivation as a result of the Ni over-oxidation or carbon formation may not take place due to the following reasons: (i) H_2 gas is always co-fed in the gas feed mixture, (ii) using an O/C ratio up to 0.45, oxygen is fully utilized within the first 10% of the reformer length. The remaining part of the reactor is dominated by steam reforming (see Halabi et al. [39]) and CO_2 sorption reactions, (iii) the composition of H_2 present along the reformer is found to be at least 1.3–2 times higher than its composition in conventional steam reformers, (iv) the concentration of CO along the reformer is in the ppm impurity level, which prevents the possibility of carbon formation due to the Boudouard reaction, (v) the process is operated at relatively low temperature of 500 ^{o}C, thus carbon formation due to methane decomposition is not likely to occur as this reaction is favored at much higher temperature.

However, we have developed and experimentally examined a ceria-zirconia supported rhodium as a novel catalyst to be used in the low temperature sorption-enhanced steam reforming process [64–68]. The ceria supported catalyst offers a unique feature of oxygen storage and exchange capacities. Thus, carbon formation can be significantly diminished due to the redox reactions of the carbonaceous species formed on the active metal surface from CH_4 dissociation with oxygen spill over from the ceria support. The simultaneous supply of lattice oxygen from steam can also reduce any carbon formation [64, 65].

5.4.9 Effect of oxygen/carbon ratio

The oxygen/carbon O/C ratio can be of high impact on the lithium zirconate based process. The high heat of reaction generated during CO_2 chemisorption on lithium zirconate is investigated to determine if it is sufficient to provide a heat supplement at lower (O/C) ratio at the adiabatic conditions of the ATR process. The dynamic conversion profiles at different O/C ratios are given in Figure 24. O/C ratios lower than 0.35 can result in a CH_4 conversion of less than 90%. This is attributed to the drop of temperature, which is demonstrated in Figure 25.

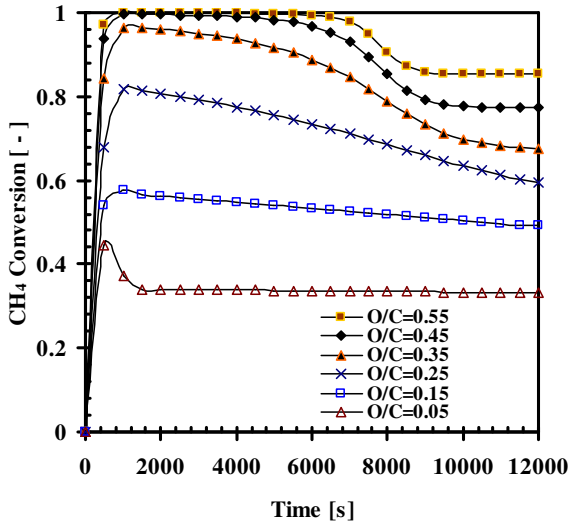

Fig. 24. Dry basis effluent concentration profiles at the reactor exit using different O/C ratios in LZC–based sorption enhanced ATR.

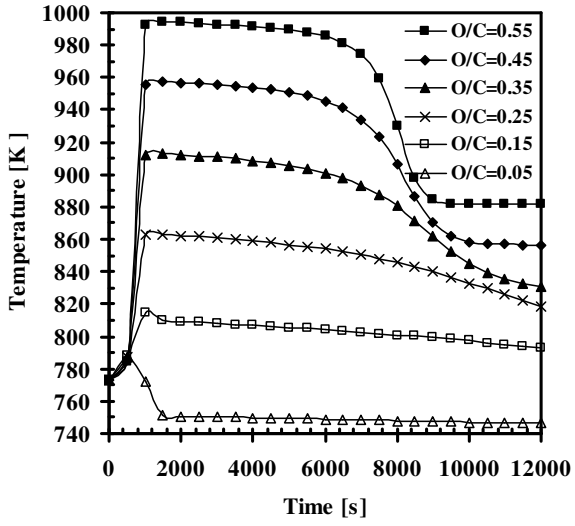

Fig. 25. Dynamic temperature profiles at the reactor exit at using different O/C ratios in LZC–based sorption enhanced ATR.

Thus, the heat of CO_2 chemisorption on lithium zirconate is not sufficient to provide high CH_4 conversion level at adiabatic operation without an assistance of O/C ratio (>0.35).

Figure 26 presents the dry basis H_2 concentration in the gas effluent at different (O/C) ratios. High O/C ratio inherently increases CH_4 conversion; however, this is a trade off with a lower selectivity towards H_2 produced. At high O/C ratios, the H_2 concentration is drastically affected and reduced from 99.5% at O/C ratio of 0.45 to as low as 36% at O/C ratio of 0.55

Thus, an O/C ratio of 0.45 is an acceptable value to be used in the sorption-enhanced ATR process. Araki et al. [69] found that a combination of S/C ratio in the range of 0–2.0 and O/C ratio in the range of 0.5–0.6 had no effect on the Ni catalyst durability during the autothermal reforming of methane. However, high S/C ratio (>3) leads to decreased catalytic activity due to the oxidation of the Ni metal to Ni_2O_3.

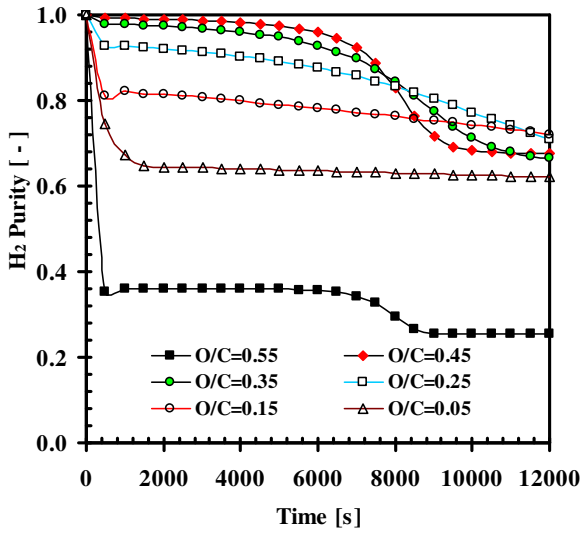

Fig. 26. H_2 effluent concentration profiles at different O/C ratios in LZC–based sorption enhanced ATR.

5. 5 Conclusions

The performance of the autothermal reforming process can be significantly improved in terms of CH_4 conversion, H_2 purity and productivity using the adsorption–enhanced reaction concept. Pure H_2 production and simultaneous in situ CO_2 capture tend to be possible in such a technique. The process is found to be efficient and applicable even at a temperature as low as 500 ^oC with respect to steam reforming reactions and at a pressure as low as 4.47 bar with respect to CO_2 adsorption. The hydrotalcite–based ATR process can provide CH_4 conversion and H_2 purity up to 85% and 96%, respectively. The adsorption kinetics of CO_2 on hydrotalcite is in comparable rate to the ATR reforming reaction. The process performance is found to be benefited from high sorbent capacity (≥2 mol/kg). The low adsorption capacity of hydrotalcite is still a challenging issue for further

research and a limiting factor in operation. Lithium zirconate provides higher CO_2 adsorption capacity than hydrotalcite although it shows slower adsorption rates. This is strongly reflected in the high CH_4 conversion and H_2 productivity obtained up to 100% in addition to the large operational time. Thus, the system investigated in this work can be considered as a significant improvement over the conventional examined processes in literature. In particular, this is the first work that describes the application of the sorption-enhanced reaction concept in the autothermal reforming process at low temperature and relatively low pressure.

The operational parameters are found to have a substantial impact on the process behavior in terms of CH_4 conversion, H_2 purity and yield, and thermal reforming efficiency. Improved process performance favor low space velocity operation (0.05 kg/m^2s), low pressure (4.47 bar), smaller pellet size (0.5–1 mm), high S/C ratio (6), and high sorbent capacity ($\geq$2 mol/kg). Operating the unit at low gas space velocity enhances the quality of H_2 produced and fuel CH_4 conversion. The optimal composition of catalyst and sorbent inside the bed should be determined according to the end application of H_2 generation stream. Using high catalyst/sorbent ratio provides high fuel conversion but low H_2 purity and low allowable operational time before the breakthrough. Direct high pressure operation at the steam reforming facility does not seem to be beneficial for fuel conversion or H_2 purity. In the lithium zirconate-based process, the heat of reaction produced as a result of CO_2 chemisorption on lithium zirconate can not provide full compensation for the energy requirement of the autothermal reforming unit if low O/C ratio (<0.35) is used.

Nomenclature

Symbol	Definition	Unit
a_v	External catalyst surface area per unit volume of catalyst bed	m^2/m^3
C_i	Concentration of species i in the gas phase	mol/m^3
$C_{i,s}$	Concentration of species i in the solid phase	mol/m^3
$C_{p,bed}$	Specific heat of the catalyst bed	J/kg.K
C_{pg}	Specific heat of the fluid	J/kg.K
D_i	Effective diffusion coefficient	m^2/s
D_m	Gas molecular diffusivity	m^2/s
D_Z	Axial dispersion coefficient	m^2/s
d_p	Catalyst particle diameter	m
E_j	Activation energy of reaction j	J/mol
G_s	Gas mass flow velocity	kg/m^2s
h_f	Gas to solid heat transfer coefficient	W/m^2s
j_D	Chilton-Colburn factor for mass transfer	–
j_H	Chilton-Colburn factor for heat transfer	–
$k_{g,i}$	Gas to solid mass transfer coefficient of component i	m^3/m^2s
k_j	Temperature dependent kinetic rate constant of reaction j	
k_{oj}	Reference temperature dependent kinetic rate constant of reaction j	
K_j	Thermodynamic equilibrium constant of reaction j	
K_{oi}	Reference adsorption constant of species i	
K_i	Adsorption constant of species i	
K_{oi}^C	Reference adsorption constant of combusting species i	
K_i^C	Adsorption constant of combusting species i	
K_D	Parameter corresponding to the viscous loss term	$Pa.s/m^2$
K_V	Parameter corresponding to the kinetic loss term	$Pa.s^2/m^3$
LHV_{H_2}	Lower heating value of H_2	MJ/kmol
LHV_{CH_4}	Lower heating value of CH_4	MJ/kmol
p_i	Partial pressure of gas species i	bar
P	Total gas pressure	bar
Pr	Prandtl number	–
r_i	Rate of consumption or formation of species i	$mol/kg_{cat}.s$
R_j	Rate of reaction j	$mol/kg_{cat}.s$
R	Universal gas constant	J/mol.K
Re	Reynolds number	–
Sc_i	Schmitt number	–
T	Gas phase temperature	K
T_s	Solid catalyst temperature	K
t	Time	s
u	Superficial gas flow velocity ($= \varepsilon_b u_{inst}$)	m/s

u_{inst}	Interstitial gas velocity	m/s
Y_i	Dry mole fraction of species i	mol/mol
z	Axial dimension	m
Greek symbols		
ΔH_i	Heat of adsorption of species i	J/mol
ΔH_i^C	Heat of adsorption of combusting species i	J/mol
ΔH_{298K}	Heat of reaction of at STP	kJ/mol
ε_b	Packing bed porosity	–
$\boldsymbol{\eta}_j$	Effectiveness factor of reaction j	–
λ_g	Average gas thermal conductivity	W/m.K
λ_s	Solid thermal conductivity	W/m.K
$\boldsymbol{\lambda}_z^f$	Effective thermal conductivity	W/m.K
μ_g	Average gas viscosity	kg/m.s
ρ_{bed}	Density of the catalyst bed	kg/m^3
$\boldsymbol{\rho}_{cat}$	Density of the catalyst pellet	kg/m^3
ρ_f	Density of the fluid	kg/m^3
$\boldsymbol{\psi}$	Particle shape factor (for spherical particles, $\psi = 1$)	–
Ω	Dominator term in the reaction kinetics	–
$\boldsymbol{\delta}$	Stoichiometric O/C ratio for adiabatic operation	–
Abbreviations		
ATR	Autothermal reforming	
HTC	Hydrotalcite	
GHSV	Gas hourly space velocity	kg/m^2hr
LDF	Linear driving force model	
LHV_{H_2}	Lower heating value of H_2	MJ/kmol
LHV_{CH_4}	Lower heating value of CH_4	MJ/kmol
O/C	Molar oxygen/carbon ratio	
S/C	Molar steam/carbon ratio	
SE–SR	Sorption enhanced steam reforming	
SE–ATR	Sorption enhanced autothermal reforming	

References

1. Rostrup-Nielsen, J.R. Production of synthesis gas. Catal. Tod. 18 (1993) 305-324.
2. Pena M.A.; Gómez, J.P.; Fierro, J.L.G. New catalytic routes for syngas and hydrogen production, App. Catal A, 144 (1996) 7-57.
3. Ayabe, S.; Omoto, H.; Utaka, T.; Kikuchi, R.; Sasaki, K.; Teraoka, Y.; Eguchi, K. Catalytic autothermal reforming of methane and propane over supported metal catalysts. App. Catal. A 241 (2003) 261.
4. Hufton, J. R., Mayorga, S., Sircar, S. Sorption-enhanced reaction process for hydrogen production. AIChE J. 45 (1999), 248–256.
5. Hufton, J., Waldron, W., Weigel, S., Rao, M., Nataraj, S., Sircar, S., Sorption enhanced reaction process SERP) for the production of hydrogen, in: Proceedings of the 2000 US DOE Hydrogen Program Review, 2000.
6. Ding, Y., Alpay, E. Adsorption-enhanced steam-methane reforming. Chem. Eng. Sci. 55 (2000) 3929–3940.
7. Ding, Y., Alpay, E. High temperature recovery of CO_2 from flue cases using hydrotalcite adsorbent. Trans IChemE. 79-B1 (2001) 45–51.
8. Yong, A., Mata, V., Rodrigues, A.E. Adsorption of carbon dioxide onto hydrotalcite-like compounds (HTlcs) at high temperatures, Ind. Eng. Chem. Res. 40 (2001) 204-209.
9. Waldron, W. F.; Hufton, J. R.; Sircar, S. Production of hydrogen by cyclic sorption enhanced reaction process. AIChE J. 47 (2001) 1477–1479.
10. Reijers, H. Th. J.; Valster-Schiermeier, S. A. E.; Cobden, P. D.; van den Brink, R. W. Hydrotalcite as CO_2 Sorbent for Sorption-Enhanced Steam Reforming of methane. Ind. Eng. Chem. Res. (2006) 45, 2522–2530.
11. Xiu, G.; Soares, J. L.; Li, P.; Rodrigues, A. E. Simulation of five-step one-bed sorption-enhanced reaction process. AIChE J. 48 (2002) 2817–2832.
12. Xiu, G.; Li, P.; Rodrigues, A. E. Sorption-enhanced reaction process with reactive regeneration. Chem. Eng. Sci. (2002) 57, 3893–3908.
13. Xiu, G.; Li, P.; Rodrigues, A. E. New generalized strategy for improving sorption-enhanced reaction process. Chem. Eng. Sci. (2003) 58, 3425–3437.
14. Xiu, G.; Li, P.; Rodrigues, A. E. Adsorption-enhanced steam-methane reforming with intraparticle-diffusion limitations. Chem. Eng. J. (2003) 93, 83–93.
15. Wang Y.N; Rodrigues A.E. Hydrogen production from steam methane reforming coupled with in situ CO_2 capture: Conceptual parametric study. Fuel (2005) 84, 1778–1789.
16. Kapil, A; Bhat, S.A.; Sadhukhan, J.Multiscale characterization framework for sorption enhanced reaction process. AICHE J. (2008) 54, 1025–1036.
17. Koumpouras GC, Alpay E, Stepanek F. Mathematical modelling of low-temperature hydrogen production with in situ CO_2 capture. Chem Eng Sci. (2007) 62, 2833–2841.

18. Koumpouras GC, Alpay E, Lapkin A, Ding Y, Frantisek S. The effect of adsorbent characteristics on the performance of a continuous sorption-enhanced steam nethane reforming process. Chem Eng.Sci. (2007), 62, 5632-5637.
19. Cobden, P. D.; van Beurden, P.; Reijers, H. Th. J.; Elzinga, G. D.; Kluiters, S. C. A.; Dijkstra, J. W.; Jansen, D.; van den Brink, R. W. Sorption-enhanced hydrogen production for pre-combustion CO_2 capture: Thermodynamic analysis and experimental results. Int. J. Greenhouse Gas Control. (200) 7, 1, 170–179.
20. van Selow, E.R; Cobden, P. D.; Verbraeken, P.A; Hufton, J.R.; van den Brink, R. W. Carbon capture by sorption –enhanced water-gas shift reaction using hydrotalcite-based material. 2009, 48, 4184-4193.
21. Reijers, H. Th. J.; Boon, J.; Elzinga, G. D.; Cobden, P. D.; Haije, W.G.;van den Brink, R. W. Modeling study of the sorption-enhanced reaction process for CO2 capture. I. model development and validation. Ind. Eng. Chem. Res., 2009, 48, 6966-6974.
22. Reijers, H. Th. J.; Boon, J.; Elzinga, G. D.; Cobden, P. D.; van den Brink, R. W. A modeling study of the sorption-enhanced reaction process for CO2 capture. II. Application to steam-methane reforming. Ind. Eng.Chem. Res., 2009, 48, 6975-6982.
23. Ding, Y.; Alpay, E. Equilibria and kinetics of CO_2 adsorption on hydrotalcite adsorbent. Chem. Eng. Sci. 2000, 55, 3461–3474.
24. Ebner, A. D.; Reynolds, S. P.; Ritter, J. A. Non-equilibrium kinetic model that describes the reversible adsorption and desorption behavior of CO2 in a K-promoted hydrotalcite-like compound. Ind. Eng. Chem. Res. 2007, 46, 1737–1744.
25. Lee, K. B.; Verdooren, A.; Caram, H. S.; Sircar, S. Chemisorption of carbon dioxide on potassium-carbonate-promoted hydrotalcite. J. Colloid Interface Sci. 2007, 308, 30–39.
26. Oliveira, E. L. G.; Grande, C. A.; Rodrigues, A. E. CO_2 Sorption on hydrotalcite and alkali-modified (K and Cs) hydrotalcites at high temperatures. Sep. Purif. Technol. 2008, 62, 137–147.
27. Lwin, Y.; Abdulla, F.; High temperature adsorption of carbon dioxide on Cu-Al hydrotalcite-derived mixed oxides: kinetics and equiblria by thermogravimetry. J. Therm. Anal. Calorim. 2009, 97, 885-889.
28. Kato, M., Yoshikawa, S., Nakagawa, K., Carbon dioxide absorption by lithium orthosilicate in a wide range of temperature and carbon dioxide concentrations, J. Mater. Sci. Lett. (2002) 21, 485.
29. M. R. Othman, Z. Helwania,b, Martunusa,b andW. J. N. Fernando. Synthetic hydrotalcites from different routes and their application as catalysts and gas adsorbents: a review, Appl. Organometal. Chem. 2009, 23, 335–346
30. J.-I. Ida, Y.S. Lin, Mechanism of high-temperature CO_2 sorption on lithium zirconate, Environ. Sci. Technol. 37 (2003) 1999.
31. R. Xiong, J. Ida, Y. Lin, Kinetics of carbon dioxide sorption on potassium-doped lithium zirconate, Chem. Eng. Sci. 58 (2003) 4377-4385.
32. J. Ida, R. Xiong, Y.S. Lin, Synthesis and CO2 sorption properties of pure and modified lithium zirconate, Sep. Purif. Technol. 36 (2004) 41-51.

33. D.J. Fauth, E.A. Frommell, J.S. Hoffman, R.P. Reasbeck, H.W. Pennline, Eutectic salt promoted lithium zirconate: novel high temperature sorbent for CO_2 capture, Fuel Process. Technol. 86 (2005) 1503-1521.
34. Y.-J.Wang, Y.-J., Qi, L., Wang, X.-Y., The study of Li_2ZrO_3 used for absorption of CO_2 at high temperature, Chin. J. Inorg. Chem. (2003), 19 531.
35. Nair, B.N., Yamaguchi, T., Kawamura, H., Nakao, S., Processing of lithium zirconate for applications in carbon dioxide separation: structure and properties of the powders, J. Am. Ceram. Soc. (2004) 87, 68.
36. E. Ochoa-Fernandez, M. Ronning, T. Grande, D. Chen, Nanocrystalline lithium zirconate with improved kinetics for high-temperature CO_2 capture, Chem. Mater. 18 (2006) 1383-1385.
37. Alina Iwana, Hazel Stephensonb,William C. Ketchiec, Alexei A. Lapkin, High temperature sequestration of CO_2 using lithium zirconates, Chem. Eng. J. 146 (2009) 249–258
38. E. Ochoa-Fernandez, H.K. Rusten, H.A. Jakobsen, M. Rønning, A. Holmen, D. Chen, Sorption enhanced hydrogen production by steam methane reforming using Li_2ZrO_3 as sorbent: sorption kinetics and reactor simulation, Catal. Today, 106 (2005) 41-46.
39. Halabi, M.H., de Croon, M.H.J.M., van der Schaaf, J., Cobden, P.D., Schouten, J.C., Modeling and analysis of autothermal reforming of methane to hydrogen in a fixed bed reformer. Chem. Eng. J. 137 (2008) 568-578.
40. Armor, J.N., Catalysis and the hydrogen economy, Catalysis Letters 101 (2005) 131–135.
41. Aasberg-Petersen, K., Christensen, T.S., Nielsen, C.S., and Dybkjaer, I., Recent developments in autothermal reforming and pre-reforming for synthesis gas production in GTL applications, Fuel Processing Tech. 83 (2003) 253–261.
42. Heinzel A, Vogel B, Hubner P., Reforming of natural gas—hydrogen generation for small scale stationary fuel cell systems, J. Power Sources 105 (2002) 202–207.
43. Ahmed, S., Krumpelt, M., Hydrogen from hydrocarbon fuels for fuel cells, Int. J. Hydrogen Energy 26 (2001) 291–301.
44. Lee, H.D., Applegate, D.V., Ahmed, S., Calderone, S.G., and Harvey, T.L, Hydrogen from natural gas: part I - autothermal reforming in an integrated fuel processor, Int. J. Hydrogen Energy 30 (2005) 829 – 842.
45. Chan, S.H, Wang, H.M., Thermodynamic analysis of natural gas fuel processing for fuel cell applications, Int. J. Hydrogen Energy 25 (2000) 441–449.
46. Halabi, M.H., de Croon, M.H.J.M., van der Schaaf, J., Cobden, P.D., Schouten, J.C., Reactor modeling of sorption–enhanced autothermal reforming of methane. Part II: Effect of operational parameters, Chem.Eng. J., Submnitted, 2011.
47. Xu, J. and Froment, G.F., Methane steam reforming, methanation and water–gas shift: I. intrinsic kinetics, AIChE. J. 35 (1989) 88–96.
48. Trimm, D.L. and Lam, C-W., The combustion of methane on platinum-alumina fibre catalysts—I. Kinetics and mechanism, Chem. Eng. Sci. 35 (1980) 1405–1413.

49. De Smet, C.R.H., de Croon, M.H.J.M., Berger, R.J., Marin, G.B., and Schouten, J.C., Design of adiabatic fixed-bed reactors for the partial oxidation of methane to synthesis gas. Application to production of methanol and hydrogen-for-fuel-cells, Chem. Eng. Sci. 56 (2001) 4849–4861.
50. De Groote, A.M. and Froment, G.F., Simulation of the catalytic partial oxidation of methane to synthesis gas", Applied Catalysis A 138 (1996) 245–264.
51. De Groote, A.M., Froment, G.F. and Kobylinski, Th., Synthesis gas production from natural gas in a fixed bed reactor with reversed flow, Can. J. Chem. Eng. 74 (1996) 735–742.
52. Gosiewski, K., Bartmann, U., Moszczynski, M. and Mleczko, L., Effect of intraparticle transport limitations on temperature profiles and catalytic performance of the reverse-flow reactor for the partial oxidation of methane to synthesis gas, Chem. Eng. Sci. 54 (1999) 4589–4602.
53. Froment, G.F., Bischoff, K.B, Chemical reactor analysis and design, Wiley, London, (1990).
54. Ergun, S., Fluid flow through packed columns, Chem. Eng. Prog. 48 (1952) 89–94.
55. Edwards, M.F., and J.F. Richardson, Gas dispersion in packed beds, Chem. Eng. Sci. 23 (1968) 109–123.
56. Yagi, S., Kunii, D., and Wakao, N., Studies on axial Effective thermal conductivities in packed beds, AIChE J. 6, (1960) 543–546.
57. Kunii, D., Smith, J.M., Heat transfer characteristics of porous rocks, AIChE J. 6 (1960) 71–78.
58. De Wash, A.P., Froment, G.F., Heat transfer in packed bed, Chem. Eng. Sci. 27 (1972) 567–576.
59. Li, C.H., Finlayson, B.A., Heat transfer in packed bed – a reevaluation, Chem. Eng. Sci. 32 (1977) 1055–1066.
60. Wakao, N., Kaguei, S., Heat and Mass Transfer in Packed Bed, Gordon and Breach, New York, (1982).
61. Reid, R.C., Prausnitz, J.M., and Poling, B.E., The Properties of Gases and Liquids, McGraw-Hill, New York, (1988).
62. Bird, R.B., Stewart, W.E., and Lightfoot, E.N., Transport Phenomena, 2nd Ed., Wiley, New York, (2002).
63. Geankoplis, C.J., Transport Processes and Unit Operations, 3rd Ed., Prentice Hall Int., 1993.
64. Halabi, M.H., de Croon, M.H.J.M., van der Schaaf, J., Cobden, P.D., Schouten, J.C., Low temperature catalytic methane–steam reforming of methane over ceria–zirconia supported rhodium catalyst, Applied Catalysis A, 10.1016/j.apcata.2010.09.004, 2010.
65. Halabi, M.H., de Croon, M.H.J.M., van der Schaaf, J., Cobden, P.D., Schouten, J.C., Intrinsic kinetics of low temperature catalytic methane–steam reforming and water gas shift over $Rh/Ce_{\alpha}Zr_{1-\alpha}O_2$ catalyst, Applied Catalysis A, 10.1016/j.apcata.2010.09.005, 2010.

66. Halabi, M.H., de Croon, M.H.J.M., van der Schaaf, J., Cobden, P.D., Schouten, J.C., A novel catalyst–sorbent system for an efficient H_2 production with in-situ CO_2 capture, Int. J. Hydrogen Energy, submitted, 2010.
67. Halabi, M.H., de Croon, M.H.J.M., van der Schaaf, J., Cobden, P.D., Schouten, J.C., Kinetic and structural requirements for a CO_2 adsorbent in sorption enhanced catalytic reforming of methane. Part I: Reaction kinetics and sorbent capacity, Ind. Eng. Chem. Res., submitted, 2010.
68. Halabi, M.H., de Croon, M.H.J.M., van der Schaaf, J., Cobden, P.D., Schouten, J.C., Kinetic and structural requirements for a CO_2 adsorbent in sorption enhanced catalytic reforming of methane. Part II: Bed characteristics, Ind. Eng. Chem. Res., submitted, 2010.
69. Araki, S., Hino, N., Mori, T., Hikazudani, S., Durability of a Ni based monolithic catalyst in the autothermal reforming of biogas, Int. J. Hydrogen Energy, 34 (2009) 4727–4734.

Chapter 6

Mechanistic Aspects of Low Temperature Methane Steam Reforming Over $Rh/Ce_{\alpha}Zr_{1-\alpha}O_2$ Catalyst

This chapter has been published as
M.H. Halabi, M.H.J.M. de Croon, J. van der Schaaf, P.D. Cobden, J.C. Schouten, Low temperature catalytic methane–steam reforming of methane over ceria–zirconia supported rhodium catalyst, Applied Catalysis A, 389, 68–79, 2010.

Abstract

This chapter presents an experimental study of the catalytic steam reforming of methane over newly developed ceria – zirconia supported rhodium as an active candidate catalyst for low temperature sorption enhanced hydrogen production from methane. The kinetic experiments are performed in a tubular fixed bed reactor over a temperature range of 475 to 750 ^{o}C and a total pressure of 1.5 bar in the absence of mass transport limitations. The over all reaction orders in methane and steam are determined to be less than 1 from 475 to 625 ^{o}C. At low temperature, most of the gas product is composed of CO_2 and H_2 due to the pronounced influence of the water–gas shift reaction. At higher temperature and low steam/carbon ratio (S/C), this influence is diminished. Inhibitory effects of H_2, CO, and CO_2 on the methane conversion rates are detected. Temperature–programmed steam reforming experiments over ceria–zirconia support revealed insignificant methane adsorption on the surface from 550 to 725 ^{o}C. Catalyst deactivation and steady state stability over time were examined. A molecular reaction mechanism is

proposed to qualitatively explain the kinetic observations. Two distinct sites are thought to be responsible for the dissociative adsorption of methane and steam on the catalyst and the support surfaces. Methane is dissociatively adsorbed on the rhodium active metal sites and steam is dissociatively adsorbed on the support surface. Surface reactions of carbon containing methane precursors on the interface between the active metal and the support are considered to be the rate determining steps.

6.1 Introduction

Steam reforming is the most vital route to convert CH_4 into H_2 as a green energy carrier. The classical steam reforming process is usually operated in a high temperature range of 700 – 900 ^oC due to the highly endothermic nature of the process [1–4]. The chemical reactions involved in steam reforming of CH_4 are represented as follows:

$$CH_4 + H_2O \leftrightarrow CO + 3H_2 \qquad \Delta H_{298K} = 206.2 \text{ kJ/mol}$$
$$CO + H_2O \leftrightarrow CO_2 + H_2 \qquad \Delta H_{298K} = -41.1 \text{ kJ/mol}$$
$$CH_4 + 2H_2O \leftrightarrow CO_2 + 4H_2 \qquad \Delta H_{298K} = 164.9 \text{ kJ/mol}$$

Water–gas shift and reverse methanation reactions are usually involved with steam reforming reactions over a catalyst at high temperatures (typically higher than 700 ^oC). However, the reverse methanation reaction is thermodynamically a resultant from CH_4 steam reforming and water–gas shift reactions but it is determined to be kinetically independent [1–4].

Ni–based catalyst employing stable inert oxide supports such as Al_2O_3, MgO, and $MgAl_2O_3$ are still commercially used due to the relatively low cost despite of the serious problems of coke formation and relatively low activity compared to noble metals [5]. However, various precious metals such as Ru, Rh, and Pt have been reported to provide high reforming activity and improved resistance towards carbon formation [9–12]. Rh is one of the most active and stable VIII metals (Ni, Ru, Rh, Pt, Pd, Ir) which can catalyze the CH_4 reforming with steam or CO_2 [6, 13–29]. Several studies have been investigating the activity of Rh based catalysts for CH_4 steam reforming over different supports, Rh/Al_2O [13–16], Rh/ZrO_2 [20, 23], Rh/SiO_2 [18, 20, 23–25], and Rh/MgO [12, 18, 20, 26].

Metal catalysts show lower activity in steam reforming when they are supported on inert oxides [15, 29]. It is evident that the reducible metal oxide supports provide high catalyst activity, catalytic and thermal stabilities, and carbon resistance [7, 30–49]. Ceria and metal oxide doped ceria are well-known for their nature to store, release and exchange oxygen within their lattice structure and they were proven to enhance the steam reforming performance in terms of catalytic activity, stability, and low tendency towards carbon formation [7, 30, 31, 40, 50].

Kurungot and Yamaguchi [15] demonstrated an improved performance of $Rh/\gamma Al_2O_3$ doped with CeO_2 in terms of activity and stability comparing to $Rh/\gamma Al_2O_3$ alone. The latter shows a large deactivation as a result of carboneous products or particle agglomeration, which yields a progressive reduction of available active sites. The stability is improved due to the kinetic and oxidative stabilization of the catalyst matrix. Kusakabe et al. [40] studied the activity of a $CeZrO_2$ supported noble metal catalyst to methane steam reforming at 500–800 ^oC. Using 10% Ni loading on the support structure of $Ce_xZr_{1-x}O_2$, they found that the structure of $Ce_{0.15}Zr_{0.85}O_2$ showed the highest CH_4 conversion at 500 – 600^oC and high H_2/CO ratio due to CO oxidation by the water–gas shift reaction.

The catalyst activity was further improved by loading Pt, Ru, and Rh. The highest catalyst activity was obtained for $Rh/Ce_{0.15}Zr_{0.85}O_2$. The reactivities of ceria and ceria doped with Gd and Nb to CH_4 were investigated using temperature programmed reactions and isothermal reaction at 900 ^oC [29]. Ceria showed activity for CH_4 conversion to H_2 and CO with only a small amount of carbon deposition. CH_4 conversion was found to be controlled by the surface reaction of the C-fragments adsorbed molecules leading to CO formation. $Ce_{0.9}Gd_{0.1}O_{2-x}$ was found to have useful activity for methane steam reforming at solid oxide fuel cell operational conditions at 900 ^oC [35]. The authors pointed out that the reaction mechanism is controlled by a slow reaction of methane with oxygen on the $Ce_{0.9}Gd_{0.1}O_{2-x}$ catalyst and a facile reaction between steam and the catalyst to replenish the oxygen. Addition of H_2 was reported to inhibit the reforming rate, and the developed catalyst was extremely resistant to carbon formation. The effect of the Ni metal loading on $CeZrO_2$ support was also examined by Dong et al. [40] to obtain high activity and stability. Temperature–programmed reduction results revealed strong interaction between the support and the metal. Two kinds of active sites are proposed; one for methane adsorption and the other for steam or oxygen. Laosiripojana and Assabumrungrat [7] showed that $Ni/CeZrO_2$ with a Ce/Zr ratio of 3/1 has the best activity for steam reforming and resistance towards carbon formation among the studied samples with different Ce/Zr ratios. The redox reaction on the support between the potential carbon formation compounds and lattice oxygen prevents the formation of carbon species from methane decomposition and Boudouard reactions at high temperature and even at a low inlet S/C ratio of 1. High surface area ceria was developed for catalytic dry reforming [37] and steam reforming [40] of methane using a surfactant assisted approach. Recently, Constantinou and Efstathiou [51] applied $Rh/Ce_{0.14}Zr_{0.81}Mg_{0.05}O_2$ catalyst to phenol steam reforming. They demonstrated better performance in terms of phenol conversion (ca. 90%) and H_2 yield (85%) compared to a commercial Ni-based catalyst.

Despite the large number of kinetic studies found in literature, little agreement can be attained for the reaction mechanism and the corresponding kinetic model for CH_4 steam reforming. This is mainly attributed to the nature of the catalyst and the support used, catalyst particle size, the preparation method, temperature and

pressure ranges, catalyst physical structure, gas composition, and to some extent, the active metal loading. Table 1 presents a comparison between several recent kinetic mechanisms available in literature.

Table 1: A comparison of several steam reforming reaction mechanisms available in literature.

Catalyst	Reaction order in CH_4	Effect of co–species	Experimental conditions	RDS	Ref.
Ni/ZrO_2	1	No negative effect of H_2O	700–1000 °C, 2–40 kPa CH_4 10–70 kPaH_2O 10–70 kPa H_2	CH_4 adsorption	41
Ni/α-Al_2O	~1 at low product concentrations	Positive effect of H_2O	475–550 °C 120–600 kPa	Surface reactions	47
Rh/Al_2O, Rh/ZrO_2	1	No effect of H_2O on order	600–750 °C 5–450 kPa CH_4 5–450kPa H_2O	CH_4 adsorption	16
$Ru/\alpha Al_2O_3$	<1	Negative effect of	450–500 °C	Surface	44
Promoted with Mn oxides	~1	H_2O on order at all temperatures	700–900 °C 100–700 kPa	reactions	
$Ni/MgOAl_2O_3$	<1	Positive effect of H_2O	500–575 °C 300–1000 kPa	Surface reactions	5

$Rh/Ce_\alpha Zr_{1-\alpha}O_2$ is under investigation in our laboratory as a promising catalyst for pure H_2 production with in situ CO_2 capture using sorption–enhanced steam reforming process. The process is determined to be operated at temperature lower than 550 °C in order to maintain a high CO_2 adsorption capacity of the sorbent. Therefore, $Rh/Ce_\alpha Zr_{1-\alpha}O_2$ is selected as an effective catalyst, which provides high reaction rates in low–temperature steam reforming (<550 °C). This is beneficial in terms of energy saving, production rates, and capital investment of the integrated reactor/adsorber. The proper design, simulation, prediction, and optimization of the process performance require a reliable kinetic model. This model must include intrinsic kinetic parameters such as the pre-exponential kinetic factors and the activation energies in addition to the detailed scheme of the involved reactions generated from intrinsic kinetic data over this specific catalyst.

The aim of this chapter is to present a kinetic analysis for the mechanistic aspects of CH_4 steam reforming over $Rh/Ce_\alpha Zr_{1-\alpha}O_2$ in the low temperature range of 475–700 °C. Experimental kinetic results are demonstrated for the steam reforming and water–gas shift reactions over the $Rh/Ce_\alpha Zr_{1-\alpha}O_2$ catalyst and the $Ce_\alpha Zr_{1-\alpha}O_2$ support. The role of the support in steam reforming reactions is illustrated and the influence of gas phase product species on the CH_4 reaction rates is examined. A molecular reaction mechanism is proposed to qualitatively describe the kinetic observations and to serve as a solid basis for the derivation of the intrinsic kinetic model, which is a continuation of this work. Moreover, the catalyst activity, stability, and resistance towards carbon formation are also investigated.

6.2 Experimental

6.2.1 Catalyst preparation

A mixture of commercially available ceria and zirconia supports with a composition ratio of (60:40 wt.%) provided by MEL chemicals UK is gradually heated at a rate of 2 ^{o}C/min up to 900 ^{o}C. The mixture is maintained at that temperature for 6 hrs and then gradually cooled to ambient temperature. The Rh is loaded on the support by dry impregnation with a $Rh(NO_3)_3$ solution to obtain a metal loading of 0.8% on a pre-defined weight of the prepared ceria–zirconia powder. Water is added until liquid volume is equal to the pore volume determined. The solution is added to the powder under constant stirring to gain an even distribution. The wet powder is dried at 80 ^{o}C with continuous stirring. The catalyst is then calcined at 400 ^{o}C at a rate of 2 ^{o}C and kept for 5 hrs at that temperature.

6.2.2 Catalyst characterization

The fresh catalyst is characterized by standard techniques to measure its physical properties. The BET surface area of the catalyst is determined using the N_2 adsorption porosimetry (ASAP 2020 Micromeritics). The metal dispersion ratio on the support is determined by the volumetric H_2 chemisorption uptake in Micromeritics Chemisorb 2750. The analysis procedure is applied according to Wei and Iglesia [16, 52] to accurately determine the Rh dispersion. A catalyst sample of 0.5 g is gradually heated up to 400 ^{o}C in a He gas at a rate of 10 ^{o}C/min for 2 h, followed by evacuation at 400 ^{o}C for 1 h. The sample is then reduced in H_2 gas at 400 ^{o}C for 2 h and calcined at 700 ^{o}C for h. This step is followed by evacuation at 50 ^{o}C for 2 h. After cooling to 30 ^{o}C, H_2 chemisorption isotherm is measured in the range of 15–67 kPa H_2. A back sorption isotherm was also measured after evacuation for 1 h at 30 ^{o}C. The isotherms are extrapolated to zero and the difference is used to measure the H_2 chemisorption uptake. Rh dispersion is then determined assuming a 1:1 stoichiometry between H atom and Rh surface atom. The structure of the mixed oxide $Ce_{\alpha}Zr_{1-\alpha}O_2$ support is examined by X-ray diffraction (XRD). The surface morphology is analyzed using scanning electron microscopy (SEM) and transmission electron microscopy (TEM). The fresh and the spent samples of the metal oxide support and the catalyst exposed to different experimental conditions are analyzed with regard to surface structure, crystallite size, and carbon deposition. The catalyst composition, metal oxidation state, and carbon deposits are tested using X-ray photon spectroscopy (XPS). Table 2 summarizes some properties of the metal oxide support, the fresh catalyst, and the spent catalyst. The spent catalyst has been exposed to several reaction gas compositions up to 750 ^{o}C for more than 100 hours time on stream.

6.2.3 Catalyst pretreatment

The fresh catalyst is pretreated in a reductive environment of a 20% vol. H_2 and 80% vol. N_2 gas mixture before the experiment starts. The catalyst is gradually heated at a rate of 3 ^{o}C/min to 400 ^{o}C using a total N_2 gas flow of 100 nml/min and kept at this temperature for 2 hrs. H_2 gas is then introduced at 400 ^{o}C for 2 hrs. The

catalyst is heated again to 700 °C at a rate of 3 °C/min and this temperature is maintained for 2 hrs.

Table 2: Catalyst properties.

	Value
Average pellet size	300 μm
Rh metal content	0.8 %
BET surface area of the support	85.7 m^2/g
BET surface area of the fresh catalyst	38.8 m^2/g
BET surface area of the spent catalyst	37.2 m^2/g
Pore volume of the catalyst	0.20 cm^3/g
Pore diameter of the catalyst	20.4 nm
Metal dispersion on the fresh catalyst	27.9 %
Metal dispersion on the spent catalyst	27.1 %
Crystallite particle size	3 nm
Ce/Zr composition ratio	0.6/0.4

6.2.4 Experimental setup

The kinetic experiments are performed in a fixed bed tubular rector setup. The reactor is 1.0 m in length and is composed of three zones; two upper – part heating sections and one reaction zone of 19.5 cm in length. The reactor is a quartz tube with an internal diameter of 4.0 mm along the heating and the reaction zones. The temperature is measured along the reactor and controlled in a temperature range of 100–750 °C. Gas flows are controlled by thermal mass flow controllers. Gas flow rates of CH_4, CO, CO_2, and H_2 in a range of 0–50 nml/min are applied, N_2 is used as an inert and a carrier gas in the flow range of 0–500 nml/min. Steam is applied to the system by evaporating distilled water in a static evaporator mixer at 80 °C with a maximum flow rate of 1500 mg/hr. The overall gas mixture contains up to 25% water on a relative humidity basis. The fluctuation in the measured water concentration is within ±7% of the set-point. The total pressure of the reactor is maintained at 1.5 bar by means of a back pressure controller. The process lines are traced at 80 °C and insulated to prevent any condensation of steam. The gas composition is measured at feed and product gas sections using online analysis gas chromatography (GC Varian CP-3800). The kinetic experiments are performed in a gas hourly space velocity (GHSV) range of (80000–229000 h^{-1}).

6.2.5 Experimental procedure

The scope of the kinetic experiments performed in this study includes the following routes:

1. Investigating the dependency of the steam reforming reaction rate on CH_4 and steam partial pressures using 16 mg 0.8% $Rh/Ce_{0.6}Zr_{0.4}O_2$.
2. Investigating the effect of gas product species (H_2, CO, and CO_2) on the steam reforming reaction rate using 16 mg 0.8% $Rh/Ce_{0.6}Zr_{0.4}O_2$.
3. Temperature–programmed steam reforming reaction experiments on the $Ce_{0.6}Zr_{0.4}O_2$ support to investigate the role of the support in this reaction from 550 to 750 °C using 150 mg support loading.

4. Temperature–programmed water–gas shift reaction experiments on the $Ce_{0.6}Zr_{0.4}O_2$ support to investigate the role of the support in this reaction from 400 to 575 ^oC using 150 mg support loading.
5. Temperature–programmed water–gas shift reaction experiments on the 0.8% $Rh/Ce_{0.6}Zr_{0.4}O_2$ catalyst to investigate the reaction relative activity and the product distribution from 100 to 700 ^oC using 150 mg catalyst loading.
6. Activity, stability, and deactivation experiments on the 0.8% $Rh/Ce_{0.6}Zr_{0.4}O_2$ catalyst using 150 mg catalyst loading.

An average size of 300 μm catalyst pellets is used throughout the experiments.

6.3 Results and discussion

3.1 Characterization results

A BET surface area of 85.7 m^2/g is obtained for the fresh support of Ce/Zr ratio of 0.6/0.4 calcined at 400 ^oC. This is in agreement with the values reported by recent studies on ceria–zirconia metal oxides [7, 38]. The surface area was found to increase as the content of Ce increased in the metal oxide. The BET surface area of the catalyst and the Rh metal dispersion were determined to be 38.8 m^2/g and 27.9%, respectively. This is very much in line with the values found in a recent study for Rh/ZrO_2 doped with ceria [45]. The significant drop of the BET surface area between the fresh support and the fresh catalyst is due to the high calcination temperature during the catalyst preparation procedure. The support is calcined at 900^oC before the Rh metal is loaded. The XRD pattern shown in Fig. 1 indicates a dominant presence of the cubic phase in the mixed oxide $Ce_{0.6}Zr_{0.4}O_2$ support of the fresh catalyst. This is expected in light of the XRD patterns for $Rh/Ce_{\alpha}Zr_{1-\alpha}O_2$ catalyst [38, 41]. Rh/ZrO_2 shows a monoclinic phase of the ZrO_2 [45]. The addition or doping with ceria significantly reduces the peak intensity of the monoclinic phase of ZrO_2 and enhances the presence of the tetragonal phase of CeO_2. The cubic phase obtained was also confirmed by previous authors [38, 46].

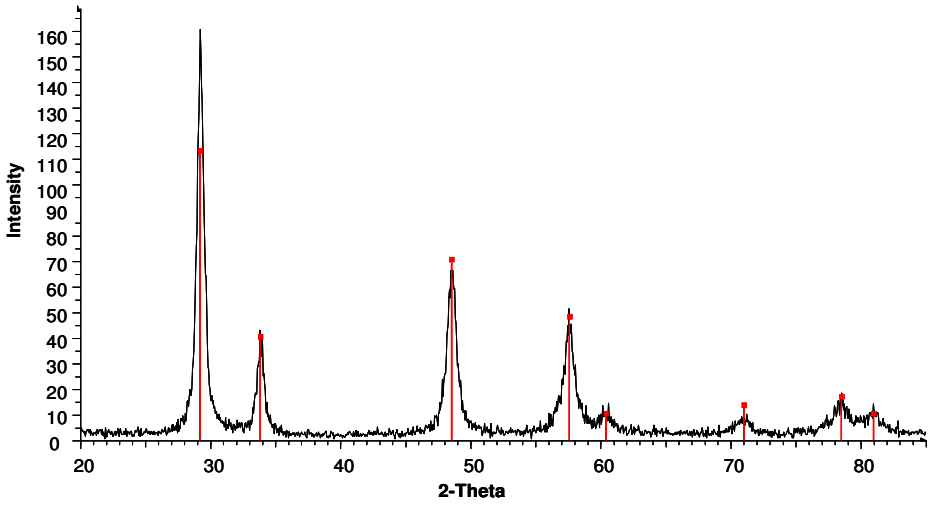

Fig. 1: XRD pattern of the mixed oxide support of the fresh catalyst $Rh/Ce_{0.6}Zr_{0.4}O_2$. Peaks represent the cubic phase structure.

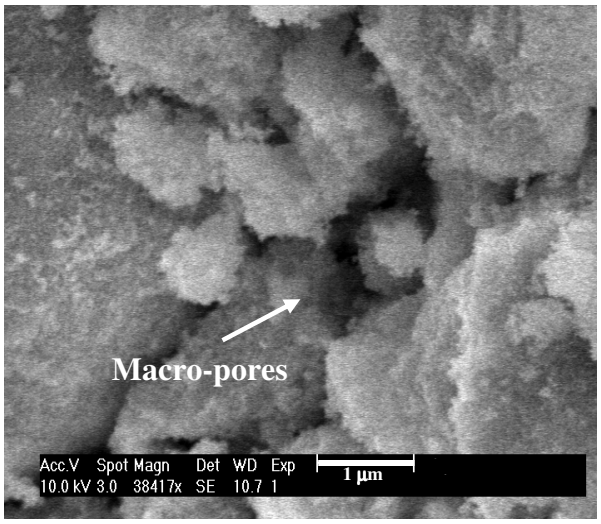

Fig. 2 SEM micrograph of the fresh catalyst.

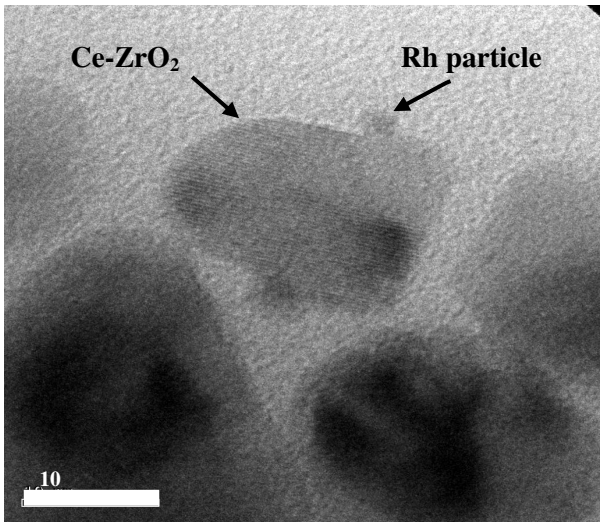

Fig. 3 TEM micrograph of the fresh catalyst.

SEM pictures for the fresh catalyst indicate a uniform morphology of the surface and well-integrated texture. The pellet size is observed to be around 300 µm on average with macro-pores of 0.5 µm on a magnification level of 1 µm surface as given in Fig. 2. The distribution of Rh active metal on the surface was not observable up to 200 nm magnifications. This indicates that the active metal crystallite is well below this size as confirmed by the TEM micrographs. This can be due to a very low metal content and a small metal size or the active metal can be penetrating through the support pores. Fig. 3 shows a TEM micrograph taken on the fresh catalyst with 0.8% Rh. It displays a clear carrier crystallite of a circular – edged rectangular shape with a size of 15 nm. The Rh active metal particle has a size of 3 nm. No crystallite agglomeration was observed on the spent samples by TEM or SEM pictures. This is a proof that sintering is not the cause of catalyst deactivation as it will be discussed later. It was difficult to observe the Rh metal particles on the support from the ex-situ TEM pictures of the spent catalyst. This can be due to oxidation when the sample is exposed to air. However, this situation is also shown by Jakobsen et al. [53]. XPS analysis confirmed the presence of 0.8% Rh and a metal composition of Ce/Zr ratio of 0.6/0.4 in the catalyst according to the preparation method.

6.3.2 Catalyst deactivation and preliminary testing

Several preliminary experiments are performed using different feed gas compositions and catalyst loadings in order to determine a convenient regime in which intrinsic kinetic data can be generated far from steam reforming thermodynamic equilibrium limitation. 16 mg of catalyst loading is used for a deactivation test at a space time of 6 kg_{cat}.s/mol CH_4. A gas flow mixture of 15 nml/min CH_4, 10 nml/min H_2, steam/carbon ratio of 4, and balance N_2 is introduced at the operational temperature and pressure of 550 ^oC and 1.5 bar, respectively. Fig. 4 presents the catalyst deactivation curve over 25 hrs time on stream. The catalyst shows a stable activity of 27% CH_4 conversion at steady state conditions over the time interval. The equilibrium conversion corresponding to these conditions is 84.4%. The initial activity decay of the catalyst within the first 5 hrs can be

attributed to surface restructuring and possible carbon formation. It is well accepted that the major source of catalyst deactivation in steam reforming reactions is carbon formation. Carbon deposition can significantly deactivate the catalyst by blocking the active sites and reducing the interaction with the gas phase reaction species on the surface. However, the following measurements are corrected for the decay. The amount of carbon deposition was measured after the entire set of experiments over a time interval of more than 100 hrs time on stream at different gas compositions. XPS analysis shows a ratio of 6.3 of carbon on the spent catalyst to that on the fresh one.

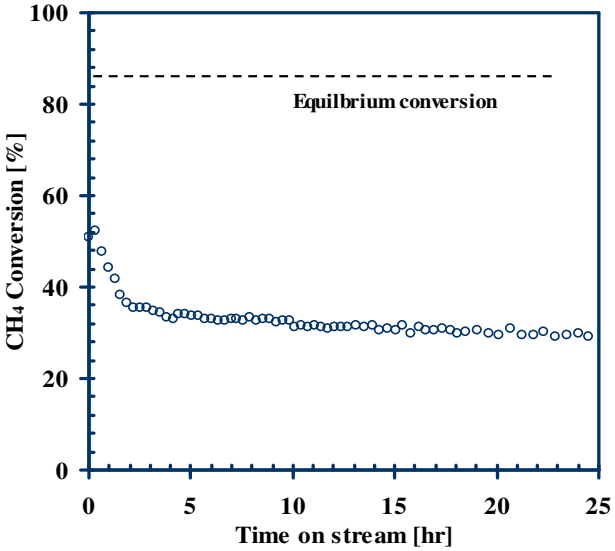

Fig. 4: Catalyst deactivation under gas composition of 15 nml/min CH_4, 10 nml/min H_2, steam/carbon ratio of 4, and balance N_2 at 550°C and 1.5 bar.

This value is somewhat low comparing to other situations where the amount of carbon is high on the spent catalysts [44, 47]. As reported by Dong et al. [39] over Ni catalyst, carbon formation occurs at 500–700 °C at the interface between a Ni crystal and the metal support, creating a large amount of fibrous carbon that ruins the catalyst activity. It is thought that Rh metal particles loaded on ceria–zirconia exhibit kink sites at the interface between the metal and the support [20]. Thereby small carbon formation can block these sites and retard CH_4 activation and accordingly deactivating the catalyst. According to the thermodynamic analysis of the data, CH_4 decomposition and Boudouard reactions are most likely to be the major source for carbon producing reactions. In addition to coke formation, the change of the catalyst oxidation state, or the support oxidation state, sintering or aggregation of the particles can also result in a significant drop of the catalyst activity [11]. No crystallite agglomeration or particle aggregation could be observed in the TEM and SEM micrographs. This denotes that metal sintering on the surface is not evident phenomenon for this catalyst using the applied conditions.

Preliminary experiments are conducted on the catalyst to guarantee that interfacial and intraparticle mass transport limitations are not predominant. The total gas flow rate of the reaction mixture was varied from 20 to 100 nml/min at two temperatures of 475 and 575 °C at constant residence time of 11.6 kg_{cat}.s/mol CH_4 fed. The gas

feed supply was adjusted to provide the same residence time with respect to methane at constant S/C ratio of 2 at every total flow rate. Fig. 5 shows that beyond a total gas flowrate of 80 nml/min, the CH_4 conversion is almost steady. Therefore, it can be said that the CH_4 reforming rate is independent of total flow velocity beyond 80 nml/min, which suggests the absence of external mass transport limitations.

Steam reforming reaction is also performed using 4 pellet sizes of 150, 300, 450, and 600 µm. The operational conditions used are an S/C ratio of 4 and a space time of 6.0kg_{cat}s/mol CH_4 at 550 °C and 1.5 bar. CH_4 reforming rates are insignificantly changing when a pellet size smaller than 300 µm is used. This suggests that internal mass transport limitations can be ignored in this case. During the proceeding experiments, a total gas flowrate of 100 nml/min and an average catalyst pellet size of 300 µm are used.

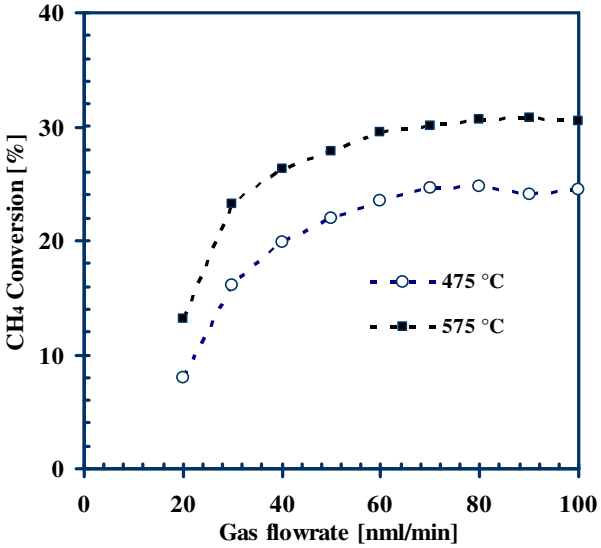

Fig. 5: Effect of total gas flow on methane conversion at a constant residence time of 11.6 kg_{cat}.s/mol CH_4, S/C ratio of 2, 1.5 bar, and at two temperatures of 475 and 575 °C.

6.3.3 Reaction orders in methane and steam

Kinetic experiments are performed in an operational regime of low conversion (typically less than 20%) and far from equilibrium conditions to prevent significant influence of gas products in backward reactions. The observed reaction rates are generated in a differential manner and corrected for the approach to equilibrium according to equation 1 and 2 to obtain.

$$r_{f,j} = \frac{r_{obs,j}}{(1 - V_j)} \tag{1}$$

$$V_j = \left(\Pi_i p_i^{\nu_i}\right)_j / K_{eq_j} \tag{2}$$

Thus, the analysis of intrinsic kinetic data of forward reaction rates is assured. Although the aim of this work is not to derive intrinsic kinetic parameters, but to focus on the qualitative trends of the mechanistic aspects for the steam reforming

reaction. However, comprehensive analysis of the corresponding kinetic model and rate laws is provided in chapter 7.

The dependency of the CH_4 reforming rate on the CH_4 partial pressure is examined at a total pressure of 1.5 bar in a temperature range of 475 to 625 ^oC as shown in Fig. 6. CH_4 partial pressure is varied from 3.45 to 12.42 kPa at a constant steam partial pressure of 22.37 kPa, and balance N_2. CH_4 reaction rates present a non-linear dependency on the CH_4 partial pressure with a temperature dependant reaction order of less than 1 ranging from 0.60 at 475 ^oC to 0.72 at 625 ^oC. A reaction order of less than 1 with respect to CH_4 implies that the steam reforming reaction is not governed by the slow activation of CH_4 molecules on the catalyst surface. Analysis of the product compositions shows that the amount of CO in the gas product was negligible at low temperature of 475 and 525 ^oC, (see Fig. 7). This suggests a strong activity of the CO oxidation via the water–gas shift reaction. The ratio of $CO/CO+CO_2$ and the CO_2 selectivity (defined as mol. CO_2 produced/ mol. CH_4 converted) show that at high temperatures of 575 and 625 ^oC and low S/C ratio, the water–gas shift activity is decreasing. At constant high temperature, the CO_2 selectivity values obtained are decreasing and the $CO/CO+CO_2$ ratio is increasing as the S/C ratio is reduced.

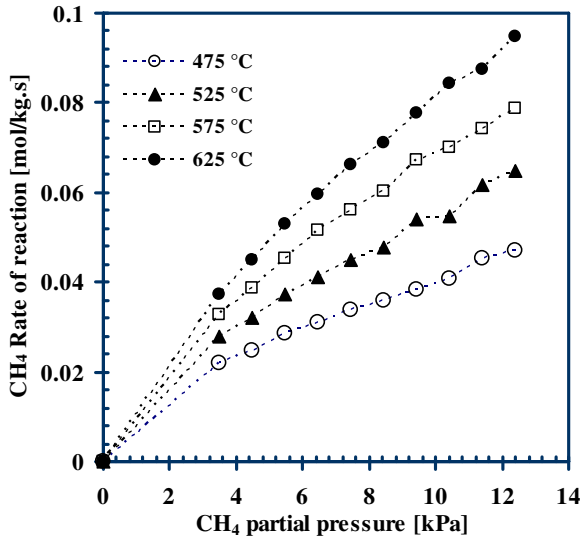

Fig. 6 CH_4 reaction rates as a function of CH_4 partial pressure at different temperatures. Feed composition is P_{CH4} = 3.48–12.42 kPa, P_{H2O} = 22.37 kPa, balance N_2.

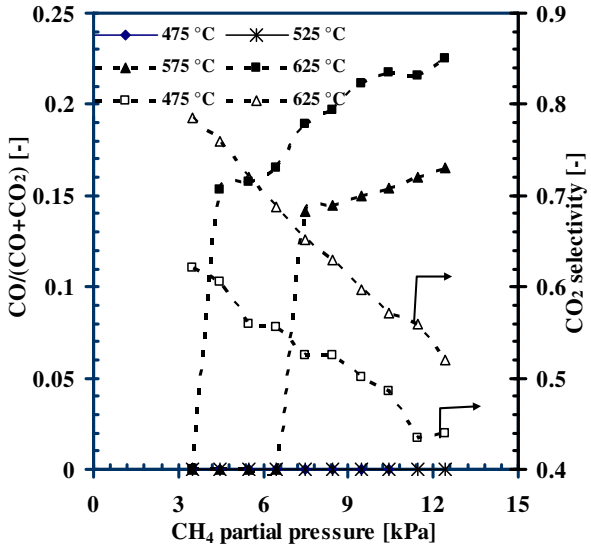

Fig. 7 $CO/CO+CO_2$ ratio and CO_2 selectivity as a function of CH_4 partial pressure at different temperatures. Feed composition is P_{CH4} = 3.48–12.42 kPa, P_{H2O} = 22.37 kPa, balance N_2.

The CH_4 reaction rates are studied with respect to the steam partial pressure at a constant CH_4 partial pressure of 3 kPa and a total pressure of 1.5 bar. The steam partial pressure is varied at two temperatures of 475 and 575 ^oC corresponding to a S/C ratio from 0 to 6 as given in Fig. 8. The reforming rates exhibit a nonlinear positive dependency on the steam partial pressure with a reaction order of less than 1 (0.28 at 475 ^oC to 0.38 at 575 ^oC). The data does not show maximum conversion rates attributed to an optimum distribution of steam and CH_4 coverages on the

catalyst surface. Thus, it is expected that CH_4 and steam do not undergo any competition in adsorbing on the same catalyst active sites at the studied conditions of temperature and composition. More competition between CH_4 and steam is thought to take place at high temperature such as 700 ^oC and at low CH_4 coverages as shown in other studies [7]. Therefore, identical experiments are conducted at 700 ^oC and relatively low CH_4 partial pressure in order to seek for a maximum reaction rate as a function of steam partial pressure (or S/C ratio). However, higher temperatures are not of interest for this study. At high CH_4 partial pressure, the coverage of CH_4 molecules on the catalyst surface is expected to be sufficiently high, which masks any possible competition with steam. It was assumed that two distinct sites are employed for CH_4 and water adsorption. Further investigation of CH_4 activation on the support as will justify this assumption as given later in this chapter.The reaction orders in CH_4 and steam in the presence of H_2 are also examined. The addition of H_2 to the steam reforming gas mixture is reported to have a contradictory effect on the CH_4 conversion and reaction rates [9, 11, 47, 51]. The reaction order in CH_4 partial pressure is reduced from 0.6 to 0.54 at 475 ^oC and from 0.72 to 0.69 at 625 ^oC in the presence of 3.3 kPa H_2. The selectivity to $CO/(CO+CO_2)$ (data is not shown) is slightly increased indicating less selectivity to the water gas shift reaction. The same trend is observed for the insertion of H_2 in steam reforming experiments with varying steam partial pressures. The reaction order in steam partial pressure is reduced and shows a non-monotonic dependency reaching stable conversion rates at a S/C ratios higher than 1.5.

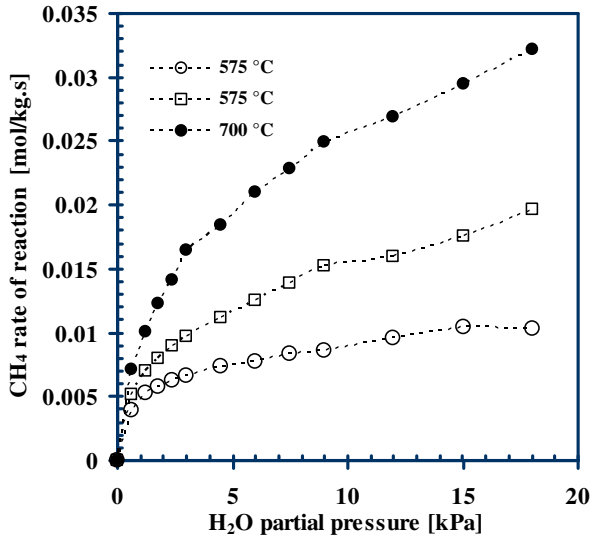

Fig. 8 CH_4 reaction rates as a function of H_2O partial pressure at different temperatures. Feed composition is P_{H2O} = 0–8 kPa, P_{CH4} = 3.0 kPa, balance N_2.

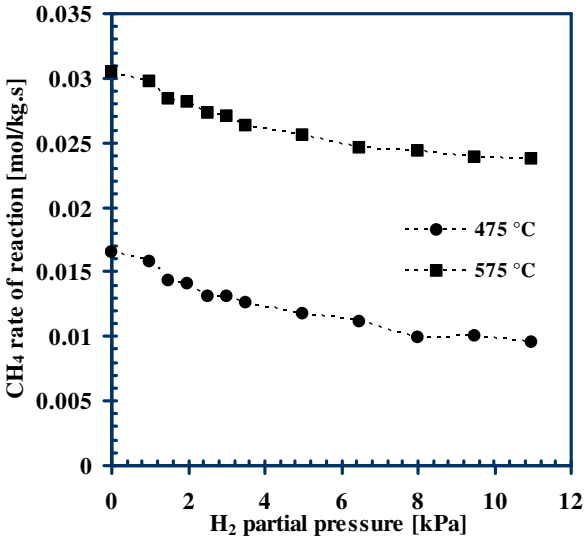

Fig. 9 CH_4 reaction rates as a function of H_2 partial pressure at different temperatures. Feed composition is P_{H2} = 0–11 kPa, P_{CH4} = 5.25 kPa, P_{H2O} = 21 kPa, balance N_2.

6.3.4 Inhibition by H_2, CO, and CO_2

Contradictory observations for effect of H_2 on steam reforming reactions rates are illustrated in literature. Wei and Iglesia [16] demonstrated that neither H_2 nor any other gas species (H_2O, CO, and CO_2) has an effect on CH_4 reforming rates over Rh. A negative effect on ceria catalyst at high temperature of 900 ^oC is determined

by Ramirez-Cabrera et al. [34]. Dicks et al. [43] reported a weak positive effect of H_2 addition on Ni/ZrO_2 catalyst at high temperatures of 700 to 1000 ^oC. Xu and Froment [5] showed that H_2 increases the reaction rates due to prevention of over oxidation of the Ni particles. A positive effect of H_2 is also reported at low partial pressure due to inhibition of carbon formation via CH_4 cracking and Boudouard reactions at high temperatures on Ni/Al_2O_3 [47] and on $Ni/CeZrO_2$ [7]. A negative effect is reported at high partial pressure due to the promotion of the reverse water–gas shift and methanation reactions [7, 47].

The CH_4 reforming rates versus H_2 partial pressure are plotted in Fig. 9 at a constant CH_4 partial pressure of 5.25 kPa and a S/C ratio of 4 at 475 and 575 ^oC. H_2 shows an inhibitory effect on the CH_4 conversion and the reaction rates at all examined conditions. The CH_4 reaction rate has a negative order in H_2 partial pressure of - 0.21 and - 0.1 at 475 and 575 ^oC, respectively. This may be explained by the fact that H_2 reduces the oxidation state of ceria leading to less steam dissociation on the support. In addition to that, H_2 can suppress the sequential loss of H from CH_4 dissociation on the catalyst surface, resulting in lower reforming rates. This inhibitory effect is diminished at high temperatures due to weakened adsorption, as can be seen from the reaction orders. However, the ratio of $CO/(CO+CO_2)$ in the gas product was negligible suggesting that a high impact of the water–gas shift is still achieved even at high H_2 partial pressures.

Fig. 10 presents the CH_4 reforming rates as a function of CO partial pressure at identical conditions as applied in the H_2 case. Both the CH_4 conversion and the reaction rates are reduced due to CO addition to the steam reforming gas mixture. Negative reaction orders of -0.23 and -0.16 are determined in CO partial pressure at 475 and 575 ^oC, respectively. The gas product composition shows an increasing high H_2 yield as CO partial pressure increases. This is explained by the promoted selectivity towards the water–gas shift reaction at the studied conditions. Apparently, CO may also be adsorbed on Rh sites and thus competes with CH_4. Thus, lower CH_4 dissociation rates followed by lower surface reactions between the carbon intermediates and the interface lattice oxygen are achieved. This eventually results in lower CH_4 conversion and reaction rates. This conclusion is envisaged by the results obtained from temperature–programmed water–gas shift experiments on the catalyst as can be seen later in this chapter. This inhibition can be also explained as CO reduces the oxidation state of ceria leading to less supply of the lattice oxygen provided by H_2O dissociation on ceria.

In CH_4 steam reforming, it is agreed that CH_4 adsorption on Rh causes initial formation of CH_x fragments followed by H_2 and CO formation and consecutive oxidation of CO. CO can be oxidized on a Rh surface much easier than H_2 leading to competition with CH_4 on the surface [6, 15, 48]. The consecutive oxidation of H_2 is less favorable owing to the comparatively higher activation energy [15]. This explains the slightly stronger negative inhibition of the reaction by CO than by H_2.

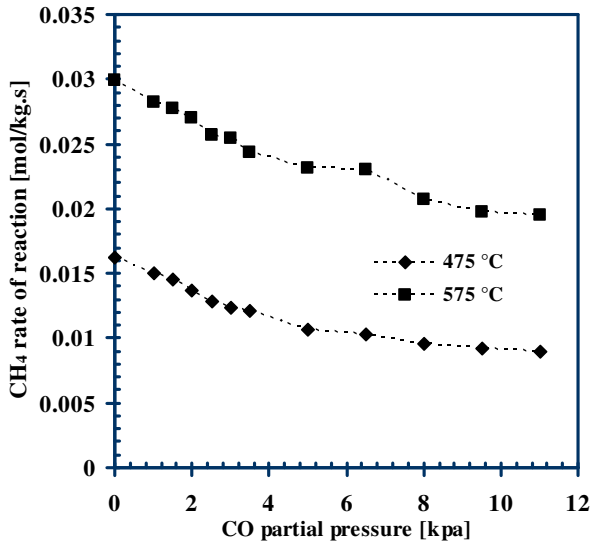

Fig. 10 CH_4 reaction rates as a function of CO partial pressure at different temperatures. Feed composition is P_{CO} = 0–11 kPa, P_{CH4} = 5.25 kPa, P_{H2O} = 21 kPa, balance N_2.

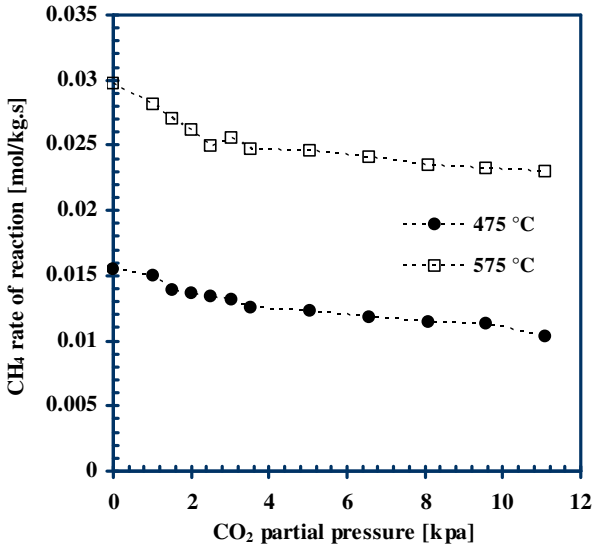

Fig. 11 CH_4 reaction rates as a function of CO_2 partial pressure at different temperatures. Feed composition is P_{CO2} = 0–11 kPa, P_{CH4} = 5.25 kPa, P_{H2O} = 21 kPa, balance N_2.

The influence of the CO_2 partial pressure on the steam reforming rates is demonstrated Fig. 11. The inhibitory effect due to CO_2 partial pressure on reaction rates is less strong than that caused by H_2 and CO as can be observed from the negative reaction orders (-0.14 at 475 and -0.08 at 575 ^oC, respectively). The amount of CO present in the product at 475 ^oC was negligible, indicating high conversion of CO by the water–gas shift reaction. At a higher temperature of 575 ^oC the ratio of $CO/(CO+CO_2)$ has detectable values as CO_2 partial pressure increases above 6.6 kPa. If CO_2 is chemisorbed on Rh it may reduce the oxidation rate of carbon intermediates produced on Rh and the sequent CO oxidation leading to lower steam reforming and water–gas shift reaction rates. CO_2 is also expected to compete with steam in adsorption on the ceria support. However, its activation on ceria is less pronounced due to the fact that ceria has a very strong tendency for H_2O dissociation [31, 33–37].

All reaction orders with respect to the examined key components and the feed composition are listed in Table 3.

6.3.5 Temperature–programmed experiments

Using an active metal catalyst as Rh supported on a reaction-involved surface as Ce-ZrO_2, a set of possible reactions on the active metal and the support can be assumed. These reactions are listed in Table 4. In steam reforming over a Rh catalyst, it is well perceived that the reaction occurs due to CH_4 and steam adsorption on vacant catalyst active sites (reactions 1 and 2) [5, 39, 45, 47] and subsequent surface reactions between the carbon containing species produced from CH_4 activation with the adsorbed oxygen produced from steam adsorption, yielding CO and H_2 as primary products (reaction 3).

Using a ceria catalyst or a ceria supported catalyst, CH_4 can react over ceria to produce a syngas mixture of H_2 and CO with a ratio of 2 [7, 30–32].The reduced ceria CeO_{2-n} may also react with CO_2 and steam to produce CO and H_2, respectively according to reactions 4, 5, and 6. Several studies have been performed on CH_4 activation and steam reforming over ceria but at high temperature of 900 ^oC [7, 33–38, 40].

Table 3: Reaction orders in terms of key components at different temperatures and a total pressure of 1.5 bar.

Key component	T [^oC]	Co-reactant species	Reaction order in key component
Methane (3.48–12.42 kPa)	475	H_2O (22.37 kPa)	0.60 ± 0.02
		H_2O (22.37 kPa), H_2 (3.3 kPa)	0.54 ± 0.02
	525	H_2O (22.37 kPa)	0.66 ± 0.02
		H_2O (22.37 kPa), H_2 (3.3 kPa)	0.59 ± 0.01
	575	H_2O (22.37 kPa)	0.69 ± 0.01
		H_2O (22.37 kPa), H_2 (3.3 kPa)	0.62 ± 0.02
	625	H_2O (22.37 kPa)	0.72 ± 0.01
		H_2O (22.37 kPa), H_2 (3.3 kPa)	0.69 ± 0.02
Steam (0.6–18 kPa)	475	CH_4 (3.0 kPa)	0.28 ± 0.01
		CH_4 (3.0 kPa), H_2 (2.85 kPa)	0.26 ± 0.02 at S/C <1.5, 0.21 ± 0.03 at S/C>1.5
	575	CH_4 (3.0 kPa)	0.38 ± 0.01
		CH_4 (3.0 kPa), H_2 (2.85 kPa)	0.29 ± 0.01 at S/C <1.5, 0.21 ± 0.02 at S/C>1.5
	700	CH_4 (3.0 kPa)	0.43 ± 0.01
		CH_4 (3.0 kPa), H_2 (2.85 kPa)	0.38 ± 0.04 at S/C <1.5, 0.18 ± 0.04 at S/C>1.5
Hydrogen (0–11 kPa)	475	CH_4 (5.25 kPa), H_2O(21.0 kPa)	-0.21 ± 0.01
	575	CH_4 (5.25 kPa), H_2O(21.0 kPa)	-0.10 ± 0.01
Carbon monoxide (0–11 kPa)	475	CH_4 (5.25 kPa), H_2O(21.0 kPa)	-0.23 ± 0.03
	575	CH_4 (5.25 kPa), H_2O(21.0 kPa)	-0.16 ± 0.01
Carbon dioxide (0–11 kPa)	475	CH_4 (5.25 kPa), H_2O(21.0 kPa)	-0.14 ± 0.01
	575	CH_4 (5.25 kPa), H_2O(21.0 kPa)	-0.08 ± 0.01

Table 4. Possible reactions on $Rh/Ce_\alpha Zr_{1-\alpha}O_2$ catalyst surface.

1. Reactions on Rh surface, *l* is a vacant active site:	
$CH_4 + xl \leftrightarrow CH_{n-x}\text{-}l + (4\text{-}n)/2H_2$	1
$H_2O + l \leftrightarrow O\text{-}l + H_2$	2
$CH_{n-x}\text{-}l + O\text{-}l \leftrightarrow CO + (n/2)H_2 + (x+1)l$	3
2. Reactions on Ce-ZrO_2 support:	
$CeO_2 + nCH_4 \rightarrow CeO_{2-n} + nCO + 2nH_2$	4
$CeO_{2-n} + nCO_2 \leftrightarrow CeO_2 + nCO$	5
$CeO_{2-n} + nH_2O \leftrightarrow CeO_2 + nH_2$	6

In order to investigate the role of ceria support in CH_4 steam reforming in this study, temperature–programmed steam reforming experiments are performed on the $Ce_{0.6}Zr_{0.4}O_2$ support over a relatively low temperature range from 550 to 750 ^oC.Water–gas shift experiments are also conducted at temperatures from 400 to 575 ^oC.

Fig. 12 demonstrates the experimental results of steam reforming at steady state conditions over 150 mg $Ce_{0.6}Zr_{0.4}O_2$ support. Discrete temperature intervals of 25 ^oC are maintained constant for 30 minutes until steady state values are assured. The gas feed is composed of CH_4 partial pressure of 7 kPa, S/C ratio of 4, H_2 partial pressure of 4.5 kPa, and balance N_2 at a total pressure of 1.5 bar. The figure shows CH_4 conversion obtained is less than 5% at temperatures lower than 700 ^oC. This is due to the difficult chemisorption of CH_4 on ceria at this low temperature range. A similar experiment is performed over an identical support loaded with 0.8% Rh. The conversion obtained at the lowest temperate of 550 ^oC was 82%. Therefore, it is guaranteed that CH_4 is not adsorbed on the $Ce_{0.6}Zr_{0.4}O_2$ support in low temperature operation (475 – 700 ^oC).

Temperature–programmed water–gas shift experiments are conducted using an identical loading of the $Ce_{0.6}Zr_{0.4}O_2$ support in the temperature range of 400 to 575 ^oC. Gas feed is composed of a CO partial pressure of 7.95 kPa, a steam partial pressure of 31.8 kPa, and balance N_2 at a total pressure of 1.5 bar. Fig. 13 shows that the ceria support is relatively active for water–gas shift reaction at the studied range of temperatures. The CO conversion approaches 35% at 575 ^oC. Thus, an important conclusion can be made here that ceria is active for CO adsorption and the role of the support in water–gas shift reaction promotion may not be ignored.

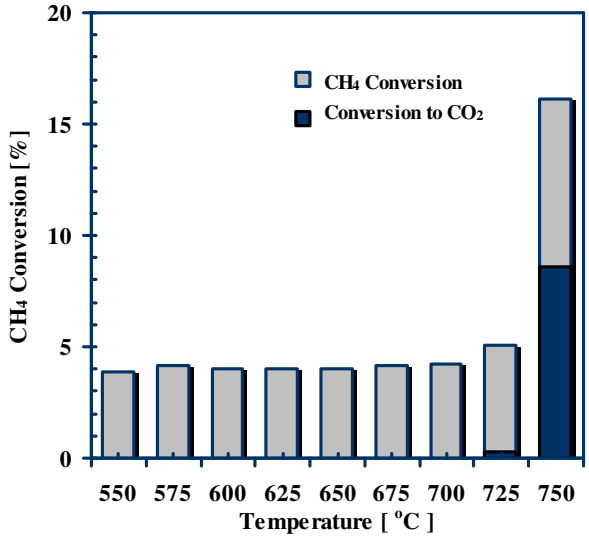

Fig. 12 Temperature programmed CH_4 steam reforming over 150 mg $Ce_{0.6}Zr_{0.4}O_2$ support. Total gas flow is 100 nm/min, P_{CH4} = 7 kPa, P_{H2O} = 28 kpa, P_{H2} = 4.5 kPa.

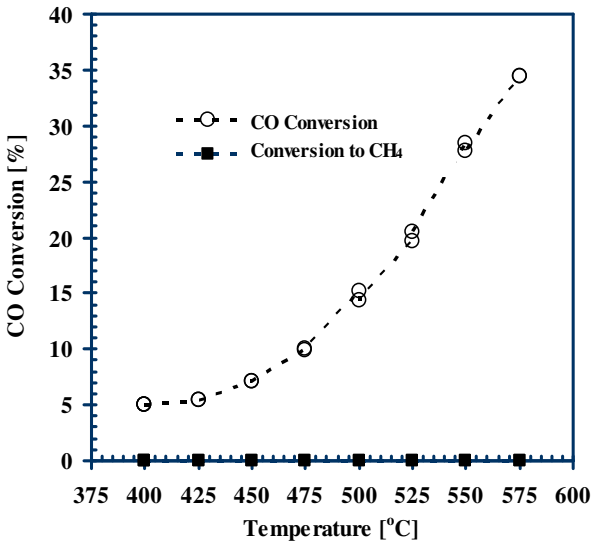

Fig. 13 Temperature programmed water-gas shift over 150 mg $Ce_{0.6}Zr_{0.4}O_2$ support. Total gas flow is 100 nm/min, P_{CO} = 7.95 kPa, P_{H2O} = 31.8 kPa.

To elucidate the extent of activity of the water–gas shift in steam reforming reactions over the temperature range of 475 – 700 ^oC, temperature–programmed

water–gas shift experiment is performed using 150 mg 0.8% $Rh/Ce_{0.6}Zr_{0.4}O_2$ catalyst. An identical gas composition is used as in the $Ce_{0.6}Zr_{0.4}O_2$ support experiment in Fig. 12. The temperature is ramped from 100 to 725 ^oC and the experimental results are plotted in Fig. 14.

The figure shows that the activity of the water–gas shift is boosted as the temperature increases up to 425 ^oC. At this temperature, a maximum CO conversion of 85.6 % is attained as a result of the water–gas shift reaction and the associated reverse steam reforming reaction (methanation reaction). Thereafter, CO conversion is almost in line with the thermodynamic values at high temperatures above 700 ^oC. The figure shows that the rates of the reverse water–gas shift and methanation reactions initiate at 325 ^oC and reach insignificant values at 575 ^oC. A maximum value for CO converted to CH_4 according to methanation reactions is determined to be 9.6% at 425 ^oC.

This temperature–based window of activity for the methanation reaction can also be seen in Fig. 15. The ratio of H_2/CO_2 produced is 1 at temperatures lower than 300 ^oC and close to 1 at temperatures higher than 700 ^oC indicating the dominance of the water–gas shift reaction only. Between these two temperatures, the ratio is less than 1 which implies that H_2 is involved in reverse steam reforming reaction (methanation) with CO.

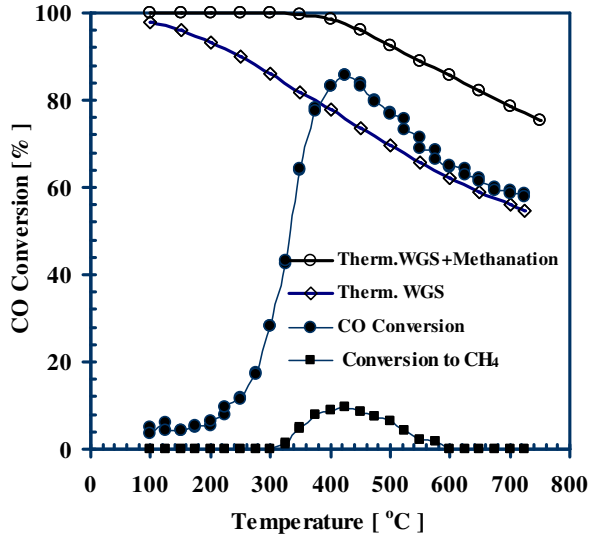

Fig. 14 Temperature programmed water gas shift over 150 mg $Rh/Ce_{0.6}Zr_{0.4}O_2$. Total gas flow is 100 nm/min, P_{CO} = 7.95 kPa, P_{H2O} = 31.8 kPa.

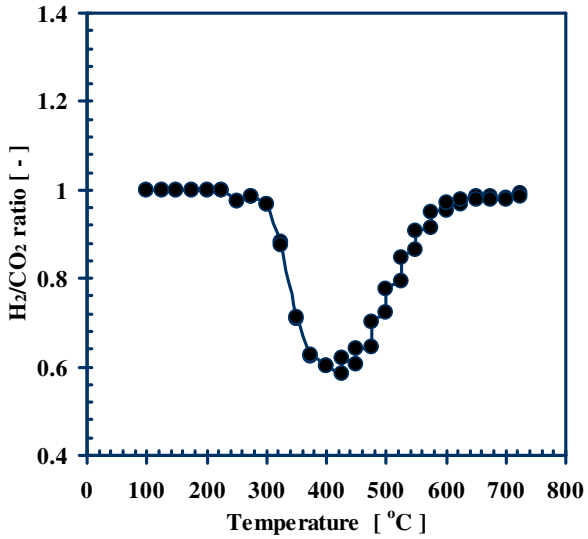

Fig. 15 Selectivity to methanation and reverse water gas shift as a function of temperature in water gas shift over $Rh/Ce_{0.6}Zr_{0.4}O_2$.

6.3.6 Catalytic activity, stability, and WGS selectivity

The performance of the catalyst is assessed in terms of long term activity and stability over more than 25 hrs time on stream. Table 5 illustrates several kinetic observations in the long term steady state conditions at different catalyst to molar CH_4 feed rate ratio W/F (kg_{cat}.s/mol CH_4).

Table 5: Catalyst activity and stability on long-term run for more than 25 hrs time on stream at different catalyst space times.

Space time, kgs/mol CH_4	Conversion, [%]	H_2 yield [mol/mol]	H_2/CO [mol/mol]	CO/(CO+CO_2) [mol/mol]	A_{SA} reduction, [%]	Deactivation ratio[a], [%]
6	27	2[b], 1	39[b], 24.5	0.11[b], 0.165	4.3	11.6[c]
15	56	2.3	6.62	0.245	1.6	5.1
27	74	2.7	11.3	0.252	1.1	2
53	80	3	15	0.28	1.1	2

[a]Catalyst activity after 100 hrs/catalyst activity after 5 hrs.
[b]Values are measured in the first 12 hrs of catalyst deactivation.
[c]Catalyst activity after 25 hrs/catalyst activity after 10 hrs.

The samples are initially tested at 550°C and 1.5 bar using a gas composition of 15 nml/min CH_4, 10 nml/min H_2, S/C ratio of 4, and balance N_2. The samples are further exposed to different gas compositions and temperatures.

During the catalyst deactivation at a low space time of 6 kg_{cat}.s/mol, the fresh catalyst provides relatively high reaction rates of about 0.034 mol/kg.s. This promotes CH_4 conversion via steam reforming and CO oxidation in the water–gas shift reaction. The high initial activity exhibits a high H_2 yield of 2, a high H_2/CO ratio of 39 and a low CO/CO+CO_2 ratio of 0.11. After the first 12 hrs, the catalyst reaches a stable activity of 27% CH_4 conversion with slow deactivation. The deactivated catalyst now shows lower reaction rates of 0.01 mol/kg.s. As a result, a lower H_2 yield of 1, a H_2/CO of 24.5, and a higher CO/CO+CO_2 ratio of 0.165 are obtained. The spent catalyst has a reduced surface area and a deactivation ratio of 5.7% and 11.6%, respectively. However, during the deactivation period a small amount of carbon was produced.

It is expected that carbon is deposited at the kink sites of Rh at the metal – support interface. Thus, the small amount of carbon detected by XPS can block the active sites in charge of CH_4 adsorption and accordingly reduce the conversion activity. At high methane conversion using higher space times, the deactivation rate is quite low. Therefore, a change over time in the H_2 yield and CO/CO+CO_2 ratios could not be observed. The catalyst sample at space time of 15 kg_{cat}.s/mol is further exposed to low S/C ratio of 1 in a temperature range of 475–700 °C. The catalyst maintained a stable activity of 56% conversion over a test time interval of 10 hrs. It showed excellent stability of a 5.1% decay ratio and 1.6% surface area reduction and an excellent resistance towards carbon formation. All tested samples deactivated at high space times (27 and 53 kg_{cat}.s/mol) show insignificant loss of surface area and activity over 100 hrs time on stream.

Catalytic activity and stability are also measured over 150 mg catalyst at 550 and 700 °C and at different gas compositions (15 nml/min CH_4, S/C ratio of 4, balance N_2, and 10 nml/min H_2, CO, or CO_2), see Table 6. The catalyst shows the highest conversion of 81.2% and 95.2% at 550 and 700 °C, respectively when CH_4 and steam are the only reactants in the gas feed. Lower conversions are achieved due to the co-feeding of any of the product species. This is a result of the promotion of the reverse water gas shift and the methanation reactions.

The highest H_2 yield obtained from these gas compositions reaches 3.5 when CO is fed at 700°C. The influence of CO on the CH_4 conversion at high temperature is apparently reduced, while more H_2 is still produced. This observation is explained by the fact that CO can retard CH_4 adsorption on the Rh surface leading to lower reforming rates and lower conversion. This inhibition is diminished when the temperature increases to 700°C. Nonetheless, CO oxidation to generate H_2 becomes more prominent on the ceria support. Therefore, high H_2 yield is achieved as a net effect of more CH_4 converted to H_2 in steam reforming at high temperature on Rh and more CO converted to H_2 in the water–gas shift on the ceria surface.

Table 6: Catalyst activity and selectivity to water–gas shift over 6 hrs steady state time interval at different gas composition and two different temperatures.

	T [°C]	Conversion, [%]	H_2 yield [mol/mol]	CO/(CO+CO_2) [mol/mol]	H_2/CO [mol/mol]	H_2/CO_2 [mol/mol]
CH_4, H_2O	550	81.2	2.98	0.24	15.6	4.84
	700	95.2	3.35	0.45	7.58	6.13
CH_4,H_2O, H_2	550	74	2.63	0.23	15.58	4.74
	700	94.2	3.19	0.48	8.33	7.59
CH_4,H_2O, CO	550	65.7	2.85	0.23	9.87	2.94
	700	91.7	3.5	0.48	4.66	4.26
CH_4,H_2O, CO_2	550	76	2.66	0.19	10.2	6.08
	700	90.8	2.98	0.37	5.29	10.1
CH_4, CO_2	550	41.8	0.84	0.64	0.89	1.58
	700	-	-	-	-	-

The catalytic selectivity towards water–gas shift is also studied at different S/C ratio, constant CH_4 partial pressure of 3 kPa and balance N_2 at different temperatures. Fig. 16 shows the composition distribution of CO and CO_2 in the product as well as the CO/(CO+CO_2) ratios against the S/C ratios at 600 and 700 °C. Production of CO is governed by the steam reforming reaction at a low S/C ratio smaller than 1.5.

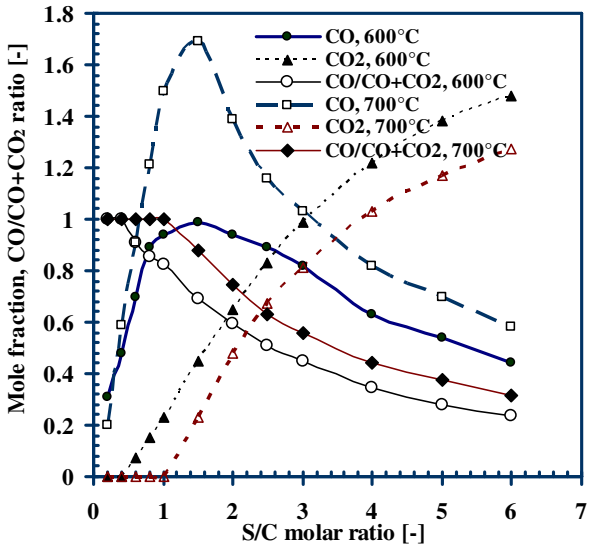

Fig. 16 Selectivity to water gas shift as a function of temperature and S/C ratio over 150 mg $Rh/Ce_{0.6}Zr_{0.4}O_2$. Total gas flow is 100 nm/min, P_{CH4} = 3 kPa, balance N_2.

CO mole fraction increases as S/C ratio is raised until it reaches a maximum at a S/C ratio of 1.5. A descending curve beyond this ratio indicates a rising impact of the water–gas shift reaction for CO_2 production. At low S/C ratio less than 1 and a high temperature of 700 ^oC, the water–gas shift has hardly any impact for CO_2 production. The selectivity to CO_2 via CO oxidation in the water–gas shift reaction is enhanced at higher S/C ratios and lower temperature of 600 ^oC. This is also depicted in the $CO/(CO+CO_2)$ ratio where lower values refer to high water–gas shift selectivity.

The tested catalyst samples demonstrate excellent stability and resistance towards carbon formation at the studied conditions even at a low S/C ratio less than 1. This feature is due to the specific structural composition of the $Rh/Ce_{0.6}Zr_{0.4}O_2$ catalyst. The use of noble metals such as Rh can substantially suppress carbon formation due to a smaller dissolution of carbon into these metals [44].

Ceria is known for its unique properties to improve the (i) thermal and structural stability of the support, (ii) the oxygen storage and release capacities, (iii) the oxidative stabilization of the noble metal, (iv) the metal dispersion on the support surface, (v) the reduction of carbon formation on the surface [7, 15, 41, 42]. These properties are due to the fact that both Ce^{+3} and Ce^{+4} are stable, allowing the oxide to shift from CeO_2 to CeO_{2-x} [19–30] The lattice oxygen released during ceria reduction can react with CH_4 and CO under rich conditions.

The addition of zirconia to ceria has been found to enhance the oxygen storage capacity of ceria and its redox properties [33, 53–55]. This is attributed to the high degree of mobilization of O^{2-} inside the fluorite lattice, therefore, enhanced reducibility of cerium (IV) in $CeZrO_2$, and high oxygen storage capacity of ceria [7]. Thus, the possible carbon producing reactions can also be diminished due to the redox reaction of the carbonaceous species formed on the Rh surface from CH_4 dissociation with oxygen spill over from the ceria. The simultaneous supply of lattice oxygen from steam can further reduce carbon formation.

6.4 Proposed reaction mechanism

The results obtained from the kinetic experiments and the temperature–programmed experiments on the catalyst and the support can elucidate major mechanistic aspects of the steam reforming reactions over the $Rh/Ce_{0.6}Zr_{0.4}O_2$ catalyst at low temperatures (475–700 ^oC). It is experimentally confirmed that no competition between steam and CH_4 in adsorption on the catalyst surface at a temperature range of 475 up to 700 ^oC even at low CH_4 partial pressure. This conclusion is made based on the fact that there is no specific S/C ratio was determined to provide a maximum conversion at optimum distribution between the reactants according to the volcano plot.

Thus, we may assume that two distinct active sites on the catalyst surface are in charge of CH_4 and steam activation. It is well known that Rh is very active towards

CH_4 dissociation [13, 15]. This adsorption tendency can be significantly enhanced via the redox reactions and oxygen exchange capacity provided by the ceria–zirconia support [49]. Ceria has a very strong tendency for steam adsorption.

Temperature–programmed steam reforming on $Ce_{0.6}Zr_{0.4}O_2$ support has shown that CH_4 has an insignificant adsorption on the ceria in the studied temperature range (<700 ^oC). Therefore, it is believed that CH_4 is dissociatively adsorbed on the Rh active metal and steam is dissociatively adsorbed on the $Ce_{0.6}Zr_{0.4}O_2$ support. However, this does not exclude that water can also be adsorbed on Rh. This conclusion is also supported by the observations of Polychronopoulou and Efstathiou [56] on phenol reforming over ceria zirconia supported Rh. They studied the spillover of labile OH, H, and O species between the support and the active metal. They confirmed that the ceria support is associated with water dissociation, while Rh surface is associated with the adsorption of hydrocarbon fragments. The same conclusion is reached by Azzam et al [57] for CO dissociation on Pd catalyst supported on ceria during the water gas–shift reaction. A mechanistic reaction concept is given as a simplified schematic in Fig. 17.

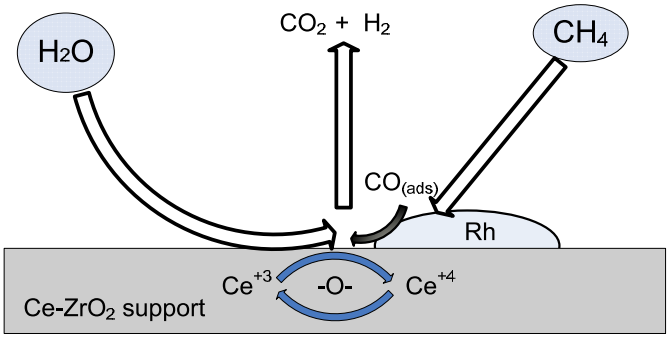

Fig. 17 Simplified schematic for the reaction mechanistic concept.

Table 7 includes a proposed molecular reaction mechanism based on the qualitative analysis of the kinetic observations presented. The elementary reaction steps are explained as follows:

1. Steam is dissociatively adsorbed on the support sites (*S*), yielding adsorbed oxygen atoms (lattice oxygen O-*S*) and gaseous hydrogen;
2. Methane is dissociatively adsorbed on the Rh sites (*l*), yielding adsorbed carbon containing species CH_3, CH_2, CH, and adsorbed hydrogen atoms;
3. The adsorbed CH species on the Rh sites (*l*) react with the lattice oxygen from the support at the interface (O-*S*) yielding an adsorbed CHO species at the (*l*) sites and a vacant lattice oxygen site S at the support;
4. CHO radicals interact with the adjacent vacant sites (*S*), yielding adsorbed CO and H atoms, or react in parallel with adjacent lattice oxygen from the support sites (O-*S*) at the interface, yielding adsorbed CO_2 and H atoms;
5. Adsorbed CO atoms on (*l*) sites may react with the lattice oxygen at the interface (O-*S*) to produce adsorbed CO_2 atoms at (*l*) sites and a vacant oxygen site (*S*) at the interface or they desorb into the gas phase;

6. Formed hydrogen and CO_2 are directly released into the gas phase or are in equilibrium with their adsorbed atoms;
7. Surface reactions of adsorbed CHO species and CO molecules with adjacent vacant sites (*S*) or lattice oxygen (O-*S*) resulting in adsorbed CO and CO_2 are considered to be the rate determining steps.

Table 7: Steam reforming molecular reaction mechanism (*l* is an active site on Rh, *S* is an active site on the Ce–ZrO_2 support).

Elementary steps of the proposed reaction mechanism	
$CH_4 + 2l \leftrightarrow CH_3\text{-}l + H\text{-}l$	1
$CH_3 + l \leftrightarrow CH_2\text{-}l + H\text{-}l$	2
$CH_2 + l \leftrightarrow CH\text{-}l + H\text{-}l$	3
$CH\text{-}l + O\text{-}S \leftrightarrow CHO\text{-}l + S$	4
$CHO\text{-}l + S \leftrightarrow CO\text{-}l + H\text{-}S$	5, RDS
$CO\text{-}l + O\text{-}S \leftrightarrow CO_2\text{-}l + S$	6, RDS
$CHO\text{-}l + O\text{-}S \leftrightarrow CO_2\text{-}l + H\text{-}S$	7, RDS
$CO\text{-}l \leftrightarrow CO + l$	8
$CO_2\text{-}l \leftrightarrow CO_2 + l$	9
$2H\text{-}l \leftrightarrow H_2\text{-}l + l$	10
$H_2\text{-}l \leftrightarrow H_2 + l$	11
$2H\text{-}S \leftrightarrow H_2\text{-}S + S$	12
$H_2\text{-}S \leftrightarrow H_2 + S$	13
$H_2O + S \leftrightarrow O\text{-}S + H_2$	14

The non-linear dependency of the reaction rate on CH_4 partial pressure eliminates the assumption that CH_4 chemisorption and activation on the catalyst surface is the rate controlling step in the temperature range of 475–625 ^oC. Therefore, steam reforming on $Rh/Ce_{0.6}Zr_{0.4}O_2$ catalyst occurs via CH_4 dissociation on the Rh surface initiating a successive loss of H_2 and production of carbon intermediates on the Rh surface (steps 1 to 4, Table 7). This is followed by consecutive surface oxidation reactions between the surface carbon intermediates and the lattice oxygen from the ceria support at the interface (steps 5 and 6, Table 7). This eventually leads to CO and H_2 production followed by a possible subsequent step of CO oxidation on Rh surface.

Lattice oxygen is significantly replenished by the rapid surface reaction of reduced ceria with steam (step 14, Table 7). This step is experimentally investigated and confirmed in several studies [33–37]. The redox surface reactions between carbon containing species and the lattice oxygen at the interface are considered as the rate determining steps. This assumption is justified by the fact that ceria shows strong metal-metal interaction with Rh and assists in electron transfer from Rh^o to CeO_2 resulting in a lower electron density on Rh ($Rh^{\delta+}$) and two redox couples of $Rh^o/Rh^{\delta+}$and Ce^{4+}/Ce^{3+} [58, 59]. The decrease in electron density on $Rh^{\delta+}$ makes it easier to accept the σ electrons resulting from the cleavage of C-H bonds. This will eventually facilitate the activation and dissociation of CH_4 on Rh. Thus, CH_4 activation is not a limiting step in our study. Moreover, Jones et al. [60] reported that the rate liming step shifts from CO formation at low temperature to CH_4

activation at high temperature. This might explain the assumption of Wei and Iglesia [16, 52] when they considered CH_4 dissociation is a rate liming step taking into account that their experiments are carried out in a temperature range of 600–800 ^oC.

The absence of competition between CH_4 and steam can be easily discerned in the reaction mechanism by employing two distinct sites for CH_4 and steam adsorption. The rate of CH_4 activation on ceria is much slower than that by CO, CO_2, or O_2 [34]. The values measured by Steele and Floyed [51] for oxygen ion diffusion coefficients on ceria are sufficiently high that the overall reaction rate is thought to be controlled by the surface reactions and not by oxygen diffusion from the bulk of the solid particle to the surface. The values measured for the turnover frequencies at 900 ^oC for reduced ceria in oxygen or CO/CO_2 gases are several orders of magnitude higher than the activity of steam reforming or direct CH_4 conversion [33, 62, 63]. This supports what has been proposed in our mechanism at the range of temperature studied (< 625 ^oC).

H_2 resulted either from steam dissociation on the ceria surface or CH_4 decomposition on the Rh surface can also be dissociatively adsorbed on both surfaces. However, molecular H_2 adsorption can be of very weak nature due to the relatively high temperature present. H_2 adsorbed on the Rh surface (step 11) suppresses the sequential loss of H from CH_4 fragments on the Rh by accelerating the backward reactions of CH_4 dissociation on the Rh surface (steps 1, 2, and 3). H_2 adsorbed on the support (step 13) reduces the oxidation state of ceria leading to (i) lower rate of H_2O dissociation on the support surface (step 14) and (ii) less lattice oxygen to be incorporated with the adsorbed CHO precursor in the surface reactions (steps 5 and 7). Therefore, the apparent CH_4 conversion rate is lower. H_2 shows stronger inhibition at high partial pressures as shown earlier, thus CH_4 conversion and reforming rates are lower due to the promotion of the reverse water–gas shift and methanation reactions. This inhibitory effect is diminished at higher temperatures due to weakened adsorption.

The inhibition effect of CO on the initial reaction rates is implicated in the mechanism in CO adsorption on Rh sites (step 8) and competition with CH_4. This leads to lower CH_4 dissociation rates followed by lower surface reaction rates between the carbon intermediates and the interface lattice oxygen (step 5). The CO_2 adsorption on Rh (step 9) is also shown to reduce the oxidation rate of carbon intermediates produced on Rh and the consequent CO oxidation, leading to lower steam reforming and water–gas shift reaction rates (steps 6 and 7).

The qualitative trends illustrated in this chapter are supported by comprehensive quantitative analysis of intrinsic reaction rates in our proceeding publication [64] given in chapter 7. A detailed kinetic model is derived according to a model discrimination and parameter estimation procedure.

6.5 Conclusions

The catalytic steam reforming of methane is investigated over $Rh/Ce_{0.6}Zr_{0.4}O_2$ catalyst in the relatively low temperature range of 475–700 ^oC. The forward reaction rates show a nonlinear dependency on CH_4 and steam partial pressures with a positive reaction order of less than 1 in a temperature range of 475–625 ^oC. CH_4 conversion and reforming rates are found to be retarded by H_2, CO, and CO_2 and a negative effect is demonstrated at all investigated conditions. Strong inhibition of the CH_4 conversion rates is found at high partial pressures due to the promotion of the reverse water–gas shift and methanation reactions. Temperature programmed steam reforming experiments on the $Ce_{0.6}Zr_{0.4}O_2$ support reveal that insignificant CH_4 adsorption can be attained at the temperature range of interest (< 700 ^oC). The catalyst shows high stability and resistance to carbon formation even at a low S/C ratio of 1. The catalytic selectivity towards the water–gas shift reaction is examined. A molecular reaction mechanism based on a two-site functional catalyst successfully describes the qualitative kinetic observations. Surface reactions between the carbonaceous fragments and the lattice oxygen leading to CO and CO_2 formation are considered as the rate determining steps.

References

1. Rostrup-Nielsen, J. R, Sehested, J., Norskov, J.K., Hydrogen and synthesis gas by steam-and CO_2 reforming, Adv. Catal. 47 (2002) 65-139.
2. Ayabe, S., Omoto, H., Utaka, T.,. Kikkuchi, R., Sasaki, K., Teraoka, Y., Eguchi, K., Catalytic autothermal reforming of methane and propane over supported metal catalysts, App. Catal. A 241 (2003) 261-269.
3. Bradford, M.C.J, Vannice, M., Catalytic reforming of methane with carbon dioxide over nickel catalysts I. Catalyst characterization and activity App. Catal. A 142 (1996) 73-96.
4. Matsumura, Y., Nakamori, T., Steam reforming of methane over nickel catalysts at low reaction temperature, App.Catal. A 258 (2004) 107-114.
5. Xu, J., Froment, G.F., Methane steam reforming, methanation and water-gas shift: I. Intrinsic kinetics, AIChE J. 35 (1989) 88-96.
6. Xu, J., Froment, G.F., Methane steam reforming: II. Diffusional limitations and reactor simulation, AIChE J. 35 (1989) 97-103.
7. Laosiripojana, N., Assabumrungrat, S., Methane steam reforming over Ni/Ce–ZrO_2 catalyst: Influences of Ce–ZrO_2 support on reactivity, resistance toward carbon formation, and intrinsic reaction kinetics, Appl. Catal. A 290 (2005) 200-211.
8. Elnashaie, S.S.E.H., Adris, A.M., Al-Ubaid, A.S., Soliman, M.A., On the non-monotonic behaviour of methane—steam reforming kinetics, Chem. Eng. Sci. 45 (1990) 491-501.
9. Rostrup-Nielsen, J.R., Bak-Hansen, J.-H., CO_2-Reforming of Methane over Transition Metals, J. Catal. 144 (1993) 38-49.

10. Bitter, J.H., Seshan, S., Lercher, J.A., Mono and Bifunctional Pathways of CO_2/CH_4Reforming over Pt and Rh Based Catalyst, J. Catal. 176 (1998) 93-101.
11. Sakai, Y., Saito, H., Sodesawa, T., Noz`aki, F., Catalytic reactions of hydrocarbon with carbon dioxide over metallic catalysts, React. Kinet. Catal. Lett. 24 (1984) 253-257.
12. Mark, M.F., Maier, W.F., CO_2-Reforming of Methane on Supported Rh and Ir Catalysts, J. Catal. 164 (1996) 122-130.
13. Wang, D., Dewaele, O., Froment, G.F., Methane adsorption on Rh/Al_2O_3, J. Mol. Catal. A 136 (1998) 301-309.
14. Hickman, D.A., Schmidt, L.D., Steps in CH_4 oxidation on Pt and Rh surfaces: High-temperature reactor simulations, AICHE J. 39 (1993) 1164-1177.
15. Kurungot, S., Yamaguchi, T., Stability Improvement of $Rh/\gamma\text{-}Al_2O_3$ Catalyst Layer by Ceria Doping for Steam Reforming in an Integrated Catalytic Membrane Reactor System, Catal. Lett. 92 (2004) 181-187.
16. Wei, J., Iglesia, E., Structural requirements and reaction pathways in methane activation and chemical conversion catalyzed by rhodium, J. Catal. 225 (2004) 116-127.
17. Portugal, U.L., Santos, A.C.S.F., Damyanova, S., Marques, C.M.P., Bueno, J.M.C., CO_2 reforming of CH_4 over Rh-containing catalysts , J. Mol. Catal. A: Chem. 184 (2002) 311-322.
18. Zhang, Z.L., Tsipouriari, V.A., Efstathiou, A.M., Verykios, X.E., Reforming of Methane with Carbon Dioxide to Synthesis Gas over Supported Rhodium Catalysts: I. Effects of Support and Metal Crystallite Size on Reaction Activity and Deactivation Characteristics, J. Catal. 58 (1996) 51-63.
19. Richardson, J.T., Paripatyadar, S.A., Carbon dioxide reforming of methane with supported rhodium, Appl. Catal. 61 (1990) 293-309.
20. Wang, H.Y., Ruckenstein, E., Carbon dioxide reforming of methane to synthesis gas over supported rhodium catalysts: the effect of support, Appl. Catal. 204 (2000) 143-152.
21. Wang, H.Y., Ruckenstein, E., CH_4/CD_4 Isotope Effect and the Mechanism of Partial Oxidation of Methane to Synthesis Gas over $Rh/\gamma\text{-}Al_2O_3$ Catalyst, J. Phys. Chem. 103 (1999) 11327-11331.
22. Tsipouriari, V.A., Efstathiou, A.M., Zhang, Z.L., Verykios, X.E., Reforming of methane with carbon dioxide to synthesis gas over supported Rh catalysts, Catal. Today 21 (1994) 579- 587.
23. Yokota, S., Okumura, Y., Niwa, M., Support Effect of Metal Oxide on Rh Catalysts in the CH_4-CO_2 Reforming Reaction, Catal. Lett. 84 (2002) 131-134.
24. Wang, H.Y., Au, C.T., Carbon dioxide reforming of methane to syngas over SiO_2-supported rhodium catalysts, Appl. Catal. A 155 (1997) 239-252.
25. Gronchi, P., Centola, P., Del Rosso, R., Dry reforming of CH_4 with Ni and Rh metal catalysts supported on SiO_2 and La_2O_3, Appl. Catal. A 152 (1997) 83-92.
26. Qin, D., Lapszewicz, J., Study of mixed steam and CO_2 reforming of CH_4 to syngas on MgO-supported metals, Catal. Today 21 (1994) 551-560.
27. Mattos, L.V., Rodino, E., Resasco, D.E., Possos, F.B., Noronha, F.B., Partial oxidation and CO_2 reforming of methane on Pt/Al_2O_3, Pt/ZrO_2, and $Pt/Ce–ZrO_2$ catalysts, Fuel Proc. Technol. 83 (2003) 147-161.

28. Roh, H.S., Jun, K.W., Park, S.E., Methane-reforming reactions over Ni/Ce-ZrO_2/θ-Al_2O_3 catalysts, Appl. Catal. A 251 (2003) 275-283.
29. Wang, X., Gorte, R.J., A study of steam reforming of hydrocarbon fuels on Pd/ceria, Appl. Catal. A 224 (2002) 209-218.
30. Otsuka, K., Ushiyama, T., Yamanaka, I., Partial Oxidation of Methane Using the Redox of Cerium Oxide, Chem. Lett. (1993) 1517-1520.
31. Otsuka, K., Hatano, M., Morikawa, A., Hydrogen from water by reduced cerium oxide, J. Catal. 79 (1983) 493-496.
32. Otsuka, K., Hatano, M., Morikawa, A., Decomposition of water by cerium oxide of δ-phase, Inorg. Chim. Acta 109 (1985) 193-197.
33. Ramirez, E., Atkinson, A., Chadwick, D., Appl. Catal. B 36 (2002) 193-206.
34. Ramı´rez-Cabrera, E., Laosiripojana, N., Atkinson, A., Chadwick, D., Methane conversion over Nb-doped ceria, Catal. Today 78 (2003) 433-438.
35. Ramı´rez-Cabrera, E., Atkinson, A., Chadwick, D., Catalytic steam reforming of methane over $Ce_{0.9}Gd_{0.1}O_{2-x}$, Appl. Catal. B 47 (2004) 127-131.
36. Laosiripojana, N., Sutthisripok, W., Assabumrungrat, S., Synthesis gas production from dry reforming of methane over CeO_2 doped Ni/Al_2O_3: Influence of the doping ceria on the resistance toward carbon formation, Chem.Eng. J. 112 (2005) 13-22.
37. Laosiripojana, N., Assabumrungrat, S., Catalytic dry reforming of methane over high surface area ceria, Appl. Catal. B: Environ. 60 (2005) 107-116.
38. Kusakabe, K., Sotowa, K-I., Eda, E., Iwamoto, Y., Methane steam reforming over Ce–ZrO_2-supported noble metal catalysts at low temperature, Fuel Process Technol., 86 (2004) 319-326.
39. Dong, W.S., Roh, H.S., Jun, K.W., Park, S.E., Oh, Y.S., Methane reforming over Ni/Ce-ZrO_2 catalysts: effect of nickel content, Appl. Catal. A 226 (2002) 63-72.
40. Laosiripojana, N., Chadwick, D., Assabumrungrat, S., Effect of high surface area CeO_2 and Ce-ZrO_2 supports over Ni catalyst on CH_4 reforming with H_2O in the presence of O_2, H_2, and CO_2, Chem. Eng. J. 138 (2008) 264-273.
41. Imamaura, S., Yamashita, T., Hamada, R., Saito, Y., Nakao, Y., Tsuda, N., Kaito, C., J. Mol. Catal. A 129 (1998) 249-256.
42. Ozawa, M., Kimura, M., Effect of cerium addition on the thermal stability of gamma alumina support, J. Mater. Sci. Lett. 9 (1990) 291-293.
43. Dicks, A.L., Pointon, K.D., Siddle, A., Intrinsic reaction kinetics of methane steam reforming on a nickel/zirconia anode, J. Power Sources 86 (2000) 523-530.
44. Berman, B., Karn, R.K., Epstein, M., Kinetics of steam reforming of methane on Ru/Al_2O_3 catalyst promoted with Mn oxides, App. Catal. A 282 (2005) 73-83.
45. Eriksson, S., Rojas, S., Boutonnet, M.,. Fierro, J.L.G., Effect of Ce-doping on Rh/ZrO_2 catalysts for partial oxidation of methane, App. Catal. A 326 (2007) 8-16.
46. Thammachart, M., Meeyoo, V., Risksomboon, T., Osuwan, S., Catalytic activity of CeO_2–ZrO_2 mixed oxide catalysts prepared via sol–gel technique: CO oxidation, Catal. Today 68 (2001) 53-61.

47. Hou, K., Hughes, R., The kinetics of methane steam reforming over a Ni/α-Al_2O catalyst, Chem.Eng. J. 82 (2001) 311-328.
48. Hofstad, K.H., Hoebink, J.H.B.J., Holmen, A., Marin, G.B., Partial oxidation of methane to synthesis gas over rhodium catalysts, Catal. Today 40 (1998) 157-170.
49. Wang, R., Xu, X., Chen, Y., Li, W., Chin. The Effect of Supports on the Activity of Methane Dissociation over Rh Catalysts, J. Catal, 28 (2007) 293-295.
50. Cardatos, H., Bunluesin, T., Studbenrauch, J., Vohs, J.M., Gorte, R.J., J. Phys. Chem. 100 (1996) 785-789.
51. Constantinou, D.A., Efstathiou, A.M., Low-temperature purification of gas streams from phenol by steam reforming over novel supported-Rh catalysts, App. Catal. B 96 (2010) 276-289.
52. Wei, J.M., Iglesia, E., Mechanism and Site Requirements for Activation and Chemical Conversion of Methane on Supported Pt Clusters and Turnover Rate Comparisons among Noble Metals, J. Phys. Chem. B 108 (2004) 4094-4103.
53. Jakobsen, J.G., Jorgensen, T.L., Chorkendorff, I., Sehested, J., Steam and CO_2 reforming of methane over a Ru/ZrO_2 catalyst, App. Catal. A 377 (2010) 158-166.
54. Rao, G.R., Kaspar, J., Meriani, S., Dimonte, R., Graziani, M., NO decomposition over partially reduced metallized CeO_2-ZrO_2 solid solutions, Catal. Lett. 24 (1994) 107-112.
55. Fornasiero, P., Dimonte, R., Rao, G.R., Kaspar, J., Meriani, S., Trovarelli, A., Graziani, M., Rh-Loaded CeO_2-ZrO_2 Solid-Solutions as Highly Efficient Oxygen Exchangers: Dependence of the Reduction Behavior and the Oxygen Storage Capacity on the Structural-Properties, J. Catal. 151(1995) 168-177.
56. Polychronopoulou, K., Efstathiou, A.M., Spillover of labile OH, H, and O species in the H_2 production by steam reforming of phenol over supported-Rh catalysts, Catal. Today 116 (2006) 341-347.
57. Azzam, K.G., Babich, I.V., Seshan, K., Lefferts, L., Bifunctional catalysts for single-stage water–gas shift reaction in fuel cell applications: Part 1. Effect of the support on the reaction sequence, J. Catal. 251 (2007) 153-162.
58. Wang, R., Xu, H., Liu, X., Ge., Q., Li, W., Role of redox couples of $Rh^0/Rh^{\delta+}$ and Ce^{4+}/Ce^{3+} in CH_4/CO_2 reforming over $Rh–CeO_2/Al_2O_3$ catalyst, App. Catal. A 305 (2006) 204-210.
59. Wang, R., Xu, H., Liu, X., Ge, Q., Chin, L., The Effect of Supports on the Activity of Methane Dissociation over Rh Catalysts, . J. Catal. 28 (2007) 293-295.
60. Jones, G., Jakobsen, J.G., Shim, S.S., Kleis, J., Andersson, M.P., Rossmeisl, J., Abild-Pedersen, F., Bligaard, T., Helveg, S., Hinnemann, B., Rostrup-Nielsen, J-R., Chorkendorff, I., Sehested, J., Norskov, J., First principles calculations and experimental insight into methane steam reforming over transition metal catalysts, J. Catal. 259 (2008) 147-160.
61. Steele, B.C.H., Floyd, J.M., Proc. Br. Ceram. Soc. 19 (1971) 55-59.
62. Floyd, J.M., Interaction of tranposrt phenomena in non-stoichiometric ceria, Indian J. Technol. 11 (1973) 589-594.

63. Vlaic, G., Fornasiero, P., Geremia, S., Kaspar, J., Graziani, M., Relationship between the Zirconia-Promoted Reduction in the Rh-Loaded $Ce_{0.5}Zr_{0.5}O_2$Mixed Oxide and the Zr–O Local Structure, J. Catal. A 168 (1997) 386-392.
64. Halabi, M.H., de Croon, M.H.J.M, van der Schaaf, J., Cobden, P.D., Schouten, J.C., Intrinsic kinetics modeling of catalytic methane–steam reforming and water–gas shift over $Rh/Ce_{\alpha}Zr_{1-\alpha}O_2$ catalyst, App. Catal. A (2010) 10.1016/j.apcata.2010.09.005.

Chapter 7

Intrinsic Kinetics of Catalytic Methane Steam Reforming Over $Rh/Ce_{\alpha}Zr_{1-\alpha}O_2$ Catalyst

This chapter has been published as
M.H. Halabi, M.H.J.M. de Croon, J. van der Schaaf, P.D. Cobden, J.C. Schouten, Intrinsic kinetics of low temperature catalytic methane–steam reforming and water gas shift over $Rh/Ce_{\alpha}Zr_{1-\alpha}O_2$ catalyst, Applied Catalysis A, 389, 80–91, 2010.

Abstract

This chapter presents the intrinsic kinetics of CH_4 steam reforming developed over $Rh/Ce_{0.6}Zr_{0.4}O_2$ catalyst in a relatively low temperature range of 475–575 ^{o}C and 1.5 bar pressure. The kinetic experiments are conducted in an integral fixed bed reactor with no mass and heat transport limitations and far from equilibrium conditions. Therefore, intrinsic reaction rate measurements are guaranteed. The model is based upon two-site adsorption surface hypothesis, and 14 elementary reaction steps are postulated. CH_4 is dissociatively adsorbed onto the Rh active sites, and steam is dissociatively adsorbed on the ceria support active sites as an influential adsorption surface shown in the model. Therefore, no competition between CH_4 and steam in adsorbing on the same site surface is observed. The kinetic rate expressions are derived according to the Langmuir-Hinshelwood formalism. The redox surface reactions between the carbon containing species and the lattice oxygen leading to CO and CO_2 formation are considered as rate

determining steps. The inhibitory effect of gaseous product species is also reflected in the kinetics. The model is found to be statistically accurate and thermodynamically consistent. The estimated activation energies and adsorption enthalpies are in agreement with literature for CH_4 steam reforming reaction over Rh. The reaction kinetics is validated by steam reforming experiments at 550 ^oC and 1.5 bar using 150 mg catalyst in a diluted bed of 5 cm length. The kinetic model is implemented in a one-dimensional pseudo-homogenous plug flow reactor model and thus simulated at identical experimental conditions. The simulation results are in excellent agreement with the experimental values.

7.1 Introduction

H_2 is a principal feedstock for major petrochemical industries and has been considered as a renewable energy alternative for near future applications. The increasing demand for H_2 production and the stringent policies for the reduction of CO_2 emissions are driving forces for research during the recent years. Sorption enhanced catalytic steam reforming of natural gas is a promising pre-combustion decarbonization technology for high purity H_2 generation with in situ CO_2 capture [1–3]. The sorption enhanced reforming concept generally requires low temperature operation in order to maintain high CO_2 adsorption capacity of the employed sorbent. The conventional steam reforming process is operated at relatively high temperature (700–900 ^oC) due to the highly endothermic nature of the reaction [4–6]. Therefore, an active catalyst which can provide high reforming reaction rates at low temperature (<550 ^oC) is required. Rh is one of the most active VIII noble metals that can catalyze the reforming of CH_4 with steam or CO_2. The activity of Rh supported on different supports has been illustrated in literature, Rh/Al_2O [7–13], Rh/ZrO_2 [12, 14–16], Rh/SiO_2 [17–19], Rh/MgO [9, 14, 20, 21], Rh/CeO_2 [22–28] Rh–CeO_2/ Al_2O_3 [12, 23–25], Rh/$Ce_{1-x}Gd_xO_{2-x}$ [27], and Rh/$Ce_\alpha Zr_{1-\alpha}O_2$, [25, 26, 28,29].

The addition of a reducible metal oxide support such as ceria to the noble metal has been proven to enhance the catalyst activity, stability, and resistance towards carbon formation [30–42]. Rh/$Ce_\alpha Zr_{1-\alpha}O_2$ is used in our investigation as an effective catalyst for sorption enhanced steam reforming. This is beneficial in terms of energy saving, production rates, and capital investment of the integrated reactor/adsorber.

The available literature includes major discrepancies concerning the reaction mechanisms and the corresponding kinetic models in addition to the large span of activation energies reported for steam reforming reaction. This is in the first place explained by the different types of the catalyst and the support used. Moreover, temperature and pressure ranges, gas composition, and presence of mass transport limitations can play a dominant role in restructuring the kinetic rates.

Dicks et al. [43] determined a first order dependency on CH_4 with a weak positive effect of H_2 and stronger negative effect of steam over Ni/ZrO_2 at 700–1000 ^oC.

Hou and Hughes [44] studied the kinetics of steam reforming accompanied by the reverse water–gas shift reaction on a commercial Ni/α-Al_2O from 475 to 550 ^oC. They concluded that the rate of CH_4 disappearance is proportional to CH_4 partial pressure at low product concentrations. The effect of total pressure on initial rates indicated that the rate determining steps of steam reforming are surface reactions between adsorbed species. Wei and Iglesia [13] investigated the CH_4 reforming with steam and CO_2 over Rh clusters in a temperature range of 600–800 ^oC. They found that CH_4 activation is the only relevant step and the reaction rates are independent of any other gas species, either the reactants (steam or CO_2) or the products. Berman et al. [45] studied the reaction dependency of steam reforming on CH_4 and steam partial pressures over Ru/αAl_2O_3 catalyst promoted with Mn oxides from 500 to 900^oC and a total pressure of 1 to 7 bar. They reported a positive reaction order < 1 in CH_4 at 450–500 ^oC and close to 1 at 700–900 ^oC and a negative reaction order in steam at all temperatures.

Xu and Froment [46] formulated a relatively extended kinetic model for steam reforming over Ni/MgO-Al_2O_3 at 500–670 ^oC. The derived model accounts for the adsorption of gas phase components of CO, CO_2, and H_2 on the same adsorption sites occupied by CH_4 and steam. The mechanism proposes surface reactions to be the rate determining steps with a reaction order of < 1 in CH_4.

A reliable design, simulation, and optimization of the sorption enhanced steam reforming process demands a concrete intrinsic kinetic model for the catalyst employed. In our previous work [29], the mechanistic aspects of CH_4 reforming with steam are studied over Rh/$Ce_\alpha Zr_{1-\alpha}O_2$ in a temperature range of 475–700 ^oC and 1.5 bar. We have determined that the reaction order in CH_4 is <1 and CH_4 activation is not rate limiting step in the temperature range of 475–625 ^oC. A molecular reaction mechanism based on a catalyst surface with two-site adsorption is postulated.

The major goal of this chapter is to present a comprehensive derivation for the intrinsic kinetics of CH_4 steam reforming over Rh/$Ce_\alpha Zr_{1-\alpha}O_2$ in a low temperature range of 475–575 ^oC and a pressure of 1.5 bar. The measured kinetic data are guaranteed to be far from equilibrium and mass transfer limitations. The derived mathematical model is checked for thermodynamic consistency and validated with experimental data using a one–dimensional pseudo–homogenous plug flow model.

7.2 Experimental

7.2.1 Catalyst

The Rh/$Ce_\alpha Zr_{1-\alpha}O_2$ catalyst is prepared by impregnation of 0.8% Rh loaded from a $Rh(NO_3)_3$ solution onto a commercially available mixture of ceria–zirconia supports with a weight ratio of 60:40. The catalyst is calcined at 400 ^oC for 5 hrs. The catalyst is characterized by classical techniques of XRD, TEM, SEM, and XPS. The BET surface area is determined by N_2 adsorption porosimetry and the metal dispersion is determined by H_2 chemisorption. More details of the catalyst

characterization techniques are given in our previous work [29]. The fresh catalyst is pretreated in a (20 vol.% H_2: 80 vol.% N_2) gas mixture. The catalyst is gradually heated up to 700 ^oC and maintained for 2 hrs. Some physical properties of the catalyst are listed in Table 1.

Table 1: Catalyst properties.

	Value
Average pellet size	300 μm
Rh metal content	0.8%
BET surface area of the fresh catalyst	38.8 m^2/g
Pore diameter of the catalyst	20.4 nm
Metal dispersion on the fresh catalyst	29.7%
Crystallite particle size	3 nm
Ce/Zr composition ratio	0.6/0.4

7.2.2 Experimental setup

The kinetic experiments are performed in an integral fixed bed rector. The reactor is a quartz tube of 4.0 mm internal diameter and 1.0 m length. A reaction zone of 19.5 cm is placed at the bottom and two heating upper parts on the top. Reaction gas flow-rates are controlled by thermal mass flow controllers in the range of 0–50 nml/min. N_2 is used as an inert carrier in the range of 0–500 nml/min. The temperature is controlled in a range of 25–750 ^oC. Water is evaporated in a controller evaporator mixer and supplied to the reactor. The overall gas mixture contains up to 25% water on relative humidity basis. Inlet and outlet gas compositions are online-analyzed using gas chromatography (GC Varian CP-3800). 10 mg catalyst is diluted with 450 mg α–alumina of 300 μm particle size. The total length of the bed in the reaction zone is 5.0 cm.

7.2.3 Catalyst deactivation and preliminary testing

The catalyst is initially deactivated for 30 hrs time on stream at 550 ^oC and 1.5 bar using a 100 nml/min reaction gas mixture of (4.7 vol.% CH_4, 1.5 vol.% H_2, an S/C ratio of 4.0, and balance N_2). Fig. 1 shows the catalyst deactivation curve in terms of CH_4 conversion versus time on stream. The catalyst activity slowly decays after the first 10 hrs approaching a stable activity of 28%. However, the measured CH_4 conversion data during the kinetic experiments are further corrected for the infinitesimal activity decay with time.

7.2.4 Interparticle and intraparticle mass and heat transport limitations

The conversion rate can either be controlled by the intrinsic chemical reaction kinetics or by the external mass transport rate from the gas phase to the catalyst surface or the internal diffusion rate in the pores. In exothermic and endothermic reactions, the temperature gradient over the catalyst bed or the difference in temperature between the bulk gas and the catalyst surface may also affect the observed reaction rate. Therefore, the interfacial and intraparticle mass and heat transport limitations are checked to preclude any effect on the intrinsic conversion rate.

The external mass transport limitations are experimentally investigated. CH_4 conversion is measured using different total volumetric flow rates from 20 to100 nml/min at constant residence time with respect to CH_4 molar feed. The inlet reaction gas composition including the inert gas was modified at every total flow rate to provide a space time of 10 $kg_{cat}s/mol$ CH_4 and a S/C ratio of 2. The measured CH_4 conversion reach steady values of 27% using gas flowrate (> 80 nml/min). Thus, any higher total gas flowrate can preclude the effect of interfacial mass transport limitations. Table 2 includes diagnostic criteria to check that the internal and external transport limitations are not predominant. The corresponding parameters used are given in Table 3.

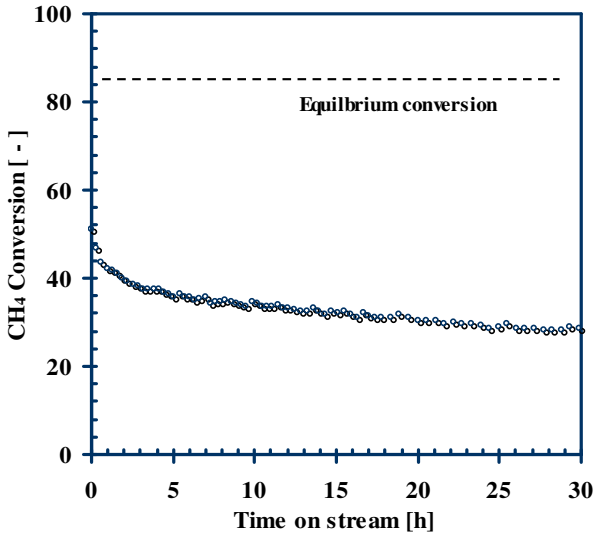

Fig. 1: Catalyst deactivation under gas composition of 4.7 vol.% CH_4, 1.5 vol.% H_2, steam/carbon ratio of 4, and balance N_2 at 550°C and 1.5 bar.

Table 2: Kinetic criteria for mass and heat transport limitations

Weisz modulus for intraparticle mass transfer limitation, [47]

$$\Phi = \frac{(n+1)R_{obs}\cdot\rho_{cat}\left(d_p/6\right)^2}{2D_{eff}C_s} \quad (1)$$

Mears criterion for external heat transfer limitation, [48]

$$\frac{\left|\Delta H^o_{rxn}\right|R_{obs}\cdot\rho_{cat}d_pE}{h_fT^2R} < 0.3 \quad (2)$$

Mears criterion for intraparticle heat transfer limitation, [48]

$$\frac{\left|\Delta H^o_{rxn}\right|R_{obs}\cdot\rho_{cat}d_pE}{\lambda_pT^2R} < 3.0 \quad (3)$$

The internal mass transport limitations were experimentally and theoretically checked. CH_4 conversion is measured at 500 °C and 1.5 bar using different catalyst pellet sizes of 150, 300, 450, and 600 µm. Gas composition consist of 15 nml/min CH_4, 10 nml/min H_2, S/C ratio of 2 and balance N_2. CH_4 conversion does not change using a pellet size smaller than 300 µm. The Weisz modulus [47] is used as a diagnostic criterion to check that the internal pore diffusion is not binding. The

value of Weisz modulus calculated according to Eq. 1 is $3.0*10^{-2}$.Weisz modulus with a value smaller than 0.25 suggests a high effectiveness factor larger than 0.95. Therefore, the criterion is satisfied. The criteria proposed by Mears [48] in Table 2 are used to check the significance of external and internal heat transport limitations. The calculated values of the RHS of Eq. 2 and 3 at 773 K are 0.14 and $4.4*10^{-5}$; respectively. The criteria are satisfied and therefore heat transport limitations can be ignored.

Table 3: Kinetic criteria–related parameters for mass and heat transport limitations

	Unit	Value
Reaction order, n	–	0.7
Catalyst pellet diameter, d_p	m	300 µm
Observed reaction rate, R_{obs}	mol/kg_{cat}s	0.97
Effective pore diffusion coefficient, D_{eff}	m^2/s	$1.05*10^{-5}$
Gas concentration on the catalyst surface, C_s	mol/m^3	1.0
Bulk catalyst density, ρ_{cat}	kg/m^3	15.9
Reaction enthalpy, ΔH^o_{rxn}	kJ/mol	206.2
Reaction activation energy, E	kJ/mol	100
Heat transfer coefficient, h_f	W/m.K	130
Solid thermal conductivity, λ_p	W/m.K	18

7.3 Results and discussion

7.3.1 Experimental results

The steam reforming reaction is performed over a relatively low temperature range of 475–575 °C and a pressure of 1.5 bar using a constant S/C ratio of 2 and a H_2/CH_4 ratio of 1. The reason of low temperature measurements is to be close to the operational conditions of the sorption enhanced process [51]. Figures 2 and 3 show the experimental data of the overall CH_4 conversion and CH_4 conversion to CO_2 versus the ratio of W/F (kg_{cat}s/mol CH_4), respectively.

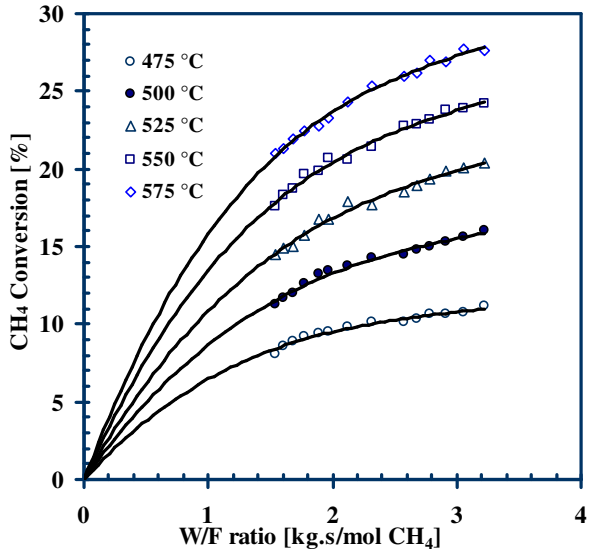

Fig. 2: Total CH_4 conversion versus W_{cat}/F_{CH4} ratio (kg_{cat}.s/mol CH_4) at 1.5 bar and S/C= 2, H_2/CH_4= 1.

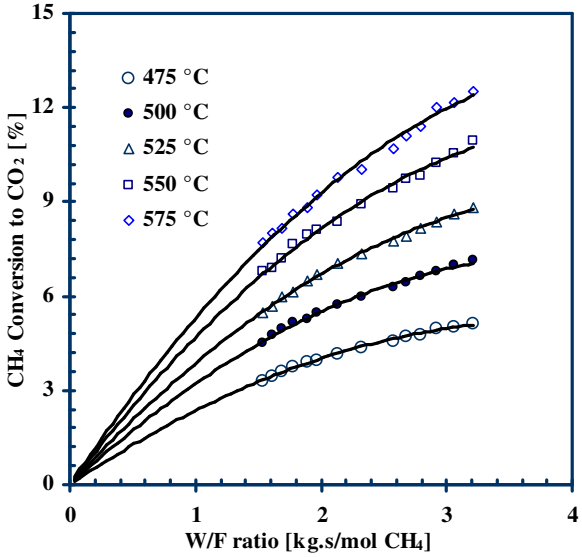

Fig. 3: CH_4 conversion to CO_2 versus W_{cat}/F_{CH4} ratio (kg_{cat}.s/mol CH_4) at 1.5 bar and S/C= 2, H_2/CH_4= 1.

These conversions are calculated according to Equations 4 and 5.

$$x_{CH_4} = \frac{F_{CH_4,in} - F_{CH_4,out}}{F_{CH_4,in}} \quad (4) \qquad x_{CO_2} = \frac{F_{CO_2,out}}{F_{CH_4,in}} \quad (5)$$

$$x'_{CO_2} = \frac{F_{CO_2,in} - F_{CO_2,out}}{F_{CO_2,in}} \quad (6) \qquad x'_{CH_4} = \frac{F_{CH_4,out}}{F_{CO_2,in}} \quad (7)$$

From our previous analysis of the steam reforming kinetic data [29], water–gas shift reaction was found to be involved in the reaction and close to equilibrium. Therefore, reverse water–gas shift reaction experiments are performed over the same catalyst loading used in steam reforming experiments but in a lower temperature range of 400–500 ^{o}C in order to determine accurate kinetic parameters of the water–gas shift reaction. Constant feed ratio of H_2/CO_2 of 1 is used. The overall conversion of CO_2 and the conversion of CO_2 to CH_4 are determined by Eq. 6 and 7; respectively. The CO_2 conversions versus residence time are given in Fig. 4 and 5.

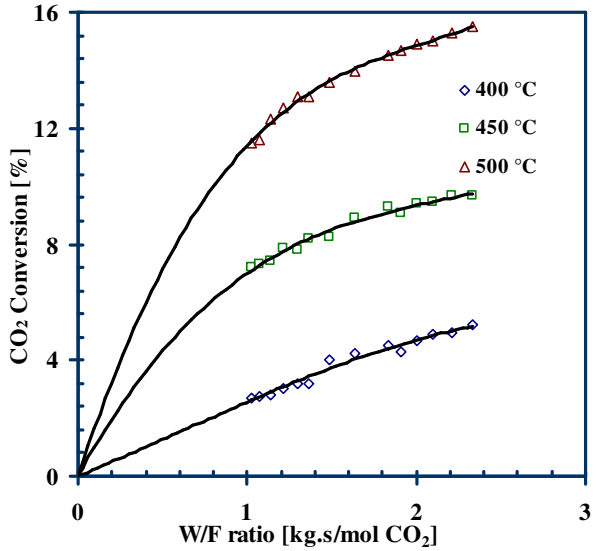

Fig. 4: Total CO_2 conversion versus W_{cat}/F_{CO2} ratio (kg_{cat}.s/mol CO_2) at 1.5 bar and H_2/CO_2= 1.

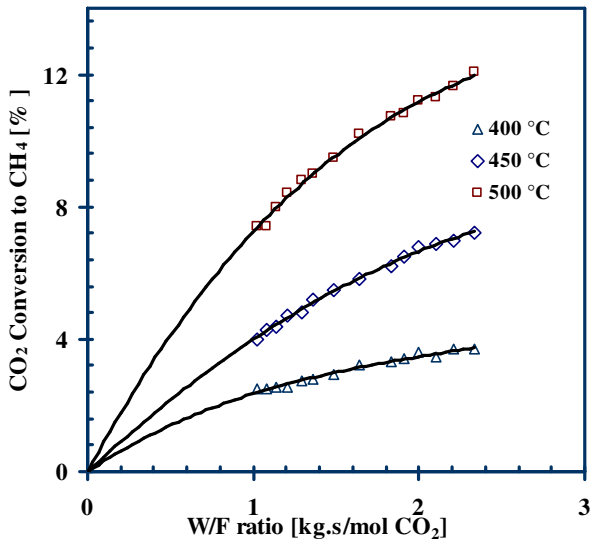

Fig. 5: CO_2 conversion to CH_4 versus W_{cat}/F_{CO2} ratio (kg_{cat}.s/mol CO_2) at 1.5 bar and H_2/CO_2= 1

7.3.2 Thermodynamic analysis

CH_4 steam reforming reaction can produce CO, CO_2, and H_2 as gas phase components in addition to possible formation of carbon according to the prospective set of reactions presented in Table 4. The potential direction of the reaction from a thermodynamic point of view can be determined according to the V_j ratio.

$$V_j = \left(\Pi_i p_i^{\nu_i}\right)_j \Big/ K_{eq_j} \quad (8)$$

If the V_i value is <1 the reaction is expected to proceed forward to the right; otherwise the reaction shows a tendency to approach equilibrium or proceeds backward.

The analysis of the product composition in the steam reforming experiments at the lowest and the highest temperature range shows that R_1 and R_3 have V_i values much smaller than 1, see Fig. 6. Their values monotonically increase with the W/F ratio (kg_{cat}.s/mol CH_4) and temperature. Thus, these two reactions proceed to the right.

Table 4: Possible reactions involved in steam reforming of methane

	Reaction	ΔH_{298K} kJ/mol
R_1.	$CH_4 + H_2O \leftrightarrow CO + 3H_2$	206.2
R_2.	$CO + H_2O \leftrightarrow CO_2 + H_2$	– 41.1
R_3.	$CH_4 + 2H_2O \leftrightarrow CO_2 + 4H_2$	165
R_4.	$CH_4 + CO_2 \leftrightarrow 2CO + 2H_2$	247.3
R_5.	$CH_4 + 3CO_2 \rightarrow 4CO + 2H_2O$	330.0
R_6.	$CH_4 \leftrightarrow C + 2H_2$	74.8
R_7.	$2CO \leftrightarrow C + CO_2$	–173.3
R_8.	$CO + H_2 \leftrightarrow C + H_2O$	–131.3
R_9.	$CO_2 + 2H_2 \leftrightarrow C + 2H_2O$	– 90.1
R_{10}.	$CH_4 + 2CO \leftrightarrow 3C + 2H_2O$	– 187.6
R_{11}.	$CH_4 + CO_2 \leftrightarrow 2C + 2H_2O$	– 15.3

The V_j values obtained for the WGS reaction R_2 given in Fig.7 suggest that R_2 can proceed to the right at low temperature (475 ^oC) and low W/F ratio (kg_{cat}.s/mol CH_4), (i.e. low conversion) as V_j <1. At relatively higher temperature of 575 ^oC and high conversion, the reaction tends to approach equilibrium or moves to the left when V_j >1. In this case, CO can be partially produced from R_2. The dry reforming reactions R_4 and R_5 resulted in V_j values <1, which means that these reactions proceed to the right. Nonetheless, the observed CH_4 disappearance rate decreases as the CH_4 conversion and hence the CO_2 concentration increase. This is in contradiction with progression of R_4 and R_5 or they might proceed in very slow rates.

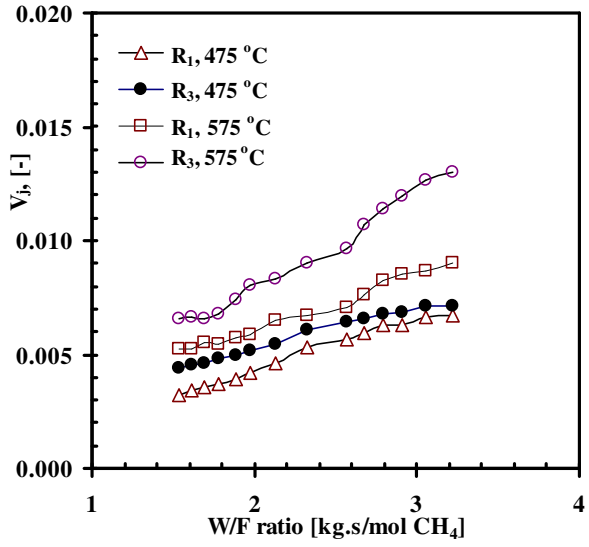

Fig. 6: V_j distribution for reaction R_1 and R_3 versus W_{cat}/F_{CH4} ratio (kg_{cat}s/mol CH_4) at 457 and 575 ^oC.

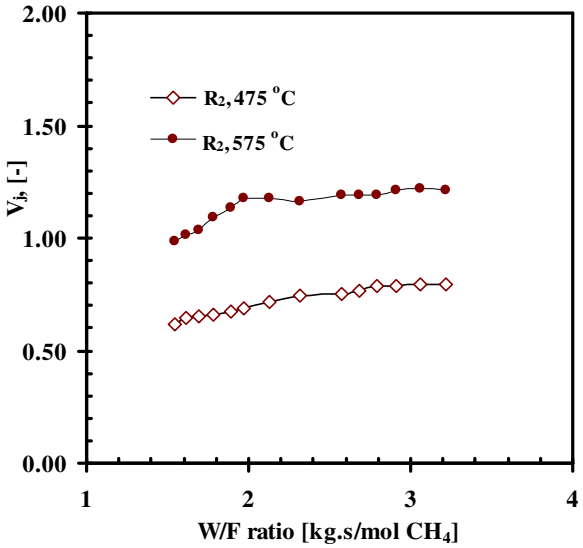

Fig. 7: V_j distribution for reaction R_2 versus W_{cat}/F_{CH4} ratio (kg_{cat}s/mol CH_4) at 457 and 575 ^oC.

Therefore, these reactions are eliminated from the possible reactions scheme from the point of view of kinetic analysis. The V_j values obtained for reaction R_6–R_{11} are exceeding 1.They tend to proceed to the left if they take place, thus no carbon formation may occur at these conditions according to thermodynamics. Therefore, these reactions are also eliminated. In conclusion, reactions R_1, R_2, and R_3 are the only possible reactions considered for CH_4 steam reforming.

7.4 Model development

7.4.1 Proposed reaction mechanisms

CH_4 steam reforming reaction over a catalyst is generally viewed as CH_4 and steam adsorption on vacant active sites, followed by surface reactions between the carbon–containing fragments generated from CH_4 activation from one side, and adsorbed oxygen resulted from water dissociation to produce CO and H_2 as primary compounds. There are different mechanisms postulated in literature to describe these steps. Using $Rh/Ce_\alpha Zr_{1-\alpha}O_2$ catalyst, the ceria support surface plays an important role in determining the reaction mechanism and the kinetic rate [23–25, 29]. Since both the active metal catalyst and the support can provide vacant surface sites for the reaction; CH_4 and water can undergo different possible reactions on the two surfaces. These reactions are listed in Table 5. In this chapter, only the most relevant and realistic reaction mechanisms are considered in the analysis, and thereafter subjected to a model discrimination and parameter estimation procedure. This is mainly due to the tedious effort required for identifying accurate and physically consistent estimates for the kinetic parameters, activation energies, and adsorption enthalpies. The proposed mechanisms are listed in Table 6.

Table 5. Possible reactions on a $Rh/Ce_\alpha Zr_{1-\alpha}O_2$ catalyst surface.

1. Reactions on Rh surface, *l* is a vacant active site *:*	
$CH_4 + xl \leftrightarrow CH_{n-x}\text{-}l + (4\text{-}n)/2H_2$	1
$H_2O + l \leftrightarrow O\text{-}l + H_2$	2
$CH_{n-x}\text{-}l + O\text{-}l \leftrightarrow CO + (n/2)H_2 + (x+1)l$	3
2. Reactions on $Ce\text{-}ZrO_2$ support *:*	
$CeO_2 + nCH_4 \rightarrow CeO_{2-n} + nCO + 2nH_2$	4
$CeO_{2-n} + nCO_2 \leftrightarrow CeO_2 + nCO$	5
$CeO_{2-n} + nH_2O \leftrightarrow CeO_2 + nH_2$	6

The general differences between these mechanisms are based on the following postulations:

1. One–site surface is used for CH_4 and water adsorption as in M.1, M.2, and M.3
2. Two–site surface is used for reactant adsorption. CH_4 is adsorbed on a vacant *l* site on Rh and water is adsorbed on vacant S site on the ceria support as in M.4–M9.
3. Water is adsorbed as molecular adsorption on the surface as M.1, and M.2.
4. Water is adsorbed with dissociation into adsorbed oxygen and gaseous H_2 as in M.3–M9.

5. The consecutive steps of CH_4 activation on the surface lead to CHO formation as in M.3, M.7–M.9.
6. The formation of CO in adsorbed state is due to the interaction between an adsorbed carbon and adsorbed oxygen on adjacent site as in M.1, M2, M.5, and M.6.
7. The formation of CO in adsorbed state is due to the interaction between an adsorbed CHO fragment and adsorbed oxygen on adjacent site as in M.3, M7, M.8, M.9.
8. CH_4 activation is the only kinetically relevant step and the C-H bond activation elementary steps are irreversible as presented by M.1 or in equilibrium as in M.2.
9. Surface reactions between adsorbed carbon containing species and adjacent vacant site or adsorbed oxygen leading to the formation of an adsorbed CO and/or CO_2 are considered as rate determining steps as in M.3–M9.

The first mechanism M.1 proposed by Wei and Iglesia on Rh/Al_2O_3 [13] suggests that the CH_4 disappearance rate is proportional to CH_4 partial pressure and independent of the co-reactant (steam) partial pressure. CH_4 activation is considered as the only rate determining step. Consecutive C-H bond activation steps are irreversible. Thus, no influence of any product gas species on the reaction rate can be detected. Furthermore, it shows that the involvement of the support in the activation of the co-reactant is kinetically irrelevant. It also ignores the properties of oxygen present in the reaction kinetics.

These remarks are very much in contradiction with the experimentally derived kinetic data on $Rh/Ce_{\alpha}Zr_{1-\alpha}O_2$ catalyst [29]. We have determined that CH_4 reaction rate has an order of <1 in the CH_4 partial pressure in the temperature range of 475–575 ^{o}C. An inhibitory effect is also observed for the product gas compounds (CO, CO_2, and H_2). The ceria support has a remarkable role in dissociation of CH_4 and thus the reaction kinetics. Therefore, this mechanism is rejected from the analysis.

Mechanism M.2 [52] is similar to M.1 but it differs in assuming that CH_4 activation steps are in equilibrium. This allows CO and H_2 gases to appear in the final reaction rate expression. However, it is also rejected following the same analysis of M.1.

M.3. is based on the derivation of Xu and Froment [46], which assumes the formation of CHO fragment due to the further interaction between adsorbed carbon and adsorbed oxygen. The surface reactions leading to CO and CO_2 formation are thought to be rate determining steps. M.4. suggests a two-site surface for the adsorption of the reactants. CH_4 is dissociatively adsorbed on Rh vacant active site into an adsorbed C-species and an adsorbed H_2; water is dissociatively adsorbed onto a vacant site of the support surface into lattice oxygen and gaseous H_2. However, the interaction step between a gaseous CO and lattice oxygen on the surface yielding a gaseous CO_2 and a free active site is not a likely valid

assumption [24, 26, 39, 41, 53–55]. M.5 and M.6 also presume two–site adsorption surface.

Table 6: Proposed molecular reaction mechanisms for steam reforming*.

M.1		**M.2**		**M.3**	
$CH_4 + 2l \rightarrow CH_3\text{-}l + H\text{-}l$	**1**	$CH_4 + 2l \leftrightarrow CH_3\text{-}l + H\text{-}l$	**1**	$CH_4 + 2l \leftrightarrow CH_3\text{-}l + H\text{-}l$	1
$CH_3 + l \rightarrow CH_2\text{-}l + H\text{-}l$	2	$CH_3 + l \leftrightarrow CH_2\text{-}l + H\text{-}l$	2	$CH_3 + l \leftrightarrow CH_2\text{-}l + H\text{-}l$	2
$CH_2 + l \rightarrow CH\text{-}l + H\text{-}l$	3	$CH_2 + l \leftrightarrow CH\text{-}l + H\text{-}l$	3	$CH_2 + l \leftrightarrow CH\text{-}l + H\text{-}l$	3
$CH\text{-}l + l \rightarrow C\text{-}l + H\text{-}l$	4	$CH\text{-}l + l \leftrightarrow C\text{-}l + H\text{-}l$	4	$CH\text{-}l + O\text{-}l \leftrightarrow CHO\text{-}l + l$	4
$C\text{-}l + O\text{-}l \leftrightarrow CO\text{-}l + l$	5	$C\text{-}l + O\text{-}l \leftrightarrow CO\text{-}l + l$	5	$CHO\text{-}l + l \leftrightarrow CO\text{-}l + H\text{-}l$	**5**
$CO\text{-}l \leftrightarrow CO + l$	6	$CO\text{-}l \leftrightarrow CO + l$	6	$CO\text{-}l + O\text{-}l \leftrightarrow CO_2\text{-}l + l$	**6**
$H\text{-}l + H\text{-}l \leftrightarrow H_2\text{-}l + l$	7	$H\text{-}l \leftrightarrow 1/2H_2 + l$	7	$CHO\text{-}l + O\text{-}l \leftrightarrow CO_2\text{-}l + H\text{-}l$	**7**
$OH\text{-}l + l \leftrightarrow H\text{-}l + O\text{-}l$	8	$OH\text{-}l + l \leftrightarrow H\text{-}l + O\text{-}l$	8	$CO\text{-}l \leftrightarrow CO + l$	8
$H_2O\text{-}l + l \leftrightarrow OH\text{-}l + H\text{-}l$	9	$H_2O\text{-}l + l \leftrightarrow OH\text{-}l + H\text{-}l$	9	$CO_2\text{-}l \leftrightarrow CO_2 + l$	9
$H_2O + l \leftrightarrow H_2O\text{-}l$	10	$H_2O + l \leftrightarrow H_2O\text{-}l$	10	$2H\text{-}l \leftrightarrow H_2\text{-}l + l$	10
				$H_2\text{-}l \leftrightarrow H_2 + l$	11
				$2H\text{-}l \leftrightarrow H_2\text{-}l + l$	12
				$H_2\text{-}l \leftrightarrow H_2 + l$	13
				$H_2O + l \leftrightarrow O\text{-}S + H_2$	14

M.4		**M.5**		**M.6**	
$CH_4 + 2l \leftrightarrow CH_3\text{-}l + H\text{-}l$	1	$CH_4 + 2l \leftrightarrow CH_3\text{-}l + H\text{-}l$	1	$CH_4 + 2l \leftrightarrow CH_3\text{-}l + H\text{-}l$	1
$CH_3 + l \leftrightarrow CH_2\text{-}l + H\text{-}l$	2	$CH_3 + l \leftrightarrow CH_2\text{-}l + H\text{-}l$	2	$CH_3 + l \leftrightarrow CH_2\text{-}l + H\text{-}l$	2
$CH_2 + l \leftrightarrow CH\text{-}l + H\text{-}l$	3	$CH_2 + l \leftrightarrow CH\text{-}l + H\text{-}l$	3	$CH_2 + l \leftrightarrow CH\text{-}l + H\text{-}l$	3
$CH\text{-}l + l \leftrightarrow C\text{-}l + H\text{-}l$	4	$CH\text{-}l + l \leftrightarrow C\text{-}l + H\text{-}l$	4	$CH\text{-}l + l \leftrightarrow C\text{-}l + H\text{-}l$	4
$C\text{-}l + O\text{-}S \leftrightarrow CO + S + l$	**5**	$C\text{-}l + O\text{-}S \leftrightarrow CO\text{-}l + S$	**5**	$C\text{-}l + O\text{-}S \leftrightarrow CO\text{-}S + l$	**5**
$CO + O\text{-}S \leftrightarrow CO_2 + S$	**6**	$CO\text{-}l + O\text{-}S \leftrightarrow CO_2\text{-}l + S$	**6**	$CO\text{-}S + O\text{-}S \leftrightarrow CO_2\text{-}S + S$	**6**
$2H\text{-}l \leftrightarrow H_2 + 2l$	7	$CO\text{-}l \leftrightarrow CO + l$	7	$CO\text{-}S \leftrightarrow CO + S$	**7**
$H_2O + S \leftrightarrow O\text{-}S + H_2$	8	$CO_2\text{-}l \leftrightarrow CO_2 + l$	8	$CO_2\text{-}S \leftrightarrow CO_2 + S$	8
		$2H\text{-}l \leftrightarrow H_2\text{-}l + l$	8	$2H\text{-}l \leftrightarrow H_2\text{-}l + l$	9
		$H_2\text{-}l \leftrightarrow H_2 + l$	9	$H_2\text{-}l \leftrightarrow H_2 + l$	10
		$H_2O + S \leftrightarrow O\text{-}S + H_2$	10	$H_2O + S \leftrightarrow O\text{-}S + H_2$	11

M.7		**M.8**		**M.9**	
$CH_4 + 2l \leftrightarrow CH_3\text{-}l + H\text{-}l$	1	$CH_4 + 2l \leftrightarrow CH_3\text{-}l + H\text{-}l$	1	$CH_4 + 2l \leftrightarrow CH_3\text{-}l + H\text{-}l$	1
$CH_3 + l \leftrightarrow CH_2\text{-}l + H\text{-}l$	2	$CH_3 + l \leftrightarrow CH_2\text{-}l + H\text{-}l$	2	$CH_3 + l \leftrightarrow CH_2\text{-}l + H\text{-}l$	2
$CH_2 + l \leftrightarrow CH\text{-}l + H\text{-}l$	3	$CH_2 + l \leftrightarrow CH\text{-}l + H\text{-}l$	3	$CH_2 + l \leftrightarrow CH\text{-}l + H\text{-}l$	3
$CH\text{-}l + O\text{-}S \leftrightarrow CHO\text{-}S + l$	4	$CH\text{-}l + O\text{-}S \leftrightarrow CHO\text{-}l + S$	4	$CH\text{-}l + O\text{-}S \leftrightarrow CHO\text{-}l + S$	4
$CHO\text{-}S + S \leftrightarrow CO\text{-}S + H\text{-}S$	**5**	$CHO\text{-}l + l \leftrightarrow CO\text{-}l + H\text{-}l$	**5**	$CHO\text{-}l + S \leftrightarrow CO\text{-}l + H\text{-}S$	**5**
$CO\text{-}S + O\text{-}S \leftrightarrow CO_2\text{-}S + S$	**6**	$CO\text{-}l + O\text{-}S \leftrightarrow CO_2\text{-}l + S$	**6**	$CO\text{-}l + O\text{-}S \leftrightarrow CO_2\text{-}l + S$	**6**
$CHO\text{-}S + O\text{-}S \leftrightarrow CO_2\text{-}S + H\text{-}S$	**7**	$CHO\text{-}l + O\text{-}S \leftrightarrow CO_2\text{-}l + H\text{-}S$	**7**	$CHO\text{-}l + O\text{-}S \leftrightarrow CO_2\text{-}l + H\text{-}S$	**7**
$CO\text{-}l \leftrightarrow CO + l$	8	$CO\text{-}l \leftrightarrow CO + l$	8	$CO\text{-}l \leftrightarrow CO + l$	8
$CO_2\text{-}l \leftrightarrow CO_2 + l$	9	$CO_2\text{-}l \leftrightarrow CO_2 + l$	9	$CO_2\text{-}l \leftrightarrow CO_2 + l$	9
$2H\text{-}l \leftrightarrow H_2\text{-}l + l$	10	$2H\text{-}l \leftrightarrow H_2\text{-}l + l$	10	$2H\text{-}l \leftrightarrow H_2\text{-}l + l$	10
$H_2\text{-}l \leftrightarrow H_2 + l$	11	$H_2\text{-}l \leftrightarrow H_2 + l$	11	$H_2\text{-}l \leftrightarrow H_2 + l$	11
$2H\text{-}S \leftrightarrow H_2\text{-}S + S$	12	$2H\text{-}S \leftrightarrow H_2\text{-}S + S$	12	$2H\text{-}S \leftrightarrow H_2\text{-}S + S$	12
$H_2\text{-}S \leftrightarrow H_2 + S$	13	$H_2\text{-}S \leftrightarrow H_2 + S$	13	$H_2\text{-}S \leftrightarrow H_2 + S$	13
$H_2O + S \leftrightarrow O\text{-}S + H_2$	14	$H_2O + S \leftrightarrow O\text{-}S + H_2$	14	$H_2O + S \leftrightarrow O\text{-}S + H_2$	14

*Reaction step in bold represents a rate determining step

In M.5, an adsorbed carbon on a Rh site receives an oxygen atom migrating from a lattice oxygen from adjacent site on the support and form a CO molecule adsorbed on Rh site (*l*). Thus, this adsorbed molecule can react with lattice oxygen to produce an adsorbed CO_2 molecule. These two steps are considered rate determining. M.6. presents slightly different approach. It indicates that the

adsorbed carbon species produced from CH_4 decomposition migrates from its site to reach lattice oxygen on the support and therefore, resulting in CO molecule adsorbed on the support. This molecule undergoes a series reaction with neighboring lattice oxygen to form adsorbed CO_2.

M.7 shows a very dominant role of the support in deciding the kinetics. Rh surface is only employed for series activation steps of CH_4 to finally yield adsorbed CHO molecules on the support. The interaction of this molecule with adjacent free support site or lattice oxygen can give rise to CO and CO_2 adsorbed on the support.

M.8 and M.9 show very vivid interplay between the adsorbed carbon containing species on the Rh and the adjacent free support site or a support site which is occupied by lattice oxygen. M.9 is discussed in details by Halabi et al. [29].

M.3 to M.9 are plausible candidate mechanisms, which are subjected to model discrimination and parameter estimation procedure.

7.4.2 Derivation of experimental reaction rates

The experimental CH_4 conversion data obtained are treated in an integral approach. The relationship between overall CH_4 conversion and CH_4 conversion to CO_2 versus space time (W_{cat}/F_{CH4}) at constant temperature and pressure can be analytically described in terms of polynomial functions [44, 46, 50, 51].

$$x_{CH_4} = a_0 + a_1\left(\frac{W_{cat}}{F_{CH_{4,in}}}\right) + a_2\left(\frac{W_{cat}}{F_{CH_{4,in}}}\right)^2 + a_3\left(\frac{W_{cat}}{F_{CH_{4,in}}}\right)^3 \tag{9}$$

$$x_{CO_2} = b_0 + b_1\left(\frac{W_{cat}}{F_{CH_{4,in}}}\right) + b_2\left(\frac{W_{cat}}{F_{CH_{4,in}}}\right)^2 + b_3\left(\frac{W_{cat}}{F_{CH_{4,in}}}\right)^3 \tag{10}$$

Assuming that steam reforming reaction proceeds only in the presence of catalyst; therefore the following boundary condition holds

$$\text{At} \quad \frac{W_{cat}}{F_{CH_{4,in}}} = 0.0 \qquad x_{CH_4} = x_{CO_2} = 0.0$$

The parameters in these polynomials can be determined by data fitting. Once these polynomials are defined the experimental rate of overall CH_4 conversion and the rate of CH_4 conversion to CO_2 at different space times can be obtained by differentiating these functions with respect to space time W_{cat}/F_{CH4}.

$$r_{CH_4} = \frac{dx_{CH_4}}{d\left(W_{cat}/F_{CH_4,in}\right)} = a_1 + 2a_2\left(\frac{W_{cat}}{F_{CH_4,in}}\right) + 3a_3\left(\frac{W_{cat}}{F_{CH_4,in}}\right)^2 \tag{11}$$

$$r_{CO_2} = \frac{dx_{CH_4}}{d\left(W_{cat}/F_{CH_4,in}\right)} = b_1 + 2b_2\left(\frac{W_{cat}}{F_{CH_4,in}}\right) + 3b_3\left(\frac{W_{cat}}{F_{CH_4,in}}\right)^2 \tag{12}$$

Similarly, the same approach can be applied for the reverse water–gas shift experiments. The experimental overall conversion rate of CO_2 and CO_2 conversion into CH_4 at different space time W_{cat}/F_{CO2} can be determined according to

$$r'_{CO_2} = \frac{dx_{CO_2}}{d\left(W_{cat}/F_{CO_2,in}\right)} = a_1 + 2a_2\left(\frac{W_{cat}}{F_{CO_2,in}}\right) + 3a_3\left(\frac{W_{cat}}{F_{CO_2,in}}\right)^2 \quad (13)$$

$$r'_{CH_4} = \frac{dx_{CO_2}}{d\left(W_{cat}/F_{CO_2,in}\right)} = b_1 + 2b_2\left(\frac{W_{cat}}{F_{CO_2,in}}\right) + 3b_3\left(\frac{W_{cat}}{F_{CO_2,in}}\right)^2 \quad (14)$$

The fitted values for the coefficients of these polynomials are listed in Table 7. The maximum initial reaction rates that can be generated primarily depend on temperature, pressure, and the operating S/C ratio. Fig. 8 shows these rates at different temperatures and at 1.5 bar using S/C ratio=1 and H_2/CH_4=1.
The temperature–dependent rate coefficients and the adsorption coefficients can then be determined from data treatment by substituting the rates of CH_4 disappearance and CO_2 formation into the experimental rates of overall CH_4 conversion and CH_4 conversion to CO_2 and solving by iteration.

$$r_{CH_4} = R_1 + R_3 \quad (15)$$

$$r_{CO_2} = R_2 + R_3 \quad (16)$$

Similarly, the overall CO_2 conversion rate and CO_2 conversion into CH_4 can be obtained from the experimental rates of reverse water–gas shift experiments as

$$r'_{CO_2} = -(R_2 + R_3) \quad (17)$$

$$r'_{CH_4} = -(R_1 + R_3) \quad (18)$$

Table 7. Possible reactions on $Rh/Ce_\alpha Zr_{1-\alpha}O_2$ catalyst surface.

		$a_1(b_1)$	$a_2(b_2)$	$a_3(b_3)$
Steam reforming experiments				
475 °C	x_{CH4}	8.7092	– 2.5288	0.2745
	x_{CO2}	2.7051	– 0.3493	
500 °C	x_{CH4}	11.278	– 2.9781	0.2868
	x_{CO2}	3.6782	– 0.4629	
525 °C	x_{CH4}	13.951	– 3.4392	0.3327
	x_{CO2}	4.3809	– 0.5166	
550 °C	x_{CH4}	18.398	– 4.7119	0.4839
	x_{CO2}	5.2909	– 0.6081	
575 °C	x_{CH4}	21.903	– 5.6707	0.6024
	x_{CO2}	5.9737	– 0.6484	
Reverse WGS experiments				
400 °C	x_{CH4}	2.7047	– 0.4863	
	x_{CO2}	2.8894	– 0.2771	
450 °C	x_{CH4}	4.7325	– 0.7029	
	x_{CO2}	5.8024	– 0.8225	
500 °C	x_{CH4}	9.2865	– 2.3002	0.2301
	x_{CO2}	10.097	– 2.0027	0.1174

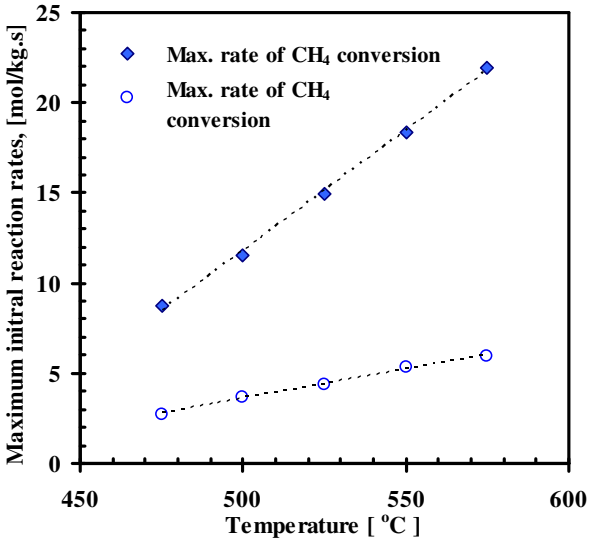

Fig. 8: Maximum initial reaction rates at different temperatures and 1.5 bar using S/C ratio=1, H_2/CH_4=1.

7.4.3 Model discrimination and parameter estimation

Considering the conversion data obtained from the kinetic experiments; a total of 448 points are collected to produce experimental reaction rates data. 56 data points are used at every temperature of (475, 500, 525, 550, and 575 °C) for steam reforming reaction and at (400, 450, and 500 °C) for reverse water–gas shift reaction. A kinetic model is derived for each of the proposed reaction mechanisms (M.3–M.9) according to Langmuir–Hinshelwood formalism. The rate expression is written for each rate determining step. The concentrations are then eliminated based on the Langmuir equilibrium relations and the active site balance for the vacant and occupied sites**.**

The estimation of the kinetic model parameters from the experimental set of data is performed in gPROMS modelling software package. The parameter estimation optimization solver uses the maximum–likelihood approach. This approach is based upon the minimization of a specific objective function Φ that considers the difference ξ_i between the experimental values $z_i^{\sim}$ and the model predicted values $z_i(\theta)$ for measurement *i* with different variance models. The Gaussian probability density function used by the algorithm assumes that ξ_i is independent and normally distributed with zero means and standard deviation σ_i. A constant variance model in which the measurement error has constant standard deviation is used.

The adequacy of fitting is determined by the weighted residuals (WR) and (χ^2) values. A weighted residual less than (χ^2) value is considered a good fit. The accuracy of parameter estimate is determined by the t-value and the 95% confidence interval. The t-value associated to a parameter is compared with the reference 95% t-value, which is calculated using internal statistical functions. A t-value larger than the reference t-value indicates that the corresponding parameter has been accurately estimated. Smaller t-values indicate poor estimates.

$$\Phi = \frac{N}{2}\ln(2\pi) + \frac{1}{2}\min_{\theta}\left\{\sum_{i=1}^{NE}\sum_{j=1}^{NV_i}\sum_{k=1}^{NM_{ij}}[\ln(\sigma_{ijk}^2) + \frac{(z_{ijk}^{\sim} - z_{ijk})^2}{\sigma_{ijk}^2}]\right\} \quad (19)$$

$$\xi_i = z_i^{\sim} - z_i(\theta) \quad (20)$$

The discrimination between the suggested models is conducted based on (1) the physical consideration of the parameter estimates, i.e. if one of the constants are found to be negative, which is supposed to positive, the corresponding model is rejected (2) the adequacy of fitting according to the (WR) and (χ^2) values, and (3) the consistency of the activation energies and the adsorption enthalpies obtained with their physical values reported in literature.

As a result of these criteria, only two models (M.8 and M.9) retained after the parameter estimation procedure. However, the activation energy of the steam reforming reaction (R_1) obtained from model M.8. was 203 kJ/mol. This is relatively high activation energy for steam reforming over Rh–based catalyst [13, 27]. The model also gives a very low adsorption enthalpy of CH_4 (-25.6 kJ/mol). Therefore, this model is also rejected. The failure of this model is attributed to the fact that it suggests that CH_4 steam reforming (R_1) proceeds on the Rh active sites (l) only. The kinetic rate generated from this step ignores that the presence of ceria as a support creates a strong interaction with the active metal and facilitates the dissociation of CH_4. Thus, the catalyst activity and the CH_4 reforming rates are mis-estimated.

By analyzing the product gas composition in the steam reforming experiments, CO was found to be present in negligible amounts due to the high activity of the water–gas shift reaction. The latter was also found to be close to equilibrium as determined from the thermodynamic analysis. Therefore, the kinetic parameters associated with CO adsorption (K_{CO}) and water–gas shift reaction (k_2) could not be estimated from steam reforming experiments. These parameters are significantly estimated from the reverse water–gas shift experiments.

The rate equations and the final values of the kinetic parameters corresponding to the retained model M.9 are given in Tables 8 and 9; respectively.

Table 8: The derived kinetic model corresponding to mechanism (M.9).

Reaction rate equation	
$R_1 = \frac{k_1}{p_{H_2}^{2.5}}\left(p_{CH_4}p_{H_2O} - \frac{p_{H_2}^3 p_{CO}}{K_I}\right) * \Omega_I\Omega_S$	(21)
$R_2 = \frac{k_2}{p_{H_2}}\left(p_{CO}p_{H_2O} - \frac{p_{H_2}p_{CO_2}}{K_{II}}\right) * \Omega_I\Omega_S$	(22)
$R_3 = \frac{k_3}{p_{H_2}^{3.5}}\left(p_{CH_4}p_{H_2O}^2 - \frac{p_{H_2}^4 p_{CO_2}}{K_{III}}\right) * \Omega_I\Omega_S$	(23)
$\Omega_I = \frac{1}{1 + k_{CH_4}P_{CH_4}/P_{H_2}^{0.5} + k_{CO}p_{CO} + k_{CO_2}p_{CO_2} + k_{H_2}P_{H_2}}$ $\Omega_S = \frac{1}{1 + k_{H_2O}p_{H_2O}/p_{H_2} + k_{H2}p_{H_2}}$	(24)

Table 9. Final estimated values for the kinetic parameters corresponding to model M.9.

		k_1	k_2	k_3	K_{CH4}	K_{H2}	K_{CO}	K_{CO2}	K_{H2O}	χ^2	WR
Steam reforming experiments											
475 °C											
	Value	200.8	_	280.5	0.12	0.51	_	0.11	0.53	1450	649
	t-value	2.35		3.25	2.61	2.90		1.91	1.93		
500 °C											
	Value	383.1	_	480.7	0.07	0.41		0.08	0.91	1435	603
	t-value	3.55		2.08	1.86	2.74	_	1.84	2.52		
525 °C											
	Value	505.9	_	610.5	0.05	0.23		0.04	1.7	1411	628
	t-value	3.77		4.85	1.95	2.82	_	1.74	2.11		
550 °C											
	Value	752.6	_	1156.6	0.03	0.16		0.02	2.4	1395	592
	t-value	4.24		2.67	1.85	2.05	_	1.88	2.83		
575 °C											
	Value	1234.7	_	1409.3	0.01	0.10		0.01	3.3	1402	641
	t-value	3.96		2.99	2.61	2.87	_	1.66	2.07		
Reverse WGS experiments											
400 °C											
	Value	50.2	16105	61.9	0.695	2.756	6.231	_	_	1205	713
	t-value	4.02	3.62	4.58	1.93	3.11	3.72				
450 °C											
	Value	143.9	18230	179.9	0.209	0.942	3.732	_	_	1319	544
	t-value	2.86	3.96	3.35	1.89	2.98	3.24				
500 °C											
	Value	359.9	22303	460.8	0.071	0.361	0.601	_	_	1229	840
	t-value	3.54	4.66	3.15	1.81	2.08	2.90				

Fig. 9 shows the Arrhenius plot of the final estimated kinetic rate coefficients (k_1, k_2, k_3) versus temperature. The estimated adsorption constants are also plotted versus temperature and given in Fig. 10. The pre-exponential rate constants and the activation energies are calculated by applying the Arrhenius equation at different

temperatures, Eq. (25). Similarly, the reference adsorption constants and the adsorption enthalpies for each species are determined from van't Hoff equation at different temperatures (Eq. 26).

$$k_j = k_{j,o} * exp\left(-\frac{E_j}{RT}\right) \tag{25}$$

$$K_i = K_{i,o} * exp\left(-\frac{\Delta H_{ads,i}}{RT}\right) \tag{26}$$

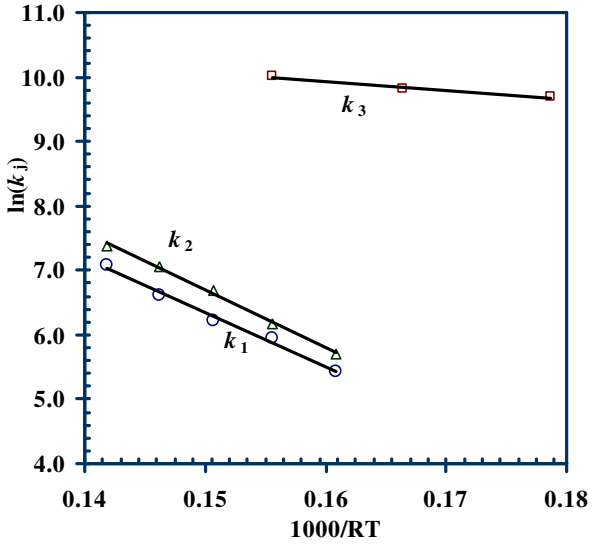

Fig. 9: Temperature-dependent rate constants according to Arrhenius equation.

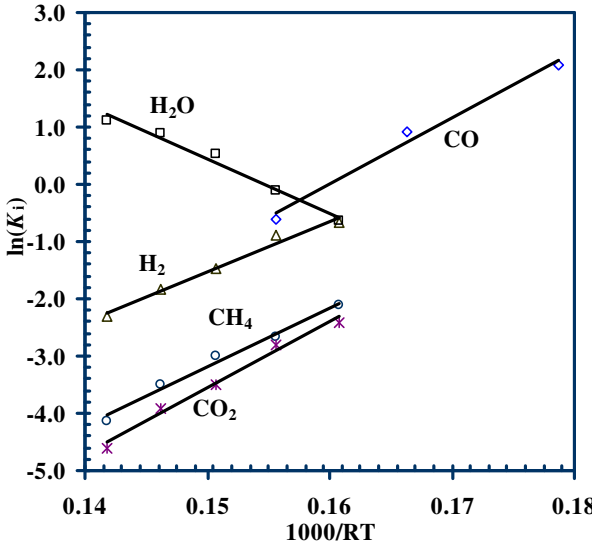

Fig. 10: Temperature-dependent adsorption constants according to van't Hoff equation

The final values of the Arrhenius kinetic parameters and the apparent activation energies are presented in Table 10. The adsorption parameters and adsorption enthalpies are shown in Table 11.

Table 10: Arrhenius kinetic parameters

Reaction, j (see Table 4)	$k_{j,o}$ [mol/kg$_{cat}$.s]	E_j [kJ/mol]
1	$1.62*10^{8}$ kPa$^{0.5}$	83.8
2	$2.34*10^{5}$ kPa^{-1}	15.1
3	$4.55*10^{8}$ kPa$^{0.5}$	89.2

Table 11: Van't Hoff adsorption parameters

Reaction, j (see Table 4)	$K_{i,o}$ [kPa^{-1}]	ΔH_i [kJ/mo]
CH_4	$1.49*10^{-8}$	– 98.8
CO	$2.34*10^{-8}$	–111.2
CO_2	$8.33*10^{-10}$	–115.6
H_2	$3.88*10^{-7}$	–88.2
H_2O	$2.91*10^{6}$	112.3

Finally, the predicted rates produced by model M.9 show excellent agreement with the experimentally derived rates. Petri plots of this compassion are given for steam reforming and reverse water–gas shift experiments in Fig. 11 and 12; respectively.

The activation energy for steam reforming reaction over the studied catalyst (83.8 k/mol) is found to be consistent with values reported for this reaction over Rh [13, 27]. However, it is somewhat smaller than that determined by Wei and Iglesia for Rh over alumina (109 kJ/mol) [13]. This is attributed to the higher activity shown by catalyst when it is supported over ceria–zirconia. The adsorption energies of CH_4, CO, and H_2 are also in the range of the physical values estimated in other studies for CH_4 activation or CO/H_2 adsorption over Rh. Vorgin et al. [52] and Maroto-Valiente et al. [53] studied the adsorption of CO and H_2 over Rh. They determined an adsorption enthalpy of (60–130 kJ/mol) for H_2 and an enthalpy of CO (90–120 kJ/mol) depending on the active metal loading and the species coverage on the surface. This consistency increases firms our confidence in the suggested model to describe CH_4 steam reforming over Rh at low temperatures.

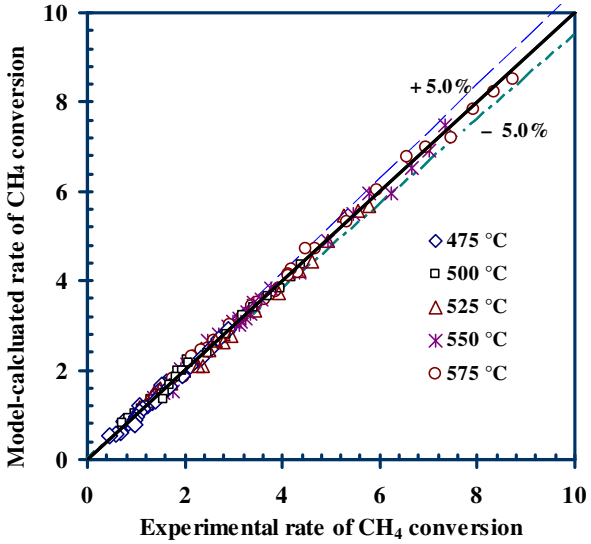

Fig. 11.: A comparison between the experimental rates of CH_4 conversion and the predicted rates obtained from model M.9 for steam reforming experiments.

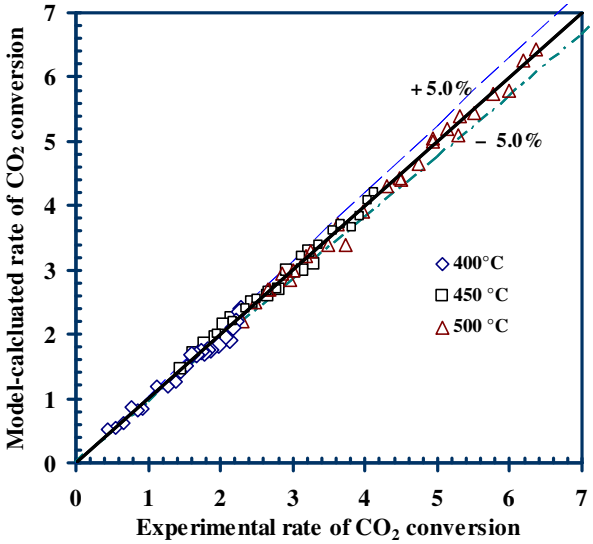

Fig. 12.: A comparison between the experimental rates of CO_2 conversion and the predicted rates obtained from model M.9 for reverse water–gas shift experiments.

6.4.4 Satisfaction of thermodynamic criteria

The final retained model should satisfy a number of thermodynamic criteria proposed by Boudart et al. [60] for the adsorption constants:

$$(1)\ \Delta S^{o}_{i,a} < 0.0 \ \textbf{or}\ exp\left(\frac{\Delta S^{o}_{i,a}}{R}\right) = K_{i,o} < 1.0 \qquad (27)$$

The pre-exponential constants obtained for the gas species satisfy this criterion, see Table 12.

Table 12: Satisfaction of thermodynamic rule (1)

Species, i	$K_{i,o}$ [kPa^{-1}]	$\Delta S^{o}_{i,a}$ J/mol.K
CH_4	$1.49*10^{-8}$	–149.8
CO	$2.34*10^{-8}$	–146.1
CO_2	$8.33*10^{-10}$	–173.8
H_2	$3.88*10^{-7}$	–122.7

For the non-dissociative adsorption, the following rule should be satisfied:

$$(2)\ \left|\Delta S_{i,a}^{o}\right| < S_{i,g}^{o} \quad \text{or} \quad K_{i,o} > exp\left(-\frac{S_{i,g}^{o}}{R}\right) \tag{28}$$

The pre-exponential constants fulfills this rule, see Table 13.

Also, the following criterion should be satisfied:

$$(3)\ \Delta S_{i,a}^{o} \geq \left(0.0014\Delta H_{i,ads} - 12.2\right) \quad \text{or} \quad ln\left(K_{i,o}\right) \leq \left(12.2 - 0.0014\Delta H_{i,ads}\right)/R \tag{29}$$

According to the estimates of the adsorption parameters, this rule is also fulfilled. The values of the parameter of this rue are shown in Table 14.

Table 13: Satisfaction of thermodynamic rule (2)

Species, i	$K_{i,o}$ [kPa^{-1}]	$\left\|\Delta S_{i,a}^{o}\right\|$ J/mol.K	$S_{i,g}^{o}$ J/mol.K	$exp\left(-S_{i,g}^{o}/R\right)$
CH_4	1.49*10^{-8}	149.8	186.1	1.9*10^{-10}
CO	2.34*10^{-8}	146.1	198.5	4.3*10^{-11}
CO_2	8.33*10^{-10}	173.8	213.0	7.5*10^{-12}
H_2	3.88*10^{-7}	122.7	130.5	1.5*10^{-07}

Table 14: Satisfaction of thermodynamic rule (3)

Species, i	$ln\left(K_{i,o}\right)$	$\left(12.2 - 0.0014\Delta H_{i,ads}\right)/R$
CH_4	–18.02	18.10
CO	–17.57	20.19
CO_2	–20.91	20.93
H_2	–14.67	16.32

(4) Usually, the absolute values for entropy changes for the non-dissociative adsorption are greater than 42 J/mol. Since the absolute $\Delta S_{i,a}^{o}$ values for CH_4, CO, CO_2, and H_2 given in Table 13 are obliviously higher than 42 J/mol, therefore, this criterion is also satisfied.

However, it is observed that the adsorption of steam could not follow these rules. This situation is experienced by different researchers [44, 46, 56]. Since steam is easily adsorbed on different surfaces, the equilibrium adsorption constant K_{H2O} resulted from steam adsorption on the support could not be seen as a true equilibrium constant. Steam is considered to be primarily adsorbed on the support; however, we can not exclude its adsorption on the catalyst. Therefore, the equilibrium adsorption constant K_{H2O} reflects only steady state condition reached by more than one adsorption step. Thus, it does not follow the thermodynamic rules discussed earlier. H_2 adsorption on both surfaces of the Rh metal and the ceria support can also be envisaged in the same manner as it is for steam. Nevertheless, the logical value of the H_2 adsorption enthalpy (-88.2 kJ/mol) and its corresponding adsorption constant reveals that the equilibrium adsorption/dissociation steps of H_2 on either the support sites (*S*) or the Rh sites (*l*) are very fragile comparing to the other. It is also possible that one of these steps on either surface is not in

equilibrium. Therefore, calculated value for the adsorption enthalpy reflects in this case true adsorption equilibrium on one surface only. Thus the thermodynamic rules are satisfied for H_2 adsorption.

7.5 Model validation

A steam reforming experiment is performed over 10 mg catalyst diluted with 450 mg α-alumina (catalyst bulk density is 15.9 kg/m^3) at 550 ^{o}C and 1.5 bar using the following operational conditions (7.0 kPa CH_4, 28.0 kPa H_2O, and 4.0 kPa H_2). A total volumetric flow rate of 100 nml/min is used. The catalyst is placed in a fixed bed integral reactor of a 4.0 mm inside diameter. The length of the catalyst and the diluent packed inside the reactor was 5.0 cm. The experimental CH_4 conversion and H_2 yield obtained at steady state condition are 81% and 3.0 mol H_2/mol CH_4 fed; respectively.

A one-dimensional pseudo homogenous plug flow model is constructed to validate the accuracy of the derived kinetic model by real experiments. A simplified mass balance equation can then be written for the experimental reactors as

$$\frac{\partial C_i}{\partial t} + \frac{\partial (uC_i)}{\partial z} = \rho_{bulk} r_i \tag{30}$$

The following assumptions have been made:
1. Isothermal operation;
2. Negligible pressure drop;
3. No mass transport limitations.

The model is simulated at identical conditions of the experiment. The set of algebraic differential equations produced is implemented and solved in gPROMS software package. Spatial discretization of backward difference over a uniform grid of 50 points is used as a discretization method.

Basic simulation results at steady state conditions are presented in Fig. 13 and 14. The gas composition profiles are given in terms of the partial pressures of the components. Fig. 13 illustrates a conventional decrease in the reactant partial pressures (CH_4 and steam) and a natural increase in the product partial pressures of (CO, CO_2, and H_2) along the reactor length. The composition significantly changes along the first 30% of the reactor length. At steady state, CH_4 conversion and H_2 yield approach 79% and 2.95 mol H_2/mol CH_4; respectively as shown in Fig. 14. These simulated results are in very good agreement with the measured values produced from the experiments (81% and 3, respectively). Although a simplified mathematical model is used in simulating the experiment, but it provides sufficient confidence in the derived reactions kinetics. Therefore, the reaction kinetics developed in this work has enough accuracy to describe the steam reforming reactions in a low temperature range of (475–575 ^{o}C) over $Rh/Ce_\alpha Zr_{1-\alpha}O_2$ catalyst.

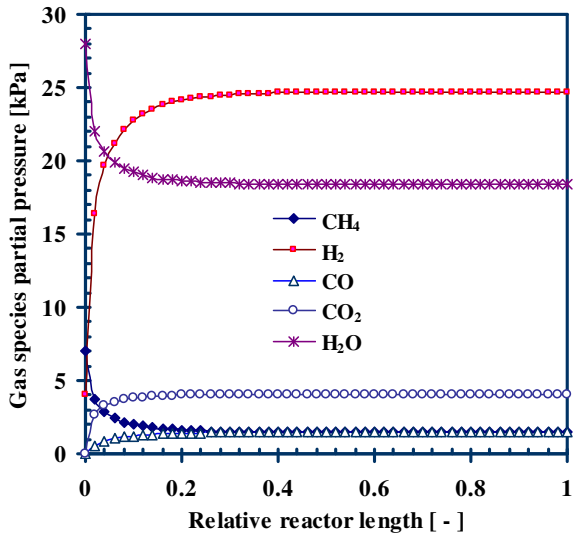

Fig. 13: Steady state gas composition profile versus the relative reactor length at 550 °C and 1.5 bar.

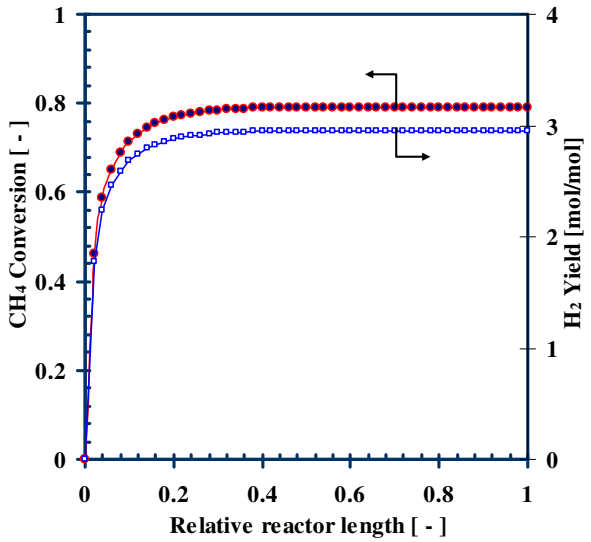

Fig. 14: Steady state CH_4 conversion and H_2 yield profiles versus the relative reactor length at 550 °C and 1.5 bar.

The activity of the $Rh/Ce_{\alpha}Zr_{1-\alpha}O_2$ catalyst and the performance of the kinetic model are further compared to the conventional Ni–based catalyst of steam reforming. The kinetics of Xu and Froment [46] is sued for this comparison. Fig. 15 demonstrates the steady state CH_4 conversion profile along the relative length of a 5 cm fixed bed reactor for the two catalysts at 550 °C and 1.5 bar. The gas composition used is (7.0 kPa CH_4, 28.0 kPa H_2O, and 4.0 kPa H_2). 10 mg of the catalyst loading is initially used for both catalysts. Xu & Froment kinetics [46], and correspondingly, the Ni–based catalyst yield a maximum CH_4 conversion of 64%; the kinetic model derived in this work for Rh–based catalyst predicts a maximum CH_4conversion of 79% as aforementioned. This is obviously attributed to the high activity of Rh catalyst in comparison to Ni catalyst. The Ni catalyst loading is required to be increased 14 times in order to match the activity of Rh catalyst as it is also shown in the figure.

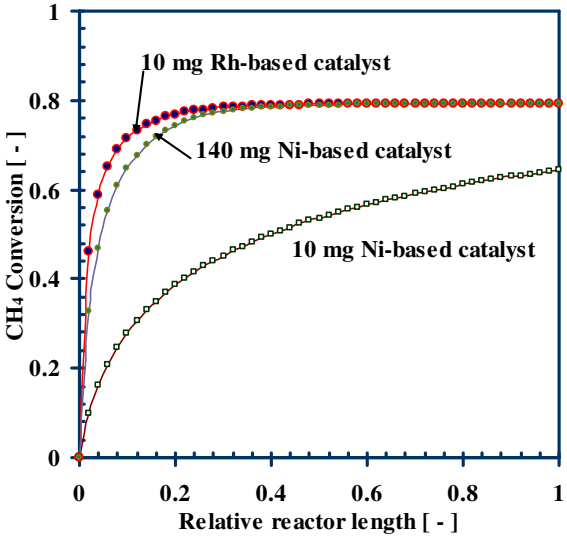

Fig. 15: Model–based comparison of steady state CH_4 conversion between $Rh/Ce_{0.6}Zr_{0.4}O_2$ catalyst and Ni–based catalyst (using Xu & Froment kinetics [46]) at 550 °C and 1.5 bar.

7.6 Conclusions

The intrinsic kinetics of CH_4 steam reforming is developed over $Rh/Ce_{0.6}Zr_{0.4}O_2$ catalyst in a relatively low temperature range of 475–575 ^oC and 1.5 bar. The kinetic experiments are conducted in an integral fixed bed reactor with no mass and heat transport limitations and far from equilibrium conditions. Therefore, intrinsic reaction rate measurements are guaranteed. The kinetic rate expression is derived according to Langmuir-Hinshelwood formalism. The model is based upon two-site adsorption surface with 14 elementary reaction steps. CH_4 is dissociatively adsorbed onto the Rh active sites, and steam is dissociatively adsorbed on the ceria support active sites as an influential adsorption surface shown in the model. Therefore, no competition between CH_4 and steam in adsorbing on the same site surface is reflected in the kinetic rates. However, this does not exclude the possibility of steam adsorption on Rh. The surface reactions between the carbon containing radials and the lattice oxygen leading to CO and CO_2 formation are considered as rate determining steps. The inhibitory effect of gaseous product species is also reflected in the model denominator. The model is found to be statistically accurate and thermodynamically consistent. The estimated activation energies and adsorption enthalpies are in agreement with literature for CH_4 steam reforming reaction over Rh.

Nomenclature

Symbol	Definition	Unit
$C_{i,s}$	Concentration of species i in the solid phase	mol/m^3
D_{eff}	Effective diffusion coefficient	m^2/s
d_p	Catalyst particle diameter	m
E_j	Activation energy of reaction j	J/mol
F_i	Molar flow rate of species i	mol/s
h_f	Gas to solid heat transfer coefficient	W/m^{2}s
k_j	Temperature dependent kinetic rate constant of reaction j	
$k_{j,o}$	Arrhenius kinetic rate constant of reaction j	
$K_{eq,j}$	Thermodynamic equilibrium constant of reaction j	kPa$^{\Sigma \nu_{ij}}$
$K_{i,o}$	Reference adsorption constant of species i	1/kPa
K_i	Adsorption constant of species i	1/kPa
n	Reaction order	
N	Total number of measurements taken in all experiments	
NE	Number of performed experiments	
NV_i	Number of variables measured in experiment *i*	
NM_{ij}	Number of measurements of variable *j* in experiment *i*	
p_i	Partial pressure of gas species i	kPa
r_i	Rate of consumption or formation of species i	mol/kg$_{cat}$.s
R_{obs}	Observed rate of conversion of CH_4	mol/kg$_{cat}$.s
R_j	Rate of reaction j	mol/kg$_{cat}$.s
R	Universal gas constant	J/mol.K
$S^o_{i,g}$	Standard entropy of gas species i	J/mol.K
T	Gas phase temperature	K
u	Superficial gas flow velocity	m/s
u_{inst}	Interstitial gas velocity	m/s
W_{cat}	Catalyst loading in the reactor	kg
$\tilde{z_i}$	The experimental value for the *k*th measurement of variable *j* in experiment *i*,	–
$z_i(\boldsymbol{\theta})$	The model prediction for the *k*th measurement of variable *j* in experiment *i*	–

Greek symbols

ΔH_i $\Delta H_{ads,i}$	Heat of adsorption of species i	J/mol
ΔH_{298K}, ΔH_{rxn}	Heat of reaction of at STP	kJ/mol
$\Delta S^o_{i,a}$	Entropy change of species i in adsorbed state	J/mol.K
$\boldsymbol{\theta}$	The set of model parameters to be estimated	–
η_j	Effectiveness factor of reaction j	–
Φ	The objective function to be minimized in the parameter estimation solver	–
σ^2_{ijk}	The variance of the *k*th measurement of variable *j* in experiment *i*	–
σ_i	The standard deviation for measurement i.	–
ξ_i	The difference between experimental and predicted value for measurement *i*	–
ν_{ij}	Stoichiometric coefficient of species i in reaction j	–
λ_p	Solid thermal conductivity	W/m.K

ρ_{bulk}	Bulk density of the catalyst pellet	kg/m^3
Ω_j	Dominator term in the kinetic rate of reaction j	–

References

1. Hufton, J. R., Mayorga, S., Sircar, S. Sorption-enhanced reaction process for hydrogen production. AIChE J. 45 (1999) 248–256.
2. Ding, Y., Alpay, E. High temperature recovery of CO_2 from flue cases using hydrotalcite adsorbent. Trans IChemE. 79-B1 (2001) 45–51.
3. Xiu, G.; Soares, J. L.; Li, P.; Rodrigues, A. E. Simulation of five-step one-bed sorption-enhanced reaction process. AIChE J. 48 (2002) 2817–2832.
4. Rostrup-Nielsen, J. R, Sehested, J., Norskov, J.K., Hydrogen and synthesis gas by steam-and CO_2 reforming, Adv. Catal. 47 (2002) 65-139.
5. Ayabe, S., Omoto, H., Utaka, T.,. Kikkuchi, R., Sasaki, K., Teraoka, Y., Eguchi, K., Catalytic autothermal reforming of methane and propane over supported metal catalysts, App. Catal. A 241 (2003) 261-269.
6. Bradford, M.C.J, Vannice, M., Catalytic reforming of methane with carbon dioxide over nickel catalysts I. Catalyst characterization and activity App. Catal. A 142 (1996) 73-96.
7. Bitter, J.H., Seshan, S., Lercher, J.A., Mono and Bifunctional Pathways of CO_2/CH_4Reforming over Pt and Rh Based Catalyst, J. Catal. 176 (1998) 93-101.
8. Sakai, Y., Saito, H., Sodesawa, T., Noz`aki, F., Catalytic reactions of hydrocarbon with carbon dioxide over metallic catalysts, React. Kinet. Catal. Lett. 24 (1984) 253-257.
9. Mark, M.F., Maier, W.F., CO_2-Reforming of Methane on Supported Rh and Ir Catalysts, J. Catal. 164 (1996) 122-130.
10. Wang, D., Dewaele, O., Froment, G.F., Methane adsorption on Rh/Al_2O_3, J. Mol. Catal. A 136 (1998) 301-309.
11. Hickman, D.A., Schmidt, L.D., Steps in CH_4 oxidation on Pt and Rh surfaces: High-temperature reactor simulations, AICHE J. 39 (1993) 1164-1177.
12. Kurungot, S., Yamaguchi, T., Stability Improvement of Rh/γ-Al_2O_3 Catalyst Layer by Ceria Doping for Steam Reforming in an Integrated Catalytic Membrane Reactor System, Catal. Lett. 92 (2004) 181-187.
13. Wei, J., Iglesia, E., Structural requirements and reaction pathways in methane activation and chemical conversion catalyzed by rhodium, J. Catal. 225 (2004) 116-127.
14. Wang, H.Y., Ruckenstein, E., Carbon dioxide reforming of methane to synthesis gas over supported rhodium catalysts: the effect of support, Appl. Catal. 204 (2000) 143-152.
15. Wang, H.Y., Ruckenstein, E., CH_4/CD_4 Isotope Effect and the Mechanism of Partial Oxidation of Methane to Synthesis Gas over Rh/γ-Al_2O_3 Catalyst, J. Phys. Chem. 103 (1999) 11327-11331.

16. Tsipouriari, V.A., Efstathiou, A.M., Zhang, Z.L., Verykios, X.E., Reforming of methane with carbon dioxide to synthesis gas over supported Rh catalysts, Catal. Today 21 (1994) 579- 587.
17. Yokota, S., Okumura, Y., Niwa, M., Support Effect of Metal Oxide on Rh Catalysts in the CH_4-CO_2 Reforming Reaction, Catal. Lett. 84 (2002) 131-134.
18. Wang, H.Y., Au, C.T., Carbon dioxide reforming of methane to syngas over SiO_2-supported rhodium catalysts, Appl. Catal. A 155 (1997) 239-252.
19. Gronchi, P., Centola, P., Del Rosso, R., Dry reforming of CH_4 with Ni and Rh metal catalysts supported on SiO_2 and La_2O_3, Appl. Catal. A 152 (1997) 83-92.
20. Zhang, Z.L., Tsipouriari, V.A., Efstathiou, A.M., Verykios, X.E., Reforming of Methane with Carbon Dioxide to Synthesis Gas over Supported Rhodium Catalysts: I. Effects of Support and Metal Crystallite Size on Reaction Activity and Deactivation Characteristics, J. Catal. 58 (1996) 51-63.
21. Qin, D., Lapszewicz, J., Study of mixed steam and CO_2 reforming of CH_4 to syngas on MgO-supported metals, Catal. Today 21 (1994) 551-560.
22. Sadi, F., Duprez, D., Gerard, F., Miloudi, A., J. Catal. 213 (2003) 226-234.
23. Wang, R., Xu, H., Liu, X., Ge., Q., Li, W., Role of redox couples of $Rh^0/Rh^{\delta+}$ and Ce^{4+}/Ce^{3+} in CH_4/CO_2 reforming over Rh–CeO_2/Al_2O_3 catalyst, App. Catal. A 305 (2006) 204-210.
24. Wang, R., Xu, H., Liu, X., Ge, Q., Chin, L., The Effect of Supports on the Activity of Methane Dissociation over Rh Catalysts, . J. Catal. 28 (2007) 293-295.
25. J.A. Wang, T. Lopez, X. Bokhimi, O. Novaro, Phase Composition, Reducibility and Catalytic Properties of Rh/zriconia and Rh/zirconia-ceria Catalysts, J. Mol. Catal. A: Chem. 239 (2005) 249-256.
26. Cao, L., Pan, L., Ni, C., Yuan, Z., Wang, S., Fuel Proc. Technol. 91 (2010) 306-312.
27. Hennings, U., Reimert, R., App. Catal. A, 337 (2008) 1-9.
28. Kusakabe, K., Sotowa, K-I., Eda, E., Iwamoto, Y., Methane steam reforming over Ce–ZrO_2-supported noble metal catalysts at low temperature, Fuel Process Technol., 86 (2004) 319-326.
29. Halabi, M.H., de Croon, M.H.J.M, van der Schaaf, J., Cobden, P.D., Schouten, J.C., Low temperature catalytic methane–steam reforming over ceria–zirconia supported rhodium, App. Catal. A (2010) 10.1016/j.apcata.2010.09.004.
30. Otsuka, K., Ushiyama, T., Yamanaka, I., Partial Oxidation of Methane Using the Redox of Cerium Oxide, Chem. Lett. (1993) 1517-1520.
31. Otsuka, K., Hatano, M., Morikawa, A., Hydrogen from water by reduced cerium oxide, J. Catal. 79 (1983) 493-496.
32. Otsuka, K., Hatano, M., Morikawa, A., Decomposition of water by cerium oxide of δ-phase, Inorg. Chim. Acta 109 (1985) 193-197.
33. Ramirez, E., Atkinson, A., Chadwick, D., Appl. Catal. B 36 (2002) 193-206.
34. Ramı´rez-Cabrera, E., Laosiripojana, N., Atkinson, A., Chadwick, D., Methane conversion over Nb-doped ceria, Catal. Today 78 (2003) 433-438.
35. Ramı´rez-Cabrera, E., Atkinson, A., Chadwick, D., Catalytic steam reforming of methane over $Ce_{0.9}Gd_{0.1}O_{2-x}$, Appl. Catal. B 47 (2004) 127-131.

36. Laosiripojana, N., Sutthisripok, W., Assabumrungrat, S., Synthesis gas production from dry reforming of methane over CeO_2 doped Ni/Al_2O_3: Influence of the doping ceria on the resistance toward carbon formation, Chem.Eng. J. 112 (2005) 13-22.
37. Laosiripojana, N., Assabumrungrat, S., Catalytic dry reforming of methane over high surface area ceria, Appl. Catal. B: Environ. 60 (2005) 107-116.
38. Kusakabe, K., Sotowa, K-I., Eda, E., Iwamoto, Y., Methane steam reforming over Ce–ZrO_2-supported noble metal catalysts at low temperature, Fuel Process Technol., 86 (2004) 319-326.
39. Dong, W.S., Roh, H.S., Jun, K.W., Park, S.E., Oh, Y.S., Methane reforming over Ni/Ce-ZrO_2 catalysts: effect of nickel content, Appl. Catal. A 226 (2002) 63-72.
40. Laosiripojana, N., Chadwick, D., Assabumrungrat, S., Effect of high surface area CeO_2 and Ce-ZrO_2 supports over Ni catalyst on CH_4 reforming with H_2O in the presence of O_2, H_2, and CO_2, Chem. Eng. J. 138 (2008) 264-273.
41. Imamaura, S., Yamashita, T., Hamada, R., Saito, Y., Nakao, Y., Tsuda, N., Kaito, C., J. Mol. Catal. A 129 (1998) 249-256.
42. Laosiripojana, N., Assabumrungrat, S., Methane steam reforming over Ni/Ce-ZrO_2 catalyst: Influences of Ce-ZrO2 support on reactivity, resistance toward carbon formation and intrinsic reaction kineticsAppl. Catal. A: Gen.290 (2005) 200-211.
43. Dicks, A.L., Pointon, K.D., Siddle, A., Intrinsic reaction kinetics of methane steam reforming on a nickel/zirconia anode , J. Power Sources 86 (2000) 523-530.
44. Hou, K., Hughes, R., The kinetics of methane steam reforming over a Ni/α-Al_2O catalyst, Chem.Eng. J. 82 (2001) 311-328.
45. Berman, B., Karn, R.K., Epstein, M., Kinetics of steam reforming of methane on Ru/Al_2O_3 catalyst promoted with Mn oxides, App. Catal. A 282 (2005) 73-83.
46. Xu, J., Froment, G.F., Methane steam reforming, methanation and water-gas shift: I. Intrinsic kinetics, AIChE J. 35 (1989) 88-96.
47. Weisz, P.B, Prater, C.D., Interpretation of measurements in experimental catalysis, Adv.Catal. 6 (1954) 143-196.
48. Mears, D.E., diagnostic criteria for heat transport limitations in fixed bed reactors, J. Catal. 20 (1971) 127-131.
49. Halabi, M.H., de Croon, M.H.J.M, van der Schaaf, J., Cobden, P.D., Schouten, J.C., Modeling and analysis of autothermal reforming of methane to hydrogen in a fixed bed reformer, Chem. Eng. J. 137 (2008) 568-578.
50. Perry, R.H., Green, D.W., Perry's Chemical Engineering's Handbook, 7th Ed. McGraw Hill, (1997).
51. Halabi, M.H., de Croon, M.H.J.M, van der Schaaf, J., Cobden, P.D., Schouten, J.C., A novel catalyst–sorbent system for an efficient H_2 production with in-situ CO_2 capture, Int. J. Hydrogen Energy, submitted, (2010).
52. Jones, G., Jakobsen, J.G., Shim, S.S., Kleis, J., Andersson, M.P., Rossmeisl, J., Abild-Pedersen, F., Bligaard, T., Helveg, S., Hinnemann, B., Rostrup-Nielsen, J-R., Chorkendorff, I., Sehested, J., Norskov, J., First principles calculations

and experimental insight into methane steam reforming over transition metal catalysts, J. Catal. 259 (2008) 147-160.
53. Mullins, D.R., Overbury, S.H., CO dissociation on Rh deposited on reduced cerium oxide thin films J. Catal. A, 188 (1999) 340-345.
54. Jenewein, B., Fuchs, M., Hayek, K., The CO methanation on Rh/CeO_2 and CeO_2/Rh model catalysts: a comparative study, Surf. Sci. 532-533 (2003) 364-369.
55. Eck, S., Castellarin-Cudia, C., Surnev, S., Prince, K.C., Ramsey, M.G., Netzer, F.B., Adsorption and reaction of CO on a ceria–Rh(1 1 1) "inverse model catalyst" surface, Surf. Sci. 536 (2003) 166-176.
56. Hoang, D.H., Chan, S.H., Ding, O.L., Kinetic and modelling study of methane steam reforming over sulfide nickel catalyst on a gamma alumina support, Chem.Eng. J. 112 (2005) 1-11.
57. G.F. Froment, K.B. Bischoff, Chemical Reactor Analysis and Design, 2nd Ed., John Wiley, NY, (1990).
58. Vorgin, A.I. Tripol'skii, N.V. Pavlenko, G.D. Zakumbaeva, Characteristics of hydrogen and carbon monoxide adsorption on supported rhodium-containing bimetallic catalysts, Theor. Exp. Chem. 31 (1995) 99-104.
59. Maroto-Valiente, A., Rodriguez-Ramos, I., Guerreo-Ruiz, A., Surface study of rhodium nanoparticles supported on alumina, Catal. Today, 93-95 (2004) 567-574.
60. Boudart, M.; Mears, D. E.; Vannice, M. A. Kinetics of heterogeneous catalytic reactions. Ind. Chim. Belge 1967, 32, 281.

Chapter 8

Kinetic and Structural Requirements for a CO_2 Adsorbent in Sorption Enhanced Catalytic Reforming of Methane

This chapter has been submitted for publication as
1. M.H. Halabi, M.H.J.M. de Croon, J. van der Schaaf, P.D. Cobden, J.C. Schouten, Kinetic and structural requirements for a CO_2 adsorbent in sorption enhanced catalytic reforming of methane. Part I: Reaction kinetics and sorbent capacity, Fuel, submitted, 2011.
2. M.H. Halabi, M.H.J.M. de Croon, J. van der Schaaf, P.D. Cobden, J.C. Schouten, Kinetic and structural requirements for a CO_2 adsorbent in sorption enhanced catalytic reforming of methane. Part II: Bed characteristics, Fuel, submitted, 2011.

Abstract

This chapter presents a theoretical analysis of the applicability of integration of a highly active $Rh/Ce_{\alpha}Zr_{1-\alpha}O_2$ catalyst with two candidate CO_2 sorbents of hydrotalcite and lithium zirconate in low temperature–sorption enhanced steam reforming of methane. The presence of this active catalyst dictates strict requirements on the sorbent in terms of fast adsorption kinetics for an efficient performance of the process. The maximum CH_4 conversion enhancement is a strong function of sorption kinetics. This enhancement is not affected by a higher sorbent capacity at slow adsorption kinetics. The process is studied using two fixed

bed configurations of an integrated dual function particle and an admixture bed of catalyst/sorbent particles. The optimal catalyst/sorbent ratio is determined to be a function of the operating conditions. This ratio is represented in a catalyst composition of 1–3 wt.% in the admixture bed or in the dual function particle at low temperature of 550°C, intermediate pressure of 4.65 bar, and low gas flow rate of 0.05 kg/m^2.s. The catalyst composition is increased to 10 wt.% at higher pressure of 15 bar and higher gas flowrate of 1.5 kg/m^2.s. CH_4 conversion enhancement is studied at different temperature and pressure. The maximum enhancement is found at low temperature of 450 °C and high pressure of 15.6 bar at which ($CO+CO_2$) impurities can be as low as 100 ppm. Optimal operating conditions for the hydrotalcite–based system are identified to provide CH_4 conversion of 98% with high H_2 purity of 99.8% and low CO_2 contamination (<250 ppm). The lithium zirconate–based system can provide CH_4 conversion and H_2 purity of 99.9% at identical conditions. The dual function particle system and the admixture bed system show a very similar performance in terms of maximum CH_4 conversion and product composition in case of the lithium zirconate sorbent. Discrepancy in performance is observed in case of the hydrotalcite sorbent. The effect of the physical characteristics of the particle and the bed on CH_4 conversion and adsorption rates is determined at different particle size, particle voidage, pore diameter, tortuosity, and bed voidage.

8.1 Introduction

Catalytic steam reforming of methane is still worldwide the major route for H_2 production from fossil fuel. The conventional process is operated at high temperature range of 700–900 °C due to the highly endothermic nature of the steam reforming reactions. The natural gas feedstock conversion and the productivity of H_2 in this process are severely limited to the thermodynamic equilibrium bounds of the steam reforming reactions. The sorption enhanced catalytic reforming of natural gas as a pre-combustion decarbonization technique is an innovative concept of fossil fuel conversion into high purity H_2 with in situ CO_2 capture [1– 5]. This process eventually aims to achieve high CH_4 conversion (>90%) and high H_2 purity throughput (>95%) with ppm level of CO and CO_2 impurities [2, 5–10].

Generally, the proper sorbent material used in this process must have (i) high adsorption capacity (ii) adequate adsorption/desorption kinetics, (iii) high selectivity for CO_2, (iv) adequate mechanical strength, and (v) stable capacity versus adsorption/desorption cycles in operation. Hydrotalcite-like compounds and lithium zirconate solids have received considerable attention during the recent years [4, 11–25] as promising CO_2 sorbents. Hydrotalcite and K–promoted hydrotalcite are typical examples of an adsorbent having relatively fast kinetics but low capacity in the range of 0.5–0.75 [3–10]. Lithium zirconate materials are considered as high capacity candidate sorbents at high temperature [19–25]; although these materials show relatively slow kinetics due to the strong chemisorption of CO_2 [19, 20]. Addition of K_2CO_3 and Li_2CO_3 to the Li_2ZrO_3

material remarkably improves the CO_2 sorption rate [21, 22]. Fauth et al. [23] also showed that the sorbent capacity and the sorption rate can be significantly improved by promoting Li_2ZrO_3 with a combination of binary and ternary alkali carbonates of K_2CO_3, $NaCO_3$, Li_2CO_3 and KF and NaF eutectics.

There are significant attempts made to theoretically understand the process performance using Ni as a catalyst and hydrotalcite as a sorbent [5–10, 26–28]. Xiu et al. [6] developed a model to describe the sorption–enhanced steam reforming in a fixed bed. They considered a multi-component system with overall mass and energy balances, pressure drop, nonlinear adsorption equilibrium for CO_2 over hydrotalcite in addition to the SR reactions. They obtained an average H_2 purity up to 80% with traces of CO and CO_2. Using more reactor length, Xiu et al. [78] obtained 88% H_2 purity and less than 30 ppm CO. The model was further extended to include the effect of the catalyst to sorbent ratio [8]. The intraparticle diffusion for the two–particle catalyst–sorbent system was also studied by considering the component mass balance inside the particle [9]. Wang and Rodrigues [10] investigated a two–section reactor with an upstream equilibrium conversion reformer section and a downstream adsorption section. They studied the effects of the operational parameters such as S/C ratio, bed length, temperature, pressure, and catalyst/sorbent ratio on process performance.

Kapil et al. [26] developed heterogeneous bulk scale and particle scale models. They found that the purity and productivity at bulk scale are sensitive to wall temperature, bed voidage, and feed composition. At particle scale, they highlighted the role of the catalyst to sorbent distribution inside the particle and the ratio of the pore radius to tortuosity. Koumpouras et al. [27, 28] modeled a reactor–regenerator in which the adsorbent particles are passed through a stationary SR catalyst monolith. They concluded that the CH_4 conversion enhancement and CO_2 recovery show a strongly nonlinear dependency on both sorption capacity and kinetics.
For the Li_2ZrO_3–based sorption enhanced reforming system, very limited modeling studies have been reported in literature. Fernandez et al. [29] demonstrated a dynamic one-dimensional pseudo-homogenous model for a fixed bed reactor where they used hydrotalcite-derived Ni catalyst and Li_2ZrO_3 sorbent. They obtained a H_2 purity of 90 to 95% with a corresponding CH_4 conversion of 70 to 87% depending on the S/C ratio.

$Rh/Ce_{\alpha}Zr_{1-\alpha}O_2$ is under investigation in our laboratory as a promising catalyst for low–temperature sorption enhanced steam reforming of methane using hydrotalcite and lithium zirconate solids as sorbents. $Rh/Ce_{\alpha}Zr_{1-\alpha}O_2$ is selected as an effective catalyst, which provides high reaction rates in low–temperature steam reforming (<550 ^{o}C) in order to maintain a high CO_2 adsorption capacity of the sorbent. This integration implies several benefits in terms of much lower catalyst loading, intensified reactor volume, energy saving, production rates and quality, and capital investment of the integrated reactor/adsorber.

Yet to date, the experimental and theoretical studies that have been reported in literature for sorption enhanced steam reforming primarily deal with the Ni–based catalyst as a conventional steam reforming catalyst. The presence of a highly active catalyst such as Rh in an integrated reaction/adsorption process imposes special kinetic and capacity requirements for the associated sorbent.

This chapter inherently presents a theoretical analysis for the sorption enhanced process on three fundamental modeling levels; a heterogeneous particle–based level, a heterogeneous bulk–scale level, and a homogenous bulk–scale level for a fixed bed reactor at low temperature. The principal motivation of this study is to investigate the applicability of the integration of a highly active catalyst such as Rh with the currently available hydrotalcite and lithium zirconate solids for an efficient H_2 production with in situ CO_2 capture.

The CO_2 sorbent is identified in terms of the adsorption kinetic limitations and the capacity requirements for a high CH_4 conversion >99%, H_2 purity >99.5%, and low ($CO + CO_2$) impurities. The process performance is evaluated in terms of the optimal catalyst/sorbent ratio, and the configuration of the catalyst/sorbent in an integrated dual-function particle and in an admixture reaction bed. The effect of the physical characteristics of the particle and the bed on CH_4 conversion and adsorption rates is determined at different particle size, particle voidage, pore diameter, tortuosity, and bed voidage. The maximum allowable operating pressure for a low capacity sorbent is also characterized.

8.2 Steam reforming catalyst

It is widely accepted that steam reforming of methane over a catalyst can be represented by the following reactions:

R_1. $CH_4 + H_2O \leftrightarrow CO + 3H_2$ $\quad \Delta H_{298K}$ = 206.2 kJ/mol

R_2. $CO + H_2O \leftrightarrow CO_2 + H_2$ $\quad \Delta H_{298K}$ = -41.1 kJ/mol

R_3. $CH_4 + 2H_2O \leftrightarrow CO_2 + 4H_2$ $\quad \Delta H_{298K}$ = 164.9 kJ/mol

These reactions are thermodynamically dependant but kinetically independent. Halabi et al. [30] examined and evaluated the activity of $Rh/Ce_\alpha Zr_{1-\alpha}O_2$ catalyst for low–temperature sorption enhanced steam reforming of methane. The catalyst showed high resistance towards carbon formation and very good stability over a long period of time on stream. The high activity of the catalyst is thought to overcome the current operational constrains on low temperature and high pressure. This eventually leads to complete CH_4 conversion with high H_2 purity >99.5% and ($CO+CO_2$) impurities <100 ppm at low temperature (550 ^oC) and even at high pressure. Moreover, the reactor will be significantly intensified; very low catalyst loading is to be employed and the reactor volume will be essentially occupied by the sorbent. Halabi et al. [31] extended their work by determining comprehensive intrinsic kinetics for steam reforming of methane over $Rh/Ce_\alpha Zr_{1-\alpha}O_2$ catalyst in a

temperature range of 475–575 °C and a pressure of 1.5 bar. They reported measured reaction rates far from thermodynamic equilibrium and diffusion limitations. The kinetic model is given in Table 1 and the reaction equilibrium constants are given in Table 2. The model Arrhenius kinetic parameters and the van't Hoff adsorption parameters are given in Tables 3 and 4, respectively.

Table 1: Steam reforming kinetic reaction model for $Rh/Ce_{\alpha}Zr_{1-\alpha}O_2$ catalyst [31].

Reaction rate equation	
$R_1 = \frac{k_1}{p_{H_2}^{2.5}}\left(p_{CH_4}p_{H_2O} - \frac{p_{H_2}^3 p_{CO}}{K_I}\right) * \Omega_l \Omega_S$	(1)
$R_2 = \frac{k_2}{p_{H_2}}\left(p_{CO}p_{H_2O} - \frac{p_{H_2}p_{CO_2}}{K_{II}}\right) * \Omega_l \Omega_S$	(2)
$R_3 = \frac{k_3}{p_{H_2}^{3.5}}\left(p_{CH_4}p_{H_2O}^2 - \frac{p_{H_2}^4 p_{CO_2}}{K_{III}}\right) * \Omega_l \Omega_S$	(3)
$\Omega_l = \frac{1}{1 + k_{CH_4}P_{CH_4}/P_{H_2}^{0.5} + k_{CO}p_{CO} + k_{CO_2}p_{CO_2} + k_{H_2}P_{H_2}}$ $\Omega_S = \frac{1}{1 + k_{H_2O}p_{H_2O}/p_{H_2} + k_{H2}p_{H_2}}$	(4)

Table 2: Reaction equilibrium constants [31].

Reaction, j (see Table 1)	K_j [mol/kg_{cat}.s]
1	$K_I = 1.198*10^{17}$ exp(-26830/T) $(kPa)^2$
2	$K_{II} = 1.767*10^{-2}$ exp(4400/T)
3	$K_{III} = 2.117*10^{15}$exp(-22430/T) $(kPa)^2$

Table 3: Arrhenius kinetic parameters [31].

Reaction, j (see Table 1)	$k_{j,o}$ [mol/kg_{cat}.s]	E_j [kJ/mol]
1	$1.62*10^8$ $kPar^{0.5}$	83.8
2	$2.34*10^5$ kPa^{-1}	15.1
3	$4.55*10^8$ $kPa^{0.5}$	89.2

Table 4: Van't Hoff adsorption parameters [31].

Species, i	$K_{i,o}$ [kPa^{-1}]	ΔH_i [kJ/mo]
CH_4	$1.49*10^{-8}$	– 98.8
CO	$2.34*10^{-8}$	–111.2
CO_2	$8.33*10^{-10}$	–115.6
H_2	$6.11*10^{-6}$	–60.8
H_2O	$3.14*10^8$	126.9

8.3 CO_2 adsorbent

8.3.1 Hydrotalcite–based system

CO_2 adsorption on hydrotalcite is considered to show a rapid irreversible chemisorption on the fresh sorbent followed by relatively weaker physical adsorption on the material according to Ding and Alpay [11]. The CO_2 rate of adsorption on the hydrotalcite-based sorbent is given by the linear driving force model (LDF). The effective mass transfer coefficient, which is appearing in the LDF model, considers the intraparticle mass transfer limitation which is governed by internal pore diffusion. Molecular diffusion and surface diffusion are found to be insignificant in comparison to pore diffusion. The CO_2 adsorption equilibrium model is given by the Langmuir isotherm at wet conditions assuming a monolayer adsorption. The saturation capacity used in this study at base case conditions is 0.65 mol/kg, which represents a relatively low sorbent capacity. However, this capacity is varied up to 5 mol/kg at different simulation conditions to test the capacity requirements of hydrotalcite as presented later in this chapter. The temperature dependant Langmuir model parameter is given by the van't Hoff equation. Table 5 gives the CO_2 adsorption model on hydrotalcite.

Table 5: CO_2 adsorption kinetics on hydrotalcite (HTC), [3]

CO_2 rate of adsorption is given by the LDF model

$$r_{ads}\frac{\partial q_{CO_2}}{\partial t} = k_{CO_2}\left(q^*_{CO_2} - q_{CO_2}\right) \tag{5}$$

q_{CO_2} is the CO_2 concentration on solid sorbent, $q^*_{CO_2}$ is the equilibrium CO_2 concentration following the Langmuir isotherm

Effective mass transfer coefficient

$$k_{CO_2} = \frac{15}{r_p^2}\cdot\frac{\varepsilon_p D_p}{\varepsilon_p + (1-\varepsilon_p)\rho_p RT\cdot\left(\partial q^*_{CO_2}/\partial p_{CO_2}\right)} \tag{6}$$

where $D_p = 1.1*10^{-6}$ m^2/s (sorbent pore diffusion coefficient)

Langmuir adsorption isotherm on hydrotalcite

$$q^*_{CO_2} = \frac{m_{CO_2} b_{CO_2} p_{CO_2}}{1 + b_{CO_2} p_{CO_2}} \tag{7}$$

m_{CO_2} is the saturation capacity of the sorbent (0.65 mol CO_2/kg sorbent)

Temperature dependant adsorption isotherm constant

$$b_{CO_2} = b_{CO_2,ref}\, exp\left[-\frac{\Delta H_{ads}}{R}\right]\left(\frac{1}{T} - \frac{1}{T_o}\right) \tag{8}$$

$b_{CO_2,ref} = 23.6$ bar^{-1}, ΔH_{ads} is the heat of adsorption of CO_2 on HTC (-17 kJ/mol), and T_o is 673 K.

8.3.2 Lithium zirconate–based system

CO_2 can chemically be adsorbed on lithium zirconate at high temperature and generating relatively high heat according to the following reaction

R4. $Li_2ZrO_3 + CO_2 \leftrightarrow Li_2CO_3 + ZrO_2$ $\qquad \Delta H_{298K} = -160$ kJ/mol

Although the lithium zirconate sorbent shows relatively slow kinetics comparing to CO_2 adsorption rates on hydrotalcite, the high adsorbent capacity of this material (5.0 mol/kg) is a beneficial factor to be used in adsorption enhanced reactions. However, recent studies have demonstrated fast CO_2 uptake rates by promoting the sorbent with alkali carbonates and alkali eutectic salts. The CO_2 rate of adsorption is represented by the extent rate of reaction according to Ochoa-Fernandez et al. [29]. This rate expression is modified in this work to be in consistence with the LDF model on the hydrotalcite as shown in Table 6. The expression is changed accordingly to be in terms of the CO_2 concentration in the sorbent solid.

Table 6: CO_2 adsorption kinetics on lithium zirconate (LZC), modified from [29]

CO_2 rate of adsorption is given by $r_{ads} = \frac{dq_{CO_2}}{dt} = k_{CO_2} C_{CO_2}^{n} \left(m_{CO_2} - q_{CO_2}\right)$ C_{CO_2} is the concentration in the gas phase , q_{CO_2} is the CO_2 concentration on solid sorbent, m_{CO_2} is the maximum saturation capacity of the sorbent (5 mol CO_2/kg sorbent)	(9)
Temperature dependant adsorption constant $k_{CO_2} = k_{ref} e^{\left(\frac{-E_{ads}}{R}\left(\frac{1}{T_s}-\frac{1}{T_o}\right)\right)}$ $k_{ref} = 4.9*10^{-5}$, $E_{ads} = 8.94*10^{4}$ J/mol, and the heat of adsorption of CO_2 on LZC is -160 kJ/mol. T_o is 673 K.	(10)

8.4 Mathematical modeling

The fast kinetics of the steam reforming reaction on the Rh catalyst mainly can dictate certain requirements on the associated sorbent with regard to the CO_2 adsorption kinetics. The large difference between the reaction rates and the CO_2 adsorption rates at constant gas velocity through the reactor results in a low enhancement of CH_4 conversion, low product purity, and tailed adsorption waves. Hence, it is essential to describe the dynamics of the reaction and adsorption inside the particle as well as to understand the nature of the species distribution profiles and the effect of varying particle characteristics on the reaction/adsorption rates along a convective flow bulk scale reformer. Therefore, three levels of models have been constructed.

8.4.1 Heterogonous particle–based model

A dynamic heterogeneous diffusion model is constructed for the particle to consider the species dynamic profiles due to diffusion, reaction, and adsorption. The following assumptions are made:

1. Ideal gas behavior;
2. Uniform temperature and isothermal particle;
3. Uniform pore structure;
4. Uniform distribution of the catalyst and the sorbent inside the particle;

5. Non-instantaneous adsorption of CO_2;
6. Five reactive species (CH_4, H_2O, H_2, CO, and CO_2) are involved in the model;
7. CO_2 is the only species adsorbed in the sorbent; the rate of adsorption R_{ads} is zero for the non-adsorbing species.

The component mass balance equations for this model, the boundary and initial conditions are given in Table 8.

Table 8: Heterogeneous particle–base model and the corresponding boundary and initial conditions

Component mass balances inside the solid particle

$$\varepsilon_P \frac{\partial C_{i,P}}{\partial t} = D_{eff,i}\left[\frac{1}{r^2}\frac{\partial^2\left(r^2\partial^2 C_{i,P}\right)}{\partial r^2}\right] + (1-\varepsilon_P).v_{cat}.\rho_P R_i - (1-\varepsilon_P).v_{ads}.\rho_P R_{ads} \quad \forall\ r \in \left[0^+ - R_P^-\right] \tag{11}$$

Boundary conditions

At the particle surface $r = R_P$	At particle center $r = 0$	
$C_{i,P} = C_{i,bulk}$	$-D_{eff,i}\frac{\partial C_{i,P}}{\partial r} = 0$	(12)

Initial condition

$$C_{i,P} = 0 \tag{13}$$

8.4.2 Heterogonous bulk–scale model

A 1-D heterogeneous plug-flow model is constructed to investigate the sorption enhanced dynamic performance in a fixed bed reformer. A dual function particle is used in this model. The catalyst and the sorbent are combined in one single particle. In addition to the assumptions listed for the particle-based model, the following assumptions are included:

1. Isothermal operation;
2. Axial mass dispersion is considered with negligible radial gradients;
3. Concentration gradients in the radial direction are ignored;
4. Uniform particle temperature; no temperature gradient inside particle;
5. Interfacial mass transport resistances are ignored; therefore the species concentration in the bulk gas and at the particle surface are identical;
6. No homogenous gas phase reactions are considered as the temperatures are lower than 600 ^oC.
7. Pressure drop is considered;
8. Uniform particle size along the bed;
9. Constant bed voidage.

The mass transfer inside the particle is connected to the rate of mass transfer in the bulk scale model via the flux at the surface of the particle. The component mass balance equations for this model, and the boundary and initial conditions are given in Table 9.

Table 9: 1-D Heterogeneous plug-flow model with the corresponding boundary and initial conditions

Component mass balances in the gas phase

$$\varepsilon_b \frac{\partial C_{i,b}}{\partial t} + \frac{\partial (u C_{i,b})}{\partial z} = \varepsilon_b D_Z \frac{\partial^2 C_{i,b}}{\partial z^2} + F_{i,P}(1-\varepsilon_b).\frac{3}{R_P} \qquad \forall\ z \in 0^+ - L^- \tag{14}$$

Diffusion rate at the solid particle surface

$$F_{i,P} = -D_{eff,i} \left.\frac{\partial C_{i,P}}{\partial r}\right|_{r=R_P} \qquad \forall\ z \in [0-L] \tag{15}$$

Component mass balances inside the solid particle

$$\varepsilon_P \frac{\partial C_{i,P}}{\partial t} = D_{eff,i}\left[\frac{1}{r^2}\frac{\partial^2 (r^2 \partial^2 C_{i,P})}{\partial r^2}\right] + (1-\varepsilon_P).v_{cat}.\rho_P R_i - (1-\varepsilon_P).v_{ads}.\rho_P R_{ads} \tag{16}$$

$$\forall\ z \in [0^+ - L^-] \qquad \forall\ r \in [0^+ - R_P^-]$$

Pressure drop

$$\frac{\partial P}{\partial z} = -K_D u - K_V u^2 \qquad \forall\ z \in [0^+ - L] \tag{17}$$

Boundary conditions

At the reformer inlet $z = 0$	At the reformer exit $z = L$
$\varepsilon_b D_Z \frac{\partial C_{i,b}}{\partial z} = u(C_{i,in} - C_{i,b})$	$\frac{\partial C_{i,b}}{\partial z} = 0$ (18)
At the particle surface $r = R_P$	At particle center $r = 0$
$C_{i,P} = C_{i,bulk}$	$-D_{eff,i}\frac{\partial C_{i,P}}{\partial r} = 0$ (19)

Initial condition

$$C_{i,b} = C_{i,in} \qquad \forall\ z \in [0^+ - L^-]\ ; \quad C_{i,P} = 0 \quad \forall\ r \in [0^+ - R_P^-] \tag{20}$$

8.4.3 Homogenous bulk–scale model

In this model, we study the dynamic performance of the process in a fixed bed packed with admixture particles of catalyst and sorbent. A 1-D pseudo homogenous plug-flow model is constructed; isothermal operation and mass axial dispersion are also considered. The model equations are shown in Table 10.

The effective diffusion coefficient used in these models is considered to account for the molecular and Knudsen diffusion. Pressure drop along the axial direction in the fixed bed is described by the Ergun equation [32]. K_D and K_V are parameters corresponding to the viscous and kinetic loss terms, respectively. The axial dispersion coefficient to account for the non-ideal flow and local mixing at turbulent velocities plus the diffusive flow is estimated using the equation of Edwards and Richardson [33].

The correlations used for the effective diffusion coefficient, K_D and K_V pressure drop terms, and the axial dispersion coefficient are given Table 11. Gas properties such as the fluid density and viscosity are functions of temperature as well as of

composition, and they are changing along the reformer length and might vary with time. However, at isothermal conditions; composition dependent expressions are employed in the model to calculate the gas properties throughout the reactor [35, 36].

Table 10: 1-D pseudo homogenous plug-flow model with the corresponding boundary and initial conditions

Component mass balances in the gas phase

$$\varepsilon_b \frac{\partial C_i,b}{\partial t} + \frac{\partial (uC_{i,b})}{\partial z} = \varepsilon_b D_Z \frac{\partial^2 C_i}{\partial z^2} + \rho_{b,cat} R_i - \rho_{b,ads} R_{ads} \qquad \forall\ z \in [0^+ - L^-] \tag{21}$$

Pressure drop

$$\frac{\partial P}{\partial z} = -K_D u - K_V u^2 \qquad \forall\ z \in [0^+ - L] \tag{22}$$

Boundary conditions

At the reformer inlet $z = 0$ At the reformer exit $z = L$

$$\varepsilon_b D_Z \frac{\partial C_{i,b}}{\partial z} = u(C_{i,in} - C_{i,b}) \qquad \frac{\partial C_{i,b}}{\partial z} = 0 \tag{23}$$

Initial condition

$$C_{i,b} = C_{i,in} \qquad \forall\ z \in [0^+ - L^-] \tag{24}$$

Table 11: Relevant correlations employed in the model

Effective diffusion coefficient [34]

$$D_{eff,i} = \frac{\varepsilon_P}{\tau} \frac{1}{\left(\frac{1}{D_{m,i}} + \frac{1}{D_{k,i}}\right)} \tag{25}$$

$$D_{k,i} = \frac{d_{pore}}{3} \left(\frac{8RT}{\pi Mw}\right)^2 \tag{26}$$

Semi-empirical relations for K_D and K_V [32]:

$$K_D = \frac{150\mu_g (1-\varepsilon_b)^2}{d_p^2 \varepsilon_b^3}\ (\text{Pa.s/m}^2); \quad K_V = \frac{1.75(1-\varepsilon_b)\rho_f}{d_p \varepsilon_b^3}\ (\text{Pa.s}^2/\text{m}^3) \tag{27}$$

Mass axial dispersion coefficient [33]:

$$D_Z = 0.73 D_m + \frac{0.5 u d_p}{1 + 9.49 D_m / u d_p} \tag{28}$$

8.4.4 Numerical solution

The mathematical model consisting of coupled partial differential and algebraic equations is implemented and solved in gPROMS modeling environment (Process Systems Enterprise Ltd.). Backward difference of first order (BFDM) is used as a spatial discretization method on the axial direction over a uniform grid of 50 intervals. The integration over the time domain is performed by the DAE integrator based on the variable time step of the backward differentiation formula. The radial

direction inside the particle is discretized using the central difference of second order method (CFDM) over a uniform grid of 50 intervals.

Reactor parameters, operating conditions, and average gas properties which are globally used throughout the modeling study are listed in Table 12.

Table 12: Global parameters, operating conditions, and average gas properties used in the model simulations

	Unit	Value
Reactor length	m	1.0
Gas feed temperature	^{o}C	550
Catalyst temperature	^{o}C	550
Pressure	kPa	465
Pellet density	kg/m^3	2000
Pellet diameter	m	1*0^{-3}
Pore diameter	m	50*10^{-9}
Pellet tortuosity	–	1.0
Pellet voidage	–	0.4
Catalyst/sorbent ratio	–	0.05/0.95
Bed voidage	–	0.4
Gas mass flow velocity	kg/m^{2}s	0.0
Steam/carbon molar ratio	–	6.0
Gas viscosity	kg/m.s	0.031*10^{-3}

8.5 Results and discussion

8.5.1 Kinetic requirements

In conventional adsorption columns, slow adsorption kinetics results in tailed adsorption waves throughout the column and fast adsorption kinetics yields sharp breakthrough curves. The slow kinetics limitations are usually handled by operating the column at low gas flow rates to provide enough residence time for the molecules to diffuse in the sorbent particle. The utilization of a highly active catalyst such as Rh in sorption enhanced steam reforming process has not yet been investigated in literature. The large difference between the refroming reaction rates and the CO_2 adsorption rates might not lead to high utilization of the solid particle and therefore, poor reactor performance. In this study, the light is shed on the lithium zirconate as this sorbent presents slow adsorption kinetics. A dual function particle composed of 5% Rh/$Ce_{\alpha}Zr_{1-\alpha}O_2$ catalyst and 95% lithium zirconate sorbent of 1 mm size is simulated using the particle–based model at the reactor inlet conditions as the reaction rates are at maximum. The particle is subjected to a CH_4 partial pressure of 66 kPa, S/C ratio of 6 and 3 kPa H_2 at a total pressure of 4.65 bar and a temperature of 550 ^{o}C. The particle performance is analyzed at different adsorption kinetics represented by the CO_2 adsorption rate constant k_{CO2} (m^3/mol.s) which is resembling the LDF effective mass transfer coefficient. The dynamic profiles of local CO_2 adsorbed inside the solid particle and the CO_2 gas concentration profiles in the pores at the center of the particle are given in Figures 1

and 2, respectively. Slow adsorption kinetics shows very weak CO_2 adsorption and high unabsorbed CO_2 gas phase concentration in the pores. The corresponding local rates of CO_2 adsorption at the particle center are shown in Figure 3.

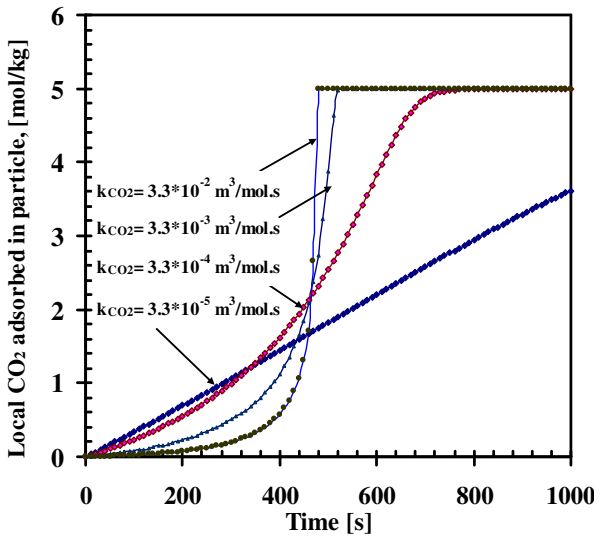

Fig. 1: Dynamic adsorbed CO_2 profiles at the integrated Rh/LZC particle center at 550 °C, 4.65 bar, S/C=6.

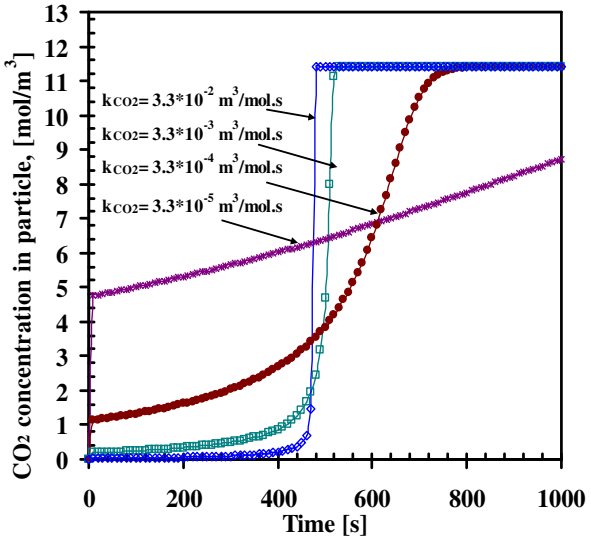

Fig. 2: Dynamic CO_2 gas concentration profiles at the integrated Rh/LZC particle center at 550 °C, 4.65 bar, S/C=6.

A reformer of 1.0 m length and 4 mm inside diameter is simulated using the heterogeneous bulk scale plug-flow model at mass space velocity of 0.05 kg/m^{2}s, a temperature of 550 °C, a pressure of 4.65 bar and identical gas feed composition which is used over the single particle. The local adsorbed CO_2 profiles at the reactor exit are shown in Figure 4. The sorbent can easily reach its maximum capacity when the adsorption rates calculated at the particle surface are higher than 2.4*10^{-3} mol/kg.s (corresponding to k_{CO2} =3.3*10^{-4} 1/s).

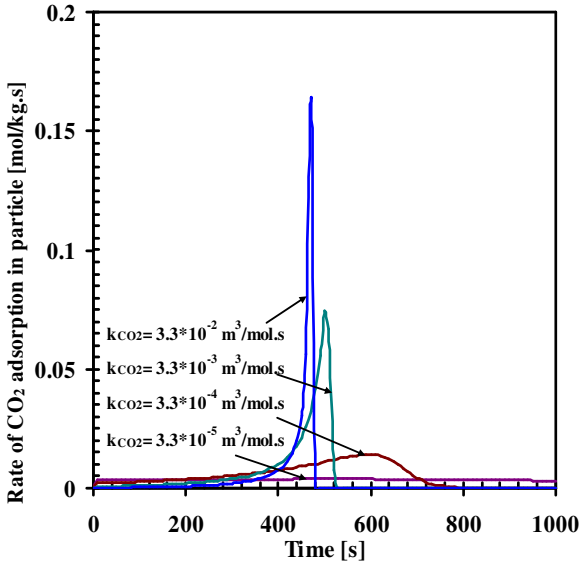

Fig. 3: Dynamic local rates of CO_2 adsorption at the integrated Rh/LZC particle center at 550 °C, 4.65 bar, S/C=6.

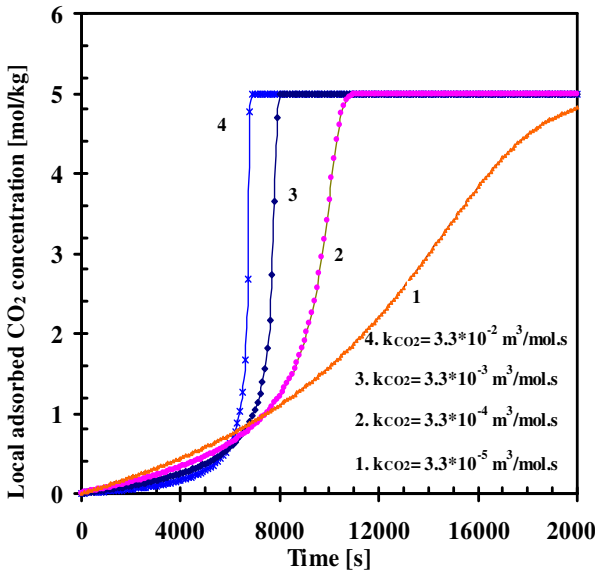

Fig. 4: Dynamic profiles of the local CO_2 adsorbed in the integrated Rh/LZC particle at the reformer exit at 550 °C, 4.65 bar, S/C=6, and G_s=0.05 kg/m^2.s.

The CH_4 conversion profiles and the dry basis CO_2 concentration profiles versus the operational time at the reformer exit are given in Figure 5. Improving the CO_2 adsorption rate by two orders of magnitude (from $4*10^{-3}$ mol/kg.s to 0.163 mol/kg.s, calculated inside the particle at inlet reaction conditions or from $4.4*10^{-4}$ to 0.024 mol/kg.s, calculated at the particle surface along the reactor) can significantly enhance the process performance.

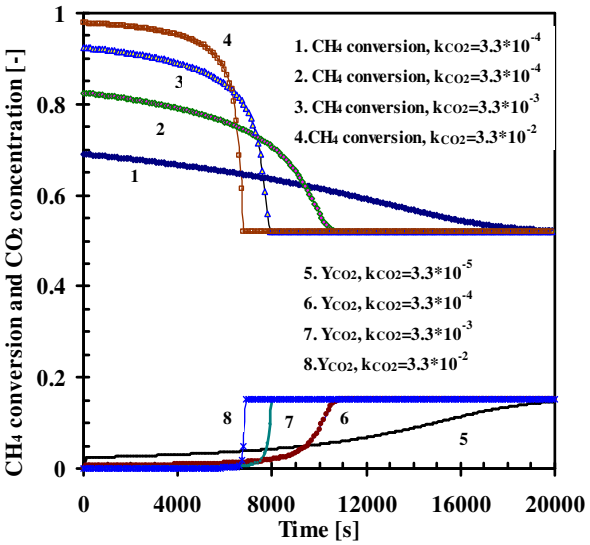

Fig. 5: Dynamic profiles of the CH_4 conversion and CO_2 dry concentration for the integrated Rh/LZC particle at the reformer exit at 550 °C, 4.65 bar, S/C=6, and G_s=0.05 kg/m^2.s.

The CH_4 conversion obtained at the reformer exit can be increased from 69% to 98% and the CO_2 escape in the gas product can be reduced from 2.9% to less than 245 ppm. This clearly shows the importance of fast adsorption kinetics in a synergic effect with a high active catalyst. Therefore, lithium zirconate can be effectively used in a combined particle with Rh catalyst if it provides high adsorption rates with a corresponding CO_2 uptake rate constant larger than $3.3*10^{-2}$ m^3/mol.s at 550 °C.

8.5.2 Capacity requirements

The sorbent capacity has a high impact on the CH_4 conversion enhancement and the recovery of CO_2. However, this is thought to be true when a relatively low activity catalyst as Ni is used in steam reforming. In this study, hydrotalcite is mainly considered for investigation due to its low capacity limitations. A fixed bed reformer is simulated at the base case conditions of 550 °C, 465 kPa, S/C ratio of 6 and CH_4 partial pressure of 66 kPa using 5% catalyst in a catalyst-sorbent particle. The process performance is analyzed using low capacity (0.65 mol/kg) and high capacity (5 mol/kg) hydrotalcite at slow and fast adsorption kinetics (corresponding to k_{CO2}=0.043 and 0.43 1/s, respectively). The results of CH_4 conversion attained at the reformer exit are given in Figures 6 and 7, respectively.

Comparing the dynamic CH_4 conversion profiles at the reformer exit, it is observed that the maximum CH_4 conversion attained using slow kinetics sorbent having low

and high capacity is almost identical in both cases with a value of 88%. In other words, at slow adsorption kinetics increasing the sorbent capacity from 0.65 to 5 mol/kg does not improve the attainable CH_4 conversion.

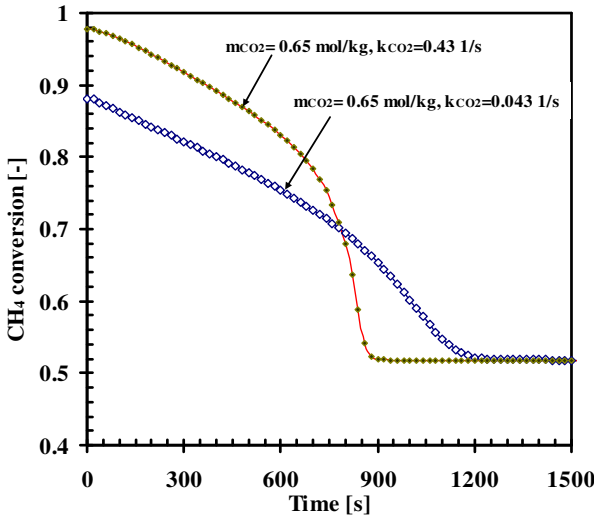

Fig.6: Effect of CO_2 adsorption kinetics on the CH_4 conversion profiles at the reformer exit using low capacity HTC particle, 550 °C, 4.65 bar, S/C=6, and G_s=0.05 kg/m^2.s.

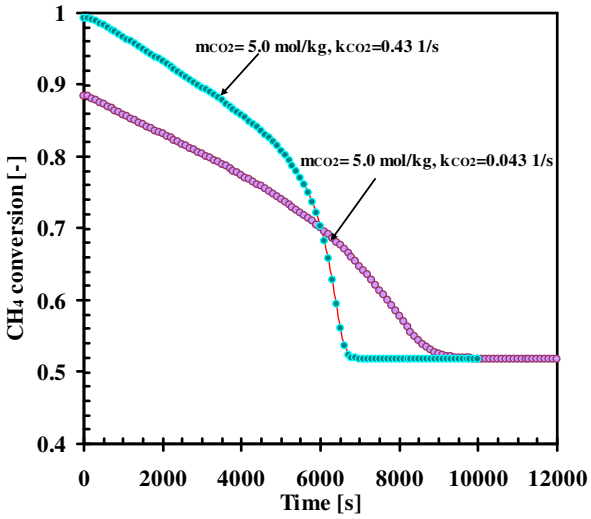

Fig. 7: Effect of CO_2 adsorption kinetics on the CH_4 conversion profiles at the reformer exit using high capacity HTC particle, 550 °C, 4.65 bar, S/C=6, and G_s=0.05 kg/m^2.s.

However, the operational time is drastically elongated. Using a sorbent of fast adsorption kinetics with even low capacity can enhance the conversion to 97.7 %. This value can be further increased to reach 100% using a higher sorbent capacity. H_2 is then produced at a 99.7% purity and <250 ppm CO_2 contamination. The conversion enhancement as a result to a higher sorbent capacity is almost negligible in comparison to the significant role of fast kinetics. However, this enhancement can still be distinguished using fast kinetics. From these profiles, it is stated that hydrotalcite with low capacity and fast kinetics can be considered as an attractive sorbent in combination with a Rh catalyst.

The CH_4 conversion enhancement is studied as a function of the hydrotalcite sorbent capacity at different low/high temperatures and low/high pressures provided fast adsorption kinetics. The results are shown in Figure 8. A maximum conversion enhancement of 276%; which is corresponding to a 64% CH_4 conversion can be achieved using a capacity of 5 mol/kg at high pressure of 15 bar and low temperature of 450 °C. The minimum enhancement achieved is 50.5% using 0.5 mol/kg capacity at high temperature of 600 °C and low pressure of 4.65 bar, although the absolute CH_4 conversion reached is 99.9%. However, according to the temperature resistance limitations of the currently available hydrotalcite, 600 °C is considered a high temperature. In selecting the optimal operational conditions of temperature and pressure, the conversion enhancement can not be considered as a sole criterion; the absolute conversion should be emphasized. Therefore, low temperature of 500–550 °C and low pressure of 4.65 bar can result in an efficient hydrotalcite performance yielding CH_4 conversion >99.5%. The limits of allowable

pressure for high CH_4 conversion and product purity will be further discussed in this chapter.

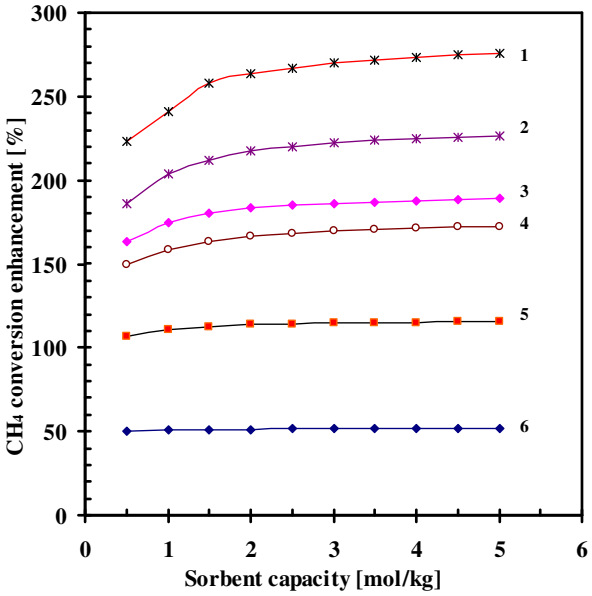

Fig. 8: CH_4 conversion enhancement as a function of hydrotalcite sorbent capacity. (1). 450 ^oC and 15 bar, (2). 500 ^oC and 15 bar, (3). 450 ^oC and 4.65 bar, (4). 550 ^oC and 15 bar, (5). 600 ^oC and 15 bar, (6). 600 ^oC and 4.65 bar

The choice between lithium zirconate and hydrotalcite as a proper sorbent for specific operating conditions is not a trivial issue. Each sorbent offers particular advantage over the other. The performance of the two sorbents in an integrated catalyst/sorbent particle is compared in a bulk–scale reactor model at identical capacity and adsorption rate coefficient.

Figure 9 demonstrates the CH_4 conversion profiles for each sorbent at the reactor exit using sorbent capacity of 5 mol/kg, a value of 0.043 1/s for the effective mass transfer constant of hydrotalcite and the CO_2 adsorption rate coefficient of the lithium zirconate. Relatively high gas flow is inserted at a rate of 0.1 kg/m^{2}s using S/C ratio of 6 at 550 ^oC and 4.65 bar. Lithium zirconate system gives a maximum CH_4 conversion of 97.4%, which is only 2.2% higher than the conversion obtained from hydrotalcite–based particle. However, the difference is significantly observed in the break through operational time according to the criterion time defined as the time at which CH_4 conversion and H_2 purity are higher than 90% and 95%, respectively. Hydrotalcite system can maintain this criterion up to 1050 s, while the time is elongated to 3000 s using lithium zirconate. At this criterion time H_2 purity was 97% using both sorbents as shown in Figure 10. CO_2 concentration in the gas effluent at the criterion breakthrough time was detected to be 1950 ppm using lithium zirconate and 1850 ppm for hydrotalcite. The major reason for the different performance of the two sorbents is that lithium zirconate provides higher adsorption rates than hydrotalcite at identical capacity and rate constant.

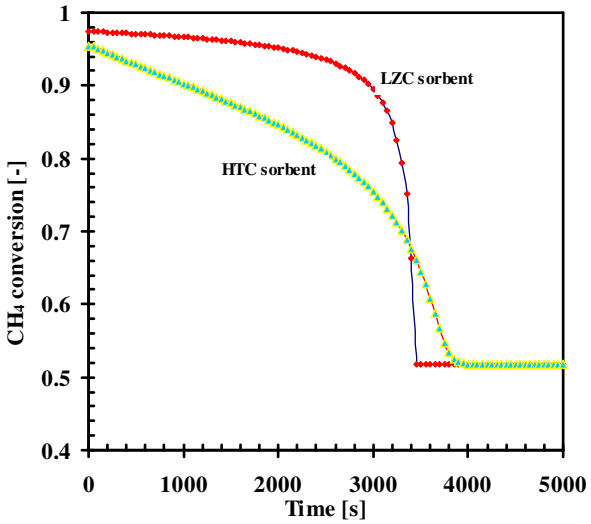

Fig. 9: A CH_4 conversion comparison between LZC and HTC integrated particle at identical capacity and sorption kinetic constant at 550 ^oC, 4.65 bar, 4.65 bar, S/C=6, and G_s=0.1 kg/m^2.s.

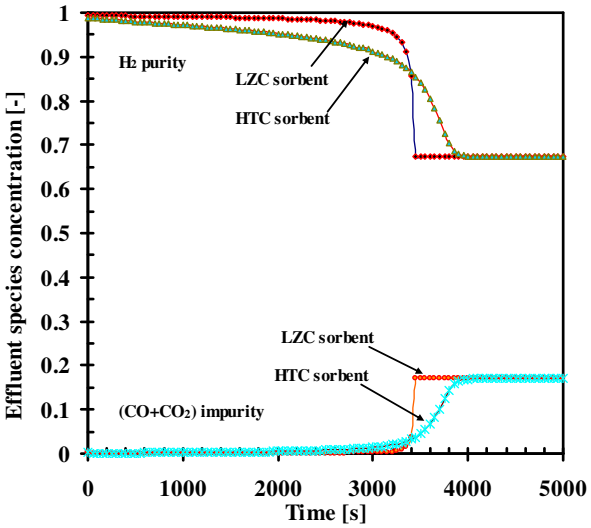

Fig. 10: A species concentration comparison between LZC and HTC integrated particle at identical capacity and sorption kinetic constant at 550 ^oC, 4.65 bar, 4.65 bar, S/C=6, and G_s=0.1 kg/m^2.s.

Figure 11 displays that the adsorption rates generated by lithium zirconate is almost 4 folds of those obtained from hydrotalcite. This is, however, due to the chemical nature of CO_2 adsoprtion on lithium zirconate. Its adsorption rate is a strong function of the gas phase CO_2 concentration, see Eq.9; while in the case of hydrotalcite, the adsorption rate is implicitly related to the gas phase concentration (or CO_2 partial pressure) via the equilibrium isotherm.

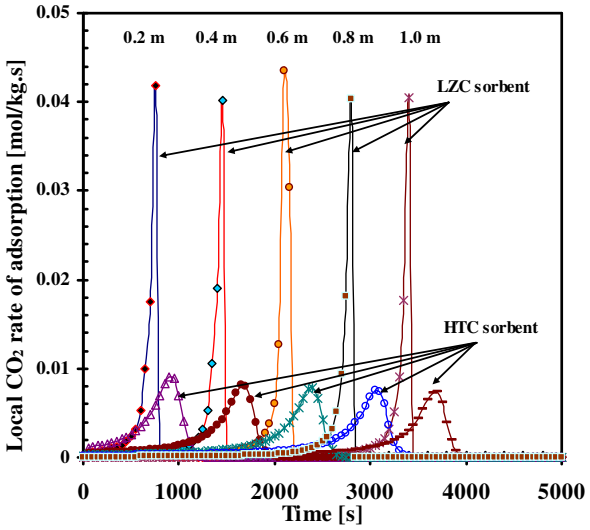

Fig. 11: A comparison of local CO_2 sorption rates between LZC and HTC integrated particle at identical capacity and sorption kinetic constant at 550 ^oC, 4.65 bar, 4.65 bar, S/C=6, and G_s=0.1 kg/m^2.s.

8.5.3 Allowable operating pressure

This part of the analysis presents an operational pressure range at which hydrotalcite can be used for an efficient H_2 production and high CH_4 conversion. It is assumed that hydrotalcite retains its low capacity of 0.65 mol/kg and furnishes

high sorption kinetics (k_{CO2}=0.43 1/s). Figure 12 demonstrates the effect of operating pressure on CH_4 conversion enhancement and the useful operational time according to the time criterion at which CH_4 conversion and H_2 purity > 90and 95%, respectively. Figure 13 shows the maximum CH_4 conversion and product concentration at criterion time at different operating pressure.

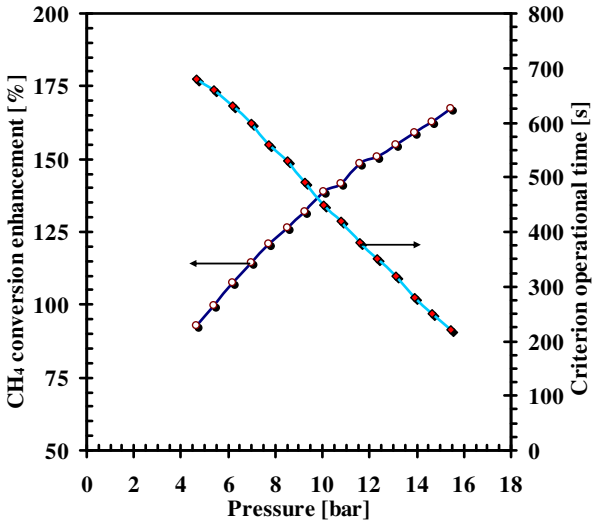

Fig. 12: Allowable pressure for an optimal CH_4 conversion enhancement and operational time using Rh/HTC integrated sorbent at 550 ^oC, 4.65 bar, S/C=6, and G_s=0.05 kg/m^2.s.

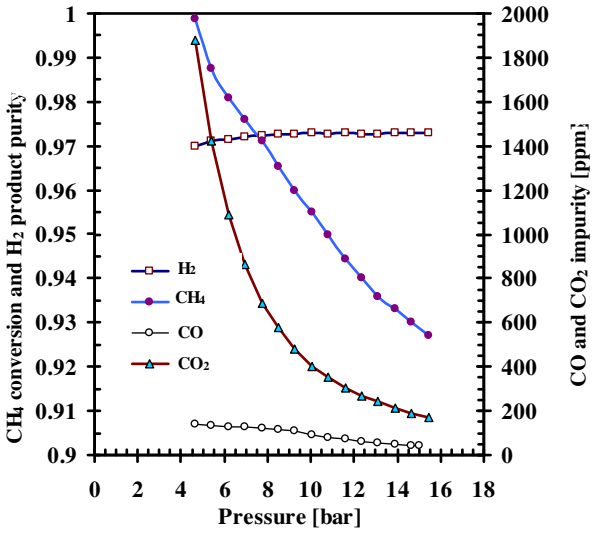

Fig. 13: Allowable pressure for an optimal CH_4 conversion and operational time using Rh/HTC integrated sorbent at 550 ^oC, S/C=6, and G_s=0.05 kg/m^2.s.

Although the enhancement in conversion and the low impurities of CO and CO_2 present in the gas product are benefited from high pressure operation; nonetheless the absolute CH_4 conversion and useful operational time are seriously limited as seen in Figure 12.

The optimal operational pressure is a trade off between CH_4 conversion and operational time on the one side and low product impurity on the other side. At low pressure of 4.65 bar, CH_4 conversion is 99.9% with 140 and 1870 ppm level of CO and CO_2 impurities, respectively. At high pressure of 15.6 bar, CH_4 conversion is reduced to 92.7%. The gas product can retain (CO+CO_2) contamination as low as 100 ppm; respectively. However, H_2 purity is found to be not affected by higher pressure. It is 97% at 4.65 bar and 97.3% at 15.6 bar.

The end application of the H_2 product stream decides the optimal operation pressure. In case of very high CH_4 conversion is required; then low pressure of 4.65 bar, low temperature of 550 ^oC, and gas flow rate of 0.05 kg/m^2s, are determined to provide an optimal operation for the process using hydrotalcite even at low sorption capacity.

8.5.4 Physical characteristics of the particle and the bed

The particle size and the particle's internal structure play very prominent roles in defining the entire process performance in terms of CH_4 conversion, temperature

profile, product quality, operational time, and pressure drop due to their impact on diffusion/reaction limitations inside the particle. The effect of particle size is studied using hydrotalcite sorbent in an integrated catalyst/sorbent particle due to the fact that the CO_2 adsorption constant of hydrotalcite is a strong function of the particle structure, density, size, in addition to temperature, see Eq. 6 (Table 5).

The particle size is varied from small particles of 0.2 mm diameter to a relatively large pellets of 5 mm diameter at constant temperature and pressure of 500 ^oC and 4.65 bar, respectively, and gas flow rate of 0.05 kg/m^{2}s. CH_4 conversion is drastically reduced from 98% using a particle smaller than 0.5 mm to 70% using particle of 5 mm, see Figure 14.

Figure 15 shows the dynamic CH_4 conversion and CO_2 concentration profiles at the reactor exit using three particle sizes. Using large particle diameter of 5 mm results in high CO_2 product impurity of 3540 ppm and relatively low H_2 purity of 90.3%. The high CH_4 conversion of 98% obtained using a particle diameter 0.2 mm is associated with a high H_2 purity and very low CO_2 contamination of 99.5% and 73.7 ppm, respectively. The reason of this efficient performance is due to the fast adsorption rates generated in smaller particle. Figure16 suggests that reducing the size from 5 mm to 0.2 mm yields improved CO_2 adsorption rates of at least one order of magnitude higher. Generally, large particle size imposes severe internal diffusion limitations that can reduce the mass transfer rate for adsorption.

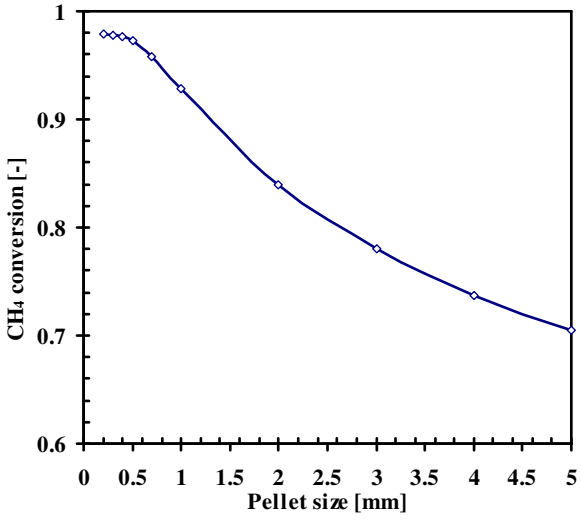

Fig. 14: Effect of pellet size on the maximum CH_4 conversion for the Rh/HTC integrated particle. 550 ^oC, 4.65 bar, S/C=6, and G_s=0.05 kg/m^2.s.

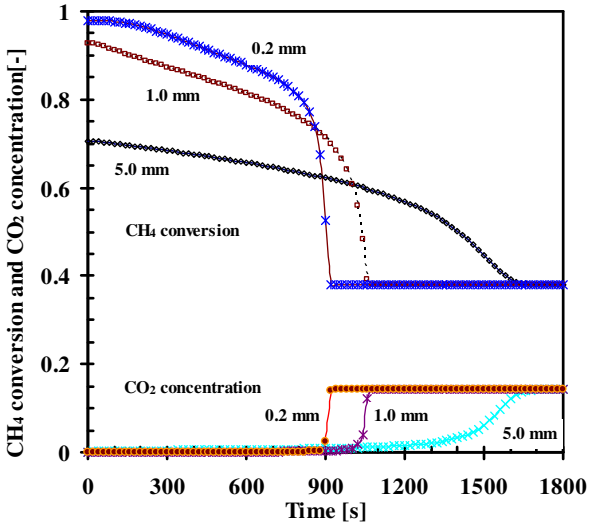

Fig. 15: Effect of pellet size on the CH_4 conversion and CO_2 concentration profiles at the reformer exit for the Rh/HTC integrated particle at 550 ^oC, 4.65 bar, S/C=6, and G_s=0.05 kg/m^2.s.

The pressure drop produced as a result of small particle size of 0.2 mm is determined to be 2.1%, see Figure 17. This is explained by the fact that low gas flowrate is used (0.05 kg/m^{2}s). However, increasing the gas flow rate to 0.42 kg/m^{2}s will significantly increase the pressure drop up to 23.3%. Such high

pressure drop is not favored in fixed bed operation. Therefore, it is concluded that smaller particle size of hydrotalcite can be optimally utilized in fixed bed sorption enhanced process only at low flowrate. This generates high adsorption kinetics and ultimately high conversion and product purity. One the other hand, it is feasible to use small size of the integrated catalyst/sorbent particle at high gas velocities in fluidized bed sorption enhanced process.

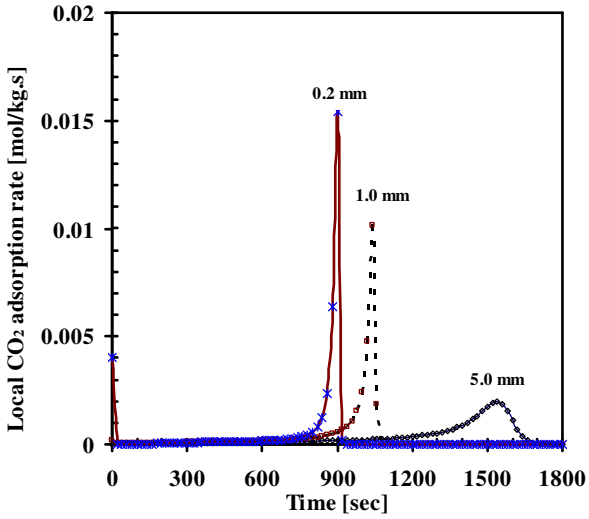

Fig. 16: Effect of pellet size on the CO_2 adsorption rates for the Rh/HTC integrated particle at 550 ^{o}C, 4.65 bar, S/C=6, and G_s=0.05 kg/m^2.s.

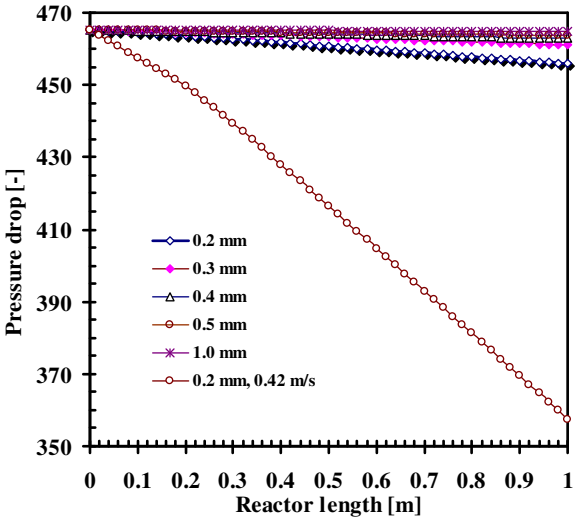

Fig. 17: Effect of pellet size on the pressure drop along the reformer for the Rh/HTC integrated particle at 550 ^{o}C, 4.65 bar, S/C=6.

The effect of pellet voidage of the integrated particle on the CH_4 conversion is studied. Figure 18 suggests that the optimal pellet voidage that can maximize the CH_4 conversion is 0.65, at which the conversion reaches 93.9%. Large internal voidage results in a lower conversion due to less sorbent occupying the internal volume of the particle and therefore, lower enhancement of the conversion. Small values of the pellet voidage indicate severe diffusion limitations for the reaction and the adsorption, and the process can solely controlled by pore diffusion.

Bed voidage is also varied in a realistic manner for fixed bed reactors from 0.4 to 0.5. Figure 19 suggests that the maximum CH_4 conversion is not sensitive to the changes in bed voidage. However, the operational time before the breakthrough wave can still be affected.

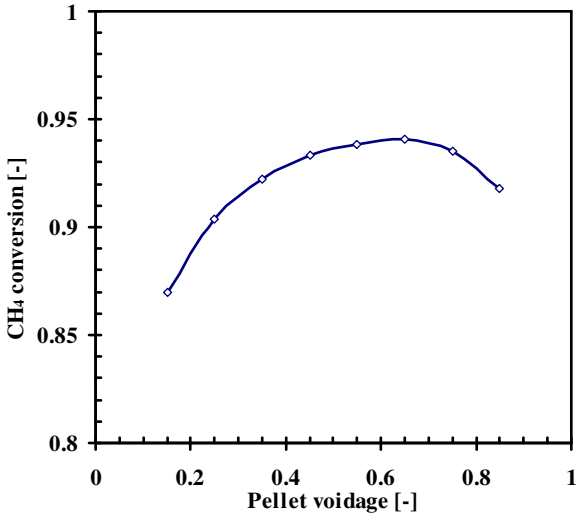

Fig. 18: Effect of pellet voidage on the maximum CH_4 conversion for the Rh/HTC integrated particle at550 ^oC, 4.65 bar, S/C=6, and G_s=0.05 kg/m^2.s.

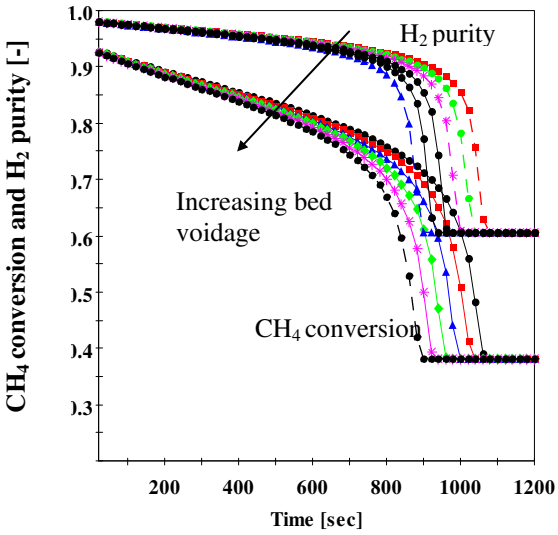

Fig. 19: Effect of bed voidage on the CH_4 conversion and H_2 concentration profiles at the reformer exit for the Rh/HTC integrated particle at 550 ^oC, 4.65 bar, S/C=6, and G_s=0.05 kg/m^2.s.

8.5.5 Catalyst/sorbent ratio

The integration of a highly active catalyst with a sorbent in one single particle or as an admixture catalyst sorbent particle in a reactor bed is thought to provide high reaction rates, and improved CO_2 recovery from the gas mixture at very low catalyst loading. The volume of the reactor is suggested to be largly occupied by the sorbent. Therefore, if a low sorbent capacity is used, the overwhelming sorbent loading will compensate for the shortcomings of adsorption due to low capacity.

The effect of catalyst/sorbent ratio is analyzed for the Rh/ hydrotalcite–based system at relatively low temperature of 500 ^oC and high pressure of 15 bar at two different gas flow rates. These conditions are chosen because the effect of catalyst/sorbent ratio on fuel conversion can be amplified at low temperature and high pressure. At low gas flow rate of 0.05 kg/m^2s, the optimal catalyst composition of 5 %inside the catalyst/sorbent particle is found to provide a maximum CH_4 conversion, see Figure 20.

Using a higher gas flow rate of 1.5 kg/m^2s, this composition is increased to 10% because more catalyst is required to process higher feed flow rates. However, at low pressure of 4.65, a temperature of 550 ^oC and low gas flow rate for hydrotalcite based system; the optimal catalyst compossition is between 1–3 % inside the integrated particle yielding almost complete CH_4 conversion of 99.9%

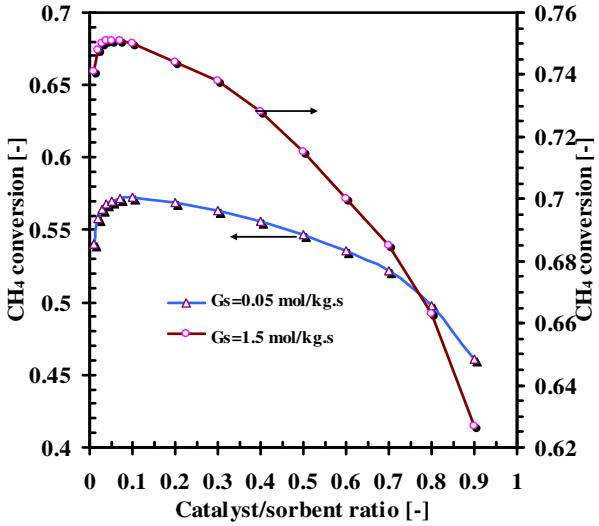

Fig. 20: Effect of catalyst/sorbent ratio on the maximum CH_4 conversion for the Rh/HTC integrated particle. 500 ^oC, 4.65 bar, S/C=6.

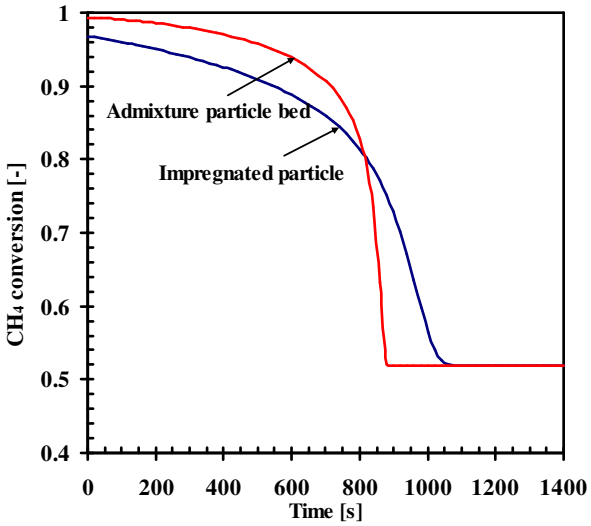

Fig. 21: Effect of catalyst/sorbent particle and bed configuration on the CH_4 conversion profiles for the Rh/HTC system. 550 ^oC, 4.65 bar, S/C=6 and G_s=0.05 kg/m^2.s.

5.6 Integrated particle and admixture bed configurations

The process performance is finally investigated in terms of two bed configurations: (1) the bed is composed of dual function particles where 5% catalyst is integrated with 95% sorbent in one particle; (2) the bed is composed of an admixture of catalyst and sorbent particles with identical composition ratio. The process is studied for the two sorbents of hydrotalcite and lithium zirconate.

Figure 21 shows the CH_4 dynamic conversion profiles of the two bed configurations for Rh/hydrotalcite system at 550 ^oC and 4.65 bar. The admixture particle bed provides a CH_4 conversion of 99.4%, which is higher than the conversion obtained by the integrated particle bed with a 2.8%. The difference in behavior is enlarged in breakthrough time according to the 90% CH_4 conversion. Integrated particle configuration presents a useful operational time of 560 s, this time is elongated for the admixture bed configuration by 28.6% to 720 s. This difference is contributed to the higher adsorption rates of CO_2 shown by the admixture bed, see Figure 22.

The two bed configurations are also studied for the Rh/lithium zirconate–based systems at 4 combinations of the conventional high capacity and slow adsorption kinetics, high capacity and fast adsorption kinetics, low capacity and slow adsorption kinetics, low capacity and fast adsorption kinetics.

The Rh/lithium zirconate–based system in both bed configurations demonstrates much insignificant difference in the maximum CH_4 conversion attained and the breakthrough time according to the conversion criterion. Figure 23 shows that the admixture bed configuration gives a small increase in CH_4 conversion of 0.78% and an elongated operational time of 5.5%. These values are obtained at a high capacity of 5 kg/mol and slow adsorption kinetics (k_{CO2}=3.3*10^{-4} m^3/mol.s). At

high capacity and fast kinetics (k_{CO2}=3.3*10^{-4} m^3/mol.s), the CH_4 conversion profiles of the two configurations are almost superimposed on each other as shown in Figure 24. The time for the integrated particle system before reaching the equilibrium conditions is elongated by a 12.7%.

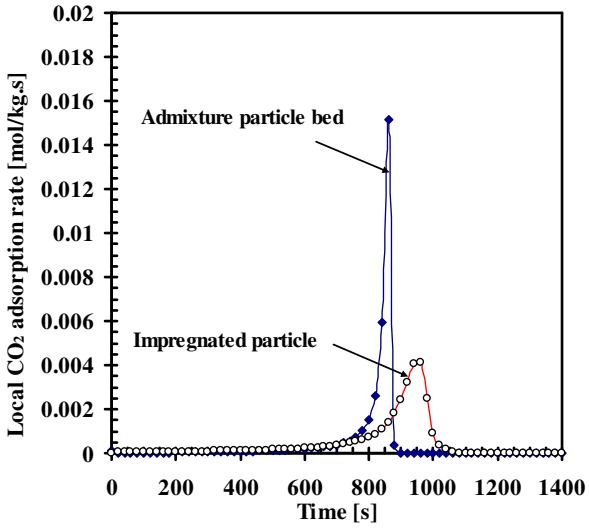

Fig. 22: Effect of catalyst/sorbent particle and bed configuration on the CO_2 adsorption rates for the Rh/HTC system. 550 °C, 4.65 bar, S/C=6 and G_s=0.05 kg/m^2.s.

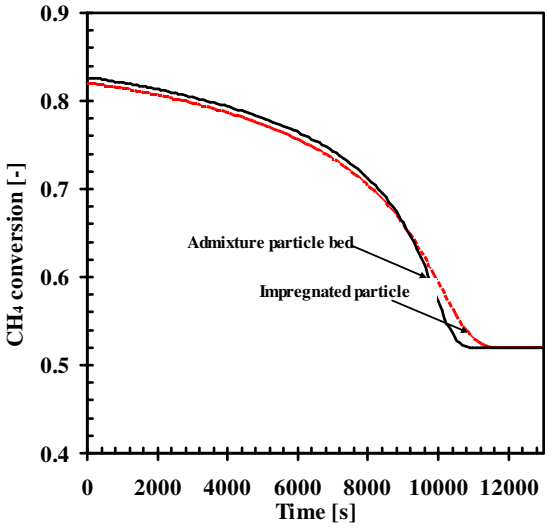

Fig. 23: Effect of catalyst/sorbent particle and bed configuration on the CH_4 conversion profiles for the Rh/LZC system at slow adsorption kinetics and high capacity. 550 °C, 4.65 bar, S/C=6 and G_s=0.05 kg/m^2.s.

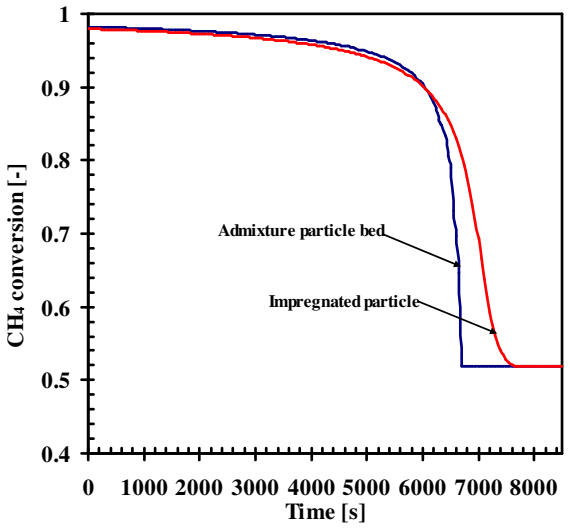

Fig. 24: Effect of catalyst/sorbent particle and bed configuration on the CH_4 conversion profiles for the Rh/LZC system at fast adsorption kinetics and high capacity. 550 °C, 4.65 bar, S/C=6 and G_s=0.05 kg/m^2.s.

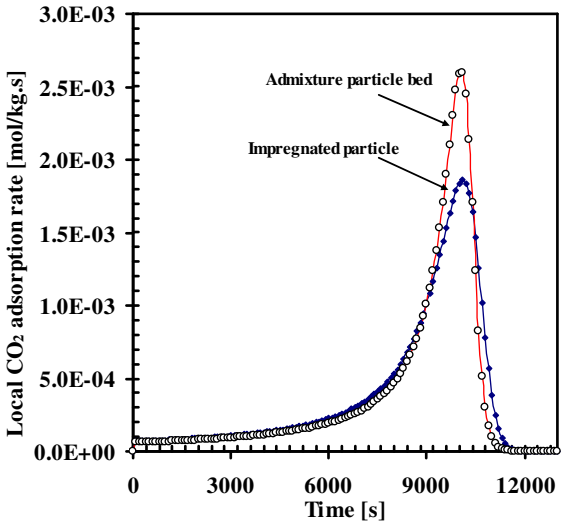

Fig. 25: Effect of catalyst/sorbent particle and bed configuration on the CO_2 adsorption rates for the Rh/LZC system at slow adsorption kinetics and high capacity. 550 °C, 4.65 bar, S/C=6 and G_s=0.05 kg/m^2.s.

The little variation between the two configurations is contributed to the difference in CO_2 adsorption rates as given in Figures 25 and 26; respectively. Finally, it is determined that using low capacity of 0.5 mol/kg for the lithium zirconate sorbent

does not lead to a change in the process performance either at fast or slow adsorption kinetics. The CH_4 conversion profiles displayed in Figure 27 clearly confirm this conclusion.

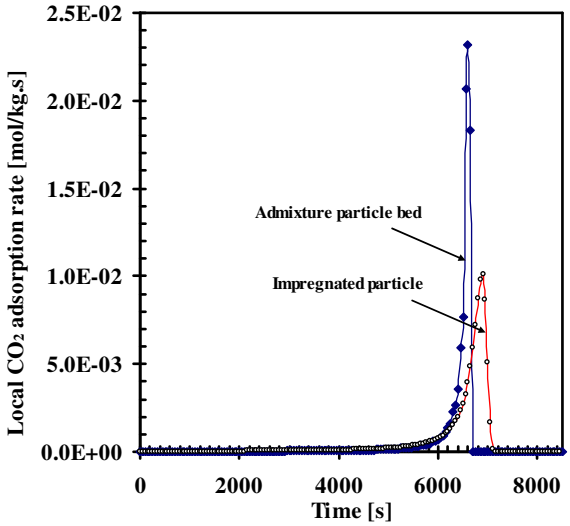

Fig. 26: Effect of catalyst/sorbent particle and bed configuration on the CO_2 adsorption rates for the Rh/LZC system at fast adsorption kinetics and high capacity. 550 ^oC, 4.65 bar, S/C=6 and G_s=0.05 kg/m^2.s.

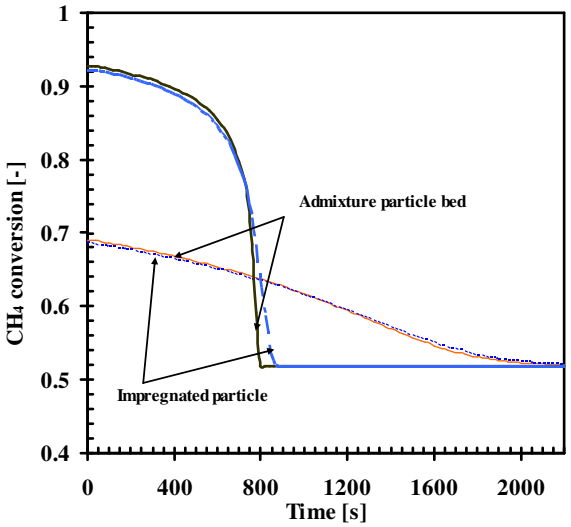

Fig. 27: Effect of catalyst/sorbent particle and bed configuration on the CH_4 conversion profiles for the Rh/LZC system using low capacity at slow/fast adsorption kinetics. 550 ^oC, 4.65 bar, S/C=6 and G_s=0.05 kg/m^2.s.

8.6 Conclusion

The applicability of integration of a highly active $Rh/Ce_\alpha Zr_{1-\alpha}O_2$ catalyst with two candidate CO_2 sorbents of hydrotalcite and lithium zirconate in low temperature–sorption enhanced steam reforming of methane is investigated. Particle–based model, heterogeneous plug flow bulk–scale model, and homogenous plug flow bulk–scale model are constructed to theoretically analyze the process. The presence of this active catalyst dictates strict requirements on the sorbent in terms of fast adsorption kinetics for an efficient performance of the process. The maximum CH_4 conversion enhancement is a strong function of sorption kinetics. Hydrotalcite–based system should provide adsorption rates with a corresponding CO_2 effective mass transfer coefficient > 10^{-1} 1/s at 550 ^oC. Lithium zirconate–based system should have a CO_2 adsorption rate constant in the range of 10^{-2} m^3/mol.s at 550 ^oC. The conversion enhancement is not affected by higher sorbent capacity at slow adsorption kinetics. However, at fast adsorption kinetics the effect of capacity can still be distinguished. The process is studied using two bed configurations of an integrated dual function particle and an admixture bed of catalyst sorbent particles. The optimal catalyst/sorbent ratio is determined to be a function of the operating conditions. The catalyst composition inside the particle is 1–3 % at low temperature of 550^{o}C and intermediate pressure of 4.65 bar and low gas flow rate of 0.05 kg/m^2.s, this composition is increased to 10% at higher pressure of 15 bar and higher gas flowrate of 1.5 kg/m^2.s. CH_4 conversion enhancement is studied at

different temperature and pressure. The maximum enhancement in conversion is found to be 276% at low temperature of 450 ^oC and high pressure of 15.6 bar using 5 mol/kg of hydrotalcite capacity; at which CO and CO_2 impurities can be as low as 40 and 170 ppm ; respectively. Optimal operating conditions for hydrotalcite–based system are identified to be 550^oC, 4.65 bar, S/C ratio of 6, and mass gas flow rate of 0.05 kg/m^2s to provide CH_4 conversion of 98% with high H_2 purity of 99.8% and low CO_2 contamination <250 ppm. Lithium zirconate–based system can provide CH_4 conversion and H_2 purity of 99.9% at identical conditions. The dual function particle system and the admixture bed system show a very similar performance in terms of maximum CH_4 conversion and product composition in case of the lithium zirconate sorbent. Discrepancy in performance is observed in case of the hydrotalcite sorbent. The effect of the physical characteristics of the particle and the bed on CH_4 conversion and adsorption rates is determined at different particle size, particle voidage, pore diameter, tortuosity, and bed voidage.

Nomenclature

Symbol	Definition	Unit
$C_{i,b}$	Concentration of species i in the bulk gas phase	mol/m^3
$C_{i,p}$	Concentration of species i in the solid pore	mol/m^3
$D_{eff,i}$	Effective diffusion coefficient of species i	m^2/s
$D_{m,i}$	Average molecular diffusivity of species i	m^2/s
$D_{k,i}$	Average molecular diffusivity of species i	m^2/s
D_Z	Axial dispersion coefficient	m^2/s
d_p	Particle diameter	m
d_{pore}	Pore diameter of the particle	m
E_j	Activation energy of reaction j	J/mol
$F_{i,P}$	Diffusion rate of species i at the solid surface	mol/m^{2}s
G_s	Gas mass flow velocity	kg/m^{2}s
k_j	Temperature dependent kinetic rate constant of reaction j	
$k_{j,o}$	Arrhenius kinetic rate constant of reaction j	
$K_{eq,j}$	Thermodynamic equilibrium constant of reaction j	kPa$^{\Sigma \nu_{ij}}$
$K_{i,o}$	Reference adsorption constant of species i	1/kPa
K_i	Adsorption constant of species i	1/kPa
k_j	Temperature dependent kinetic rate constant of reaction j	
$k_{j,o}$	Arrhenius kinetic rate constant of reaction j	
$K_{eq,j}$	Thermodynamic equilibrium constant of reaction j	kPa$^{\Sigma \nu_{ij}}$
K_D	Parameter corresponding to the viscous loss term	Pa.s/m^2
K_V	Parameter corresponding to the kinetic loss term	Pa.s^2/m^3
p_i	Partial pressure of gas species i	bar
P	Total gas pressure	bar
r	Radial particle dimension	m
R_j	Rate of consumption or formation of species i	mol/kg$_{cat}$.s
R_{adsj}	Rate of adsorption of CO_2	mol/kg$_{ads}$.s
R	Universal gas constant	J/mol.K
T	Gas phase temperature	K
t	Time	s
u	Superficial gas flow velocity ($=\varepsilon_b u_{inst}$)	m/s
Y_i	Dry mole fraction of species i	mol/mol
z	Axial dimension	m
Greek symbols		
ΔH_i	Heat of adsorption of species i	J/mol
ΔH_{298K}	Heat of reaction of at STP	kJ/mol
ε_b	Voidage of the bed	–
ε_P	Voidage of the pellet	–
ρ_P	Density of solid pellet	kg/m^3
$\rho_{b,cat}$	Bulk density of the catalyst	kg/m^3
$\rho_{b,ads}$	Bulk density of the sorbent	kg/m^3
ρ_f	Density of the fluid	kg/m^3
μ_g	Viscosity of the fluid	Kg/ms
v_{cat}	Fraction of catalyst in the integrated catalyst/sorbent particle	–

v_{ads}	Fraction of sorbent in the integrated catalyst/sorbent particle	–
τ	Tortuosity factor of the particle	–
Ω	Dominator term in the reaction kinetics	

References

1. Hufton, J. R., Mayorga, S., Sircar, S. Sorption-enhanced reaction process for hydrogen production. AIChE J. 45 (1999), 248–256.
2. Hufton, J., Waldron, W., Weigel, S., Rao, M., Nataraj, S., Sircar, S., Sorption enhanced reaction process SERP) for the production of hydrogen, in: Proceedings of the 2000 US DOE Hydrogen Program Review, 2000.
3. Ding, Y., Alpay, E. Adsorption-enhanced steam-methane reforming. Chem. Eng. Sci. 55 (2000) 3929–3940.
4. Ding, Y., Alpay, E. High temperature recovery of CO_2 from flue cases using hydrotalcite adsorbent. Trans IChemE. 79-B1 (2001) 45–51.
5. Waldron, W. F.; Hufton, J. R.; Sircar, S. Production of hydrogen by cyclic sorption enhanced reaction process. AIChE J. 47 (2001) 1477–1479.
6. Xiu, G.; Soares, J. L.; Li, P.; Rodrigues, A. E. Simulation of five-step one-bed sorption-enhanced reaction process. AIChE J. 48 (2002) 2817–2832.
7. Xiu, G.; Li, P.; Rodrigues, A. E. Sorption-enhanced reaction process with reactive regeneration. Chem. Eng. Sci. (2002) 57, 3893–3908.
8. Xiu, G.; Li, P.; Rodrigues, A. E. New generalized strategy for improving sorption-enhanced reaction process. Chem. Eng. Sci. (2003) 58, 3425–3437.
9. Xiu, G.; Li, P.; Rodrigues, A. E. Adsorption-enhanced steam-methane reforming with intraparticle-diffusion limitations. Chem. Eng. J. (2003) 93, 83–93.
10. Wang Y.N; Rodrigues A.E. Hydrogen production from steam methane reforming coupled with in situ CO_2 capture: Conceptual parametric study. Fuel (2005) 84, 1778–1789.
11. Yong, A., Mata, V., Rodrigues, A.E. Adsorption of carbon dioxide onto hydrotalcite-like compounds (HTlcs) at high temperatures, Ind. Eng. Chem. Res. 40 (2001) 204-209.
12. Reijers, H. Th. J.; Boon, J.; Elzinga, G. D.; Cobden, P. D.; Haije, W.G.;van den Brink, R. W. Modeling study of the sorption-enhanced reaction process for CO2 capture. I. model development and validation. Ind. Eng. Chem. Res., 2009, 48, 6966-6974.
13. Ebner, A. D.; Reynolds, S. P.; Ritter, J. A. Non-equilibrium kinetic model that describes the reversible adsorption and desorption behavior of CO2 in a K-promoted hydrotalcite-like compound. Ind. Eng. Chem. Res. 2007, 46, 1737–1744.
14. Lee, K. B.; Verdooren, A.; Caram, H. S.; Sircar, S. Chemisorption of carbon dioxide on potassium-carbonate-promoted hydrotalcite. J. Colloid Interface Sci. 2007, 308, 30–39.

15. Oliveira, E. L. G.; Grande, C. A.; Rodrigues, A. E. CO_2 Sorption on hydrotalcite and alkali-modified (K and Cs) hydrotalcites at high temperatures. Sep. Purif. Technol. 2008, 62, 137–147.
16. Lwin, Y.; Abdulla, F.; High temperature adsorption of carbon dioxide on Cu-Al hydrotalcite-derived mixed oxides: kinetics and equiblria by thermogravimetry. J. Therm. Anal. Calorim. 2009, 97, 885-889.
17. Niels N. A. H. Meis, Johannes H. Bitter, and Krijn P. de Jong. Support and Size Effects of Activated Hydrotalcites for Precombustion CO_2 Capture, Ind. Eng. Chem. Res. 2010, 49, 1229–1235
18. Othman, M. R., Helwania, Z., Martunusa, B, Fernando, W.J.N., Synthetic hydrotalcites from different routes and their application as catalysts and gas adsorbents: a review, Appl. Organometal. Chem. 2009, 23, 335–346
19. Kato, M., Yoshikawa, S., Nakagawa, K., Carbon dioxide absorption by lithium orthosilicate in a wide range of temperature and carbon dioxide concentrations, J. Mater. Sci. Lett. (2002) 21, 485.
20. Ida, J.-I., Lin, Y.S. Mechanism of high-temperature CO_2 sorption on lithium zirconate, Environ. Sci. Technol. 37 (2003) 1999.
21. Xiong, R., Ida, J., Lin, Y., Kinetics of carbon dioxide sorption on potassium-doped lithium zirconate, Chem. Eng. Sci. 58 (2003) 4377-4385.
22. Ida, J., Xiong, R., Lin, Y.S., Synthesis and CO_2 sorption properties of pure and modified lithium zirconate, Sep. Purif. Technol. 36 (2004) 41-51.
23. Fauth, D.J., Frommell, E.A., Hoffman, J.S, Reasbeck, R.P., Pennline, H.W., Eutectic salt promoted lithium zirconate: novel high temperature sorbent for CO_2 capture, Fuel Process. Technol. 86 (2005) 1503-1521.
24. Wang, Y.-J., Qi, L., Wang, X.-Y., The study of Li_2ZrO_3 used for absorption of CO_2 at high temperature, Chin. J. Inorg. Chem. (2003), 19 531.
25. Nair, B.N., Yamaguchi, T., Kawamura, H., Nakao, S., Processing of lithium zirconate for applications in carbon dioxide separation: structure and properties of the powders, J. Am. Ceram. Soc. (2004) 87, 68.
26. Kapil, A; Bhat, S.A.; Sadhukhan, J.Multiscale characterization framework for sorption enhanced reaction process. AICHE J. (2008) 54, 1025–1036.
27. Koumpouras G.C., Alpay E., Stepanek F. Mathematical modelling of low-temperature hydrogen production with in situ CO_2 capture. Chem Eng Sci. (2007) 62, 2833–2841.
28. Koumpouras G.C, Alpay E., Lapkin A., Ding Y., Frantisek S. The effect of adsorbent characteristics on the performance of a continuous sorption-enhanced steam methane reforming process. Chem Eng.Sci. (2007), 62, 5632-5637.
29. Ochoa-Fernandez, E., Rusten, H.K., Jakobsen, H.A, Rønning, M., Holmen, A., Chen, D., Sorption enhanced hydrogen production by steam methane reforming using Li_2ZrO_3 as sorbent: sorption kinetics and reactor simulation, Catal. Today, 106 (2005) 41-46.
30. Halabi, M.H., de Croon, M.H.J.M, van der Schaaf, J., Cobden, P.D., Schouten, J.C., Low temperature catalytic methane–steam reforming over ceria–zirconia supported rhodium, App. Catal. A (2010) 10.1016/j.apcata.2010.09.004.
31. Halabi, M.H., de Croon, M.H.J.M, van der Schaaf, J., Cobden, P.D., Schouten, J.C., Intrinsic kinetics modeling of catalytic methane–steam reforming and

water–gas shift over $Rh/Ce_{\alpha}Zr_{1-\alpha}O_2$ catalyst, App. Catal. A (2010) 10.1016/j.apcata.2010.09.005.
32. Ergun, S., Fluid flow through packed columns, Chem.Eng.Prog. 48 (1952) 89–94.
33. Edwards, M.F., and J.F. Richardson, Gas dispersion in packed beds, Chem.Eng.Sci. 23 (1968) 109–123.
34. Froment, G.F., Bischoff, K.B, Chemical reactor analysis and design, Wiley, London, (1990).
35. Reid, R.C., Prausnitz, J.M., and Poling, B.E., The Properties of Gases and Liquids, McGraw-Hill, New York, (1988).
36. Bird, R.B., Stewart, W.E., and Lightfoot, E.N., Transport Phenomena, 2nd Ed., Wiley, New York, (2002).

Chapter 9

Experimental Study of Sorption Enhanced Catalytic Methane Steam Reforming Over Newly Developed Catalyst–Sorbent Materials

This chapter has been submitted for publication as

1. M.H. Halabi, M.H.J.M. de Croon, J. van der Schaaf, P.D. Cobden, J.C. Schouten, A novel catalyst–sorbent system for an efficient H_2 production with in-situ CO_2 capture, Int. J. Hydrogen Energy, accepted, 2011.
2. M.H. Halabi, M.H.J.M. de Croon, J. van der Schaaf, P.D. Cobden, J.C. Schouten, High capacity potassium–promoted hydrotalcite for CO_2 capture in H_2 production, Int. J. Hydrogen Energy, submitted, 2011.

Abstract

This chapter presents an experimental investigation for an improved process of sorption-enhanced steam reforming of methane in an admixture fixed bed reactor. A highly active $Rh/Ce_{\alpha}Zr_{1-\alpha}O_2$ catalyst and K_2CO_3–promoted hydrotalcite are utilized as novel catalyst/ sorbent materials for an efficient H_2 production with in situ CO_2 capture at low temperature (450–500^{o}C). The process performance is demonstrated in response to temperature (400–500 ^{o}C), pressure (1.5–6.0 bar), and steam/carbon ratio (3–6). Thus, direct production of high H_2 purity and fuel

conversion >99% is achieved with low level of carbon oxides impurities (<100 ppm). A new set of adsorption data is reported for CO_2 adsorption over K-hydrotalcite at 400 ^oC. The equilibrium sorption data obtained from a column apparatus can be adequately described by a Freundlich isotherm. The sorbent shows fast adsorption rates and attains a relatively high sorption capacity of 0.95 mol/kg on the fresh sorbent. CO_2 desorption experiments are conducted to examine the effect of humidity content in the gas purge and the regeneration time on CO_2 desorption rates. A large portion of CO_2 is easily recovered in the first few minutes of a desorption cycle due to a fast desorption step, which is associated with a physi/chemisorption step on the monolayer surface of the fresh sorbent. The complete recovery of CO_2 was then achieved in a slower desorption step associated with a reversible chemisorption in a multi-layer surface of the sorbent. The sorbent shows a loss of 8% of its fresh capacity due to an irreversible chemisorption, however, it preserves a stable working capacity of about 0.89 mol/kg, suggesting a reversible chemisorption process. The sorbent also presents a good cyclic thermal stability in the temperature range of 400–500 ^oC.

9.1 Introduction

The increasing demand for H_2 as a major feedstock in many petrochemical industries or as an energy carrier in fuel cells or gas turbine cycles has been shifting the world into a hydrogen-based energy economy [1–5]. The global awareness of climate change has imposed stringent control and regulations on the reduction, the disposal, and even the elimination techniques of CO_2 emissions [6]. H_2 is still commercially produced by the conventional steam reforming of natural gas at high temperature range of 700–900 ^oC [2–5]. This process is limited in H_2 productivity and CH_4 feedstock conversion due to the thermodynamic bounds of the steam reforming reactions. The sorption enhanced catalytic reforming concept presents a potential intensified technique in which the co-generated CO_2 is selectively removed from the product gas mixture by an efficient sorbent material [1,7–9]. The sorbent is then regenerated via a temperature or pressure swing operation. This eventually circumvents the thermodynamic equilibrium limitations and implies a high purity H_2 production (>95%) and high CH_4 conversion (>90%) with very low impurities of CO and CO_2 at relatively much lower temperature (400–500 ^oC). A typical sorbent that can employed in this process must have several requirements [10,11] (i) selective sorption of CO_2 at the process temperature and in presence of steam, CH_4, CO, and H_2, (ii) adequate working CO_2 capacity at the process operational temperature, (iii) adequate rates of sorption and desorption, and (iv) adequate thermal and cyclic stability at the process conditions.

A variety of materials has been studied and reported in literature for CO_2 (ad)sorption. These materials can be classified as (i) microporous and mesoporous inorganic and organic materials such as zeolites [12–14], silica gel [11,15], alumina [16], and activated carbon [17–19], (ii) mixed oxide materials such as CaO [20–29], (iii) lithium metal oxides such as lithium zirconate (LZC) [30–37] and lithium

orthosilicate (LOS) [38,39], (iv) and hydrotalcite-like materials (HTC) [40–46]. The first type of materials tends to show high physical adsorption rate for CO_2 with a reasonable high adsorption capacity at low temperature (near ambient) [12–29]. The low to moderate isosteric heats of adsorption of these materials allow reversible adsorption and desorption of CO_2 at relatively low temperature [12,15,17,20]. However, these physisorbents have major operational limitations [12,15,17,20]: (i) CO_2 working capacity drastically diminishes to be almost negligible as the temperature increases above 250 ^oC, (ii) polar adsorbents such as silica gel, alumina, and zeolites show very poor performance in presence of polar gases as they selectively adsorb water over CO_2 [12–14].

CaO has also been reported to show strong affinity for CO_2 sorption at high temperature above 500 ^oC. CaO can react with CO_2 in a bulk chemical carbonation reaction according to:

$$CaO + CO_2 \leftrightarrow CaCO_3 \qquad \Delta H_{298K} = -182 \text{ kJ/mol}$$

CaO offers a very high temperature-independent stoichiometric sorption capacity of 17.8 CO_2 mol/kg [22,25,28]. However, CaO has also some operational limitations [26–29]: (i) the CO_2 working capacity is much lower than the stoichiometric capacity unless the material is regenerated at high temperature of 900 ^oC due to the thermodynamically unfavorable desorption of CO_2, thus (ii) slow kinetics of sorption/desorption at low temperature of about 500 ^oC, (iii) cyclic stability of CaO in terms of CO_2 is significantly reduced due to the buildup of the irreversible $CaCO_3$, and (iv) sintering of the CaO active surface is also a concern during desorption at high temperature.

Lithium zirconate (LZC) and lithium orthosilicate (LOS) have recently received more attention due to their ability to retain good CO_2 chemisorption capacity at high temperature (5.0 mol/kg [36] and 6.13 mol/kg [39], respectively). However, the slow sorption kinetics and the high heat of reaction due to the strong chemical bonding to CO_2 require a high regeneration temperature (900 ^oC for LZC [30–37] and 700 ^oC for LOS [38,39], respectively).

$$Li_2ZrO_3 + CO_2 \leftrightarrow Li_2CO_3 + ZrO_2 \qquad \Delta H_{298K} = -160 \text{ kJ/mol}$$
$$Li_4SiO_4 + CO_2 \leftrightarrow Li_2SiO_3 + Li_2CO_3 \qquad \Delta H_{298K} = -142 \text{ kJ/mol}$$

Hydrotalcite–like materials have been found to have an adequate CO_2 working sorption capacity (0.45–1.0 mol/kg) at high temperature of 400–450 ^oC [40–46], infinite selectivity for CO_2 even in the presence of steam, steam has been determined to enhance the sorption capacity and stability [43], very good cyclic stability, fast sorption kinetics, and relatively easy desorption rates due to low to moderate heats of chemisorption in the Henry's law region (weak bonding to CO_2) [11, 44, 45]. Therefore, these materials are considered to be promising sorbents for high purity H_2 production in the sorption enhanced steam reforming of methane.

However, the sorbent composition and the preparation methods will eventually determine the final properties of the material [46,47].

Several studies have been reported in literature to investigate the characteristics of CO_2 sorption on different types of HTC and K_2CO_3 promoted HTC [40–46]. Ding and Alpay [43] derived a Langmuirian type adsorption isotherm for CO_2 on HTC with a maximum monolayer capacity of 0.65 mol/kg in wet conditions at 400 ^oC and pressure range of 0–1.0 bar. Their measurements suggested rapid and irreversible chemisorption on the fresh sorbent followed by reversible and relatively weak physical adsorption thereafter. Lee et al. [44] have proposed a reversible CO_2 chemisorption on K_2CO_3–promoted HTC at temperatures of 400 and 520 ^oC. The CO_2 equilibrium isotherms were of the Langmuir type for low CO_2 partial pressure (<0.2 bar) region. The isotherms deviated from the Langmuir type in a higher pressure region. The authors developed an analytical model that combines a Langmuirian reversible CO_2 chemisorption on the surface followed by a reversible chemical complexing reaction between the gaseous and the sorbed CO_2 molecules. Oliveira et al. [45] have suggested a bi-Langmuirian isotherm for CO_2 chemisorption on K and Cs promoted HTC at 306, 403, and 510 ^oC. Very good cyclic stability of the sorbent was demonstrated. The effect of the preparation method on the irreversible and reversible sorption of CO_2 on HTC is investigated [46]. The effects of K_2CO_3 impregnation loading and the Mg/Al ratio in the HTC composition on the CO_2 capacity are also reported [47].

Nearly all the experimental attempts on the utilization of HTC in sorption enhanced H_2 production apply a conventional low activity Ni-based catalyst in an admixture fixed bed reactor [7–9, 48–50]. Hufton et al. [7] achieved a H_2 product stream with a purity of 95% and CH_4 fuel conversion of 80% and $CO+CO_2$ concentration of less than 50 ppm at 450 ^oC and 4.7 bar. They further [9] determined that the multi-cycle operation failed to maintain the same performance of a single cycle process due to the unrecovered sorbent capacity during the pressure swing regeneration cycles. They obtained CH_4 conversion and H_2 purity of 54 and 88.7%, respectively. Ding and Alpay [48] obtained 75% CH_4 conversion and H_2 purity >90% in a laboratory scale fixed bed of 22 cm in length using S/C ratio of 6 at 450 ^oC and 4.45 bar. Lee et al. [49] demonstrated improved process performance in larger scale column (2.0 m length and 1.73 cm diameter) using the temperature swing regeneration and better capacity HTC sorbent. They reached a CH_4 conversion and H_2 purity of 96 and 99.99%, respectively, at reaction temperature of 490 ^oC and 1.5 bar. The bed is regenerated using steam purge at 590 ^oC. Beaver et al. [50] reported almost the same performance for a fuel-cell grade H_2 with CO impurity <20 ppm at a slightly higher temperature range of 520–550 ^oC and ambient pressure in a 1.73 m long reactor.

We recently studied $Rh/Ce_{\alpha}Zr_{1-\alpha}O_2$ as a promising catalyst for H_2 production from steam reforming of methane [51]. A detailed kinetic model of the steam reforming reactions is also derived in a low temperature operation (450–570 ^oC) [52]. This chapter presents an experimental investigation study of Rh-based/K-promoted HTC

materials as a novel catalyst/sorbent system for direct high purity H_2 production from sorption enhanced steam reforming with in situ CO_2 capture. $Rh/Ce_{\alpha}Zr_{1-\alpha}O_2$ is selected as an effective catalyst, which provides high reaction rates in low–temperature steam reforming (<500 ^{o}C) in order to maintain a high CO_2 sorption capacity of the HTC sorbent. This integration implies several benefits in terms of (i) much lower capital costs due to the significantly smaller reactor volume, (ii) much lower catalyst loading, the reactor can be packed with catalyst as low as 1–10% only, (iii) high purity fuel-cell grade H_2 production at low temperature (450–500 ^{o}C) and pressure (1.5–4.5 bar), (iv) high pressure operation can also yield high purity H_2 for electricity generation in gas turbine cycles. A new set of experimental data for CO_2 sorption on a high-capacity K-promoted HTC is presented. CO_2 desorption and HTC cyclic stability are also demonstrated.

9.2 Experimental and materials

9.2.1 Steam reforming catalyst

The $Rh/Ce_{\alpha}Zr_{1-\alpha}O_2$ catalyst is prepared by the dry impregnation method. Rh metal is loaded from a $Rh(NO_3)_3$ solution onto a commercially available mixture of a ceria–zirconia support with a weight composition of (60:40), which is provided by MEL chemicals, UK. The catalyst is heated at a rate of 2 ^{o}C/min up to 450 ^{o}C and calcined at that temperature for 5 hrs. The catalyst is characterized by standard techniques of XRD, TEM, SEM, and XPS. The BET surface area is determined by N_2 adsorption porosimetry and the metal dispersion is determined by the volumetric H_2 chemisorption uptake in a Micromeritics Chemisorb 2750. More details of the catalyst characterization techniques are given in our previous work [51]. The catalyst performance under the steam reforming reactions was extensively studied at sorption enhanced steam reforming conditions in the temperature range of 350 – 750 ^{o}C and at a S/C ratio of 1–6 [51]. The catalyst showed very high activity in terms of CH_4 conversion, very good stability over 100 h time on stream, and excellent resistance towards carbon formation. Some physical properties of the catalyst are listed in Table 1.

Table 1: Catalyst properties.

	Value
Average pellet size	300 μm
Rh metal content	0.8 %
BET surface area of the support	85.7 m^2/g
BET surface area of the fresh catalyst	38.8 m^2/g
BET surface area of the spent catalyst	37.2 m^2/g
Pore volume of the catalyst	0.20 cm^3/g
Pore diameter of the catalyst	20.4 nm
Metal dispersion on the fresh catalyst	27.9 %
Metal dispersion on the spent catalyst	27.1 %
Crystallite particle size	3 nm
Ce/Zr composition ratio	0.6/0.4

In the sorption enhanced reforming experiments, a catalyst loading of 120 mg is used. The fresh catalyst is pretreated in a reductive environment to prevent over oxidation of the surface at high S/C ratio. The catalyst bed (including the sorbent) is exposed to a 20% vol. H_2 and 80% vol. Ar gas mixture before the experiment starts. The catalyst is gradually heated at a rate of 3 ^oC/min to 450 ^oC using a total Ar gas flow of 100 nml/min and maintained at this temperature for 2 h. H_2 gas is then introduced at 450 ^oC for 2 h.

9.2.2 K_2CO_3–promoted hydrotalcite sorbent

Hydrotalcite (HTC) belongs to the anionic and basic clays, also known as layered double hydroxides (LDH) [10,11,42]. This structure is composed of positively charged brucite-like layer and negatively charged interlayer. The positive charge is generated from the trivalent cations partially substituting divalent cations in the brucite structure. The excess positive charge is balanced by anions and water molecules present in the interlayer. The general formula of the HTC structure can be represented as $\left[M^{2+}_{1-x}M^{3+}_{x}(OH)_2\right]^{x+}\left(A^{n-}_{x/n}\right).mH_2O$, where M^{2+} can be any of the following elements Mg, Cu, Ni, Mn, Zn; M^{3+} can be any of the following elements Al, Fe, Cr, V; A^{n-} is the interlay anion and can be one of these ions CO_3^{2-}, Cl^-, NO_3^-, SO_4^{2-} and x can be 0.1–0.33. However, the different combinations of the cations, anions, and the ratio of cations M^{2+}/M^{3+}, preparation and activation methods will eventually determine the final properties of the material [40,47]. The most common composition of HTC used as a chemisorbent for CO_2 at high temperature contains Mg^{2+}, Al^{3+}, and CO_3^{2-} as $Mg_{1-x}Al_x(OH)_2(CO_3)_{x/2}\cdot mH_2O$ [10,11,45].

The sorption capacity of HTC at high temperature is strongly related to the basicity of the surface and to the available surface area to a less extent [47]. The number of surface basic sites is a function of the HTC chemical composition (e.g. Mg/Al ratio) and the degree of impregnation with alkali metal carbonate such as K_2CO_3. Maximum adsorption capacity is obtained as the K_2CO_3 loading increased to an optimum value of about 20% despite of the reduction in the BET surface area and the pore volume. Higher loading tends to block some small active pores for CO_2 adsorption; therefore the capacity is negatively affected.

The hydrotalcite sorbent used in the experiments reported in this work is PURAL MG61 HT with a $MgO:Al_2O_3$ metal composition of (61:39 wt%) and provided by SASOL-Germany. The sorbent is first calcined at 400 ^oC for 4 h. The sorbent is then loaded with 22 wt% K_2CO_3 (Merck) using the dry impregnation method. The powder is dried over night at 120 ^oC and then calcined at 400 ^oC for 4 h. A sieve fraction of 0.212–0.425 mm is used throughout the experiments. Several physical properties of the fresh K_2CO_2 promoted HTC sorbent are listed in Table 2.

9.2.3 Experimental setup and analysis

The CO_2 adsorption and the sorption enhanced steam reforming experiments are performed in a fixed bed tubular rector setup. The reactor is 1.0 m in length and is composed of three zones; two upper–part heating zones and one reaction zone of

19.5 cm in length. The reactor is a quartz tube with an internal diameter of 9.0 mm along the heating and the reaction zones.

Table 2: K-HTC sorbent properties.

	Value
Average pellet size	400 μm
BET surface area of the HTC sorbent	15.61 m^2/g
BET surface area of the K-HTC sorbent	5.38 m^2/g
Pore volume of the fresh K-HTC sorbent	0.037 cm^3/g
Pore diameter of the fresh K-HTC sorbent	18.7 nm
Mg/Al (M^{2+}/M^{3+}) cation composition ratio	1.56
K_2CO_3 promoter loading	22 wt%
Bulk density of the fresh sorbent bed	748.6 kg/m^3

The temperature is measured along the reactor and controlled in a temperature range of 100–550 ^oC. Gas flows are controlled by thermal mass flow controllers. Gas flow rates of CH_4, CO, CO_2, and H_2 in a range of 0–50 nml/min are applied, Ar is used as an inert and a carrier gas in the flow range of 0–500 nml/min. Steam is applied to the system by evaporating distilled water in a static evaporator mixer at 80 ^oC with a maximum flow rate of 1500 mg/hr. The fluctuation in the measured water concentration is within ±7% of the set-point. The overall gas mixture contains up to 25% water on a relative humidity basis. The total pressure of the reactor is maintained by means of a back pressure controller in the desired range of 1.0–6.0 bar. The process lines are traced at 80 ^oC and insulated to prevent any condensation of steam.

The gas composition of the feed and the product is measured using an online mass spectrometer (ESS II). A quadrupole mass analyzer (QMS 422) is used to sort out the generated ions according to their mass/charge ratios under electromagnetic field. A multiple ion detector (MID) of CH-THRON type is used to measure the current intensities of the ions. Direct quantitative analysis for the gases was possible through the multiple concentration detection channel (MCD) in which the concentration of the element is calculated by multiplying the ion current intensity measured in the MID detector by its corresponding calibration factor. Mass scale is calibrated for the gases according to the following mass/charge (amu) ratios: H_2=2, CH_4=15, H_2O=18, CO=28, Ar=40, CO_2=44. Ar gas is used as an internal standard throughout all the measurements. The mass scale calibration is corrected for any deviation from the theoretical mass/charge ratios in order to identify the exact peak locations. The gas sampling line (1/16″) was insulated and traced at 130 ^oC to prevent any steam condensation.

The mass scale is re-calibrated for each set of experiments that is performed at a certain pressure to minimize any inaccurate measurements (i.e. each pressure is associated with a new calibration). The mass scale is also re-calibrated if any contaminant gases reach to the vacuum chamber in case that the reactor is opened to ambient atmosphere.

9.2.4 Experimental procedure

The scope of the experiments performed in this study includes the following routes:

- CO_2 effluent breakthrough experiments

CO_2 (ad)sorption experiments are conducted in a fixed bed dynamic column. 2 g of K-promoted HTC sorbent is packed in the bed forming a 4.0 cm bed height. CO_2/Ar and/or CO_2/steam/Ar gas mixture is introduced over the sorbent bed in dry and wet conditions, respectively at 400 ^oC. The gas transient effluent is measured to generate the CO_2 concentration breakthrough curves in absence/presence of steam, and thus the CO_2 sorption isotherms. In dry conditions, CO_2 gas is inserted into the bed in a partial pressure range of 0.05–0.7 bar. In wet conditions, steam partial pressure of 0.24–0.35 bar was used over a CO_2 partial pressure range of 0.1–0.9 bar. The breakthrough time (t_B, s) considered in the data analysis is defined as the time at which the effluent CO_2 concentration (Y_{CO_2}) is equal to 5% of the equilibrium concentration ($Y^{eq}_{CO_2}$).

The CO_2 sorbent capacity (m_{CO_2}, mol/kg) is defined as the CO_2 (ad)sorbed (mol) up to the breakthrough time (t_B) according to

$$m_{CO_2} = \frac{Y_{CO_2,in} \cdot F \cdot t_B}{W} \qquad \text{Eq. 1}$$

Where F is the molar gas feed rate (mol/s), $Y_{CO_2,in}$ is the CO_2 concentration in the feed, and W is the fresh sorbent weight (kg) before activation. These experiments can elucidate the rates and kinetics of CO_2 sorption on the studied sorbent. The CO_2 sorption isotherm is constructed at a certain temperature from the equilibrium concentration data obtained from the column dynamic effluent breakthrough curves. A typical adsorption cycle is composed of the following steps: (i) the sorbent bed is purged with 150 nml/min Ar gas or 20/80 vol% steam/Ar gas at 400 ^oC and ambient pressure for 2 h, (ii) counter-current pressurization at a predefined pressure and temperature using Ar/steam purge, (iii) CO_2 (ad)sorption at a predefined temperature in CO_2/Ar or steam/CO_2/Ar gas mixture, (iv) counter-current depressurization step to ambient pressure. During the activation step (i), the effluent gas composition is measured until the CO_2 concentration level can not be detected or is effectively approaching zero.

- Sorption enhanced steam reforming experiments

The presence of a highly active catalyst such as Rh in the process of sorption enhanced steam reforming of methane implies certain requirements on the associated sorbent in terms of kinetics. Halabi et al. [53,54] determined that the maximum enhancement in CH_4 conversion is not significantly affected by the use of a high capacity sorbent in case of a relatively slow sorption kinetics comparing to a very fast reaction kinetics. Thus, sorption enhanced steam reforming

experiments are conducted as a proof of concept for the utilization of newly developed catalyst/sorbent materials in H_2 production at low temperature with in situ CO_2 capture. The process performance is demonstrated in response to the temperature effect in the range of 400–500 ^oC, the pressure effect in the range of 1.5–6.0 bar, and the effect of steam/carbon ratio in the range of 3–6. The reaction zone of the fixed bed is loaded with 120 mg of catalyst mixed with 2 g sorbent. The final bed height inside the reactor was 4.2 cm. The average size of the catalyst and the sorbent pellets used throughout the experiments was 0.3 mm.

A typical sorption enhanced reaction cycle consists of the following steps: (i) the fresh catalyst-sorbent admixture bed is purged with 150 nml/min Ar/steam gas mixture of 20/80 vol% in composition at 400 ^oC and at ambient pressure for 2 h, (ii) the admixture bed is heated up to a predefined temperature using 150 nml/min gas purge of H_2/Ar mixture of (20/80 vol%) in composition at ambient pressure, (iii) counter-current pressurization to a predefined pressure using H_2O/Ar and/or H_2/H_2O/Ar to a predefined pressure, (iv) sorption enhanced reaction by switching to CH_4/H_2O/Ar or $CH_4/H_2O/H_2$/Ar reaction gas mixture at a defined temperature and pressure, (v) counter-current depressurization to ambient pressure, (vi) ambient pressure gas purge of 150 nm/min H_2/H_2O/Ar for 1 h.

- CO_2 desorption experiments

The sorbent must have high affinity for rapid regeneration (desorption) of the adsorbed CO_2. The CO_2 recovery and the sorbent regeneration are studied in terms of the desorption time and the humidity ratio in the desorption purge stream. A series of typical sorption enhanced steam reforming cycles are conducted at 400 ^oC and 4.5 bar using S/C ratio of 6. The performance of the sorbent desorption is then studied against variable humidity composition of 0–20% vol. in 150 nml/min Ar purge stream ambient pressure. The desorption time for the CO_2 release is recorded. A similar series of sorption cycles is also conducted to investigate the effect of the desorption time on the CO_2 sorption capacity under CO_2 partial pressure of 0.85 bar and steam partial pressure of 0.24 bar. The sorption enhanced CH_4 conversion is also measured for each cycle in which the sorbent is exposed to a different desorption time.

- Cyclic experiments

The stability of the sorbent in terms of CO_2 uptake capacity, sorption reversibility/irreversibility, and the CO_2 recovery are tested at 400 ^oC and 4.5 bar over a series of 30 sorption/desorption cycles. The sorbent stability during the sorption enhanced steam reforming reaction is examined in a similar cyclic operation using a S/C ratio of 6. Thermal stability of the sorbent is also investigated over an identical number of cycles, pressure and S/C ratio at three different temperatures of 400, 450, and 500 ^oC, respectively.

9.3 Results and discussion

9.3.1 CO_2 sorption experiments

Hydrotalcite material is a very open structure for physical and chemical manipulations [55,56]. The sorption properties of the material towards selective CO_2 sorption depend on the HTC composition (structural cations and interlayer charge-compensating anions) [47], promoter type and loading, preparation method, and presence of steam–rich conditions [40,42,43]. The selected HTC sorbent should generally provide selective CO_2 sorption with adequate capacity at high temperature (400–500 ^oC), fast kinetics, good thermal and cyclic stability, and ease of regeneration. In presence of a highly active catalyst ($Rh/Ce_{\alpha}Zr_{1-\alpha}O_2$), the high CO_2 sorption/desorption rates furnished by the sorbent is greatly emphasized. Therefore, it is essential to understand the sorption characteristics of the modified K-HTC for an efficient application in the process of methane steam reforming. HTC sorbent of 2.0 g loading is exposed to CO_2/Ar and CO_2/steam/Ar gas mixtures of different compositions in a typical adsorption column apparatus at 400 ^oC. The experimental adsorption data are used to generate the breakthrough curves and therefore the sorption isotherms are accordingly established. The effluent gas concentrations are measured with time. The breakthrough times are corrected for the dead time which needed to transfer the gas via the sampling line to the analysis chamber.

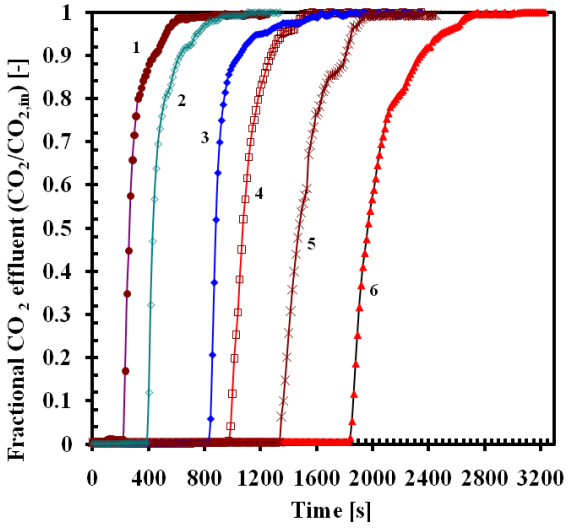

Fig. 1: Typical breakthrough curves of effluent CO_2 on HTC sorbent at dry and wet conditions at 400 ^oC. 1. P_{CO2}= 0.1 bar, 2. P_{CO2}= 0.3, 3. P_{CO2} = 0.75 bar and P_{H2O}=0.24 bar, 4. P_{C2}= 0.36 bar and P_{H2O}=0.24 bar, 5. P_{CO2}= 0.05 bar, 6. P_{CO2}= 0.1 bar and P_{H2O}=0.24 bar. Note: time scale of these curves include the dead-times, for exact compositions and corresponding breakthrough times, refer to Table 3.

The measured gas effluent is considered at equilibrium when there is no change in the CO_2 concentration for at least 5 minutes. Figure 1 demonstrates few examples for typical breakthrough profiles of the effluent CO_2 measured at different gas adsorption conditions in the absence/presence of steam. The CO_2 concentration is thus normalized with respect to the equilibrium effluent concentration. The breakthrough times show a range of 2.6 to 22.1 min depending on the gas

composition and the total pressure used. In wet conditions, the gas mixture is fed at rate of 35–107 nml/min with different CO_2/Ar compositions and 20 vol% steam under a total pressure of 3.5 bar. The experimental conditions used and the data obtained are presented in Table 3. In dry conditions, a total pressure of 1.5 bar is used except for the last two gas compositions given in Table 3, in which CO_2 partial pressure was 0.57 and 0.67, a total pressure of 3.5 bar is used.

Table 3: CO_2 equilibrium sorption data at 400 ^oC

P_{CO2} [bar]	CO_2 effluent [mol/min]	Breakthrough time [min]	Sorption capacity [mol/kg]
Dry conditions			
0.05	4.19×10^{-5}	18.5	0.38
0.09	2.49×10^{-4}	2.6	0.32
0.14	2.42×10^{-4}	2.9	0.35
0.18	1.73×10^{-4}	4.3	0.37
0.27	2.54×10^{-4}	3.8	0.48
0.37	3.52×10^{-4}	2.9	0.51
0.47	4.49×10^{-4}	2.6	0.58
0.57	2.31×10^{-4}	6.8	0.77
0.67	2.75×10^{-4}	6.2	0.85
Wet conditions			
0.09	3.79×10^{-4}	22.1	0.42
0.34	1.40×10^{-4}	8.0	0.56
0.52	2.14×10^{-4}	7.0	0.75
0.63	2.56×10^{-4}	6.2	0.79
0.72	2.95×10^{-4}	6.1	0.89
0.85	3.45×10^{-4}	5.6	0.97

The effluent CO_2 concentration curves show steep shape at the breakthrough times indicating fast adsorption kinetics. These curves also exhibit a dispersed front or non-uniformity in the trailing edge when the CO_2 concentration approaches equilibrium. Lee et al. [11,44] attributed this to the non-isothermality of the bed. However, in the experiments conducted in this work the bed height (4.0 cm) was relatively small to reveal non-isothermal conditions. The temperature gradient along the bed as measured by the three-point K-type thermocouple was ± 3 ^oC. Therefore, the dispersed front can be rather attributed to mass transfer effects as assumed by Ding and Alpay [43].

van Selow et al. [57] studied CO_2 sorption on K-prompted HTC (PURALOX MG70) at 400 ^oC and at high pressure. They observed that the CO_2 effluent in the breakthrough curve does not attain the equilibrium concentration of the feed after the breakthrough; it rather continues to increase. The CO_2 concentration slightly decreases just after the breakthrough and then rises up demonstrating a sorbent capacity of 8 mol/kg albeit on a much lower rate. This is explained by postulating two adsorption steps; a fast adsorption step, which is associated with the relatively low sorption capacity, and a slower adsorption step, which is associated with high sorption capacity. Ebner et al. [40,41] also observed that the CO_2 uptake on their tested sample of K-promoted HTC can reach equilibrium only after a long time of

about 700 min of adsorption cycle. They surmised that CO_2 adsorption on that material consists of three reversible reactions. Two of these reactions are of Langmuir-Hinshelwood type with slow and intermediate kinetics, and one is a mass-transfer limited chemisorption reaction with very fast kinetics. The slow reaction step is considered to be associated with the high sorption capacity. However, this trend of increasing CO_2 concentration in the gas effluent was not observed in the experiments conducted here. The equilibrium is attained in few minutes beyond the breakthrough point.

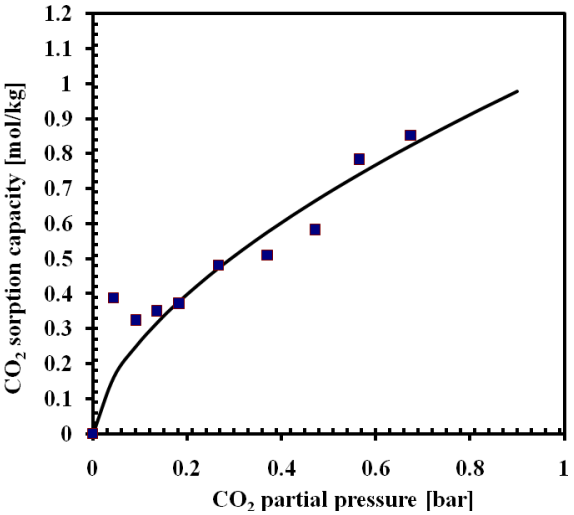

Fig. 2.A: CO_2 sorption isotherm on K-HTC sorbent at 400 °C. 1. Experimental data is fitted to Freundlich isotherm. P_{CO2}= 0.05–0.7 bar.

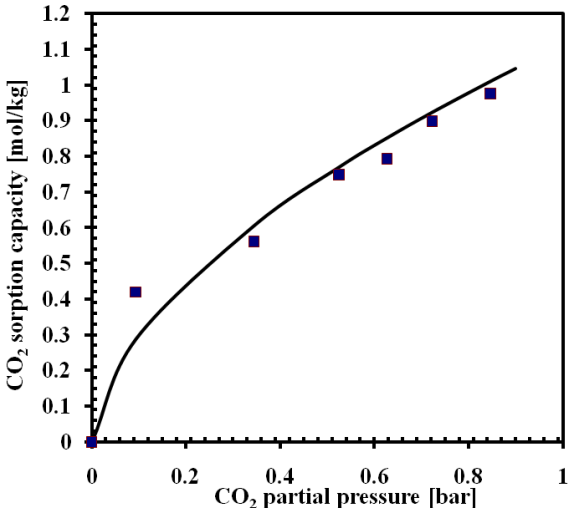

Fig. 2.B: CO_2 sorption isotherm on K-HTC sorbent at 400 °C in presence of steam. Experimental data is fitted to Freundlich isotherm. P_{CO2}= 0.1–0.85 bar, P_{H2O}=0.24 bar.

The amount of CO_2 adsorbed at equilibrium is used according to Eq.1 to determine the CO_2 sorption capacity at different CO_2 partial pressures in dry and wet environments. The experimental data are presented in Figures 2-A and 2-B, receptively. The experimental data over the entire range of CO_2 partial pressures can be adequately described by the Freundlich isotherm according to the following equation:

$$q_{CO_2} = k\left[P_{CO_2}\right]^{\frac{1}{n}} \qquad \text{Eq. 2}$$

Where q_{CO_2} is the CO_2 saturation capacity of the sorbent (mol/kg), P_{CO_2} is the partial pressure of CO_2 in the gas phase in equilibrium with the CO_2 adsorbed phase. k (mol/kg.bar$^{1/n}$) is the Freundlich isotherm parameter and can be interpreted as the gas-solid interaction parameter. n is a dimensionless fitting parameter. The fitting parameters of the sorption isotherms at 400 °C are given in Table 4. The maximum sorption capacity obtained is 0.97 mol/kg in presence of steam at a corresponding CO_2 partial pressure of 0.85 bar. The CO_2 sorption isotherms demonstrate that the CO_2 uptake on HTC is considerably enhanced in the presence of steam. The CO_2 sorption capacity is increased by 10 to 17% over the tested range of pressure. This result was also reported in previous studies [43]. Reijers et al. [58] studied CO_2

adsorption on PURAL MG70 HTC sample promoted with 22% K_2CO_3 at 400 ^{0}C. They presented their CO_2 uptake data according to the Freundlich isotherm in a low pressure region (CO_2 partial pressure range is 0.02–0.25 bar). Ding and Alpay [43] constructed a Langmuirian isotherm to illustrate equilibrium sorption data at 400 ^{o}C on K-promoted HTC up to a CO_2 partial pressure of 0.6 bar. The maximum monolayer capacity obtained was 0.65 mol/kg at wet conditions. Lee et al. [44] presented an analytical isotherm composed of a Langmuirian part in the low pressure region (P_{CO2}<0.2 bar) and a chemical complexation term, which accounts for the higher pressure region. The chemical complexation term considers a reaction between the gaseous CO_2 and the sorbed CO_2. The monolayer capacity achieved at 400 ^{o}C was relatively low (0.25 mol/kg); however, the sorbent showed a total capacity of 0.875 mol/kg.

Table 4: Fitting parameters of the Freundlich sorption isotherms at 400 ^{o}C

	k [mol/kg.bar$^{1/n}$]	n [-]
Dry conditions	1.04	1.68
Wet conditions	1.11	1.76

Oliveira et al. [45] screened different HTC samples (PURAL MG30, MG50, MG70) promoted with K or Cs in the temperature range of 403–510 ^{o}C. A bi-Langmuirian isotherm is derived to describe the CO_2 sorption capacity over the different samples up to a CO_2 pressure of 0.5 bar. The isotherm considers two sites of adsorption available on the sorbent surface. Therefore, one part of the isotherm is associated with physical adsorption and low isosteric adsorption enthalpy (-40 kJ/mol). The second part is associated with chemisorption via an endothermic chemical reaction with an enthalpy of 130.8 kJ/mol. The inconsistency observed in the illustration of the CO_2 sorption isotherms over HTC is principally due to the large span of HTC nature, composition, preparation method, promoter type and impregnation degree, pressure range, and temperature range. Table 5 presents a comparison of the most relevant studies of CO_2 sorption on (Mg, Al, CO_3) HTC.

It is well-accepted to perceive HTC and K-promoted HTC as a physi/chemisorbent material for CO_2 (ad)sorption, particularly at a high temperature range (>300 ^{o}C) [11,41,44,45]. Physical adsorption is an exothermic spontaneous process attributed to Van der Waals and electrostatic forces [45]. It is typically characterized by a low enthalpy of adsorption in the order of 25 kJ/mol. Chemical adsorption is an exothermic and frequently irreversible process. It is characterized by the relatively high heat evolved during the reaction (ca. 200 kJ/mol). Nevertheless, HTC material exhibits a unique property of being an (ir) reversible chemisorbent with low adsorption enthalpy (<40 kJ/mol). The small irreversible portion of the CO_2 adsorption on the fresh HTC sorbent is attributed to a strong chemisorption process [43]; thereafter the sorbent shows a weaker but reversible physisorption process. Adsorption enthalpies of 10 and 17 kJ/mol are determined for CO_2 adsorption at 400 ^{o}C at dry and wet conditions, respectively.

Table 5: Effect of steam/carbon on process performance at 450 °C and at different pressure.

Reference	Sorbent capacity [mol/kg]	Sorption isotherm	HTC type	Temperature [°C]	Remarks
Ding & Alpay [43]	0.65[a]	Langmuir	K-promoted	400	Wet
Lee et al. [44]	0.25[a], 0.875[b]	Langmuir+ complexation term	K-promoted	400	Dry
Reijers et al. [58]	0.46[c]	Freundlich	22% K_2CO_3 Mg/Al=2.3	400	Wet
Ebner et al. [41]	0.932[a]	–	Mg/Al=0.75, K/Al=1	400	Dry
Oliveira et al. [45]	0.806[a]	bi-Langmuir	20% K_2CO_3, Mg/Al=0.3	403	Wet
Hutson and Attwood [55]	2.29[d]	Fruendlich	Mg/Al=3	330	Dry
This work	1.02[e]	Fruendlich	22% K_2CO_3 Mg/Al=1.65	400	Wet

[a]Monolayer capacity, [b]Maximum capacity, [c]At P_{CO2}=0.25 bar, [d]At P_{CO2}=1.1 bar, [e]At P_{CO2}=0.85 bar.

Lee et al. [44] measured an isosteric heat of adsorption of 21 kJ/mol in the Henry regime of CO_2 chemisorption on HTC. Ebner et al. [41] showed a completely reversible chemisorbent in a temperature range of 250–500 °C. Hutson and Atwood [55] studied CO_2 adsorption on HTC in dry conditions at 330 °C. The combined sorption isotherm of physical and chemical sorption contributions revealed very high capacity of 2.29 mol/kg, in which nearly 90% of this capacity is attributed to physisorption. The strong adsorption behavior in the low pressure region (P_{CO2}< 0.2 bar) is associated with physisorption. Nonetheless, as soon as the temperature increases to 400 °C and above, the chemisorption part is strongly expected to dominate the process. The physisorbent shows lower rates of adsorption and reduced sorption capacity as the temperature is elevated.

Oliveira et al. [45] measured the capacity of K-HTC at the following temperatures 306, 403, and 510 °C, the maximum capacity obtained was found at 403 °C. This observation can not follow the trend a physisorbent behavior, and thus, a large contribution due to chemisorption is proposed. The isosteric heat of adsorption was determined to be -40 kJ/mol. However, the ease of desorption/regeneration and the reversible nature of the K-HTC chemisorbent is mainly attributed to the relatively low heat of adsorption. This low heat is due to the unique nature of weak chemical bonding between the HTC basic sites and the CO_2 molecules.

According to the sorption isotherm data obtained in this work, the sorbent can be typically recognized as a chemisorbent for the following reasons: (i) the sorbent shows fast adsorption rates and attains relatively high sorption capacity at high temperature of 400 °C; (ii) if the Freundlich isotherm parameter k (mol/kg.bar$^{1/n}$) is determined for the low CO_2 partial pressure (0.025–0.15 bar) in the Henry region "linear dependency", hence the values obtained for k as a Henry's law constant (mol/kg.bar) at dry and wet conditions are found to be 3.243 and 3.516, respectively. These values are much higher than Henry's law constant

corresponding to CO_2 physisorption, for instance, on 5 A zeolites at 400 °C (0.0284 mol/kg.bar). Thus, the K-HTC sorbent demonstrates a CO_2 chemisorption behavior; this comparison is also presented by Lee et al.[44]; (iii) physisorption is mainly controlled by the available external surface area for adsorption. K-Promoted HTC provides much higher CO_2 capacity albeit of a reduced surface area and pore volume. Therefore, the CO_2 adsorption process can not be seen as entirely a physisorption; (iv) the sorbent offers a relatively high working capacity in cyclic operation due to the reversible chemisorption nature of the sorbent, this point is further discussed in the sorbent stability section 9.3.4.

9.3.2 Sorption enhanced experiments

A series of sorption enhanced steam reforming experiments is performed in the low-temperature range of 400–500 °C, and the pressure range of 1.5–6.0 bar, using a variable S/C ratio of 3–6. The principal goal of these experiments is to examine the advantage of using a newly developed catalyst/sorbent materials for an efficient H_2 production with in situ CO_2 capture in a fixed bed operation. Nevertheless, the key operational parameters are studied to demonstrate an operational window for low pressure (<6.0 bar) applications.

- Typical composition profiles

A catalyst loading of 120 mg is mixed with a 2.0 g sorbent and packed inside the reactor presenting average bulk densities of 50.4 and 748.6 kg/m^3 for the catalyst and the sorbent, respectively in a bed height of 4.2 cm. The bed is activated at 400 °C using 150 nml/min (20:80 vol%) H_2O/Ar gas for 2 h and then exposed to reducing media using (20:80 vol%) H_2/Ar gas at 450 °C. A total gas flow rate of 107 nml/min is fed into the reactor at temperature of 450 °C and a pressure of 1.5 bar. The reaction gas mixture contains 4.5 vol% CH_4 with a corresponding S/C ratio of 6, less than 0.1 vol% H_2, and balance Ar. Figure 3 presents the dry-basis gas effluent composition at the reactor exit during the reaction/sorption time.

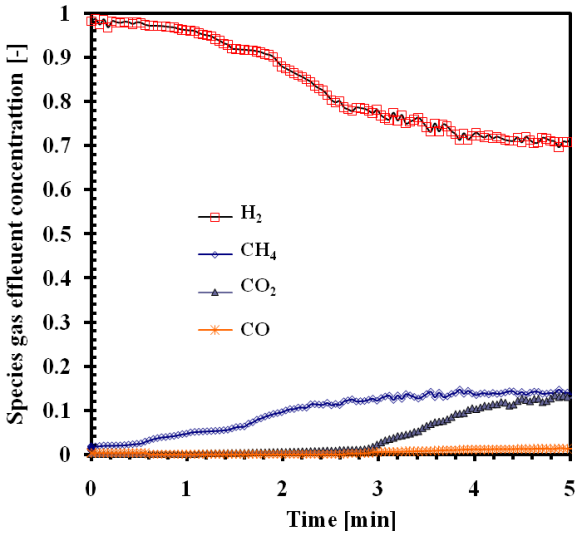

Fig. 3: Dynamic gas effluent concentration profiles on dry basis in sorption enhanced steam reforming process at 450 °C and at 1.5 bar using G_s=0.014 kg/m^2.s and S/C=6.0.

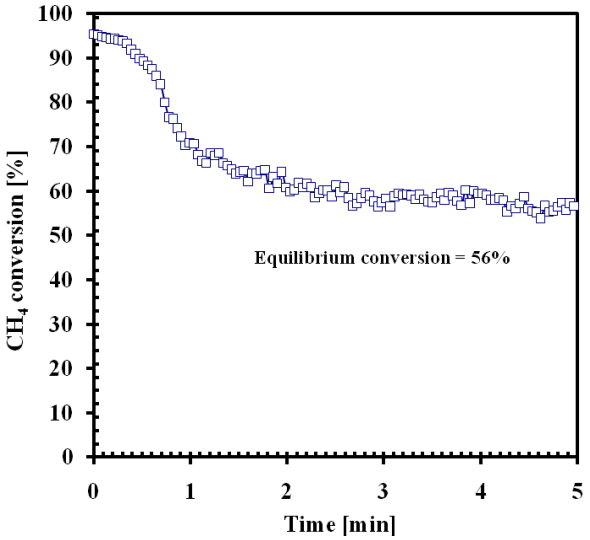

Fig. 4: Dynamic profile of CH_4 conversion at the exit of the sorption enhanced steam reformer at 450 °C and at 1.5 bar using G_s=0.014 kg/m^2.s and S/C=6.0.

The transient gas effluent concentrations show that H_2 can be produced with a high purity > 98% and a contamination level of $CO+CO_2$ impurities <100 ppm in the sorption-enhanced regime. The gas concentrations slowly change with time to approach the thermodynamic equilibrium condition in the non-sorption enhanced regime (69% H_2, 13.9% CH_4, 16.9% CO_2, and 1.1% CO). The transient period is approximately 3.6 min at the studied conditions.

Figure 4 presents the dynamic CH_4 conversion profile at the reactor exit during the time of the transient operation. The process reaches a maximum CH_4 conversion of 95.5%, which is a 71% enhancement over the thermodynamic equilibrium of steam reforming reactions. The corresponding H_2 yield obtained is 3.82 (defined as mol H_2 produced/mol CH_4 fed). In practice, the reactor length and the gas space velocity are major factors to be specified.

Depending on the design gas throughput and mass transport limited situation, the gas space velocity can be chosen to provide a practical operational time. However, a bed size of a larger length can maintain the useful operational time for high CH_4 conversion with a high concnetrattion of the corresponding H_2 product for a longer period.

- Effect of temperature

Steam reforming reactions are favored by high temperature and low pressure operation, whereas the associated CO_2 sorption is favored by low temperature and high pressure operation. However, the structural stability of the HTC sorbent imposes a maximum temperature of ~600 ^oC [11], beyond this temperature the material looses its sorption properties and can be converted into a molten solid. The lower the temperature the lower the energy costs required in the operation. Thus, the process performance is studied at two different temperatures of 400 and 450 ^oC and at a total gas pressure of 4.5 bar in the presence of H_2 in the feed. A total gas flow rate of 107 nml/min (4.7 vol%, 2.7 vol% H_2, S/C ratio of 3.5, and balance Ar) is inserted into the reactor. A relatively significant amount of H_2 and low S/C ratio are used in the gas mixture to demonstrate the effect of temperature under unfavorable conditions. Nonetheless, the effect of temperature is further studied in the range of 400–500 ^oC during the cyclic operation of the process, (see the thermal stability analysis presented in section 9.3.4).

The effluent gas composition and CH_4 conversion given in Figures 5 and 6, respectively present poor performance. H_2 product is obtained at a purity of 83% and 91% at 400 and 450 ^oC, respectively. CH_4 conversion can only reach 47% and 68% at 400 and 450 ^oC, respectively. Although the process is severely affected by low S/C ratio and H_2 inhibition but the enhancement made by the presence of the sorbent shows that the total concentration of ($CO+CO_2$) impurities can be as low as 100 ppm during the sorption enhanced transient period.

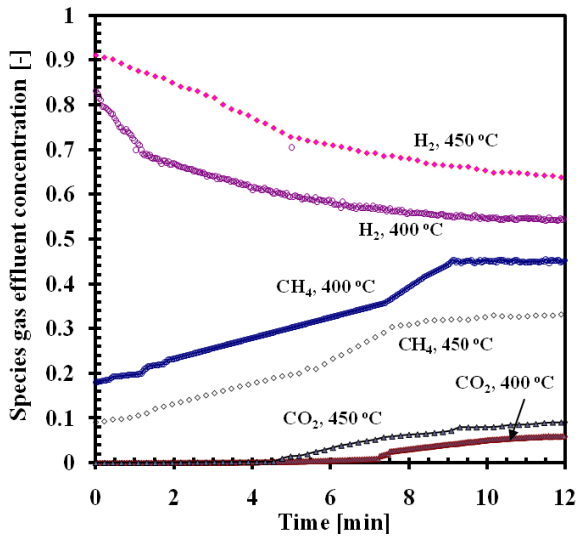

Fig. 5: Dynamic temperature profiles at the exit of sorption enhanced steam reformer at two temperatures 400 and 450 °C, and at 4.5 bar using G_s=0.01 kg/m^2.s, P_{CH4}=21.23 kPa, P_{H2}=12.2 kPa and S/C=3.5.

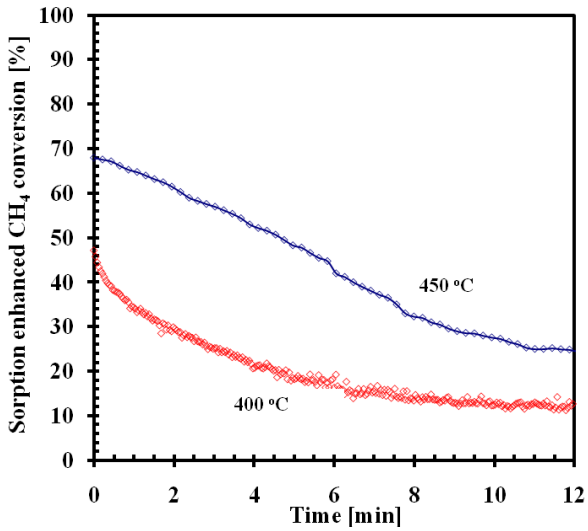

Fig. 6: Dynamic profile of CH_4 conversion at exit of sorption enhanced steam reformer at two temperatures 400 and 450 °C, 4.5 bar using G_s=0.01 kg/m^2.s, P_{CH4}=21.23 kPa, P_{H2}=12.2 kPa and S/C=3.5.

- Effect of steam/carbon ratio

At high temperature of operation, a high S/C ratio can be used to prevent or diminish the affinity of the steam reforming gas mixture towards CO production via the reverse water–gas shift reaction, and thus enhances H_2 production. A high S/C ratio can also be used at low operational temperature to inhibit carbon formation via the following two pathways: ($CO + H_2 = H_2O + C$) and ($CO_2 + 2H_2 = 2H_2O + C$). Carbon formation results from CH_4 decomposition and Boudouard reactions can more likely suppress the catalyst activity at high temperatures. However, the economic burden associated with a high S/C ratio becomes more intense in large size power production plants. The effect of variable S/C operational ratio on the process performance is studied at a temperature of 450 °C and at different pressures in the range of 1.5–6.0 bar. Table 6 lists the experimental values obtained for CH_4 conversion and product composition during the sorption enhanced reaction.

Feed gas mixture composed of (3.94 vol% CH_4, 0.1vol% H_2, variable S/C ratio, and balance Ar) is applied at a rate of 75 nml/min. The average breakthrough times were determined in the range of 4–15 min before the equilibrium condition is approached when the sorption bed is saturated with CO_2. At low pressure of 1.5 bar and using high S/C ratio of 6.0, the process yields a maximum CH_4 conversion and a H_2 purity of 99.6 and 99.8 %, respectively.

This is associated with a thermal efficiency factor of 1.2, which is the maximum thermal efficiency that can be obtained from methane steam reforming. Thermal efficiency is defined as mol H_2 produced per 1 mol of CH_4 times the ratio of the lower heating values of H_2 to CH_4. However, the enhancement in CH_4 conversion (162%) is more prominent at high pressure (6.0 bar) and steam S/C ratio of 4.0 due

to the high impact of local CO_2 sorption rates, though the absolute conversion is relatively low (83.4%).

Table 6: Effect of steam/carbon on process performance at 450 °C and at different pressure.

S/C ratio	Pressure [bar]	CH_4 equil. conversion [%]	CH_4 conversion [%]	H_2 concentration [%]	$CO+CO_2$ concentration [ppm]	Thermal efficiency [-]*
3	1.5	45.3	82.0	94.7	1870	0.97
	4.5	32.1	74.9	91.9	588	0.89
	6.0	29.2	72.0	91.3	364	0.87
4	1.5	51.2	92.7	98.0	840	1.11
	4.5	36.1	85.2	95.6	320	1.03
	6.0	31.8	83.4	95.3	250	1.00
5	1.5	55.6	98.0	99.5	380	1.18
	4.5	39.6	93.4	98.2	216	1.12
	6.0	35.9	91.4	97.5	166	1.09
6	1.5	59.4	99.6	99.8	100	1.20
	4.5	42.4	97.5	99.2	130	1.16
	6.0	38.5	95.2	98.8	112	1.15

*Thermal efficiency is defined as $\frac{\text{moles } H_2 \text{ produced}}{\text{moles } CH_4 \text{ fed}} \cdot \frac{LHV_{H_2}}{LHV_{CH_4}}$; $LHV_{H_2} = 240$ MJ/kmol $\cdot$ $LHV_{CH_4} = 800$ MJ/kmol $\cdot$

The results clearly prove that if high fuel conversion (>90%) is wanted at low temperature (~ 450 °C) and low pressure (~ 1.5 bar), then a S/C ratio of 4–5 can be used. To maintain a desirable process performance at high pressure operation, thus, either high S/C ratio (>5) can be used or the temperature should be slightly increased to 500 °C. However, the loss of catalyst activity as a result of carbon formation or catalyst oxidation in presence of high steam loading was not observed. The catalyst shows very good stability and resistance against carbon formation over 150 h time on stream [51]. This is strongly attributed to the improved catalytic properties provided by the ceria-zirconia support of the catalyst. Again the ability of the ceria support to undergo reduction/oxidation cycles via the lattice oxygen sites revealed very high stability in the presence of a highly oxidative media. Therefore, high S/C ratio is not a critical issue when ceria-zirconia supported Rh is employed as a steam reforming catalyst. However, it can be a serious obstacle for Ni–based process. HTC is also found to benefit from the presence of steam because of enhanced CO_2 sorption capacity. This is further discussed in the next section.

- Effect of pressure

Gas turbine cycles intended for electricity generation are based on syngas mixture and conventionally operated at high pressure (13–45 bar). The performance of an industrial–size steam reformer for direct-delivery product at such high pressure range is definitely poor due to thermodynamic limitations. Although, the CH_4 conversion enhancement and maintaining a very low level of $CO+CO_2$ impurities are benefited from high pressure, the absolute CH_4 conversion and the useful operational time are seriously limited. This is basically attributed to the relatively low CO_2 sorption capacity of the sorbent used. Thus, H_2 production via sorption-enhanced steam reformer for such high pressure application is still a challenge and can be economically infeasible. Nonetheless, a different route of low pressure

steam reforming and subsequent compression units to deliver a high pressure gas effluent also presents enormous costs to the process. Therefore, small size H_2 generation plants for residential or industrial application operated at a relatively low pressure range <4.5 bar seem to be a realistic approach.

However, the optimal operational pressure is still a trade off between CH4 conversion and operational time from one side and low product impurity on the other side. Sorption enhanced experiments are conducted at 450 ^{o}C and at three different pressures of 1.5, 4.5, and 6.0 bar using S/C ratio of 4 and a total gas flow rate of 75 nml/min. The feed gas mixture contains 3 vol% CH_4, 0.1 vol% H_2. Figure 7 illustrates that a maximum CH_4 conversion of 97% can be obtained at 1.5 bar presenting 70% enhancement over the thermodynamic conversion. At a pressure of 6.0 bar, the process reaches 90% conversion. The transient period during the sorption enhanced reaction step is also increased from 10 to 14.5 min upon the increase of the pressure from 1.5 to 6 bar, respectively.

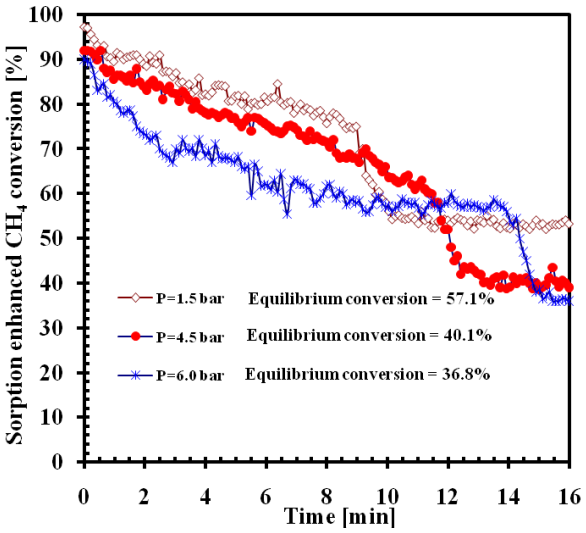

Fig. 7: Effect of pressure on sorption enhanced CH_4 conversion at 450 ^{o}C using 75 nml/min gas flowrate with 3% CH_4 and S/C ratio of 4.

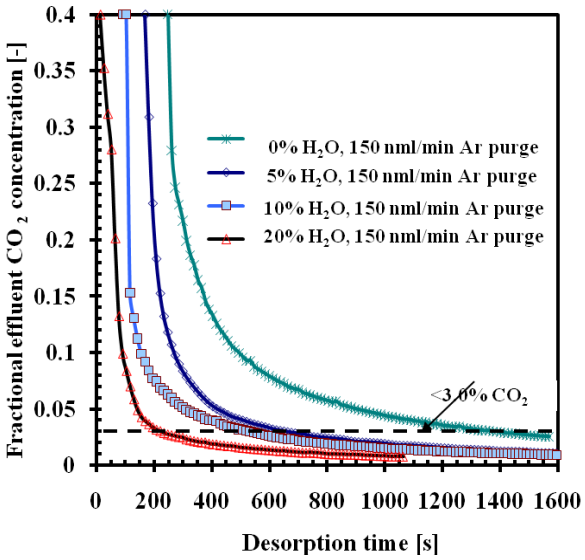

Fig. 8: Effect of humidity ratio in the Ar gas purge stream on the CO_2 desorption rate at 400 ^{o}C and at ambient pressure.

9.3.3 CO_2 desorption experiments

A series of sorption/desorption experiments is conducted at 400 ^{o}C to examine the influence of water humidity and desorption time on the sorbent properties in terms of the CO_2 desorption rate and the sorbent capacity, respectively. Four fresh sorbent samples (after pretreatment) are exposed to a typical CO_2 adsorption cycle of 1600 s using CO_2/steam/Ar gas mixture, with a CO_2 partial pressure of 0.85 bar, 20 vol% H_2O, and balance Ar under a total pressure of 3.5 bar. The breakthrough time was achieved in approximately 5.9 min and the gas composition approached equilibrium in few minutes beyond the breakthrough. Each sample is then subjected to a typical pressure-swing desorption cycle of 1600 s using 150 nml/min Ar purge stream with different H_2O humidity content at ambient pressure.

The fractional CO_2 effluent concentration with respect to the equilibrium CO_2 concentration is measured over time. Figure 8 shows that increasing the humidity content in the Ar purge stream from 0 vol% (dry conditions) to 20 vol% results in a significant reduction in the desorption time required to reach a fully regenerated sorbent.

For example, the time required for the desorption gas effluent to reach a concentration of 3% of the equilibrium CO_2 concentration, is reduced by factor of 7 upon the use of an Ar purge with 20 vol% humidity content. Thus, CO_2 desorption is significantly facilitated in the presence of water. However, the initial CO_2 desorption rate was very rapid, the fractional CO_2 effluent reached to <3% in about 3 min. Much slower desorption rate is then observed until the end of the desorption cycle time. It is important to mention that the fractional CO_2 effluent concentration is not meant to stand for the CO_2 recovery ratio. CO_2 recovery is represented as the amount of CO_2 desorbed in time *t* with respect to the amount of CO_2 adsorbed, (i.e., at equilibrium concentration after breakthrough).

A spent sorbent sample (exposed to 0.85 bar CO_2) is then subjected to typical wet desorption cycles (20:80% steam/Ar purge) with different desorption times from 5 to 110 min. CO_2 effluent concentration at the end of each desorption cycle is recorded, and then the sorbent is subjected to a new adsorption cycle. The effects of initial state of the regenerated sorbent and the desorption time on the sorption capacity is thus analyzed.

Figure 9 presents that on a long desorption time larger than 60 min the sorbent reaches a stable capacity of about 0.89 mol/kg, whereas, during the regeneration step, CO_2 appears in the gas effluent with a concentration of less than 100 ppm. The capacity obtained from these experiments is not, however, the fresh sorbent capacity. Hence, it can be considered as the sorbent working capacity defined as the CO_2 desorbed in the desorption cycle divided by the equilibrium CO_2 adsorbed in the adsorption cycle. The fresh capacity was measured in the isotherm calculations to be 0.97 mol/kg, this indicates that the sorbent lost 8.3% of its capacity during the repetitive sorption/desorption cycles.

This figure also shows that the sorbent can attain up to 74% of its working capacity if it is exposed to a regeneration time of 12 min. The regenerated sorbent is then subjected to a typical sorption enhanced reaction cycle at 400 ^{o}C, and 4.5 bar to assess the sorbent performance under steam reforming conditions in terms of the CH_4 conversion. Reaction gas flow of the following conditions (3.94 vol% CH_4, S/C ratio of 6, and balance Ar) is applied at a rate of 75 nml/min.

Figure 10 demonstrates that 75% CH_4 conversion can be reached if the sorbent is regenerated for about 12 min However, the maximum conversion approaches 80% using a fully regenerated sorbent which is desorbed for more than 50 min. Analyzing these experiments given in Figures 8, 9, and 10 suggests that large portion of CO_2 is easily recovered in the first few minutes of the regeneration cycle

as a result of a fast desorption step, which is associated with a physi/chemisorption step on the monolayer surface of the fresh sorbent.

The complete recovery of CO_2, achieved within 40 to 60 min, thereafter, represents a slower desorption step. This step is associated with a reversible chemisorption step in a multi-layer surface of the sorbent.

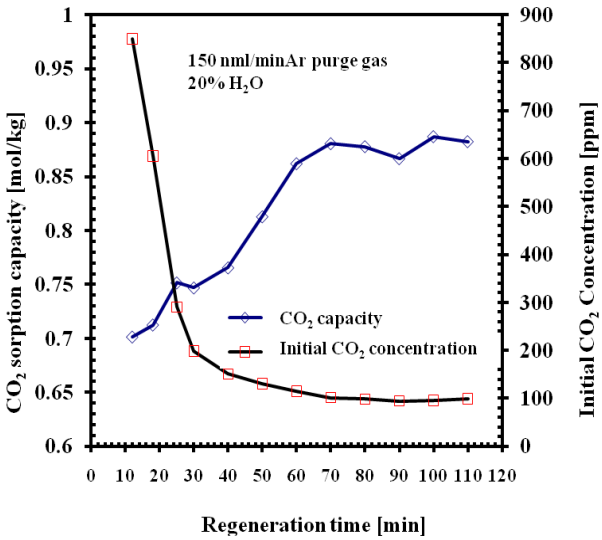

Fig. 9: Effect of the regeneration time on CO_2 desorption and the corresponding CO_2 sorption capacity at 400 ^oC using 150 nml/min steam/Ar purge stream of (20/80 vol.%) in composition.

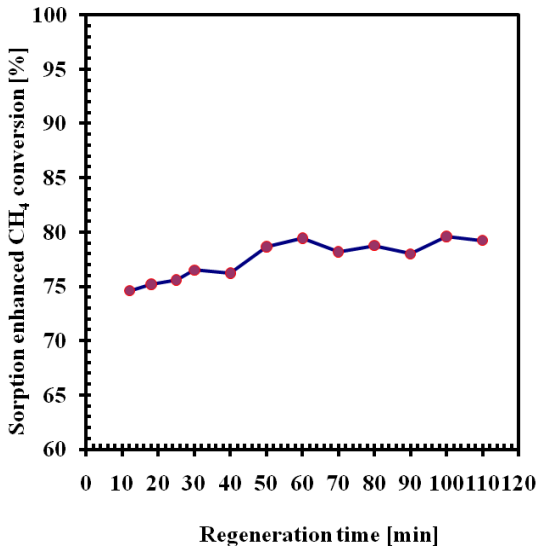

Fig. 10: Effect of the sorbent regeneration time on the sorption enhanced CH_4 conversion at 400 ^oC and 4.5 bar using 75 nml/min gas flowrate with 3.94% CH_4 and S/C ratio of 6.

9.3.4 Sorbent stability

In practice, the cyclic process performance is of high importance due to the fact that the sorbent must persist the variations in the gas composition and the operational conditions during the sorption/desorption cycles. Therefore, the sorbent is employed in a typical sorption/desorption operation for 30 cycles. A gas flow rate of 46 nml/min with 20% water content and a CO_2 partial pressure of 0.85 bar is fed over the sorbent bed at 400 ^oC. The adsorption cycle is conducted for 1600 s (26.6 min) and the CO_2 effluent is measured. The sorbent is thus regenerated in steam/Ar purge via pressure swing from 3.5 to 1.0 bar over 30 and 90 min desorption cycles.

Figure 11 shows that CO_2 recovery is obtained to approximately 90% when the desorption cycles are operated for 30 min time intervals. Using a higher desorption time of 90 min over the cycles, CO_2 recovered from the fresh sorbent sample during the first cycle is slightly increased to 95%. However, it is found that CO_2 recovery ratio can be more than 100% (up to 108%) over the repetitive cycles. This means that CO_2 desorbed is somewhat higher that CO_2 adsorbed. CO_2 release in these experiments is thus attributed to the decarbonation process through the loss of the interlayer charge compensating anion (CO_3^{2-} evolved as CO_2) and the dehydroxylation of the octahedral layers (evolved as H_2O). This phenomenon is

observed on HTC by means of a weight loss in the materials due to water and CO_2 release as temperature is increased from 227–427 ^oC [55].

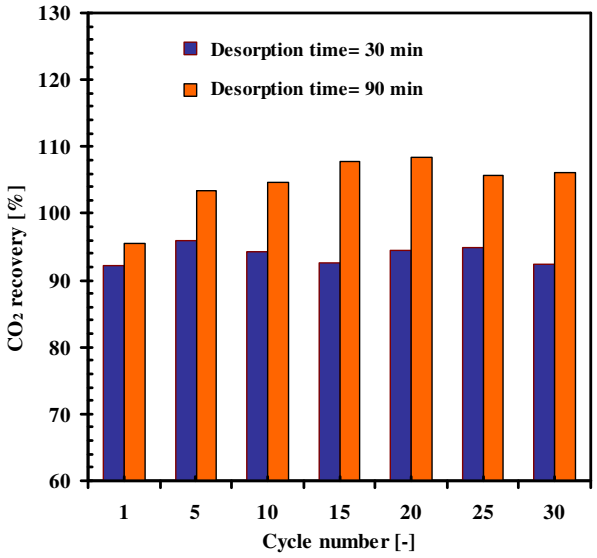

Fig. 11: Cyclic recovery of CO_2 from the sorbent at 400 ^oC using 150 nml/min steam/Ar purge stream of (20/80 vol.%) in composition.

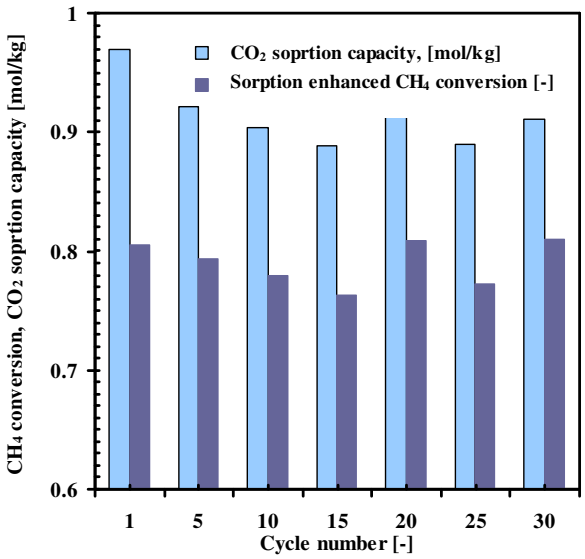

Fig. 12: Cyclic stability of the sorbent in terms of the CO_2 sorption capacity and the corresponding sorption enhanced CH_4 conversion at 400 ^oC and 1.5 bar.

The stability of the sorbent over cyclic operation is given Figure 12. The sorbent shows a loss of 8% of its fresh capacity after the first cycle, however, it preserves a stable working capacity of about 0.89 mol/kg over the tested number of cycles. These results suggest that an irreversible chemisorption process is responsible of the relatively small loss of the capacity; and hence, the stable sorbent capacity is attributed to a reversible chemisorption process. However, this loss in the sorption capacity is not significantly reflected in the CH_4 conversion attained during the sorption enhanced reaction cycles. The cycles are conducted at 400^oC and 4.5 bar using a gas mixture of (3.94 vol% CH_4, S/C ratio of 6, and balance Ar) and applied at a flow rate of 75 nml/min. A stable conversion of about 80% is achieved.

An identical gas mixture is used to investigate the thermal stability of the sorbent during cyclic operation of the sorption enhanced reaction at 4.5 bar. Typical sorption-enhanced/desorption cycles of 30 min each are performed over three temperatures of 400, 450, and 500 ^oC. Figure 13 demonstrates a stable CH_4 conversion 80, 96, and >99% at temperatures of 400, 450, and 500^oC, respectively. A maximum H_2 purity and yield obtained at 500 ^oC are >99.98% and 4.0, respectively with a corresponding $CO+CO_2$ level <100 ppm. The figure clearly presents a good cyclic thermal stability of the sorbent and (the sorption enhanced process) at the studied conditions, even in the presence of high amount of steam.

Many studies have recently reported that HTC shows a good thermal stability up to 600 ^oC. However, different preparation methods would affect the desorption properties if the sorbent is heated above 400 ^oC. Leon et al [46] determined that a

preparation technique tends to increase the basicity of the surface will results in unidentate carbonates that remain after evacuation at temperature >400 °C. Unidentate carbonates then correspond to the strong adsorption sites and eventually cause irreversible adsorption of CO_2.

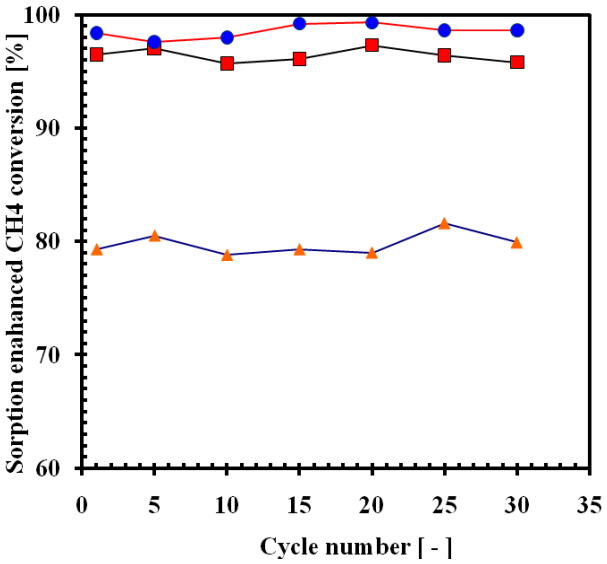

Fig. 13: Cyclic thermal stability of the sorbent in terms of achieved sorption enhanced CH_4 conversion at different temperatures and at 4.5 bar using 75 nml/min gas flowrate with 3.94% CH_4 and S/C ratio of 6.

Table 7: A performance comparison of the most relevant studies on sorption-enhanced methane steam reforming process.

Reference	H_2 purity [%]	CO+CO_2 [ppm]	CH_4 conversion [%]	Experimental conditions	Catalyst/sorbent ratio
Hufton et al [7]	95.0	<50	80.0	450°C, 4.6 bar, S/C=6	1/1 Ni/K-HTC
Waldron et al [9]*	94.4	<40	73.0	490°C, 1.7 bar, S/C=6	1/2 Ni/HTC
	88.7	<136	54.4	490°C, 4.5 bar, S/C=6	
Ding & Alpay [48]	90.0	<2000	80.0	450°C, 4.4 bar, S/C=6	1/2.1Ni/K-HTC
Lee et al. [49]	>99.0	<20	98.6	550°C, 1.0 bar, S/C=5	1/2 Ni/K-HTC
This work	99.9	95	99.9	500°C, 4.5 bar, S/C=6	1/16 Rh/K-HTC
	99.2	130	97.5	450°C, 4.5 bar, S/C=6	(150 mg/2.0 g)
	99.6	100	99.8	450°C, 1.5 bar, S/C=6	
	99.5	380	98.0	450°C, 1.5 bar, S/C=5	

*Multi-cycle operation

The performance of the process studied in this work is compared to the most relevant work reported in literature for sorption enhanced steam reforming. Table 7 presents a summary of this comparison in terms of the major indicative parameters such as CH_4 conversion, H_2 purity, and CO_x impurities in addition to the experimental conditions used. It can be seen that the conventional low activity Ni-based catalyst is typically used in all works. Hufton et al. [7] achieved a H_2 product stream with a purity of 95% and CH_4 fuel conversion of 80% and CO+CO_2 concentration of less than 50 ppm. They demonstrated the process performance at

450 ^{o}C and 4.7 bar using 1:1 catalyst/sorbent ratio and steam/carbon (S/C) ratio of 6 in single cycle fixed bed of 1.52 m in length. They further determined that the multi-cycle operation failed to maintain the same performance of a single cycle process due to the unrecovered sorbent capacity during the pressure swing regeneration cycles.

Waldron et al. [9] reached a CH_4 conversion and H_2 purity of 73 and 94%, respectively in multi-cycle operation at a lower pressure of 1.7 bar using a reactor of 6.1 m in length. Ding and Alpay [48] obtained 75% CH_4 conversion and H_2 purity >90% in a laboratory scale fixed bed of 22 cm in length using a S/C ratio of 6 at 450 ^{o}C and 4.45 bar. The measured CO_2 capacity of the HTC sorbent used in their study was higher than that measured by Hufton et al. [7,8]. Lee et al. [49] demonstrated an improved process performance in a column with (63.4 cm in length and 1.73 cm in diameter) using the temperature swing regeneration and better capacity HTC sorbent. They reached a CH_4 conversion and H_2 purity of 98.6% and 99.99%, respectively, at reaction temperature of 550 ^{o}C and 1.0 bar. The bed is regenerated using steam purge at 590 ^{o}C. In the experiments presented in this work, high fuel conversion and H_2 purity >99% can be achieved at comparable operation conditions (relatively lower temperature of 450–500 ^{o}C and a pressure of 1.5–4.5 bar) using much smaller reactor size and much less catalyst/sorbent ratio. This is directly related to lower capital costs in terms of the reactor size and to lower operational costs with respect to the energy requirements and material loading.

9.4 Conclusions

$Rh/Ce_{\alpha}Zr_{1-\alpha}O_2$ catalyst and K_2CO_3–promoted hydrotalcite are experimentally investigated as novel catalyst/sorbent materials for an efficient H_2 production with in situ CO_2 capture at low temperature (450–500^{o}C) and pressure (1.5–4.5 bar). The effect of temperature, pressure, and S/C ratio on the process performance is demonstrated. Thus, direct production of high H_2 purity and fuel conversion >99% is achieved with low level of carbon oxides impurities <100 ppm. Therefore, it can be stated that the process of H_2 production via sorption enhanced steam reforming is significantly improved in terms of CH_4 conversion and H_2 purity obtained using a much smaller reactor size and much less catalyst/sorbent ratio.

Despite the expensive price of Rh catalyst compared to Ni catalyst, the enormous reduction of the reactor size, material loading, catalyst/sorbent ratio, and energy requirements are beneficial key factors for the success of the concept. Small size H_2 generation plants for residential or industrial application operated at a relatively low pressure range <4.5 bar seem to be a realistic approach.

However, the optimal operational pressure is still a trade off between CH_4 conversion and operational time from one side and low product impurity on the other side. The equilibrium sorption data obtained from column apparatus can be adequately described by Freundlich isotherm. The sorbent shows fast adsorption rates and attains relatively high sorption capacity of 0.95 mol/kg on the fresh sorbent. CO_2 desorption experiments showed that a purge stream with 20 vol% water content results in a desorption time reduction by a factor of 7. A large portion of CO_2 is easily recovered in the first few minutes of a typical desorption cycle as a result of a fast desorption step, which is associated with a physi/chemisorption step on the monolayer surface of the fresh sorbent. The complete recovery of CO_2 is then achieved in a slower desorption step associated with a reversible chemisorption in a multi-layer surface of the sorbent. CO_2 release during the desorption experiments is attributed to the decarbonation process through the loss of the interlayer charge compensating anion (CO_3^{2-} evolved as CO_2). The sorbent shows a loss of 8% of its fresh capacity due to an irreversible chemisorption; however, it preserves a stable working capacity of about 0.89 mol/kg, suggesting a reversible chemisorption process. Cyclic experiments indicate a good thermal stability of the sorbent in the temperature range of 400–500 ^{o}C.

References

1. Harrison, D.P. Sorption-enhanced hydrogen production: A Review, Ind. Eng. Chem. Res., 47 (2008) 6486–6501.
2. Rostrup-Nielsen, J.R. Fuels and energy for the future: The role of catalysis. Catal. Rev. 46 (2004) 247–270.
3. Rostrup-Nielsen, J.R. Production of synthesis gas. Catal. Tod. 18 (1993) 305-324.
4. Pena M.A.; Gómez, J.P.; Fierro, J.L.G. New catalytic routes for syngas and hydrogen production, App. Catal A, 144 (1996) 7-57.
5. Ayabe, S.; Omoto, H.; Utaka, T.; Kikuchi, R.; Sasaki, K.; Teraoka, Y.; Eguchi, K. Catalytic autothermal reforming of methane and propane over supported metal catalysts. App. Catal. A 241 (2003) 261.
6. Feng, B.; An, H.; Tan, E. Screening of CO_2 adsorbing materials for zero emissions power generation systems. Energy and Fuel. 21 (2007) 426-434.
7. Hufton, J. R., Mayorga, S., Sircar, S. Sorption-enhanced reaction process for hydrogen production. AIChE J. 45 (1999) 248–256.
8. Hufton, J., Waldron, W., Weigel, S., Rao, M., Nataraj, S., Sircar, S., Sorption enhanced reaction process SERP) for the production of hydrogen, in: Proceedings of the 2000 US DOE Hydrogen Program Review, 2000.
9. Waldron, W. F.; Hufton, J. R.; Sircar, S. Production of hydrogen by cyclic sorption enhanced reaction process. AIChE J. 47 (2001) 1477–1479.
10. Yong, A., Mata, V., Rodrigues, A.E. Adsorption of carbon dioxide onto hydrotalcite-like compounds (HTlcs) at high temperatures, Ind. Eng. Chem. Res. 40 (2001) 204-209.
11. Lee, K. B.; Beaver, M. G.; Caram, H. S.; Sircar, S. Reversible chemisorbents for carbon dioxide and their potential application. Ind. Eng. Chem. Res. 47 (2008) 8048-8062.
12. Dı´az, E.; Mun˜oz, E.; Vega, A.; Ordo´n˜ez, S. Enhancement of the CO_2 retention capacity of X zeolites by Na- and Cs-treatments. Chemosphere 70 (2008) 1375–1382.
13. Inui, T.; Okugawa, Y.; Yasuda, M. Relationship between properties of various zeolites and their CO_2-adsorption behaviors in pressure swing adsorption operation. Ind. Eng. Chem. Res. 27 (1988)1103–1109.
14. Rege, S. U.; Yang, R. T.; Buzanowski, M. A. Sorbents for air prepurification in air separation. Chem. Eng. Sci. 55 (2000) 4827–4838.
15. Keller, G. E.; Anderson, R. A.; Yon, C. M. Adsorption In Handbook of Separation Process Technology; Rousseau, R. W., Ed.; Wiley Interscience: New York, 1987; Chapter 12, pp 644-696.
16. Cao, D. V.; Sircar, S. Heats of Adsorption of Pure SF6 and CO_2 on Silicalite Pellets with Alumina Binder. Ind. Eng. Chem. Res. 2001, 40,
17. Sircar, S. Gas Separation and Storage by Activated Carbons. In Adsorption by Carbons; Bottani, E., Tascon, J., Eds.; Elsevier: New York, 2008; Chapter 22, pp 565-592.

18. Yong, Z.; Mata, V. G.; Rodrigues, A. E. Adsorption of Carbon Dioxide on Chemically Modified High Surface Area Carbon-Based Adsorbents at High Temperature. Adsorption 2001, 7, 41.
19. Przepiorski, M.; Skrodzewicz, M.; Morawski, A. W. High temperature ammonia treatment of activated carbon for enhancement of CO_2 adsorption. Appl. Surf. Sci. 225 (2004) 235– 242.
20. Silaban, A.; Narcida, M.; Harrison, D. P. Characteristics of the Reversible Reaction Between CO_2(g) and Calcined Dolomite. Chem. Eng. Commun. 1996, 146, 149.
21. Abanades, J. The Maximum Capture Efficiency of CO_2 Using a Carbonation/Calcination Cycle of $CaO/CaCO_3$. Chem. Eng. J. 2002, 90, 303.
22. Lopez, A.; Harrison, D. P. Hydrogen Production Using Sorption Enhanced Reaction. Ind. Eng. Chem. Res. 2001, 40, 5102.
23. Balasubramanian, B.; Lopez, A.; Kaytakoglu, S.; Harrison, D. P.Hydrogen From Methane in a Single-Step Process. Chem. Eng. Sci. 1999, 54, 3543.
24. Yi, K. B.; Harrison, D. P. Low Pressure Sorption Enhanced Hydrogen Production. Ind. Eng. Chem. Res. 2005, 44, 1665.
25. Bandi A.; Specht, M.; Sichler, P.; Nicoloso, N. In Situ Gas Conditioning on Fuel Reforming for Hydrogen Generation. Proceedings of the 5th International Symposium on Gas Cleaning, Pittsburgh, PA, Sept. 2002.
26. Grasa, G. S.; Abanades, J. C. CO_2 Capture Capacity of CaO in Long Series of Carbonation/Calcination Cycles. Ind. Eng. Chem. Res. 2006,45, 8846.
27. Sun, P.; Lim, C.; Grace, J. R. Cyclic CO_2 Capture of Limestone-Derived Sorbent During Prolonged Calcination/Carbonation Cycling. AIChEJ. 2008, 54, 1668.
28. Hughes, R. W.; Lu, D.; Anthony, E. J.; Wu, Y. Improved Long-Term Conversion of Limestone Derived Sorbents for In-Situ Capture of CO2 in a Fluidized Bed Combustor. Ind. Eng. Chem. Res. 2004, 43, 5529.
29. Manovic, V.; Anthony, E. J. Steam Reactivation of Spent CaO-Based Sorbent for Multiple CO2 Capture Cycles. EnViron. Sci. Technol. 2007, 41, 1420.
30. Ida, J.-I., Lin, Y.S. Mechanism of high-temperature CO_2 sorption on lithium zirconate, Environ. Sci. Technol. 37 (2003) 1999.
31. Xiong, R., Ida, J., Lin, Y., Kinetics of carbon dioxide sorption on potassium-doped lithium zirconate, Chem. Eng. Sci. 58 (2003) 4377-4385.
32. Ida, J., Xiong, R., Lin, Y.S., Synthesis and CO_2 sorption properties of pure and modified lithium zirconate, Sep. Purif. Technol. 36 (2004) 41-51.
33. Fauth, D.J., Frommell, E.A., Hoffman, J.S, Reasbeck, R.P., Pennline, H.W., Eutectic salt promoted lithium zirconate: novel high temperature sorbent for CO_2 capture, Fuel Process. Technol. 86 (2005) 1503-1521.
34. Wang, Y.-J., Qi, L., Wang, X.-Y., The study of Li_2ZrO_3 used for absorption of CO_2 at high temperature, Chin. J. Inorg. Chem. 19 (2003), 531-539.
35. Nair, B.N., Yamaguchi, T., Kawamura, H., Nakao, S., Processing of lithium zirconate for applications in carbon dioxide separation: structure and properties of the powders, J. Am. Ceram. Soc. (2004) 87, 68.
36. Ochoa-Fernandez, E., Rusten, H.K., Jakobsen, H.A, Rønning, M., Holmen, A., Chen, D., Sorption enhanced hydrogen production by steam methane reforming

using Li_2ZrO_3 as sorbent: sorption kinetics and reactor simulation, Catal. Today, 106 (2005) 41-46.
37. Essaki K, Nakagawa K, Kato M, Uemoto H. CO_2 absorption by lithium silicate at room temperature. J. Chem Eng Jpn 2004;37(6):772e7.
38. Kato M, Nakagawa K, Essaki K, Maezawa Y, Takeda S, Kogo R, et al. Novel CO2 absorbents using lithium-containing oxide. Int J Appl Ceramic Technol. 2005;2(6):467e75.
39. Kato, M., Yoshikawa, S., Nakagawa, K., Carbon dioxide absorption by lithium orthosilicate in a wide range of temperature and carbon dioxide concentrations, J. Mater. Sci. Lett. (2002) 21, 485.
40. Ebner, A. D.; Reynolds, S. P.; Ritter, J. A. Non-equilibrium kinetic model that describes the reversible adsorption and desorption behavior of CO2 in a K-promoted hydrotalcite-like compound. Ind. Eng. Chem. Res. 2007, 46, 1737–1744.
41. Ebner, A. D.; Reynolds, S. P.; Ritter, J. A. Understanding the Adsorption and Desorption Behavior of CO_2 on a K-Promoted HTLC Through Non-Equilibrium Dynamic Isotherms. Ind. Eng. Chem. Res. 2006, 45, 6387.
42. Ding, Y., Alpay, E. High temperature recovery of CO_2 from flue cases using hydrotalcite adsorbent. Trans IChemE. 79-B1 (2001) 45–51.
43. Ding, Y., Alpay, E. Eluilbria and kinetics of CO_2 adsorption on hydrotalcite adsorbent. Chem. Eng. Sci. 55 (2000) 3461–3474.
44. Lee, K. B.; Verdooren, A.; Caram, H. S.; Sircar, S. Chemisorption of carbon dioxide on potassium-carbonate-promoted hydrotalcite. J. Colloid Interface Sci. 2007, 308, 30–39.
45. Oliveira, E. L. G.; Grande, C. A.; Rodrigues, A. E. CO_2 Sorption on hydrotalcite and alkali-modified (K and Cs) hydrotalcites at high temperatures. Sep. Purif. Technol. 2008, 62, 137–147.
46. Leon, M; Diaz, E.; Bennici, S.; Vega, A.; Oronez, S.; Auroux, A. Adsorption of CO_2 on Hydrotalcite-Derived Mixed Oxides: Sorption Mechanisms and Consequences for Adsorption Irreversibility. Ind. Eng. Chem. Res. 47 (2010) 3663–3671.
47. Yang, J.; Kim, J.-N. Hydrotalcite for adsorption of CO_2 at high temperature. Korean J. Chem.Eng. 23 (2006) 77-80.
48. Ding, Y., Alpay, E. Adsorption-enhanced steam-methane reforming. Chem. Eng. Sci. 55 (2000) 3929–3940.
49. Lee, K. B.; Beaver, M. G.; Caram, H. S.; Sircar, S. Novel Thermal Swing Sorption Enhanced Reaction Process Concept for Hydrogen Production by Low Temperature Steam-Methane Reforming. Ind. Eng. Chem. Res. 2007, 46, 5003.
50. Beaver, M. G.; Caram, H. S.; Sircar, S. Sorption enhanced reaction process for direct production of fuel-cell grade hydrogen by low temperature catalytic steam-methane reforming. J. Power Sour. 195 (2010) 1998-2002.
51. Halabi, M.H., de Croon, M.H.J.M, van der Schaaf, J., Cobden, P.D., Schouten, J.C., Low temperature catalytic methane–steam reforming over ceria–zirconia supported rhodium, App. Catal. A (2010) doi:10.1016/j.apcata.2010.09.004.
52. Halabi, M.H., de Croon, M.H.J.M, van der Schaaf, J., Cobden, P.D., Schouten, J.C., Intrinsic kinetics modeling of catalytic methane–steam reforming and

water–gas shift over $Rh/Ce_{\alpha}Zr_{1-\alpha}O_2$ catalyst, App. Catal. A (2010) doi:10.1016/j.apcata.2010.09.005.
53. Halabi, M.H., de Croon, M.H.J.M, van der Schaaf, J., Cobden, P.D., Schouten, J.C., Kinetic and structural requirements for a CO_2 adsorbent in sorption enhanced catalytic reforming of methane. Part I: Reaction kinetics and sorbent capacity, Ind. Eng. Chem. Res., submitted, 2010.
54. Halabi, M.H., de Croon, M.H.J.M, van der Schaaf, J., Cobden, P.D., Schouten, J.C., Kinetic and structural requirements for a CO_2 adsorbent in sorption enhanced catalytic reforming of methane. Part II: Bed characteristics, Ind. Eng. Chem. Res., submitted, 2010.
55. Hutson, N.D.; Attwood, B.C. High temperature adsorption of CO_2 on various hydrotalcite-like compounds. Adsorption 14 (2008) 781-789.
56. Hutson, N.D.; S.A. Speakman; Payzant E.A. Structural effects on the high temperature adsorption of CO_2 on a synthetic hydrotalcite. Chem.Matter. 16 (2004) 4135-4143.
57. van Selow, E.R.; Cobden, P. D.; Verbraeken, P.A.; Hufton, J.R.; van den Brink, R. W. Carbon capture by sorption-enhanced water-gas shift reaction process using hydrtotalcite-based material. Ind.Eng.Chem.Res. 48 (2009) 4184-4193.
58. Reijers, H. Th. J.; Boon, J.; Elzinga, G. D.; Cobden, P. D.; Haije, W.G.;van den Brink, R. W. Modeling study of the sorption-enhanced reaction process for CO_2 capture. I. model development and validation. Ind. Eng. Chem. Res., 2009, 48, 6966-6974.

Chapter 10

Conclusions and Future Perspective

10.1 Conculsions

$Rh/Ce_{\alpha}Zr_{1-\alpha}O_2$ catalyst and K_2CO_3-promoted hydrotalcite are experimentally demonstrated as novel catalyst/sorbent materials for an efficient H_2 production with in situ CO_2 capture at a low temperature (400–500 ^{o}C) and a pressure (1.5–4.5 bar). The effect of temperature, pressure, and steam/carbon ratio on the process performance is illustrated. Direct production of high H_2 purity and fuel conversion (>99%) with low level of carbon oxides impurities (<100 ppm) is achieved. Therefore, it can be stated that the sorption–enhanced steam reforming process is significantly improved in terms of CH_4 conversion and H_2 purity using much smaller reactor size and much less catalyst/sorbent ratio. Despite the expensive price of Rhodium compared to the conventional Ni catalyst, the enormous reduction of the reactor size, material loading, catalyst/sorbent ratio, and energy requirements are beneficial key factors for the success of the concept. Small size H_2 production plants for residential or industrial applications operated at relatively low pressure range (<4.5 bar) seem to be a realistic investment according to the results obtained in this work. However, the optimal operational pressure is a trade off between the fuel conversion and the operational time from one side and low product impurity on the other side.

CO_2 adsorption on a new K-hydrotalcite material is experimentally studied at 400 ^oC. The equilibrium sorption data obtained from the column apparatus can be adequately described by the Freundlich isotherm. The sorbent shows fast adsorption rates and attains a relatively high sorption capacity of 0.95 mol/kg on the fresh material. Large portion of CO_2 is easily recovered in the first few minutes of a typical desorption cycle as a result of a fast desorption step, which is associated with a physic/chemisorption step on the monolayer surface of the fresh sorbent. The complete recovery of CO_2 was then achieved in a slower desorption step associated with a reversible chemisorption in a multi-layer surface of the sorbent. CO_2 release during the desorption experiments is attributed to the decarbonation process through the loss of the interlayer charge compensating anion (CO_3^{2-} evolved as CO_2). The sorbent shows a loss of 8% of its fresh capacity due to an irrespirable chemisorption, however, it preserves a stable working capacity of about 0.89 mol/kg suggesting a reversible chemisorption process. Cyclic experiments indicated a good thermal stability of the sorbent in the temperature range of (400–500 ^oC).

$Rh/Ce_\alpha Zr_{1-\alpha}O_2$ is selected as an effective catalyst which provides high reaction rates low–temperature sorption–enhanced steam reforming of methane in order to maintain a high CO_2 sorption capacity of the sorbent. The catalytic and the mechanistic aspects of the methane steam reforming are experimentally studied over the catalyst in the temperature range of 475–700 ^oC. The forward steam reforming reaction rates show a nonlinear dependency on CH_4 and steam partial pressures with a positive reaction order of less than 1 in a temperature range of 475–625 ^oC. CH_4 conversion and reforming rates are found to be retarded by H_2, CO, and CO_2 and a negative effect is demonstrated at all investigated conditions. Strong inhibition of the CH_4 conversion rates is observed at high partial pressures of (H_2, CO, and CO_2) due to the promotion of the reverse water–gas shift and methanation reactions. Temperature–programmed steam reforming experiments on the ceria-zirconia support reveal that insignificant CH_4 adsorption can be attained at the temperature range of interest (<700 ^oC). The catalyst shows high stability and resistance towards carbon formation even at low steam/carbon ratio of 1. A molecular reaction mechanism based on a two-site surface hypothesis is proposed to successfully describe the qualitative kinetic observations.

The intrinsic kinetics of CH_4 steam reforming over $Rh/Ce_\alpha Zr_{1-\alpha}O_2$ catalyst is developed in a relatively low temperature range of 475–575 ^oC and a pressure of 1.5 bar. The kinetic experiments are conducted in an integral fixed bed reactor with no mass and heat transport limitations and far from equilibrium conditions. The model is derived according to the L-H formalism and it is found to be statistically accurate and thermodynamically consistent. The estimated activation energies and adsorption enthalpies are in agreement with literature for CH_4 steam reforming over Rh. The reaction kinetics is validated by steam reforming experiments at 550 ^oC and 1.5 bar using 150 mg catalyst in a diluted bed of 5 cm length. The simulation results are in excellent agreement with the experimental values.

The presence of an active catalyst such as Rh in an integrated reaction/adsorption process imposes strict requirements on the associated sorbent in terms of fast adsorption kinetics for an efficient performance of the steam reforming process. The K-promoted hydrotalcite and lithium zirconate sorbents are identified in terms of the adsorption kinetic limitations and the capacity requirements for a high CH_4 conversion and H_2 purity (>99%) with ppm level of carbon oxides impurities. The process performance is evaluated in terms of the optimal catalyst/sorbent ratio, and the catalyst/sorbent configuration in an integrated dual-function particle and in an admixture reaction bed.

Hydrotalcite–based system should provide adsorption rates with a corresponding CO_2 effective mass transfer coefficient (> 10^{-1} 1/s) at 550 ^oC. Lithium zirconate–based system should have a CO_2 adsorption rate constant in the range of 10^{-2} m^3/mol.s at 550 ^oC. The CH_4 conversion enhancement is not affected by higher sorbent capacity at slow adsorption kinetics. Optimal catalyst/sorbent ratio is determined to be a function of the operating conditions. This ratio is represented by a catalyst composition of 1–3 % at low temperature of 550^oC, intermediate pressure of 4.65 bar, and low gas flow rate of 0.05 kg/m^2.s. The catalyst composition is increased to 10% at higher pressure of 15 bar and higher gas flowrate of 1.5 kg/m^2.s.

CH_4 conversion enhancement is studied at different temperature and pressure. The maximum enhancement in CH_4 conversion is found to be 276% at low temperature of 450 ^oC and high pressure of 15.6 bar using 5 mol/kg of hydrotalcite capacity; at which ($CO+CO_2$) impurities can be as low 100 ppm. Lithium zirconate–based system can provide CH_4 conversion and H_2 purity of 99.9% at identical conditions. The dual function particle system and the admixture bed system show a very similar performance in terms of maximum CH_4 conversion and product composition in case of the lithium zirconate sorbent. Discrepancy in performance is observed in case of the hydrotalcite sorbent.

The performance of the autothermal reforming of methane over a conventional Ni-based catalyst is optimized in a fixed bed reactor in terms of fuel conversion, H_2 purity, and thermal efficiency. Improved performance of the autothermal reforming process is determined to yield a CH_4 conversion of 93%, a reformer thermal efficiency of 78%, a H_2 yield and purity of 2.6 and 73%, respectively using an oxygen/carbon ratio of 0.45, a steam/carbon ratio of 6, a feed temperature of 500^oC, a pressure of 1.5 bar, and a GHSV of 3071 hr^{-1}. The reformer temperature and product gas composition are directly affected by the operating ratios of steam/carbon and oxygen/carbon in the feed, in addition to feed temperature and residence time along the catalyst bed. Unsuitable feed composition, i.e. high oxygen partial pressure (corresponding to an oxygen/carbon ratio greater than 0.45) at high-pressure operation (greater than 4.5 bar), can generate serious hot-spot formation at the catalyst surface. High-pressure operation will lower the fuel conversion and demands high steam loads (steam/carbon ratio).

The performance of the sorption–enhanced autothermal reforming process is mathematically analyzed over a conventional Ni-based catalyst and two potential sorbents of hydrotalcite and lithium zirconate in a fixed bed reactor. Pure H_2 production and simultaneous in situ CO_2 capture tend to be applicable in such a technique even at a temperature as low as 500 ^oC with respect to reforming reactions and at a pressure as low as 4.47 bar with respect to CO_2 adsorption. The hydrotalcite–based autothermal reforming process can provide CH_4 conversion and H_2 purity up to 85% and 96%, respectively. The process performance is found to benefit from low space velocity operation (0.05 kg/m^2s), low pressure (4.47 bar), smaller particle size (0.5–1 mm), high steam/carbon ratio (6), and high sorbent capacity (2 mol/kg). Lithium zirconate provides higher CO_2 adsorption capacity than hydrotalcite although it shows slower adsorption rates. This is strongly reflected in the high CH_4 conversion and H_2 productivity obtained up to 100% in addition to the large operational time. Thus, the system investigated in this work can be considered as a significant improvement over the conventional processes of steam reforming or autothermal reforming of methane.

10.2 Future perspective

The conventional technology for steam reforming or autothermal reforming processes based on a fixed bed reactor suffers from several limitations such as: (i) severe diffusion limitations where the catalyst effectiveness factor can be as low as (10^{-2}), (ii) poor heat transfer, pressure drop limitation at small particle size, (iii) partial oxidation reactions result in a large temperature gradient due to the high reaction rates (even it is mildly exothermic), (iv) catalyst deactivation, (v) carbon formation at high temperatures, (vi) stringent control of feed compositions (i.e, oxygen/fuel) is certainly necessary for operating outside the flammability limits, (vii) thermodynamic limitations in fuel conversion and H_2 yield necessitate further unit operations of water-gas shift reactors and CO_2 separation units.

Despite the challenging problems associated with the catalytic steam reforming of methane, it is still the worldwide major route for H_2 production from natural gas. The end application of H_2 produced seems to determine the optimal technology to be used. It is seriously influenced by the feedstock and the economics of scale. Thus, plenty of modifications in the process design and the operation can be applied to make it more efficient.

Using the newly developed catalyst/sorbent materials reported in this work, it is practically possible to design a dual-functionality particle to carry out the reforming reactions and simultaneously the CO_2 separation in a fluidized bed. Thus, a promising alternative for the conventional steam reforming and autothermal reforming processes can emerge. This concept provides intrinsic advantages in design and operation such as: (i) integration of the basic process units (Reforming, WGS, CO_2 separation) is achieved in one single unit, (ii) self-supply energy

requirements, (iii) uniform and relatively lower temperatures (<550^{o}C), (iv) low-pressure drop, and (v) lower carbon deposits due to continuous solid circulation.

One focal theme of future research is concerned with the CO_2 sorption kinetics of lithium zirconate. A challenging path persists in modifying the structure of lithium zirconate to suppress any diffusional limitations and eventually yields high CO_2 sorption rates.

A possible view for an experimental proposal is to study the impregnation of lithium zirconate with hydrotalcite and vice versa. This may enhance the CO_2 adsorption kinetics of lithium zirconate due to the presence of hydrotalcite and may increase the CO_2 sorption capacity and the thermal resistance of hydrotalcite due to the presence of lithium zirconate. A potential particle design configuration of shell-core catalyst-sorbent and/or sorbent-catalyst materials can be an interesting topic for further experimental investigation.

CO_2 capture and storage in geological formation is nowadays an attractive solution to overcome the global warming effect. However, it is discerned to be more attractive if the captured CO_2 is reused in useful petrochemical industries as a source of hydrocarbon. Indeed, this route encounters a lot of challenges on the level of catalysis in the first place and the process design in the subsequent stages. However, more future research should be implicated on such a technique. In conclusion, if H_2 production from renewable energy sources such as water, wind, solar, or geothermal energy becomes an economically feasible technology within the next 50 years, thus H_2 is undoubtedly the future green energy carrier with zero emissions.

List of Publications

Refereed Journal Publications

1. M.H. Halabi, M.H.J.M. de Croon, J. van der Schaaf, P.D. Cobden, J.C. Schouten, Modeling and analysis of autothermal reforming of methane for hydrogen production in fixed bed reformers, Chem. Eng. J., 137, 568–578, 2008.

2. M.H. Halabi, M.H.J.M. de Croon, J. van der Schaaf, P.D. Cobden, J.C. Schouten, Low temperature catalytic methane steam reforming over ceria–zirconia supported rhodium catalyst, Applied Catalysis A, 389, 68–79, 2010.

3. M.H. Halabi, M.H.J.M. de Croon, J. van der Schaaf, P.D. Cobden, J.C. Schouten, Intrinsic kinetics of low temperature catalytic methane–steam reforming and water gas shift over $Rh/Ce_{\alpha}Zr_{1-\alpha}O_2$ catalyst, Applied Catalysis A, 389, 80–91, 2010.

4. M.H. Halabi, M.H.J.M. de Croon, J. van der Schaaf, P.D. Cobden, J.C. Schouten, Reactor modeling of sorption–enhanced autothermal reforming of methane. Part I: Performance study of hydrotalcite and lithium zirconate–based processes, Chem. Eng. J, doi:10.1016/j.cej.2011. 02.015, 2011.

5. M.H. Halabi, M.H.J.M. de Croon, J. van der Schaaf, P.D. Cobden, J.C. Schouten, Reactor modeling of sorption–enhanced autothermal reforming of methane. Part II: Effect of operational parameters, Chem. Eng. J. doi:10.1016/j.cej.2011.02.016, 2011.

6. M.H. Halabi, M.H.J.M. de Croon, J. van der Schaaf, P.D. Cobden, J.C. Schouten, A novel catalyst–sorbent system for an efficient H_2 production with in-situ CO_2 capture, Int. J. Hydrogen Energy, accepted, 2011.

7. M.H. Halabi, M.H.J.M. de Croon, J. van der Schaaf, P.D. Cobden, J.C. Schouten, High capacity potassium promoted hydrotalcite for CO_2 capture in H_2 production, Int. J. Hydrogen Energy, accepted, 2011.

8. M.H. Halabi, M.H.J.M. de Croon, J. van der Schaaf, P.D. Cobden, J.C. Schouten, Kinetic and structural requirements for a CO_2 adsorbent in sorption enhanced catalytic reforming of methane. Part I: Reaction kinetics and sorbent capacity, Fuel, submitted, 2011.

9. M.H. Halabi, M.H.J.M. de Croon, J. van der Schaaf, P.D. Cobden, J.C. Schouten, Kinetic and structural requirements for a CO_2 adsorbent in sorption enhanced catalytic reforming of methane. Part II: Bed characteristics, Fuel, submitted, 2011.

10. M.H. Halabi, M.H.J.M. de Croon, J. van der Schaaf, P.D. Cobden, J.C. Schouten, Experimentally–based model validation for pure H_2 generation in sorption–enhanced methane steam reforming using novel catalyst–sorbent materials , Int. J. Hydrogen Energy, to be submitted, 2011.

11. M.H. Halabi, M.H.J.M. de Croon, J. van der Schaaf, P.D. Cobden, J.C. Schouten, Model–based comparison of different catalytic methane reforming routes over an effective catalyst–sorbent, Ind. Eng. Chem. Res., to be submitted, 2011.

Conferences

12. M.H. Halabi, M.H.J.M. de Croon, J. van der Schaaf, P.D. Cobden, J.C. Schouten, Experimental and modeling study of sorption enhanced catalytic methane reforming to pure hydrogen with in situ carbon dioxide capture. In P.A. Tanguy (Ed.), Proceedings of the 8th World congress of Chemical Engineering (WCCE8), 23–27Aug., (pp. 1199), Montreal, Canada, (2009).

13. M.H. Halabi, M.H.J.M. de Croon, J. van der Schaaf, P.D. Cobden, J.C. Schouten, A novel catalyst-sorbent system for an efficient H_2 production with in situ CO_2 capture. 21st North American Catalysis Society Meeting (NAM-21), 7–12 Jun., San Francisco, California, USA. (pp. OC21). USA, (2009).

14. M.H. Halabi, M.H.J.M. de Croon, J. van der Schaaf, J.C. Schouten, Experimental and modeling analysis of catalytic reforming of methane to hydrogen in an adsorption enhanced fixed bed reactor, in Proc. 10th Netherlands Catalysis and Chemistry Conference; Noordwijkerhout, Netherlands, pp. 77-77, (2009).

15. M.H. Halabi, M.H.J.M. de Croon, J. van der Schaaf, J.C. Schouten, Molecular reaction mechanism for catalytic steam reforming of methane over $Rh/Ce_{\alpha}Zr_{1-\alpha}O_2$ catalyst at low temperatures, Netherlands Process Technology Symposium; Editors: -, Veldhoven, Netherlands, pp. 1, (2008).

16. M.H. Halabi, M.H.J.M. de Croon, J. van der Schaaf, P.D. Cobden, J.C. Schouten, Mechanism and kinetics of methane steam reforming over ceria - zirconia supported rhodium catalyst at temperatures below 700 ^{o}C, in Proc. 20th Int. Symp. on Chemical Reaction Engineering; Editors: -, Kyoto, Japan, (2008).

17. M.H. Halabi, M.H.J.M. de Croon, J. van der Schaaf, P.D. Cobden, J.C. Schouten, Molecular mechanism and intrinsic kinetics of catalytic steam reforming of methane over Rh/$Ce_{\alpha}Zr_{1-\alpha}O_2$ as an efficient catalyst for H_2 production with in situ CO_2 capture, 5th Int. Conference on Environmental Catalysis, 31 Aug.–3 Sep., Belfast, UK, (2008).

18. M.H. Halabi, M.H.J.M. de Croon, J. van der Schaaf, J.C. Schouten, Determination of molecular reaction kinetics for catalytic methane steam reforming over Rh/$Ce_{\alpha}Zr_{1-\alpha}O_2$ at low temperatures, in Proc. 9th Netherlands Catalysis and Chemistry Conference; Editors: -, Noordwijkerhout, Netherlands, (2008).

19. M.H. Halabi, M.H.J.M. de Croon, J. van der Schaaf, J.C. Schouten, Modeling of an adsorptive fixed bed reactor for sorption enhanced autothermal reforming of methane using hydrotalcite and lithium zirconate solids, in Netherlands Process Technology Symposium; Editors: -, Veldhoven, Netherlands, pp. 1, (2007).

20. M.H. Halabi, P.D. Cobden, M.H.J.M. de Croon, J. van der Schaaf, J.C. Schouten, Modeling and analysis of autothermal reforming of natural gas: optimal operation in fixed bed reformers, in Proc. Europacat VIII; Editors: -, Turku, Finland, P10-18, (2007).

21. M.H. Halabi, M.H.J.M. de Croon, J. van der Schaaf, J.C. Schouten, Modeling and simulation of sorption enhanced autothermal reforming of methane using hydrotalcite and lithium zirconate sorbents, in Book of Abstracts Netherlands Catalysis and Chemistry Conference; Editors: -, Noordwijkerhout, Netherlands, P52, page 204, (2007).

22. P.D. Cobden, R.W. van den Brink, M.H. Halabi, M.H.J.M. de Croon, J.C. Schouten, Sorption-enhanced reforming of methane for electricity production and CO_2 capture, in Proc. 2nd Int. Workshop on In-Situ CO_2 removal (ISCR); Editors: -, Stuttgart, Germany, pp 1., (2005).

23. M.H. Halabi, M.H.J.M. de Croon, J. van der Schaaf, J.C. Schouten, A molecular kinetic study on catalytic steam reforming of methane over Rh/$Ce_{\alpha}Zr_{1-\alpha}O_2$ at low temperatures below 700^{o}C, in Schuit Institute of Catalysis Conference; Editors: -, St. Michielsgestel, Netherlands, pp 1., (2007).

Theses

24. M.H. Halabi, Sorption enhanced catalytic reforming of methane for pure hydrogen production: experimental and modeling, PhD thesis, Eindhoven University of Technology, 2010, The Netherlands.

25. M.H. Halabi, Photo-catalytic oxidation of contaminated water effluents, University of Twente, PD.Eng./M.Sc. thesis, 2003, The Netherlands.

26. M.H. Halabi, Design of a poly vinyl acetate production process, B.Sc. thesis, University of Jordan, Amman, 2001, Jordan.

Acknowledgement

After many extended years, a journey has come to an end, to inaugurate the onset of a new, mindful, and diligent path in my life. Once I was told “reach to the stars”, at the beginning I thought I could not even look at them, they are too far. Well, so much has changed since then, so much that distant future itself is now merely the day after tomorrow.

The stars are not that faraway. It is just a matter of ambition, hope, a little knowledge, and persistent work at least sufficient to put one on the right track. I admit I have found what it takes more.

In spite of there is no much thing as a “self-made” man, we are all made up of thousands of others. Thus, every one who had ever done a kind deed or spoken a word of encouragement has entered into my character and my thoughts as well as my success.

Therefore, I find my self – as a truthful person – obligated to retaliate those who contributed to my achievement by at least a word of reward and appreciation. I would sincerely present my upmost gratitude for Prof. Jaap Schouten for the precious opportunity he offered me in joining the world of catalysis and reaction engineering from its widest gate. Your positive decision by “consent” to be a PhD student in your group had changed my life ever and has certainly made a dream to come true. I am thankful for your extreme professionalism from which I learned a lot and eagerly looking for more.

I am extremely grateful for the ingenious scientist and the insightful teacher I have ever experienced in my life until this moment. Undoubtedly, this gratefulness is rewarded to Dr. Mart de Croon, who had been my direct supervisor during the years of my PhD. I will be ever astounded by the extent of direct-use knowledge that Mart has in chemistry, reaction engineering, and mathematics. It is awkward to forget an incident that I might tell to my children in the future. I built up a solid mathematical model to calculate sorption/desorption time for CO_2 molecule into a catalyst-sorbent particle under complicated set of steam reforming reactions and CO_2 adsorption kinetics. I had successfully generated the results and analyzed them. Well, surprisingly, Mart checked my output by out-of-an-envelope calculations – on paper only – the calculated sorption time was incredibly the same. Thus, he proved me right, and certainly he left me astonished. Many thanks Mart for your straightforward assistance and your helpful input in all stages of my work.

I owe my deepest gratitude to a very shrewd mind, Dr. John van der Schaaf, who had been my second supervisor during my PhD research and who has been an idea-generator and an inspiring force in different aspects of my work. Many thanks John, and I am very delighted to pursue our cooperation in even more successful research on the multiple spinning disc reactor technology.

I am very thankful for the real engine of our group and the most efficient secretary I have ever seen, Denise Tjallema–Dekker. You have been always a source of assistance and vigilant management for my paper work, meetings, conferences, and any other arrangements.

I am truly indebted to the wonderful, kind, and willingly helpful technicians: Frank Grootveld, Madan Bindraban, and Erik van Herk. Though, you are now a design engineer Madan. It is a sound fact that this project and its on-ground success would have not come true without your ever-ready assistance in all technical levels at construction and installation. Your contribution towards my work is not describable; I do appreciate and cherish your support. Furthermore, I express my appreciation for many people who effectively influenced the experimental wheel of my work, Anton Bombeeck, Dolf van Liempt, Marlies Coolen-Kuppens, and Carlo Buis.

Indeed, there is a key figure in the development of this project from our collaboration partner, Paul Cobden, at the Energy Research Center of the Netherlands (ECN). I am very grateful for your unconditional cooperation, fruitful discussions, concepts explanations, nice travels and conversations in formal and non-formal meetings. I really treasure your input and assistance.

I also would like to cordially thank all my friends, office mates, fellows, and colleagues, the old and the current soldiers of the SCR group, and the ST department. We all have shared the pressure, the pain, and yet the progress as well. Nonetheless, you have made my stay in research full of joy and splendid times amongst you guys. However, I should not forget to namely present my appreciation for Wim Gaakeer for translating the thesis summary into Dutch.

Finally, I barely find any words but to dedicate my success to my most loving, caring, and supportive family that I am proud of. My gorgeous sisters and my gentle brothers have ever been my innermost driving force for any step forward in life. You have always considered me as your model; and I have always seen you as my cause. I adore you all.

Eindhoven
15 October 2010

About the author

Mohamed Halabi was born in June 15th, 1978 in Mafraq, Jordan. He received the General Certificate of Secondary Education (GCSE) – scientific stream in July 1996. The author read chemical engineering at university of Jordan in Amman. In September 2001, he obtained his B.Sc. degree with a GPA (major) of 3.5 out 4.0. Six months earlier to his graduation, he was selected by Prof.dr.ir Geert Versteeg and Dr.ir. Bert Heesink to be appointed as a research assistant in the process development school at university of Twente. In December 2003, he acquired his Professional Doctor of Engineering degree (PD.Eng.), formerly called Master of Technological Design (MTD), in process technology. He performed his P.D.Eng. research thesis in the field of photo-electro-bio-catalysis of contaminated water effluents at university of Groningen under the supervision of Prof.dr.ir. Leon Janssen. In December 2003, he was employed as a project engineer at the Process Design Center in Dortmund, Germany. In the same time, he joined the laboratory of process dynamics and operations (formerly called process control) at university of Dortmund as a research associate. He was in charge of a research project in the area of modeling and optimization of complex reactor networks using the mixed integer nonlinear programming techniques (MINLP) under the supervision of Prof.Dr.-Ing. Sebastian Engell. He contributed to teaching in several courses in process control, modeling, and optimization. In September 2005, the author joined the laboratory of chemical reactor engineering to pursue his PhD degree in the field of multiphase reaction engineering under the supervision of Prof.dr.ir. Jaap Schouten and direct guidance of Dr. Mart de Croon and Dr.ir. John van der Schaaf. The PhD research project is entitled "Sorption enhanced catalytic reforming of methane for pure hydrogen production – experimental and modeling". The project was funded by *SenterNovem* and performed in collaboration with the Energy Research Center of the Netherlands (ECN). The results of the work have been reported in this thesis and published in several journals and international conferences. Since December 2010, the author has been appointed as a postdoctoral research fellow at the same group of Prof.dr.ir. Jaap Schouten working on the application of the multiple spinning disc reactor technology.